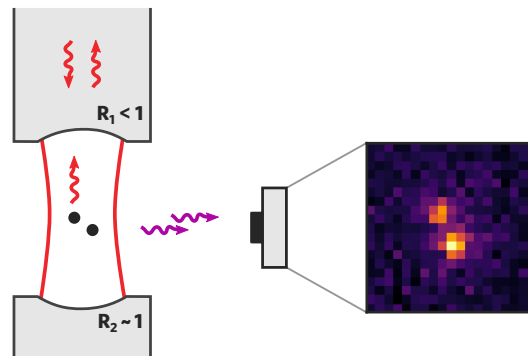


Control of Atoms in a High-Bandwidth Cavity for Quantum Nodes

Dissertation
zur
Erlangung des Doktorgrades (Dr. rer. nat.)
der
Mathematisch-Naturwissenschaftlichen Fakultät
der
Rheinischen Friedrich-Wilhelms-Universität Bonn

vorgelegt von
José Eduardo Uruñuela Castellero
aus
Guadalajara, Mexiko



Bonn, 2022

Angefertigt mit Genehmigung der Mathematisch-Naturwissenschaftlichen Fakultät der Rheinischen
Friedrich-Wilhelms-Universität Bonn

1. Gutachter: Prof. Dr. Dieter Meschede
2. Gutachter: Prof. Dr. Sebastian Hofferberth

Tag der Promotion: 20.12.2022
Erscheinungsjahr: 2023

A Natalia, por acompañarme en este camino sinuoso sin dudarlo.

A mi abuelo Marcelo, por enseñarme que “vivir es siempre ir de camino, en busca y construcción del propio destino en el tiempo”.

Abstract

Optical cavities with coupled atoms are a promising platform as the nodes of future quantum networks, enabling interchange of information between single atoms and single photons. In particular, fiber-based high-bandwidth cavities offer convenient and efficient routing of quantum information, in an interesting regime that combines strong coupling with the atom and high-rate information exchange with the quantum channel. However, critical control of coupled atoms for the quantum node operation, is hindered by the strong Purcell effect, the miniaturized geometry and the high-bandwidth property of such cavities.

In this thesis, I report on my contributions towards a high level of control of individual atoms coupled to a high-bandwidth cavity. To this end, three new experimental techniques were developed specially adapted to high-bandwidth fiber cavities, with the following specific goals: (i) intracavity ground-state cooling of single atoms; (ii) atom position detection by fluorescence imaging independent from the cavity transition; (iii) cavity loading of small atomic ensembles with increased density.

In the first part of this work, I present the experimental setup, consisting of a fiber Fabry-Pérot cavity (FFPC) coupled to ^{87}Rb atoms, and the necessary experimental apparatus to operate the system in a stable manner. I start by motivating the advantage of high-bandwidth cavities with a brief discussion on cavity-mediated light-matter interfacing, and the peculiar strong coupling regime. Then, I give an overview of the complete system with emphasis on the recent technical upgrades, such as an improved cavity stabilization, an upgraded Raman laser setup with a linewidth-reduced DBR laser, and a new cavity-compatible imaging system. Lastly, I introduce the basic experimental toolbox for atomic control that we employ to operate the atom-cavity module: (i) cavity-based atom detection; (ii) cooling with a magneto-optical trap (MOT) and trapping with a 3D lattice; (iii) state initialization by optical pumping; (iv) Raman hyperfine manipulation; (v) position detection by imaging. Most of my work was to extend such basic toolbox for an improved atomic control, with the techniques presented in the next chapters.

In Chapter 3, I report successful cooling of a single ^{87}Rb atom to its one-dimensional motional ground state while coupled to the FFPC, by degenerate Raman sideband cooling (dRSC). We overcome the challenge of cooling in such high-bandwidth atom-cavity modules, by adapting the degenerate dRSC technique to our cavity and lattice geometry. Raman cooling transitions are driven by the trapping lattice and repumping by the intracavity probe field, without the need of additional lasers and activated by the magnetic bias field. The resource-efficient and simple implementation is a highlight.

In Chapter 4, I present a newly implemented method in our system for successful fluorescence imaging of small atomic ensembles coupled to a high-bandwidth FFPC, that overcomes the inhibiting Purcell effect and the restricted optical access. It is based on techniques from the field of quantum gas microscopes and relies on the detection of repumper fluorescence on the D_1 line generated by three-dimensional (3D) continuous Raman sideband cooling (cRSC). Thus, it remains fully independent from the cavity on the D_2 line, for simultaneous operation of the atom-cavity node and position detection of the atoms. It requires only a single free-space beam together with intra-cavity fields, ideal for platforms with limited optical access, e.g. miniaturized quantum optical devices. The repumper-induced differential light shifts and the heating by dipole-force fluctuations (DFFs) are also analyzed.

In Chapter 5, I introduce a novel and simple method to load the intracavity lattice: the drive-through loading. It only relies on the dynamic control of intensity and phase of one lattice arm that works as a conveyor belt between the MOT and the intracavity lattice. I discuss the working principle of the technique, demonstrate that its efficiency, and show its tuning capability of the cavity-coupled atom number. In the last chapter, I summarize the advances presented here that extend the toolbox for control and manipulation of atom-cavity systems, impacting in the development of quantum networks. The three new techniques presented here, with a future implementation of single-atom addressing, pave the way for creating atomic arrays with predefined number and positions in the cavity: a cavity-quantum register.

Parts of this thesis have been published in peer-reviewed journals:

- [1] E. Uruñuela, W. Alt, E. Keiler, D. Meschede, D. Pandey, H. Pfeifer, and T. Macha, *Ground-state cooling of a single atom inside a high-bandwidth cavity*, (2020), Physical Review A **101**, 023415. DOI: <https://doi.org/10.1103/PhysRevA.101.023415>
- [2] E. Uruñuela, M. Ammenwerth, P. Malik, L. Ahlheit, H. Pfeifer, W. Alt and D. Meschede, *Raman imaging of atoms inside a high-bandwidth cavity*, (2022), Physical Review A **105**, 043321. DOI: <https://doi.org/10.1103/PhysRevA.105.043321>

I have permission of all my co-authors and publishers to use the articles listed above in my dissertation. Reprints of the publications are included in Appendix [A](#) and Appendix [B](#) of this document.

Contents

| | | |
|----------|--|-----------|
| 1 | Introduction | 1 |
| 2 | Scientific apparatus and experimental toolbox | 5 |
| 2.1 | A fiber-based cavity for high-bandwidth quantum nodes | 5 |
| 2.1.1 | An atom-photon interface | 6 |
| 2.2 | Overview of the experimental apparatus | 10 |
| 2.3 | Manipulation and detection of degrees of freedom of the atoms: the basic toolbox . . . | 13 |
| 2.3.1 | Non-destructive cavity-based atom presence and state detection | 14 |
| 2.3.2 | Cooling and trapping: a small MOT and an intracavity 3D lattice | 15 |
| 2.3.3 | Optical pumping for state initialization and imaging illumination | 19 |
| 2.3.4 | Raman manipulation of the hyperfine states | 21 |
| 2.3.5 | Position detection by cavity-compatible imaging | 24 |
| 2.4 | Summary and conclusions | 25 |
| 3 | Ground-state cooling of a single atom inside a high-bandwidth cavity | 27 |
| 3.1 | Simple cavity-compatible cooling with degenerate Raman transitions | 28 |
| 3.2 | Summary and conclusions | 30 |
| 4 | Raman imaging of atoms inside a high-bandwidth cavity | 31 |
| 4.1 | Three-dimensional resolved Raman sideband cooling in the cavity | 33 |
| 4.2 | Differential light shifts in a continuous Raman cooling scheme | 34 |
| 4.3 | Fluorescence imaging with continuous Raman sideband cooling | 35 |
| 4.4 | Summary and conclusions | 37 |
| 5 | Delivery of small atomic ensembles into a fiber microcavity | 39 |
| 5.1 | Intracavity lattice loading by drive-through transport | 40 |
| 5.1.1 | Overview of the drive-through loading method | 40 |
| 5.1.2 | One-dimensional classical transport model and numerical simulation | 42 |
| 5.2 | Experimental implementation of drive-through atom loading | 48 |
| 5.2.1 | Indirect measurement of the loading probability with the cavity | 49 |
| 5.2.2 | Demonstration of the drive-through loading method | 51 |
| 5.2.3 | Optimization of other relevant experimental parameters | 54 |
| 5.3 | Summary and conclusions | 56 |
| 6 | Summary and Outlook | 57 |
| | Bibliography | 59 |

| | | |
|----------|--|------------|
| A | Publication: Ground–state cooling of a single atom inside a high–bandwidth cavity | 73 |
| A.1 | I. Introduction | 74 |
| A.2 | II. Experimental setup | 74 |
| A.3 | III. Cooling method | 75 |
| A.4 | IV. Results | 75 |
| A.5 | V. Conclusion | 76 |
| B | Publication: Raman imaging of atoms inside a high–bandwidth cavity | 79 |
| B.1 | I. Introduction | 80 |
| B.2 | II. Experimental setup and methods | 81 |
| B.3 | III. Imaging with Raman cooling | 82 |
| B.4 | IV. Differential light shifts during continuous Raman sideband cooling | 83 |
| B.5 | V. Balancing cooling and heating dynamics with imaging parameters | 85 |
| B.6 | VI. Conclusion | 86 |
| B.7 | Appendix A: Linewidth-reduction prepares DBR laser for phase locking | 87 |
| B.8 | Appendix B: Three-dimensional continuous Raman sideband cooling with one free-space beam only and intracavity fields | 88 |
| B.9 | Appendix C: Justification and limitations of the two-level light-shifts model | 89 |
| B.10 | Appendix D: Dipole-force fluctuations and Monte Carlo simulation | 91 |
| | B.10.1 Scattering in dressed-state potentials | 92 |
| | B.10.2 Details of the Monte Carlo loop algorithm | 92 |
| C | The drive-through loading method: supplementary details | 97 |
| C.1 | Numerical simulation of 1D transport: implementation details | 97 |
| C.2 | Effect of transport velocity and cooling: comparison of experiment and simulation | 98 |
| C.3 | Preliminary characterization of the atom position distribution | 99 |
| D | Our high–bandwidth FFPC: supplementary material | 101 |
| D.1 | Cavity finesse degradation and permanent damage | 101 |
| D.2 | Relevant parameters of our FFPC system | 102 |

Introduction

ONE single atom placed between two tiny mirrors — a cavity, fabricated on the tips of optical fibers thin like hairs — interacts and exchanges information bits with a single quantum of light — a photon — that bounces thousands of time between the mirrors. While this idealistic scenario could well be worthy of an Isaac Asimov’s novel, it is in fact presently the core research of multiple state-of-the-art laboratories around the globe to develop new quantum technologies.

Harnessing the ability of a cavity to interface single atoms and single photons is a good illustrative example of the current *second quantum revolution* [3, 4]. This revolution applies the knowledge of the quantum world acquired from the first quantum revolution to create quantum technology devices for a broad range of applications. Along this line, the discovery by E. M. Purcell that a cavity can modify the emission properties of an atom is now an essential piece for the development of a *quantum internet* [5, 6], as will become clear later. Nowadays quantum technology has become so integrated in our society, that recently the first mobile phone with a quantum chip arrived on the market [7, 8].

A major goal pursued in quantum technology during the last decades has been to create quantum networks [9, 10] that would allow to distribute quantum information in an analogous way to distributing classical information via the present internet [5, 6]. In quantum networks, flying qubits travel through quantum channels, which are interconnected by quantum nodes capable of generating, processing and storing quantum information in the form of stationary matter qubits [11]. Given the wide spread use of optical fibers, optical photons are ideal candidates for flying qubits. However, much effort has been invested into different platforms to implement the nodes [12, 13], which have to fulfill stringent requirements to enable efficient, deterministic and coherent exchange of quantum information between the photons and the matter counterpart.

Presently, cavity quantum electrodynamics (CQED) is a well established platform to serve as the quantum nodes [14–16], enabling interchange of quantum information between single atoms (matter qubits) and single photons [17–20]. Fiber-based Fabry-Perot cavities (FFPCs) [21–23] offer a promising approach, that combines strong atom-cavity coupling g and strong Purcell effect in a cavity with high-bandwidth κ [24], characterized by $g, \kappa \geq \gamma$ and $g \approx \kappa$ with γ the free space decay rate of the atom. The main breakthrough of such miniaturized cavities is that they allow for information flow at high-rates, while still providing the necessary conditions for the strong coupling regime, with a cooperativity $C = \frac{g^2}{2\kappa\gamma} \gg 1$. This unique feature of FFPCs arises from their highly confined mode volume V that boosts the coupling strength $g \propto \frac{1}{\sqrt{V}}$.

A single-sided design, with one mirror of higher reflectivity than the other as shown in Figure 1.1 (a), further positions FFPCs as an ideal platform for quantum nodes: the intrinsic fiber coupling to a single input-output channel enables convenient and efficient routing of photons carrying quantum information

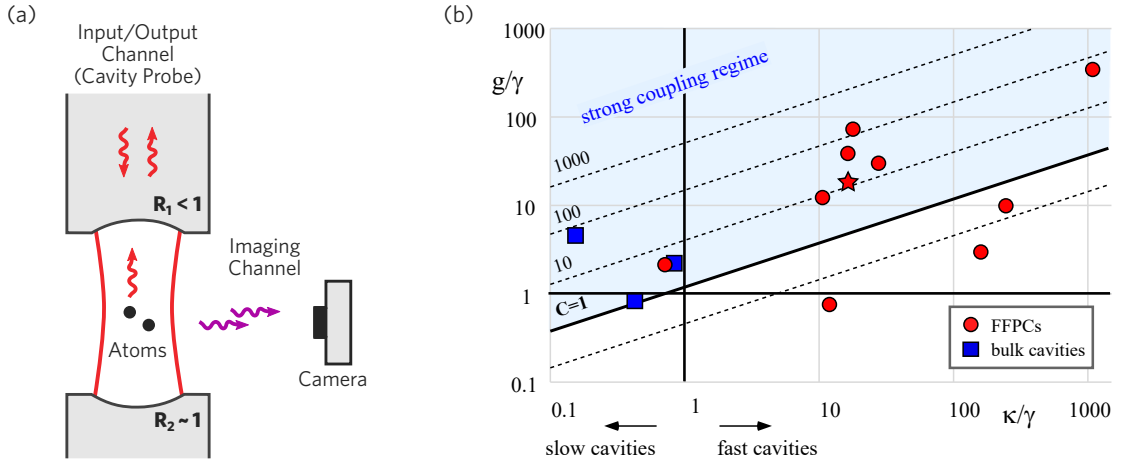


Figure 1.1: **(a)** A high-bandwidth and single-sided FFPC (reflectivities $R_1 < R_2 \simeq 1$) serves to efficiently interface atomic qubits with photonic quantum information routed on a fiber network through the quantum channel. Complementary information of number and position of the atoms is obtained through the imaging channel. The two channels are kept independent by operating at different atomic transitions. Figure from the publication [2], summarized in Chapter 4 and included in Appendix B. **(b)** Survey of cavity QED experiments (non-exhaustive) with normalized parameters $\{g, \kappa, \gamma\}$ and $C = g^2/2\kappa\gamma$ as presented in Ref. [23]. Experiments using FFPCs (in red, from left to right [24–32]) are shown with respect to atom-field coupling strength g/γ versus cavity-field outcoupling rate κ/γ , and compared to a small set of bulk-cavity systems (in blue, from top to bottom [33–35]). The FFPC used in our experiment [24] is marked with a star. Figure adapted from Ref. [23].

from and to the optical fiber, i.e. the quantum channel, mediated by the cavity-coupled atoms. The above argument is further supported when illustrated by a survey of existing cavity QED experiments in terms of the normalized strengths of atom-field coupling g/γ and cavity-field outcoupling κ/γ , as presented in [23] and shown in Figure 1.1 (b). One can directly notice the advantages of FFPCs compared to bulk cavities. The FFPC in our experiment with $(g, \kappa, \gamma) \approx 2\pi \times (80, 41, 3)$ MHz has been highlighted with a star.

In recent years, important basic functionalities of quantum nodes have been demonstrated in various proof-of-principle experiments, with a single atom (or few atoms) both in FFPCs and in bulk cavities. These breakthrough implementations include, among others, highly efficient and deterministic single photon sources [36, 37], the storage and retrieval of a single photon using just a single atom [38], the bandwidth conversion of a single photon mediated by a single cavity-coupled atom [39], and prototypes for quantum memories and quantum repeaters [26, 40]. In our experiment, most of the previous results, as the demonstration of strong Purcell broadening of an atom [24], and the storage of weak pulses beyond the adiabatic regime [41], have been performed with single cavity-coupled atoms.

For more advanced applications it is highly desirable, if not indispensable, to increase the number of atoms coupled to the cavity. The most obvious advantage is to overcome the limit for the single-atom coupling strength g , restricted by the smallest mode volume V technically achievable, by exploiting the Dicke enhancement which occurs for N_a identically coupled atoms and scales as $g_N \propto \sqrt{N_a} \cdot g$ [42–44]. Such an enhancement can boost the quantum node efficiency [45, 46], and could enable cavity-mediated bandwidth-matching between diverse quantum emitters, e.g. semiconductor quantum dots ($\gamma \approx 1$ GHz) and neutral atoms ($\gamma \approx 6$ MHz). Moreover, promising novel implementations relying on atomic ensembles inside cavities have been recently proposed, such as dissipative protocols for robust maximally entangled states [47, 48] (demonstrated with ions in Ref. [49, 50]), a highly scalable architecture for quantum computing [51] and platforms for analogue quantum chemistry simulations [52].

Most of the multi-atom implementations require a high level of control over the individual atoms, namely trapping and cooling techniques to freeze their motion, as well as detection methods to acquire knowledge on the number of emitters and their relative positions within the cavity mode [47–50, 53]. In the case of the FFPC setup shown in Figure 1.1 (a) this knowledge can be acquired through a secondary imaging channel, independent from the primary quantum channel. The detection and control of single atoms has been a vivid subject of research in the last 50 years [54, 55], prompting the development of a broad range of experimental techniques, among which fluorescence imaging has become the working horse for the detection of individual neutral atoms [56–58]. For a nondestructive imaging scheme, appropriate cooling methods [59, 60] need to be applied simultaneously to compensate for the heating induced by photon scattering, while the atoms are kept in place in conservative trapping potentials, e.g. in dipole traps and optical lattices [61–63].

However, high-bandwidth cavities impose a series of difficulties for the high-level of atom control that is required for quantum-node operation. Standard imaging and cooling techniques are hindered by the strong Purcell effect, the miniaturized geometry and the high-bandwidth property of such cavities. This motivates the need of new atom control techniques, or the clever adaptation of standard ones, e.g. for cooling, imaging and loading atoms coupled to FFPCs. Such motivation sets the stage for my thesis work following our vision of a fiber-integrated quantum node as shown in Figure 1.1 (a). In such a node small atomic ensembles are loaded into the FFPC mode where they interface photons on the quantum channel while also acquiring information through the independent auxiliary imaging channel. With this goal in mind, my thesis work consisted in developing and implementing cooling, imaging and loading techniques for atoms in our FFPC experiment.

This thesis is organized with the following structure. In Chapter 2, I give an overview of the experimental apparatus, including the basic toolbox for control and manipulation of the internal and external degrees of freedom of ^{87}Rb atoms. In Chapter 3, I present the adaptation of degenerate Raman sideband cooling (dRSC) to our lattice and cavity geometry, resulting in successful ground-state cooling of single atoms. Then, in Chapter 4, I introduce a new imaging scheme based on continuous Raman sideband cooling on the D_1 line, that ensures the independence of quantum channel and imaging channel. Further, in Chapter 5, I introduce a novel and simple method to load the intracavity lattice with multiple atoms, relying only on the intensity and phase control of the lattice. Finally, the conclusive Chapter 6 discusses the possible influence of the new atom control techniques on the development of quantum networks, and comments on the next steps towards a cavity-quantum register [64].

Scientific apparatus and experimental toolbox

SUCCESSFUL operation of an atom-cavity quantum node, as the one proposed in Figure 1.1 (a) with our experiment, requires an extraordinary level of control of single atoms inside the optical cavity [14, 19, 68, 69]. Such control relies on advanced laser-based techniques developed over the past decades for cooling, trapping and detecting individual atoms, as well as measuring and manipulating their quantum state [55, 70–73].

As mentioned in Chapter 1, fiber Fabry-Pérot cavity (FFPC) in our experiment offers clear advantages as a light-matter interface (i.e. strong coupling, high-bandwidth, intrinsic network coupling) [23]. It thus provides the necessary characteristics for a high speed quantum node, as the one proposed in Figure 1.1 (a), by coupling small atomic ensembles. However, it also entails additional challenges for the control of the cavity-coupled atoms. Consequently, standard techniques must be adapted or new methods developed to be compatible with high-bandwidth cavities. Towards the goal of a multi-atom-cavity node, a complex experimental apparatus has been developed over the course of four PhD generations, mine being the last, by my predecessors M. Martínez-Dorantes [74], J. Gallego [75] and T. Macha [76].

In this chapter*, I briefly introduce the scientific apparatus and summarize the key techniques that constitute the basic toolbox used in our experiment for control of ^{87}Rb atoms. I will start with an introduction to the light-matter coupling formalism in Section 2.1, with the aim of motivating the advantages of our high-bandwidth fiber cavity as a light-matter interface. Then in Section 2.2, while still giving a complete overview of the experiment, the main focus will be on the changes and upgrades made to the previous system. In Section 2.3 I describe the basic experimental toolbox for atom control and operation of the atom-cavity module. It comprises standard manipulation and detection techniques for the atomic external degrees of freedom — cooling and trapping (Sec. 2.3.2), and position detection by imaging (Sec. 2.3.5) — and for the internal degrees of freedom — state preparation (Sec. 2.3.3), Raman manipulation (2.3.4), and cavity-based state detection (Sec. 2.3.1) — that will be used and extended in the following chapters.

2.1 A fiber-based cavity for high-bandwidth quantum nodes

The capability of cavities to act as light-matter interfaces is based on the discovery by E. M. Purcell, who realized that the spontaneous decay rate of excited atoms could be altered by tailoring the density of

* **Contribution statement:** The upgrades to the experimental setup presented in this chapter were implemented under my lead as a team effort with my colleagues Pooja Malik, Maximilian Ammenwerth and Lukas Ahlheit. Part of the characterizations included here are contained in their respective M.Sc. theses [65–67]. Some fragments are based on my publications [1, 2].

available electromagnetic states with which it can interact, for instance by coupling the atom to an optical cavity [77].

Nowadays this surprising effect, i.e. the Purcell effect, is being applied to develop the nodes of future quantum networks [14–16]. By coupling an atom to an optical cavity, it is possible to coherently exchange quantum information between a photonic qubit and the atom [17–20]. This is the principle behind quantum memories and quantum repeaters [26, 38–40].

Specially promising for this goal are fiber-based optical cavities that feature multiple advantages, among which is their intrinsic fiber coupling to the quantum network, and the potential to provide a high-bandwidth for fast quantum information routing [41]. The regime of a high-bandwidth module and an efficient light-matter interfacing, is something very particular offered by fiber-based cavities [23, 24]. This last point sets the stage for this thesis, with the goal of coupling multiple atoms to the high-bandwidth fiber cavity in our experiment [41].

2.1.1 An atom-photon interface

A single two-level atom in a closed cavity

The light-matter interaction at the quantum level between a single two-level atom and a single quantized mode of electromagnetic field, i.e. in an ideal closed cavity system, is described by the well known Jaynes-Cummings model [78, 79]. The Hamiltonian of the system given by

$$\hat{H}_{\text{JC}} = \hbar\omega_a \hat{\sigma}^\dagger \hat{\sigma} + \hbar\omega_c \hat{a}^\dagger \hat{a} + \hbar g_0 \left(\hat{\sigma}^\dagger \hat{a} + \hat{\sigma} \hat{a}^\dagger \right), \quad (2.1)$$

where the first term represents the energy of the atom with transition frequency ω_a , the second term the energy of the quantized light field with frequency ω_c , and the third term the light-matter interaction with a coupling rate g_0 . The terms $\hat{\sigma}^\dagger$, $\hat{\sigma}$, \hat{a}^\dagger , \hat{a} are the raising and lowering operators of the respective systems. The rate g_0 , called the *single-photon Rabi frequency*, gives the coupling strength between the two-level atom and a single cavity photon, in other words the rate of coherent energy exchange between the atom and the photon. It is given by the expression

$$g_0 = d \sqrt{\frac{2\omega_c}{\hbar\epsilon_0 V}}, \quad (2.2)$$

where ϵ_0 is the vacuum permittivity and V is the volume of the cavity mode. Since the cavity mode is a Gaussian beam with a standing wave pattern, the position of the atom inside the mode affects the coupling as

$$g = g_0 |\sin(kz)| e^{-(x^2+y^2)/w_0^2}, \quad (2.3)$$

for a cavity with mode waist w_0 aligned with the z -axis.

The energy eigenvalues of the system are given by

$$\omega_{\pm} = \frac{\omega_a + \omega_c}{2} \pm \frac{\Omega_{\text{eff}}}{2}, \quad (2.4)$$

where $\Omega_{\text{eff}}^2 = 4g^2 + (\omega_c - \omega_a)^2$ is the effective single-photon Rabi frequency. The energy bands exhibit an avoided crossing, with an energy splitting with respect to the original bands of the uncoupled atom and cavity systems, with value $2\hbar g$: the so called vacuum Rabi splitting (VRS).

A single two-level atom in an open cavity

However, in real-life experiments dissipation channels must be taken into account, for instance the leakage of the cavity field and the spontaneous decay of the atom into free space. In fact, the leakage of the cavity is desired for quantum technologies because it allows the information exchange between the atom-cavity node and the user. In this case, the system is an open quantum system that is properly described by the master equation formalism [80], which goes beyond the scope of this thesis. A detailed discussion on the topic can be found in Ref. [75].

Yet, a convenient model uses the weak excitation approximation — a system of a two level atom in a cavity with a single excitation — to describe the dissipative system with the non-hermitian Hamiltonian \hat{H}_{diss} [81, 82] defined as

$$\hat{H}_{\text{diss}} = \hat{H}_{\text{JC}} - i\hbar(\gamma\hat{\sigma}^\dagger\hat{\sigma} + \kappa\hat{a}^\dagger\hat{a}), \quad (2.5)$$

where the additional term accounts for the cavity-field decay at rate κ and the spontaneous decay of the atom at a rate $\gamma = \Gamma/2$.

The eigenvalues of this system $\tilde{\omega}_\pm$ are complex numbers, that I will not display here but can be found in Ref. [32, 35]. They are nevertheless plotted in Figure 2.1 (a) as a function of the coupling strength g for the resonant case ($\omega_a = \omega_c$). Their real part $\text{Re}(\tilde{\omega}_\pm)$ determines the resonance frequency while the imaginary part $\pm\text{Im}(\tilde{\omega}_\pm)$ gives the linewidth of the resonance. The different coupling regimes will not be discussed here as a detailed description is given in Ref. [75].

A figure of merit for the light-matter interfacing of the system is the so called *cooperativity* C , given by

$$C = \frac{g^2}{2\kappa\gamma}, \quad (2.6)$$

which describes the coherent coupling g with the incoherent processes κ, γ . The cooperativity also determines the ratio of the photon emission rate by the atom into the cavity mode with respect to emission in free-space [23]

$$\eta = \frac{2C}{1 + 2C}, \quad (2.7)$$

which is a highly important parameter for efficient quantum node applications [83].

The strong coupling regime

The most interesting regime for quantum nodes is the *strong coupling regime*, with $C > 1$. The interpretation of this condition is that the atom can interact coherently with the same cavity photon multiple times before it is lost. It is in this regime that an atom-cavity quantum node can operate efficiently, since it allows the reversible exchange of information between the photon carriers and the atomic memory. On the other hand, it is highly desirable for a quantum node to have a high-bandwidth of information exchange, i.e. a large cavity linewidth κ .

In Figure 2.1 (a) we see that in the strong coupling regime, the resonance bands are well separated, such that the VRS can be measured. In fact, the ability to resolve the VRS is the unambiguous footprint of being in the strong coupling regime. Such a measurement in our system was made in Ref. [24] and an example for a single atom is shown in Figure 2.1 (c). We will see in Section 2.3.1 that this provides a non-destructive method to measure the internal states of the atoms.

In Equation (2.2) we saw that the coupling rate g depends on the cavity mode volume as $\propto V^{-1/2}$. This sets the motivation to go for miniaturized cavities, where the greatly confined mode volume can allow a high-bandwidth κ while still remaining in the strong coupling regime. This is notable case of fiber

Fabry-Pérot cavities (FFPCs) [23], as the high-bandwidth FFPC in our experiment which is the core motivation of this thesis.

Collective coupling of multiple atoms to the cavity

The coupling of multiple two-level atoms to a cavity is described by the more complex Tavis-Cummings model [84]. While I will not give any detailed description of the model, it is still worthwhile to motivate the benefits of coupling atomic ensembles to the cavity, since it is an important motivation of this thesis.

The main effect is that, in the situation of individual coupling with C_1 of each of atom N_a to the cavity mode simultaneously, the system behaves like a single “super atom” with a collective coupling $g_N = g_0 \sqrt{N_a}$. Consequently, the cooperativity depends linearly on the number of coupled atoms, i.e. $C_N = C_1 \cdot N_a$. This allows for example to tune the cooperativity of the system without any change to the cavity. Furthermore, with the right placement of the atoms in the resonator mode, the Dicke effect of coherent enhancement [42] can lead to collective effects [85] such as superradiance, which would boost the efficiency of the quantum node for collective storage and readout of photonic qubits [11].

However, in a realistic scenario, all the atoms will not couple with the same strength to the cavity, such that for the collective coupling one must consider the position distribution of the atoms in the cavity. Depending on the specific spatial distribution, the coupling g_N will be reduced by certain factor. In the end it can be seen as if a lower number of atoms (with maximal coupling C_1) was coupled to the cavity, i.e. an effective atom number $N_{\text{eff}} = \alpha N_a$. The effect on the collective coupling is then written as

$$g_N = g_0 \sqrt{\alpha N_a}, \quad (2.8)$$

where the factor α depends only on the position distribution of the atoms within the intensity profile of the cavity mode.

It is clear from Equation (2.8) that a cavity loading technique that leads to very inhomogeneous position distributions is highly detrimental for the collective coupling. This was observed in our system in Ref. [75] using the conveyor belt feedforward transport loading that will be presented in Section 2.3.2. This gave the motivation to develop a new loading technique that would lead to a more compressed denser loading, which will be presented in Chapter 5.

Our high-bandwidth FFPC

Our experiment is based on a fiber Fabry-Pérot cavity (FFPC), with the mirrors fabricated on the end facets of optical fibers [21, 22]. The top mirror has a higher transmission (HT) than the low transmission (LT) bottom mirror, creating a single-sided resonator with a single input-output channel (recall Figure 1.1 (a)), which is beneficial for optical-fiber-network integration.

The advantages of FFPCs have been well summarized in Ref. [23]: (i) high field concentration, (ii) integration with optical fibers, (iii) high optical qualities, (iv) small footprint, (v) open geometry, (vi) integration with other functional components.

In particular, FFPCs [21–23] offer an interesting regime, that combines strong atom-cavity coupling g and strong Purcell effect in a cavity with high-bandwidth κ [24], characterized by $g, \kappa \geq \gamma$ and $g \approx \kappa$.

The FFPC in our experiment is in such high-bandwidth and high-coupling regime. When coupled on the ^{87}Rb D_2 $|F = 2\rangle \rightarrow |F' = 3\rangle$ cycling transition (see Figure 2.1 (b)), we obtain CQED parameters $(g, \kappa, \gamma) = 2\pi \cdot (80, 41, 3)$ MHz [22, 24]. With this, our cavity is deep in the strong coupling regime, has a high bandwidth, and lies close to the Goldilocks condition for impedance matching with g and κ on the same order. Further relevant parameters of the system have been compiled in Appendix D.2.

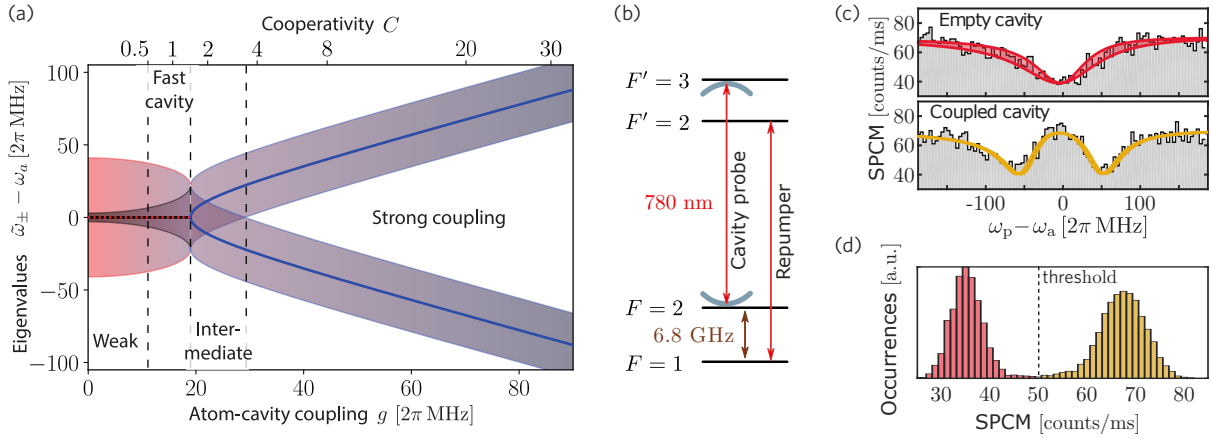


Figure 2.1: Cavity-enhanced atom-light interaction and cavity-based atom detection. **(a)** Spectrum of the open, non-driven atom-cavity system as discussed in [75], here with parameters $(\kappa, \gamma) = 2\pi \times (41, 3)$ MHz. The complex eigenvalues $\tilde{\omega}_{\pm}$ of the non-Hermitian Hamiltonian $\hat{H}_{\text{diss}} = \hat{H}_{\text{JC}} - i\hbar(\gamma\hat{\sigma}^{\dagger}\hat{\sigma} + \kappa\hat{a}^{\dagger}\hat{a})$ are plotted with respect to the atomic frequency ω_a (i.e. the detuning $\tilde{\omega}_{\pm} - \omega_a$), as a function of the atom-cavity coupling strength g . The real part of $\tilde{\omega}_{\pm}$ determines the center of the resonance, while the imaginary part gives its linewidth. Figure from Ref. [76]. **(b)** In our system, with the cavity resonant on the ^{87}Rb $|F=2\rangle \rightarrow |F'=3\rangle$ cycling transition, we measure an average $g \approx 2\pi \times 80$ MHz placing us deep in the strong coupling regime. This allows us to measure the vacuum Rabi splitting (VRS) of the energy spectrum. The cavity probe beam on the same transition serves to interrogate the system, e.g. for the non-destructive atom detection, see (c) and (d). **(c)** Exemplary measurement of the VRS for a single atom, with the cavity on resonance, by scanning the probe laser frequency ω_p and monitoring its reflection with single photon counter modules (SPCMs), as presented in Ref. [75]. As a function of detuning $\omega_p - \omega_a$, the reflection spectrum of the empty cavity (in red) is compared to the spectrum of the coupled atom-cavity system (in yellow). **(d)** Histogram of the reflection signal (binned in 10 ms) for a set of measurement repetitions, with the probe on resonance with the atom-cavity system ($\omega_p = \omega_a$) in (c), featuring a clear bimodal distribution. We then use a threshold method to discriminate single measurements between cavity-coupled (yellow) and uncoupled (red) scenarios, with $\sim 97\%$ fidelity [75]. Depending on the absence or presence of a $|F=1\rangle \rightarrow |F'=2\rangle$ repumper in (b), the measurement is a non-destructive state detection or an atom presence detection.

To put it in perspective with respect to other CQED experiments, we refer to the survey of parameters $\{g, \kappa, \gamma\}$ and $C = g^2/2\kappa\gamma$ of CQED experiments by Ref. [23] shown in Figure 1.1 (b). We identify our experiment (marked as a star) among other fiber-cavity experiments (red circles) and few bulk-cavity ones (blue squares). It directly becomes clear that fiber cavities are very superior to bulk cavities. As we discussed earlier, from Equation (2.8), the rate g and thus the cooperativity C have the potential to be enhanced by coupling small atomic ensembles to the cavity.

Previous experimental results of our system include the measurement of strong Purcell broadening of a single atom [24], and the storage and readout of short light pulses in the non-adiabatic regime. But all these experiments were mainly performed with a single cavity-coupled atom. More recent results were the development of a cooling method [1] and an imaging technique [2] adapted for high-bandwidth cavities, which are main parts of this thesis (Chapter 3 and Chapter 4). In the following section of this chapter I will then provide the knowledge and details about the experimental apparatus that is the foundation for operating our FFPC quantum node.

Sadly, the end of my thesis work was marked by the end of the fiber cavity: an accident with the ion pump of the vacuum system resulted in the permanent damage of the FFPC, triggered by the progressive finesse degradation suffered by the cavity ever since its installation in vacuum [75]. A note on this can be found in Appendix D.1.

2.2 Overview of the experimental apparatus

At the core of our experiment is a high-bandwidth FFPC with few ^{87}Rb atoms strongly coupled to its single mode field. The experimental apparatus necessary to achieve such scenario is presented graphically in a simplified form in figures 2.2 and 2.3. The first figure shows the vicinity of the cavity inside an ultra-high vacuum system (10^{-10} mbar) [74], with the main optical elements and the light fields required to operate the atom-cavity node. The second figure presents the lasers system and stabilization schemes needed to provide reliable light sources for the beams impinging on the atoms inside the cavity, as shown in Figure 2.2. A thorough discussion of the setup can be found in previous theses [74–76], thus in the following I will only give an essential description of the system, hand in hand with both Figure 2.2 and Figure 2.3 which are fairly self-explanatory. Certain modules relevant for the techniques used in this thesis will be discussed in more detail in Section 2.3.

A typical experimental sequence starts with atoms being captured and cooled with a small magneto-optical trap (MOT) [86] created ~ 1 mm away from the cavity center (see Sec. 2.4). Then, they are loaded into a standing wave dipole trap along the y -axis (the DT_y lattice) that transports the resulting atom-chain toward the cavity with the conveyor belt technique [87–89].

Within the cavity, the atoms become trapped in a three-dimensional (3D) optical lattice [61, 90], formed in the xy -plane by two pairs of red-detuned counter propagating beams, namely the DT_x and DT_y lattices with wavelength 868 nm. Along the z -axis the confinement is provided by the blue-detuned intracavity field of the lock laser that stabilizes the cavity length, namely the DT_z lattice with wavelength 770 nm. More on the optical lattice is found in Section 2.4.

To obtain a directional single-sided cavity, as desired for a network-integrated quantum node (see Chapter 1, Figure 1.1 (a)), the top mirror has a higher transmission (HT) relative to the very low transmission (LT) bottom mirror. The HT port is used as the input-output quantum channel, through which a 780 nm probe beam is coupled to resonantly interrogate the atom-cavity system. The probe laser is locked to the ^{87}Rb D_2 line with a Doppler-free polarization spectroscopy scheme [91]. The cavity is stabilized to a length that features a simultaneous resonance at 780 nm and at 770 nm, i.e. with the probe light and the lock laser respectively. In this configuration, trapping sites at intensity minima of DT_z coincide with intensity maxima of the probe standing wave at the cavity center, providing an atom-cavity interaction in the strong coupling regime [24], see Section 2.1. The probe light reflection is monitored by single-photon counter modules (SPCMs), enabling the non-destructive detection of atom presence and their internal state [24, 92], see Section 2.3.1.

At this point the system resembles a textbook-like atom-cavity node ready for interfacing single photons and coupled atoms. However, the interaction with multiple additional light fields is still needed for the required level of atom control as shown in Figure 2.2. These are also the modules in which I implemented technical upgrades to the system, which I will briefly discuss in the following.

An auxiliary atomic line for optical pumping and illumination. The bottom LT mirror is used as input port for two 795 nm beams, the optical pumping (OP) laser and the repumper, resonant with the atoms on the D_1 line but not with the cavity. These beams are sourced by two DFB lasers [76] that replace the previously used home-built grating lasers, providing high long term stability. They are stabilized by Doppler-free polarization spectroscopy to a common atomic vapour cell, to avoid differential effects due to e.g. from magnetic field fluctuations [93]. More on the optical pumping scheme of the experiment is discussed in Section 2.3.3. These beams also provide illumination light for fluorescence imaging of the atoms, providing knowledge on the number of atoms and their position within the cavity mode. Photons scattered by the atoms are collected with one of the in-vacuum high-NA lenses along the x axis and recorded with an EMCCD camera. The implementation of a fully new imaging scheme represents

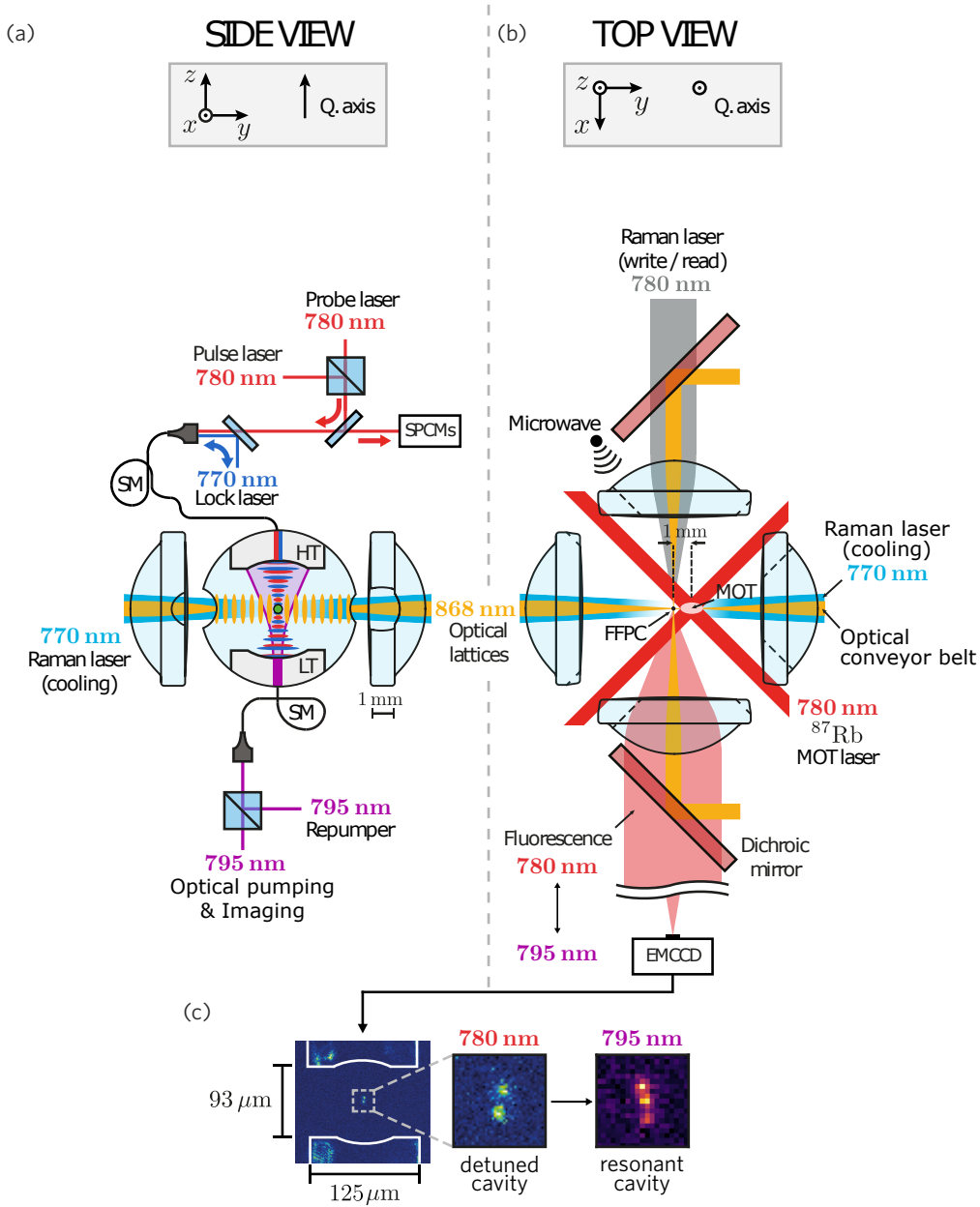


Figure 2.2: Simplified diagram (not to scale) of the experimental system to trap and couple ^{87}Rb atoms to the high-bandwidth fiber Fabry-Pérot cavity (FFPC), (a) viewed from the side and (b) from the top. Atoms captured in a MOT outside the cavity are delivered by an optical conveyor belt to its center, where they couple to the cavity mode while trapped in a 3D lattice (red-detuned in the xy -plane, blue in the z -axis). We use the intrinsic fiber coupling of the cavity to feed-in multiple laser fields. The high-transmission (HT) mirror serves as input port for the probe and pulse fields that resonantly address the atom-cavity system, monitored in reflection by single-photon counter modules (SPCMs), and additionally for the lock laser (off-resonant with the atoms) that stabilize the cavity and creates a vertical lattice. The low-transmission (LT) mirror is reserved for the cavity-off-resonant optical pumping beams. In free space an off-resonant Raman beam along the y -axis, in pair with the cavity lock laser, serves for cooling the atoms. An additional resonant Raman beam along the x -axis controls the storage of weak light pulses from the pulse laser [76]. One of the high-NA lenses that focuses the lattice beams also collects photons emitted by the atoms for imaging with an EMCCD camera, using the optical pumping beams for illumination. (c) One main upgrade to the system was to migrate the imaging method to the ^{87}Rb D_1 line from the previously used D_2 line [74, 75], enabling position detection of the atoms and simultaneous operation of the atom-cavity node which was not possible before. A more detailed description is given in the main text. The figure is adapted from Ref. [75, 76] showing the evolution in complexity of the system.

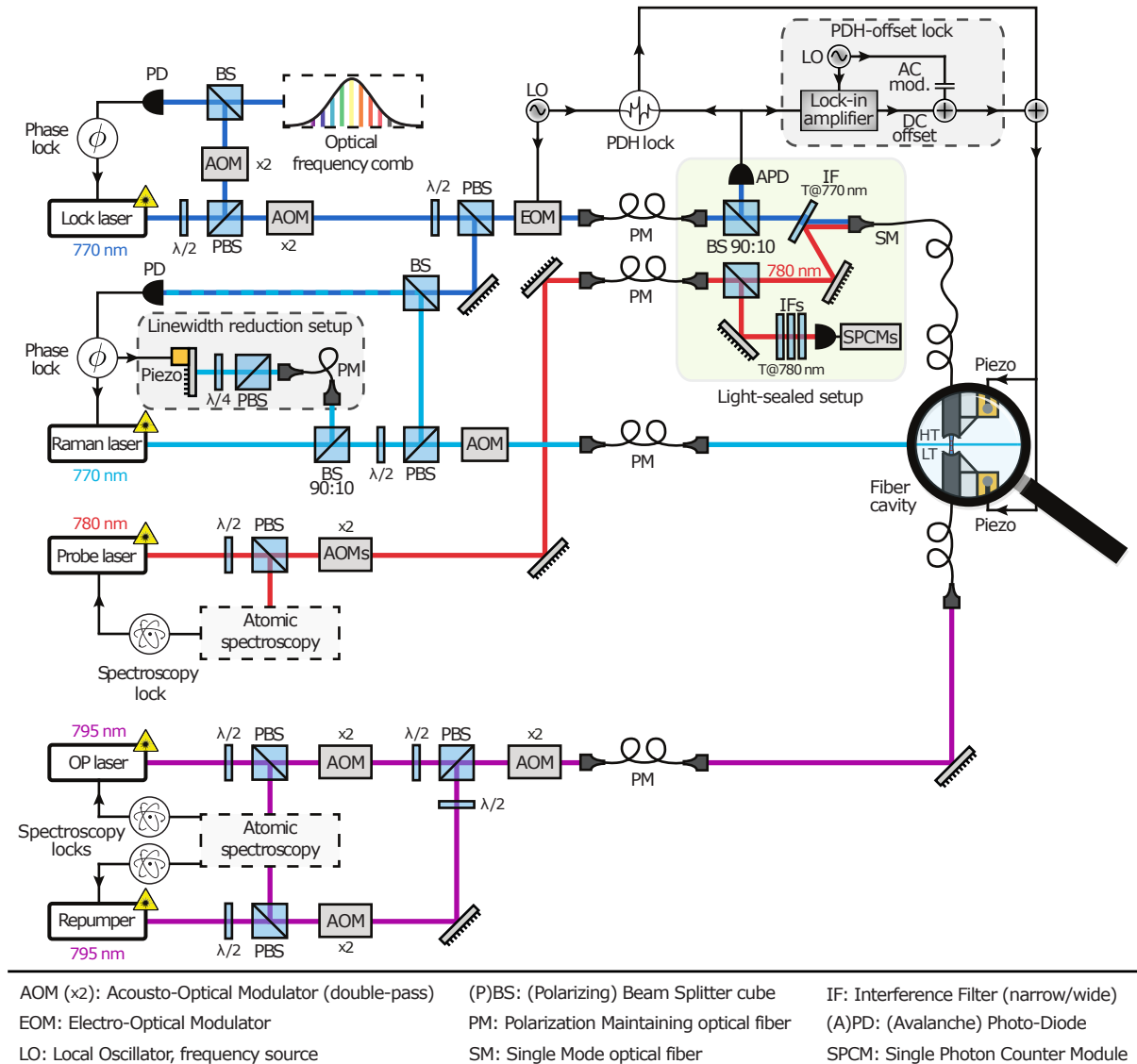


Figure 2.3: Overview of the lasers system and locking schemes needed to stabilize the fiber cavity, and to provide reliable sources for the beams involved in the experiment, see Figure 2.2. The cavity length (i.e. resonance) is stabilized with the Pound-Drever-Hall (PDH) technique to the 770 nm lock laser, which is phase-locked to an optical frequency comb. The 780 nm probe laser is referenced to a aD_2 -line spectroscopy setup. In the light-sealed module, lock and probe beams are overlapped and fiber-coupled into the cavity through the high-transmission (HT) mirror. The weak probe reflections are monitored with SPCMs for non-destructive atom detection (Sec. 2.3.1), while the lock laser reflection is detected by an APD for the PDH lock. The 770 nm Raman laser is phase-locked to the lock laser and used in pair for intracavity cooling (Sec. 2.3.4), entering the cavity in free-space from the side. The 795 nm optical pumping (OP) and repumper beams are locked to a common D_1 line atomic spectroscopy reference. They are cavity-coupled together through the low-transmission (LT) fiber mirror, and used for state initialization (Sec. 2.3.3) and as illumination beams for the new imaging scheme (Sec. 2.7). Two key upgrades to the apparatus are marked as grey shaded rounded boxes and are discussed in the main text: the linewidth reduction setup for the Raman laser and the PDH-offset lock. Omitted here are the MOT lasers module [74], the TiSa laser module to source the optical lattice beams [74, 75], and the pulse-storage module [76]. Figure adapted from Ref. [75, 76].

another upgrade to the system, see Section 2.3.5. The imaging channel on the atomic D₁ line remains fully independent from the cavity interaction on the D₂ line, and thus insensitive to the Purcell effect that did not allow for simultaneous operation in the past.

Raman transitions for cooling and imaging. An additional 770 nm beam, the so called Raman laser, is phase-locked to the lock laser and shines into the cavity in free space from the side. Together with the intracavity lock field, they form a pair of Raman beams to manipulate the hyperfine states of the atoms and cool their vibrational energy in the lattice, see Section 2.3.4. These beams are also essential for a novel Raman imaging technique presented in Chapter 4. An upgrade to the previous system consisted in replacing the light source for the Raman beam from an interference-filter laser, to a DBR laser providing long term stability, which we upgraded for linewidth-reduction with an external optical feedback (shown simplified in Fig. 2.3 as a grey-shaded rounded box, details in Appendix B.7).

An improved cavity stabilization to reduce atom heating. The cavity stability relies on a locking-chain scheme implemented by [76], where the lock laser is phase-locked to an optical frequency comb for high stability. In turn the cavity is stabilized to the lock laser with Pound-Drever-Hall (PDH) technique [94]. In previous generations, offset fluctuations of the PDH error signal zero-level were observed, attributed to interference effects in the multiple reflections of lock-laser light at the fiber splicing points [75], thus with a highly unpredictable behavior, e.g. susceptible to light air currents or temperature drifts. Efforts to reduce the fluctuations with Through the PDH feedback loop, this offset translated into an offset of the cavity resonance with respect to the lock laser placing it on one slope of the transmission spectrum instead of at the top. The direct consequence was that any phase fluctuations between the lock and the cavity (e.g. from laser noise, or mechanical resonances of the cavity mount) were converted by the frequency discrimination into intensity fluctuations of the DT_z lattice leading to strong heating of the atoms. This became evident by the lifetime of trapped atoms in the 3D lattice DT_{xyz} inside of the cavity without cooling of ~ 1 s compared to ~ 15 s in the 2D horizontal lattice DT_{xy} (lock laser blocked) [76].

As a solution, we have implemented a simple scheme to lock the offset of the PDH signal by compensating the fluctuations, shown in a grey-shaded rounded box in Figure 2.3, described in the following. A small modulation from a local oscillator (LO) is added (by capacitive coupling) to the feedback signal from the PDH lock driving the the cavity piezos, at a frequency $f \approx 600$ Hz away from any mechanical resonance and harmless for the atoms. This translates into a modulation of the reflection signal of the lock laser, at a frequency $2f$ if on resonance with the cavity but with an f -component if on the slope. The measured signal of the lock reflection is fed into a lock-in amplifier, which also receives the same signal f from the LO for demodulation. The lock-in amplifier provides a DC voltage proportional to the f -component of the reflection signal, which has the same magnitude but opposite sign than the unwanted PDH offset fluctuations. Finally the DC offset is added as a correction to the PDH signal driving the cavity piezos. When activating this additional simple stabilization scheme in our experiment, we observe an increase in trapping lifetime in the DT_{xyz} lattice to ~ 3 s from the previous ~ 1 s, without cooling. Under continuous Raman cooling it reaches ~ 1 min (see Chapter 4).

2.3 Manipulation and detection of degrees of freedom of the atoms: the basic toolbox

The successful control of individual atoms relies on addressing, manipulating and detecting the external and internal degrees of freedom of the atoms [70, 95].

By external degrees of freedom we refer to the position and velocity of the atoms, which can be controlled by standard laser cooling techniques and optical traps [60, 61, 96] (see Sec. 2.3.2), and measured with imaging methods [55] (see Sec. 2.3.5).

On the other hand, the internal degrees of freedom refer to the electronic energy states of the atoms. In particular, in our experiment we use the ^{87}Rb ground hyperfine states, $5^2\text{S}_{1/2} |F = 2, m_F = -2\rangle$ and $|F = 1, m_F = -1\rangle$, as the two qubit states for the storage of photons and their retrieval, mediated by the cavity [41]. These two internal states can be coherently coupled in our setup by microwave fields as in Ref. [75, 76], or by Raman beams (see Sec. 2.3.4). Furthermore, we use optical pumping to initialize the atom to the desired state (Sec. 2.3.3), and the cavity non-destructive measurement to detect the current hyperfine level (see Sec. 2.3.2).

More advanced cooling methods rely on coupling external and internal degrees of freedom of the atoms, for instance the Raman cooling techniques presented in this thesis in Chapter 3 and Chapter 4.

2.3.1 Non-destructive cavity-based atom presence and state detection

The non-destructive atom detection technique is based on the capability to measure the vacuum Rabi splitting (VRS) of single atoms coupled to the cavity (see Eq. (2.4)), as shown in Figure 2.1 (c). It is also the hallmark that our system is in the strong coupling regime, as discussed in 2.1.

Relevant atomic transition for the atom detection are shown in Figure 2.1 (b). The probe laser is tuned on resonance with the atom cavity system on the D_2 line $|F = 2\rangle \rightarrow |F' = 3\rangle$ cycling transition, i.e. $\omega_p = \omega_a = \omega_c$, while the probe reflection is monitored by single-photon counter modules (SPCMs). From Figure 2.1 (c) it is clear that for an empty (or uncoupled) cavity, the SPCM counts are low. However, if an atom couples to the cavity mode, the induced VRS increases the reflection signal.

For a set of measurement repetitions with different atoms and with a loading probability of $\sim 50\%$, the SPCM counts follow a clear bimodal distribution, with one low-counts Gaussian corresponding uncoupled cases, and another high-counts one from the coupled events, as can be seen in the histogram (10 ms binning) in Figure 2.1 (d). By choosing an appropriate counts value as a threshold [75], we can sort single measurements in real-time as coupled or uncoupled, featuring a binary readout of the atom-cavity coupling state with $\sim 97\%$ fidelity [24, 92].

An additional repumper beam on the $|F = 1\rangle \rightarrow |F' = 2\rangle$ transition, impinging from the cavity side (not shown in figures 2.2 and 2.3), is used to choose between atom presence detection or state detection. If the repumper is enabled, both states $|F = 1\rangle$ and $|F = 2\rangle$ provide a positive readout, and only an empty cavity gives a negative result, i.e. it is an atom presence detection. But if the repumper is disabled only the state $|F = 2\rangle$ gives a positive readout, i.e. it is a state detection. In this case an atom in the uncoupled state and an empty cavity have the same signal, but combining a presence and a state detection confirms that the atom is present but uncoupled.

In the rest of the thesis we will use extensively this cavity measurement method, both in the presence-detection variant and in the state-detection one. Since the atom does not interact with the probe photons during this measurement, i.e. the VRS inhibits the transmission of probe light into the cavity, the measurement is highly non-destructive. A limitation that we will have to deal with is that the VRS saturates with a single coupled atom, such that it is not directly applicable for detecting the number of atoms inside of the cavity. However, in Chapter 5 we will show that by statistical means the average number of atoms can still be extracted.

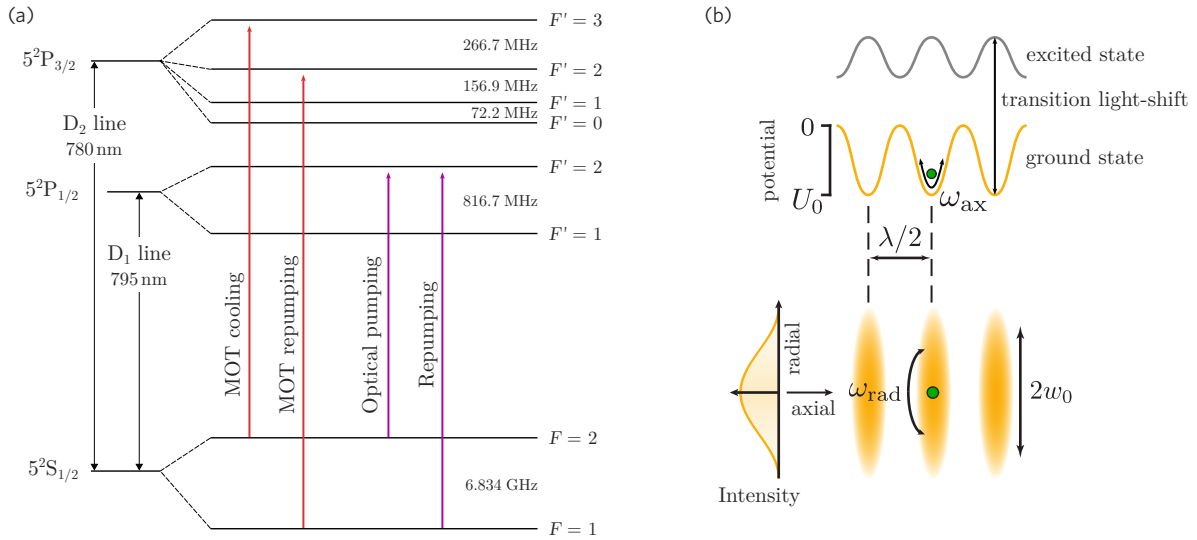


Figure 2.4: Basic techniques for atom cooling and trapping. **(a)** Relevant energy levels of ^{87}Rb for cooling the atoms (not to scale). On the D₂ line, the MOT cooling beams are tuned to the $|F = 2\rangle \rightarrow |F' = 3\rangle$ cycling transition, and the repumper beams to the $|F = 1\rangle \rightarrow |F' = 2\rangle$. Additionally, for the Raman cooling scheme (more in Sec. 2.3.4) we use the D₁ line, independent from the cavity interaction. There, an optical pumping beam and a repumping beam are near-resonant on the $|F = 2\rangle \rightarrow |F' = 2\rangle$ and $|F = 1\rangle \rightarrow |F' = 2\rangle$ transitions respectively. These beams also serve as illumination for imaging (see Sec. 2.3.5). **(b)** Working principle of an optical lattice for trapping atoms. Two counter-propagating Gaussian beams (red detuned, with beam waist w_0) interfere forming a standing-wave pattern. The ground states of the atom are shifted down, creating a chain of attractive potential wells along the axial direction, of depth U_0 and periodicity $\lambda/2$, that can trap one atom each. In the radial direction, the potential follows the beam Gaussian profile. Atoms with energy below U_0 are trapped and oscillate with characteristic axial frequency ω_{ax} and radial frequency ω_{rad} , both proportional to $\sqrt{U_0}$. With our 868 nm lattice, the excited states of ^{87}Rb shift upward by a different amount, creating a repulsive potential. Optical transitions are shifted by the sum of both shifts. For a blue-detuned lattice the roles are inverted. Figure (b) adapted from Ref. [75].

2.3.2 Cooling and trapping: a small MOT and an intracavity 3D lattice

A small magneto-optical trap

As presented in Section 2.2, the first step to deliver cold atoms into our FFPC is to capture and cool them from the ^{87}Rb background gas by a magneto-optical trap (MOT). The working principle of a MOT is broadly covered in the literature [60, 86, 97, 98].

The design and experimental implementation in our apparatus is described in detail in Ref. [74]. The relevant ^{87}Rb energy levels and the involved light fields are shown in Figure 2.4 (a). The cycling $|F = 2\rangle \rightarrow |F' = 3\rangle$ transition of the D₂ line is used for the cooling light, while the repumper works on the $|F = 1\rangle \rightarrow |F' = 2\rangle$ transition. Contrary to standard MOTs with millions of atoms, our MOT is fairly small with only few tens of atoms. It is limited by the optical access for the beams between the in-vacuum high-NA lenses that surround the cavity (see Fig. 2.2). Nevertheless these number of atoms is enough for our goal of coupling small atomic ensembles to the cavity. Given that the MOT cannot fit inside of the cavity for a direct loading, it is formed 1 mm away. The atoms are then transported to the cavity by an optical conveyor belt [87–89], i.e. the DT_y lattice.

The energy of the atoms captured by the MOT follows a Boltzmann distribution with mean temperature $T_{\text{mot}} \approx 40 \mu\text{K}$. This first cooling step in the sequence is essential for a decent loading probability into the DT_y lattice, and for staying trapped during the conveyor-belt transport into the 3D intracavity lattice.

An intracavity three-dimensional lattice

Once inside the cavity, after being shuttled by the DT_y lattice, the atoms are trapped in three dimension by the optical lattice DT_{xyz} introduced in Section 2.2. Here we revise the working principle of an optical lattice for trapping atoms and provide characteristics of the intracavity lattice in our experiment. Details on the experimental implementation are found in Ref. [74, 75].

Trapping with the dipole force. Optical dipole traps are based on the dipole coupling of an atom and an electromagnetic field far-off resonance [61]. The working principle relies on the different scaling as a function of the detuning Δ_{DT} of the light-induced potential ($\propto \Delta_{DT}^{-1}$) and the resulting scattering rate ($\propto \Delta_{DT}^{-2}$). For large detunings, it results in a conservative trapping potential given by

$$U_{DT}(\mathbf{r}) = \frac{\hbar\Gamma^2}{8\Delta_{DT}} \cdot \frac{I(\mathbf{r})}{I_{sat}} \quad (2.9)$$

where \mathbf{r} denotes the spatial coordinates, $I_{sat} = \pi\hbar\Gamma c/3\lambda^3$ is the saturation intensity of the atomic transition with decay rate Γ and wavelength λ , and $\Delta_{DT} = \omega_0 - \omega_{DT}$ is the detuning of the dipole trap frequency ω_{DT} from the atomic resonance ω_0 . In Eq. (2.9) we note that the potential is proportional to the light-intensity pattern, i.e. $U_{DT}(\mathbf{r}) = U_0 \cdot I(\mathbf{r})$ with U_0 the maximum trap depth. It also shows that the potential is attractive for red-detuned beams but repulsive for blue-detuned ones.

A 1D optical lattice. An optical lattice is generated by two counter-propagating Gaussian beams that interfere forming a standing-wave. The resulting intensity pattern is shown in Figure 2.4 (b) (lower part). Using Equation (2.9), the corresponding trapping potential is given by

$$U_{DT}(x, r) = U_0 \cdot \left(\frac{w_0}{w(x)}\right)^2 \cdot \exp\left(-2\left(\frac{r}{w(x)}\right)^2\right) \cdot \cos^2\left(\frac{2\pi}{\lambda_{DT}}x\right), \quad (2.10)$$

with (x, r) the axial and radial coordinates, λ_{DT} the lattice wavelength, and $w(x)$ the Gaussian beam waist at position x with minimum w_0 at $x = 0$. Within the Rayleigh range a good approximation is to neglect the waveform curvature and the Gouy phase of the Gaussian beam. With this, the trapping potential geometry features a chain of lattice wells (or sites) along the axial direction, shown in Figure 2.4 (b) (upper part), with depth U_0 and spacing $\lambda_{DT}/2$. In the radial direction the potential follows the Gaussian beam profile. In each site, a single atom can be trapped (in our experiment), because a double occupancy results in the loss of both atoms by light-induced collisions [99, 100].

A direct consequence of the dipole interaction is an AC-Stark shift of the atomic energy levels, also referred to as light shift. At the bottom of the trap, the ^{87}Rb ground states shift down by $\Delta_{0,g} = U_0$. However the excited states shift differently by an amount $\Delta_{0,e} = \chi \cdot \Delta_{0,g}$ where $\chi = \alpha_e/\alpha_g$ is the polarizability ratio between ground and excited states. The total shift induced by the lattice on the atomic transition between ground and excited states is then $\Delta_0 = \Delta_{0,g} + \Delta_{0,e}$.

Dynamics of a trapped atom. While the full dynamics of an atom trapped inside a lattice site, i.e. the wave function and its time evolution, can be calculated with the expression of the potential in Equation (2.10) (e.g. see [101]), here we use the convenient harmonic approximation. Then the wave function is described by the well known quantum harmonic oscillator model. We note that the harmonic approximation is reasonable for cold atoms at the bottom of the trap, but for higher energetic states the anharmonicity of the lattice potential should be considered [102].

The atom oscillates (vibrates) in the lattice well at quantized motional energy levels $E_{n,i} = \hbar\omega_i(n + 1/2)$, with $n = 0, 1, 2, \dots$ and with characteristic oscillation frequencies ω_{ax} in the axial direction and ω_{rad} in the radial direction. Throughout the thesis, I will use the notation $|F, m_F; n\rangle$ to represent the full atomic quantum state, with the hyperfine level denoted by $|F\rangle$, its magnetic sublevel by $|m_F\rangle$ and its vibrational state by $|n\rangle$. The oscillation frequencies ω_{ax} and ω_{rad} are commonly called trap frequencies. They depend both on the trap depth U_0 and on the size of the trapping potential, following the expressions [61]:

$$\omega_{\text{ax}} = 2\pi\sqrt{\frac{2U_0}{m_{\text{Rb}}\lambda_{\text{DT}}^2}}, \quad (2.11)$$

$$\omega_{\text{rad}} = 2\sqrt{\frac{U_0}{m_{\text{Rb}}w_0^2}}, \quad (2.12)$$

with m_{Rb} the atomic mass, and that are also commonly expressed as linear frequencies ν_i with $\omega_i = 2\pi \cdot \nu_i$.

Our 3D intracavity lattice. In the xy plane, the lattice is formed by two near-orthogonal red-detuned 868 nm standing-wave dipole traps (DT_x and DT_y), and in the z axis by the blue-detuned 770 nm intra-cavity lattice (DT_z), as shown previously in Figure 2.2. In this configuration, the atoms are localized at intensity maxima of the DT_{xy} lattice, but at point of vanishing intensity of the DT_z lattice. The 3D trapping region is defined by the waist of the beams at the intersection $(w_x, w_y, w_z) = (13, 11, 5) \mu\text{m}$. The lattice polarizations are defined as $(P_x, P_y, P_z) = (\pi, \pi, \sigma^+)$, with the quantization axis of our system set parallel to the cavity axis by applying a magnetic guiding field. The magnitude of the magnetic field will differ for different cooling techniques, see chapters 3 and 4.

As seen in Figure 2.2, the source of the blue-detuned lattice is the lock laser that also stabilized the cavity resonance (it will also serve as a Raman beams as we will see in Sec. 2.3.4). The source of the red-detuned beams is a Titanium Sapphire (TiSa) laser which provides narrow linewidth.

The trap features a depth of ~ 0.5 mK in each direction, that allows for confinement in the Lamb-Dicke regime [103, 104]. This permits to resolve the motional energy states of the atoms in the lattice potential wells, which is a strong requirement for resolved Raman sideband cooling. The lattice beams $\text{DT}_{x,y}$ are not fully orthogonal to DT_z , but feature small angles with respect to the normal plane of the vertical lattice ($\theta_x \approx 15^\circ$ and $\theta_y \approx 6^\circ$), which is an important feature for the 3D Raman coupling discussed in Section 2.3.4.

Later in Chapter 4 we overlap the trap frequencies of all DT_{xyz} lattice components to $\omega_{xyz,\text{ax}} \approx 2\pi \times 350$ kHz to implement simultaneous Raman cooling along all directions (see Sec. 2.3.4 for more on the Raman scheme).

Characterization of light shifts. Since the atoms sit at intensity maxima of the 868 nm light in the DT_{xy} lattice, the atomic transitions are subject to strong light shifts (see Figure 2.4 (b)). On the contrary, the light shifts induced by the 770 nm DT_z lattice are negligible because the atoms lie at intensity minima. The shifts of the different states of the D_2 line have been characterized in Ref. [74] and are not very relevant for this work. However, the shifts of the D_1 line have a great impact on our optical pumping and imaging schemes that rely on the resonance of the 795 nm optical pumping beams. What is more, when illuminating the atoms with near-resonant D_1 light, the asymmetry in light shifts of ground and excited states, i.e. the polarizability ratio χ , leads to heating induced by dipole-force fluctuations (DFFs) [58, 105]. This will play a big role for the implementation of Raman imaging in Chapter 4, see also Appendix B.10 for a discussion of DFFs.

We determine the shift of the D_1 transition by tracking the displacement of the 795 nm repumper beam as a function of the intensity of the DT_{xy} beams. For the employed lattice depths (~ 0.5 mK per direction), we measure a total lattice-induced light shift of $\Delta_0 = (32 \pm 3)$ MHz. Details of the measurement are given in Ref. [66]. To determine the polarizability ratio, we use the trap frequencies $\omega_{xy,ax} \approx 2\pi \times 350$ kHz, measured by Raman spectroscopy (see Sec. 2.3.4), to obtain the shift (by both DT_{xy}) of the ground state only $\Delta_{0,g} \approx -20.1$ MHz. It follows from simple calculations that the excited state shifts by $\Delta_{0,e} \approx 11.9$ MHz, and thus the polarizability ratio is $\chi \approx -0.59$, which coincides with the value estimated with numerical calculations in Ref. [106]. This characterization will be used in Chapter 4 for a numerical simulation of DFFs-induced heating during the Raman imaging process.

Atom loading methods by conveyor belt transport. As mentioned previously, from the MOT the atoms are delivered into the cavity by the DT_y lattice used as an optical conveyor belt [87–89]. With this feature, previously in the experiment we used two different techniques to load the intracavity lattice.

The first one uses the non-destructive cavity detection (see Sec. 2.3.1) to stop the transport when a first atom couples to the cavity mode, using a real-time feedback mechanism. This method is called *feedback transport* loading. It has been used for most of the previous result in our experiment [24, 41, 75, 76] for coupling a single atom to the cavity.

The second technique consist in transporting the whole 1D atom chain loaded from the MOT into the DT_y lattice into the center of the cavity, with the transport distance programmed beforehand. We call this method the *feedforward transport* loading. It was used in Ref. [24, 75] to couple multiple atoms to the cavity. However, the feedforward transport loading has the disadvantage that only few atoms from sparsely-loaded fit into the cavity mode, and with a very inhomogeneous position distribution. This is detrimental for the collective coupling of the atoms as commented in Section 2.1 and measured in Ref. [75].

In Chapter 5 I present a newly developed loading method, the so called *drive-through* loading. The method relies on transporting the 1D atom-chain across the 3D lattice region with a reduced depth of DT_y . It generates atom loading at the DT_{xyz} lattice intersection, which results promising for denser loading. This would lead to a more homogeneous single-atom couplings and thus higher collective light-matter interfacing.

Cooling inside the cavity

Even though the methods described above provide cold atoms from the MOT and trapped in 3D inside the cavity, additional intracavity cooling is essential to avoid losses and for efficient light-matter interfacing.

Indeed, the atoms must be kept close to the their motional ground state at the bottom of the lattice sites in DT_z to remain at intensity maxima of the resonant cavity mode [75], where the coupling rate g is highest. What is more, inside the intracavity lattice (DT_z), the atoms are susceptible to high heating rates because phase fluctuations between the cavity and the lock laser are transformed into lattice intensity fluctuations¹. Also, for fluorescence imaging of the atoms [58], scattering-induced heating must be compensated with appropriate cooling methods.

As was briefly discussed in Chapter 1, in high-bandwidth cavities as our FFPC (see Sec. 2.1), standard cooling techniques such as 3D optical molasses [97, 107, 108] and cavity cooling [109, 110] are not applicable. The former is inhibited because of the restricted optical access, i.e. the z axis is obstructed by

¹ This problem arises when the cavity resonance and the lock laser resonance do not exactly coincide (see Sec. 2.2), e.g. due to offset fluctuations of the PDH-lock zero-line [75]. To reduce the problem I implemented an active compensation of the PDH-offset fluctuations, see Section 2.2.

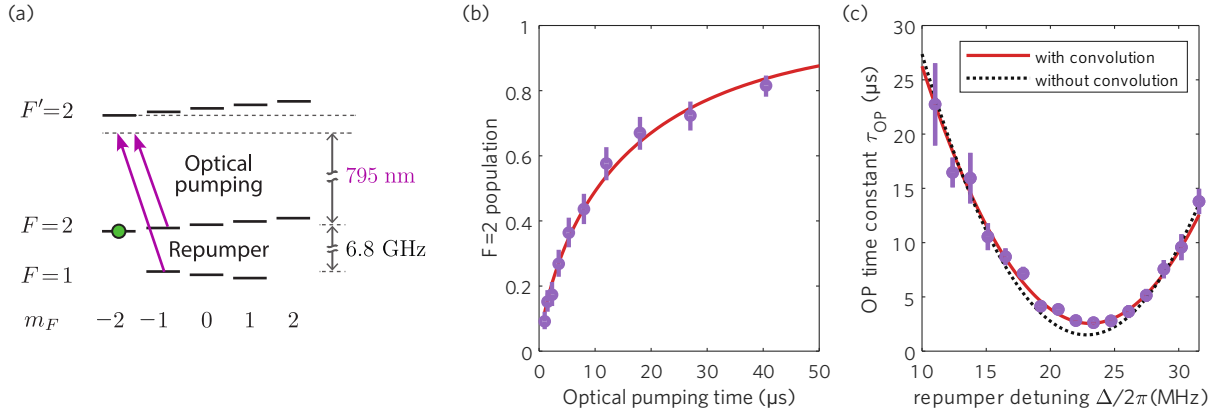


Figure 2.5: Optical pumping scheme and intracavity intensity calibration. **(a)** Relevant energy levels of ^{87}Rb on the D_1 line, that are addressed with the optical pumping and repumper beams. **(b)** Exemplary optical pumping (OP) curve by the repumper of the atomic population $|F = 1\rangle \rightarrow |F = 2\rangle$, as a function of the pulse time. We extract the characteristic time τ_{OP} from a stretched exponential fit. **(c)** Optical pumping characteristic times τ_{OP} plotted as a function of the repumper detuning Δ , to obtain the calibration of the saturation parameter $s = I_{\text{rep}}/I_{\text{sat}}$ inside of the cavity, see main text. The repumper detuning with respect to free space also includes the AC-Stark shift induced by the dipole traps on the D_1 transition (here at lower power than in Sec. 2.3.2). Figures (b,c) taken from Ref. [66].

the cavity; the latter because the temperature limit of cavity cooling is $T_{\text{cav}} = \hbar\kappa/k_B$, way higher than the Doppler limit for our characteristic $\kappa \gg \gamma$.

A core part of my work was dedicated to solve this problem by developing and implementing alternative cooling methods specially compatible with high-bandwidth cavities. In Chapter 3 I present the adaptation of degenerate Raman sideband cooling (dRSC) with cavity-assisted repumping [1] that we use in most of the experimental sequences as a precooling step. Further, in Chapter 4 I present the technique of 3D continuous Raman sideband cooling (cRSC) with only two dedicated Raman beams [2], that we employ for fluorescence imaging of the atoms (see also Sec. 2.3.5).

2.3.3 Optical pumping for state initialization and imaging illumination

Optical pumping on the D_1 transition As introduced in Section 2.2, we couple two σ^- -polarized 795 nm beams through the cavity LT mirror, to serve as optical pumping beams on the D_1 line. The ^{87}Rb energy levels that are addressed are shown in Figure 2.5 (a). The repumper beam ($|F = 1\rangle \rightarrow |F' = 2\rangle$) is used to pump the atomic population from the lower to the higher hyperfine ground state, while the optical pumping beam ($|F = 1\rangle \rightarrow |F' = 2\rangle$) is used to polarize the atoms in $m_F = -2$.

Atomic state initialization. This optical pumping (OP) scheme allows to initialize the atomic state in $|F = 2, m_F = 2\rangle$, which is a dark state. The fidelity of the state preparation thus critically depends on the polarization purity of the OP beams. To optimize the purity, we align the quantization axis of our system by measuring the optical pumping time τ_{OP} (Figure 2.5 (b)) while scanning the direction of the magnetic bias field. By minimizing the pumping time, we optimize the polarization purity of the OP beams. After optimization, we achieve state preparation fidelities of ~ 95 percent with an OP time $\tau_{\text{OP}} \approx 3 \mu\text{s}$. This is still limited by residual polarization impurity originated by random birefringence fluctuation of the in-coupling optical fiber (e.g. affected by air flow or temperature changes in the lab).

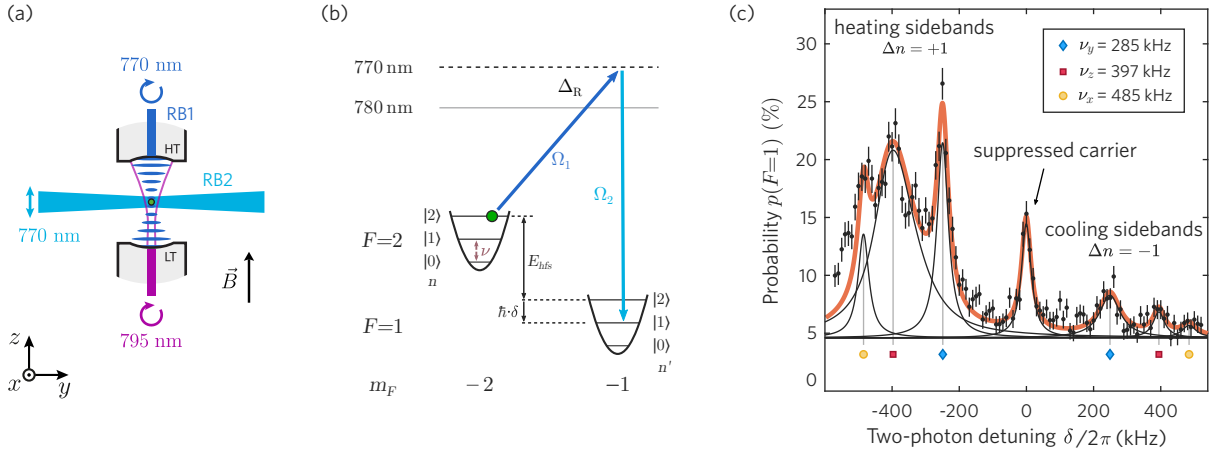


Figure 2.6: Raman manipulation of atomic hyperfine states and motional state coupling. (a) Simplified diagram of the Raman beam configuration. The 770 nm intra-cavity field also acts as a first Raman beam (RB1), and the second one (RB2) is overlapped with the y -axis lattice. For state initialization, the 795 nm optical pumping beams are coupled through the bottom LT mirror. (b) Relevant energy levels of ^{87}Rb for Raman coupling of motional states of a trapped atom in the lattice. The frequency difference of RB1 and RB2 equals the Zeeman-shifted energy splitting between the involved hyperfine levels E_{hfs} , plus a two-photon detuning δ . To drive motional sidebands, the beams are tuned to a multiple Δn of the trap frequency $\omega_{i,ax}$, i.e. $\delta = \Delta n \cdot \omega_{i,ax}$. (c) Raman spectrum of a single atom in the 3D lattice, showing all first order sidebands and the suppressed carrier. The trap frequencies ν_i are extracted by fitting the data with the sum of seven Lorentzians (orange line, individual peaks in black). We also use the spectrum for sideband-ratio thermometry, see main text. Figure (c) adapted from Ref. [2].

Calibration of the saturation parameter with pumping rates. We also use the OP beams as illumination light for the new Raman imaging scheme, on the D_1 line and thus independent from the cavity resonance on the D_2 line [93], see Figure 2.2 and Section 2.3.5. Therefore, it is essential to know the intensity I_{rep} of the illumination (mostly the repumper beam) at the atom's position inside the cavity. The presence of differential light-shifts induced by the near-resonant D_1 illumination (see Chapter 4) renders this knowledge even more critical. Clearly that is a problematic task with the current scheme because the losses in the optical fiber and through the LT mirror are unknown (these beams are not resonant with the cavity). A power measurement "on the other side" to estimate the losses is in this case impossible.

As a solution, we calibrate the saturation parameter $s = I_{\text{rep}}/I_{\text{sat}}$ by monitoring saturation of the optical pumping rates between hyperfine ground states for a single atom as a function of the intensity I_{rep} and the detuning Δ . As shown in Figure 2.5 (b,c), we measure optical pumping ($|F=1\rangle \rightarrow |F=2\rangle$) saturation curves for scans of parameters I_{rep} and Δ . For each curve we extract the characteristic pumping time τ_{OP} with a stretched exponential fit, to account for the inhomogeneous position distribution of the atoms [75]. Then, from the dependence of the pumping times τ_{OP} versus the detuning Δ (Figure 2.5 (c)), we obtain with a fit the calibration constant $c_s \approx 8 \times 10^{-4} \mu\text{W}^{-1}$ that links the measured power (P) before coupling into the LT fiber with the intracavity saturation parameter $s = c_s \cdot P$. For the fit we use the expression of the scattering rates in Ref. [111] with a Gaussian convolution to account for frequency noise of the lasers, see Ref. [66] for details.

2.3.4 Raman manipulation of the hyperfine states

Raman scheme with an intracavity field and a single free-space beam. In 2.2, we briefly introduced our Raman scheme to manipulate the ground hyperfine states of the ^{87}Rb atoms, specifically the qubit states $|F = 2, m_F = -2\rangle$ and $|F = 1, m_F = -1\rangle$ [41]. The optical setup is illustrated in a simplified diagram in Figure 2.6 (a).

The intracavity lattice DT_z with σ^+ polarization, generated by the 770 nm lock laser that stabilizes the cavity, also plays the role of a first Raman beam (RB1). A second 770 nm Raman beam (RB2) with π polarization, propagates in free-space along the y -axis and enters the cavity from the side, overlapped with the DT_y lattice. Together, RB1 and RB2 form a Raman beam pair that couples the atomic hyperfine states. The light source of RB2, the so called Raman laser, is phase-locked to RB1 (lock laser) to obtain sufficiently high resolution for driving coherent Raman transitions between hyperfine levels (see Figure 2.3)).

Such configuration of Raman beams, requiring only a single free-space beam and the intracavity lock field, is technically simple to implement, resource efficient and ideal for situations with limited optical access, e.g. for miniaturized quantum optical experiments.

A linewidth-reduced DBR Raman laser. An upgrade to the system was to exchange the light source used as the Raman laser (RB2). We replaced the home-built interference filter laser [112] previously used in [76] by a distributed Bragg reflector (DBR) laser which offers convenient and mode hop free tuning over several GHz, and good long term frequency stability. The drawback of the DBR laser, however, is its large linewidth of ~ 700 kHz, too broad for a high-quality phase lock. To reduce the linewidth, we upgrade the DBR laser with an external optical feedback setup [65], which is shown in a very simplified form in Figure 2.3. By optimizing the optical feedback power, we obtain laser linewidths of ~ 1 kHz, ideal for a high-stability phase lock. Further details about the linewidth-reduction are found in Appendix B.7 including a complete diagram of the setup. For an comprehensive description of the working principle and the linewidth-measurement method, see Ref. [65].

Carrier-suppressed Raman transitions between the hyperfine states. The relevant ^{87}Rb energy levels for Raman coupling are shown in Figure 2.6 (b). As discussed in Section 2.3.3, the atoms are initialized in the state $|F = 2, m_F = -2\rangle$ by optical pumping with the 795 nm OP lasers.

To drive coherent two-photon transitions between the qubit states, the Raman beams RB1 and RB2 are phase locked with a frequency difference ~ 6.8 GHz corresponding to the energy splitting E_{hfs} between the hyperfine levels $|2, -2\rangle$ and $|1, -1\rangle$, plus a variable two-photon detuning δ . The resonant coupling at $\delta = 0$ is called the carrier transition, i.e. without coupling to the motional states of the trapped atoms. Detrimental off-resonant scattering is suppressed by a single-photon detuning from the D_2 of $\Delta_R \approx 5$ THz.

The two-photon Raman-Rabi frequency of the carrier transition Ω_0 is given by [113]

$$\Omega_0 = \frac{\Omega_1 \Omega_2}{2\Delta_R}, \quad (2.13)$$

with Ω_1 and Ω_2 the single-photon Rabi frequencies of RB1 and RB2 respectively. In our case, from measurements of the intensity of the Raman beams² and with Eq. (2.13), we estimate a maximum coupling frequency $\Omega_0 \approx 2\pi \times 350$ kHz.

² For the intracavity lock field (RB1) at intensity maxima $I_{\text{RB1}} \approx 6.69 \times 10^5$ mW/cm², for the free-space Raman beam (RB2) $I_{\text{RB2}} \approx 7.43 \times 10^5$ mW/cm²

However, in our configuration the standing-wave intensity pattern of RB1 must be considered. At the center of the DT_z lattice sites there is no RB1 light and thus Ω_0 vanishes. Still, Raman coupling is enabled by the oscillatory motion of the atoms in lattice sites around the zero-intensity point. This leads to the suppression of the carrier transition but still allows coupling on odd-order sidebands [114, 115], as will become clear soon by means of Raman spectroscopy. Such *carrier-free* Raman coupling is not specially beneficial for coherent qubit operations (for this we have use microwave-driving in Ref. [76]) but results highly convenient for Raman cooling, since it reduces off-resonant carrier transitions that affect the cooling efficiency (see Chapter 4).

Raman coupling of motional states. As discussed in Section 2.3.2, our 3D optical lattice traps atoms in the Lamb-Dicke regime [103, 104]. In this condition, the Raman beams can resolve the motional states $|n\rangle$ of trapped atoms, also depicted in Figure 2.6 (b). By setting the two-photon detuning δ to a multiple Δn of the characteristic axial trap frequency along the i direction, i.e. $\delta = \Delta n \cdot \omega_{i,\text{ax}}$, the Raman beams couple the internal and external degrees of freedom of the atoms. In this way the Raman fields drive coherent two-photon transitions of the type $|2, -2; n\rangle \rightarrow |1, -1; n'\rangle$ with $n' = n + \Delta n$, and $\Delta n = 0$ corresponding to the carrier transition. In our case, the carrier-free characteristic discussed before imposes the condition $\Delta n = \pm 1, \pm 3, \dots$ [114, 115]. Most interesting for us are the transitions with $\Delta n = \pm 1$, i.e. the first order sidebands, with the positive side called the *heating* sideband and the negative one the *cooling* sideband. As the name suggest, the coupling offered on the cooling sideband between internal degrees of freedom and the motional states $|n\rangle \rightarrow |n - 1\rangle$ is used for Raman sideband cooling as will be discussed later.

The Raman motional coupling efficiency along a given lattice direction i , depending on the geometry of the beams, can be described by the Lamb-Dicke parameter [104]

$$\eta_i = k_{\text{eff},i} \Phi_{0,i}, \quad (2.14)$$

where $\Phi_{0,i} = \sqrt{\hbar/(2 m_{\text{Rb}} \omega_i)}$ is the spread of the ground-state wave function along the i -axis. The factor $k_{\text{eff},i} = |(\mathbf{k}_1 - \mathbf{k}_2) \cdot \hat{i}|$ is the effective wave vector magnitude in the lattice i -direction, with \mathbf{k}_1 and \mathbf{k}_2 the wave vectors of the Raman beams RB1 and RB2 respectively. The Raman-Rabi frequency on the first order sidebands scales with the Lamb-Dicke parameter as [104]

$$\Omega_{i,\text{heat}} = \Omega_0 \sqrt{n+1} \eta_i, \quad (2.15)$$

$$\Omega_{i,\text{cool}} = \Omega_0 \sqrt{n} \eta_i, \quad (2.16)$$

where the frequencies on the heating and cooling sidebands show a different dependence on the particular motional state $|n\rangle$ that is addressed.

We consider now the slight non-orthogonality of our lattice beams (see Sec. 2.3.2) featuring small angles $\theta_x \approx 15^\circ$ and $\theta_y \approx 6^\circ$ of DT_x and DT_y with respect to the plane normal to DT_z . With the configuration of our Raman beams along DT_y and DT_z , the geometry ensures that the difference of the Raman-beam wave vectors has a projection along all lattice dimensions. In other words, with the single pair of Raman beams RB1+RB2 we can couple the motional states in all directions. Using Equation (2.14), we estimate the Lamb-Dicke parameters in our lattice that describe the Raman coupling efficiency as $(\eta_x, \eta_y, \eta_z) \approx (0.03, 0.09, 0.11)$ along the respective lattice directions.

Raman spectroscopy and sideband-ratio thermometry. We use the cavity state detection presented in Section 2.3.1 to perform Raman spectroscopy with single atoms of the motional energy levels in our 3D lattice. After loading a single atom into the cavity and preparing it in the state $|2, -2\rangle$ with optical

pumping, we shine a Raman pulse with variable two-photon detuning δ , driving Rabi oscillations between the states $|2, -2\rangle$ and $|1, -1\rangle$, after which the internal state $|F\rangle$ of the atom is probed with the cavity detection.

We record Raman spectra by evaluating the transfer probability of an atom to $|F = 1\rangle$ from a set of measurement repetitions, as a function of the Raman two-photon detuning δ . In Figure 2.6(c) we show a typical spectrum after precooling with degenerate Raman sideband cooling (dRSC, see Chapter 3).

On the left side of the spectra ($\delta < 0$) we identify the heating sidebands ($\Delta n = +1$) for each lattice dimension and the corresponding cooling sidebands ($\Delta n = -1$) on the right side ($\delta > 0$). We can also see that the carrier peak is highly suppressed as expected from the standing-wave characteristic of RB1. We extract the oscillation frequencies ν_i corresponding to each lattice dimension with a fit to the spectrum using the sum of seven Lorentzian curves. We will use this information to overlap the cooling sidebands for continuous Raman sideband cooling (cRSC) as we will see later. More details on the Raman spectroscopy measurement and the full interpretation of the spectrum are found in Chapter 4 and Appendix B.8.

We also use the Raman spectrum for sideband-ratio thermometry [116]. With this technique, assuming that the motional states exhibit a thermal distribution, the mean motional excitation \bar{n}_i along the i -axis is determined by

$$\bar{n}_i = \frac{1}{R_{h/c,i} - 1}, \quad (2.17)$$

where $R_{h/c,i} = h_{\text{heat}}/h_{\text{cool}}$ is the ratio of heights of the heating (h_{heat}) and cooling (h_{cool}) sidebands in the spectrum. This method also provides a measurement of the mean temperature of the atoms as

$$T_i = \frac{\hbar\omega_i}{k_B \ln(R_{h/c,i})}, \quad (2.18)$$

and additionally the ground state population $n_{0,i}$ can be derived from \bar{n}_i , giving the expression

$$n_{0,i} = \frac{1}{1 + \bar{n}_i}. \quad (2.19)$$

In Chapter 3 and Chapter 4 we will use these expressions to evaluate the efficiency of our cooling methods.

3D Raman sideband cooling with a single Raman-beam pair. As discussed earlier in this section, the small non-orthogonality of our lattice enables Raman motional coupling along all directions. To implement simultaneous cooling in 3D, we overlap the motional sidebands at ~ 350 kHz and drive them continuously. With Equation (2.16) and the Lamb-Dicke parameters that we derived earlier, we estimate Raman-Rabi frequencies (assuming $n = 1$) of $\Omega_{xyz} \approx 2\pi \times (14, 42, 48)$ kHz. The 795 nm OP beams on the D₁ line are activated simultaneously to complete the cooling cycle.

With this scheme, directly after cooling, we estimated a residual temperature $T \approx 1.4$ μ K corresponding to motional ground state populations $n_0 > 85\%$ in each direction, based on Raman spectroscopy measurements using Eq. (2.18) and Eq. (2.19). We also observe trapping lifetimes of ~ 1 min in the 3D lattice, where the limit is attributed to background gas collisions and not to the cooling efficiency. Ultimately, we employ this cooling method for imaging the atoms as has been mentioned before, by collecting the D₁ photons scattered during optical pumping. The implementation of 3D cooling and *Raman imaging* are discussed with detail in Chapter 4 and in Appendix B.

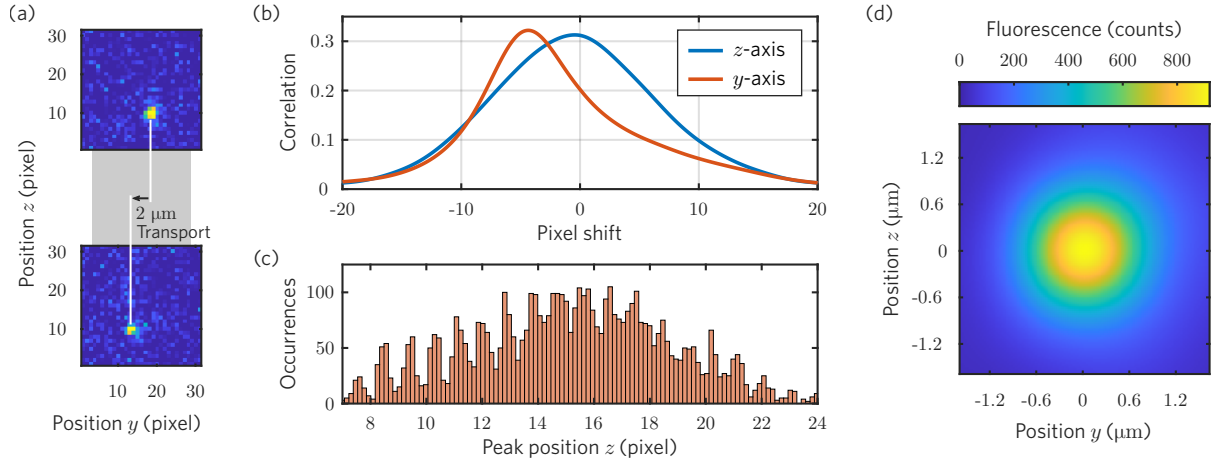


Figure 2.7: Characterization of the new imaging system. **(a)** To calibrate the magnification factor along the y -axis we take advantage of our conveyor belt transport. With a single atom (or few) loaded into the 3D lattice, two images are taken interleaved with a $2\ \mu\text{m}$ transport. **(b)** The cross correlation between the two frames in (a) is computed along both yz axes and then averaged over ~ 100 repetitions. The pixel shift value of the correlation maximum corresponds to the $2\ \mu\text{m}$ transported distance, resulting in a magnification factor $M_y \approx 35$. **(c)** Lattice reconstruction along the z -axis with the histogram of atoms positions to calibrate the corresponding magnification and compare it to the alternative method, giving a factor $M_z \approx 38$. **(d)** Point spread function (PSF) of our system reconstructed by averaging single atoms images after superimposing them by means of the position detection algorithm. We estimate a PSF Gaussian width of $\sim 0.8\ \mu\text{m}$. Figures adapted from Ref. [67].

2.3.5 Position detection by cavity-compatible imaging

New cavity-compatible imaging scheme. The last ingredient of our basic toolbox is the position detection of the atoms by fluorescence imaging. As discussed in Section 2.2 and shown in Figure 2.2(c), previously in our experiment fluorescence imaging, implemented on the ^{87}Rb D_2 line [74, 75], was only possible by detuning the cavity to avoid the inhibiting influence of the Purcell effect.

As mentioned in Chapter 1, part of my work was to implement a new imaging scheme on the D_1 line, thus independent from the cavity coupling, to allow simultaneous operation of the quantum channel and the imaging channel (recall Figure 1.1(a)). This involved the development and implementation of a new Raman imaging method using continuous Raman sideband cooling, that relies on collecting the photons scattered during the cooling repumping cycle with and in-vacuum high-NA lens (see Figure 2.2(b)), and imaging them with an EMCCD camera³. The Raman imaging method is discussed in depth in the dedicated Chapter 4. Summarizing the figures of merit: a signal to noise ratio $\text{SNR} \approx 13$ with a 1 s exposure time and an atom survival probability $> 90\%$.

My work also included the design of a new imaging system to suppress detrimental scattering from the edge of the FFPC mirrors, stemming from the fiber-coupled 795 nm illumination beams (our OP beams) injected through the bottom LT mirror. Details about this problem and the new design can be found in Ref. [66]. Furthermore, we implemented a position detection algorithm as a postprocessing step [67] to extract accurately the positions of the atoms taking into account the resolution limit. The complete characterization of the imaging system is included in Ref. [66, 67]. Here I will only summarize the characterization of two properties that are relevant for the following chapters: the magnification factor and the resolution limit.

³ Andor iXon 3: CCD chip with $512 \times 512\ \text{px}^2$, pixel size $16 \times 16\ \mu\text{m}^2$, conversion factor (15 ± 1) counts/photon.

Magnification factor. A standard method to determine the magnification factor in quantum optics experiments with optical lattices, is to use the average spatial intensity distribution of atomic fluorescence as a ruler for calibration [57, 74] the positions of highest intensity are identified as the center of the lattices sites and the resulting lattice spacing at the image plane (on the camera picture, in pixels) is compared to the corresponding real distance at the object plane, i.e. λ_{DT} .

However, in our system with only one or few atoms in the 3D lattice, this method is not practical since it implies a very high number of measurement repetitions on the order of ~ 1000 . Also, given the use of the DT_y lattice as a conveyor belt, the positions of the trapping sites are not well defined in the lab reference frame, i.e. the stopping positions shift slightly between measurements, which washes out the lattice shape when averaging.

Consequently, we employ an alternative method, first developed in Ref. [93], that takes advantage of our atom transport capability with the optical conveyor belt. The concept is shown in Figure 2.7 (a). We load a single or few atoms into the cavity where we can check the presence with the cavity detection, then acquire two images separated by a $2\ \mu\text{m}$ conveyor belt transport. Subsequently, we calculate the cross-correlation between the two frames along both axes y and z , and average over only ~ 100 measurement repetitions, as shown in Figure 2.7 (b). The pixel shift where the correlation is maximum corresponds to the transport distance of $2\ \mu\text{m}$. We then use the relation $M = c \cdot s/T$, where c is the pixel shift of the peak of the correlation function, s is the pixel size and T is the transport distance. With the size of a camera pixel $16\ \mu\text{m}$ we obtain a magnification factor $M_y \approx 35$. The very small shift of the correlation along z means there is a very small angle $< 1^\circ$ between the camera axis and the DT_y lattice, which we neglect.

To verify our alternative method, we also carry out the calibration of the magnification along the z -axis, this time with the more standard lattice reconstruction method. However, instead of averaging the intensity profile as commonly used [57, 74], we determine the position of each atom with the position-detection algorithm [67], from a set of single or few-atom images. Even if the pictures are mostly single-atom images without a common spatial reference, the intracavity lattice DT_z features a very stable phase that permits this measurement. From the histogram of extracted atom positions, shown in Figure 2.7 (c), we obtain the magnification factor $M_z \approx 38$, confirming the measurement of M_y within uncertainties.

Resolution limit. To investigate the resolution limit of our imaging system, we reconstruct the point spread function (PSF) [57], as shown in Figure 2.7 (c). For this, we select images with well isolated atoms (two close-by atoms would not work) and, average the images after superimposing them, centered by the atom positions determined with the position-detection algorithm. From the average intensity profile we estimate a PSF Gaussian width of $\sim 0.8\ \mu\text{m}$. This result compared to the lattice spacing $\lambda_{DT}/2 = 434\ \text{nm}$, means that our imaging system does not have a native single-site resolution. Nevertheless, it is still possible to achieve single-site resolution by clever postprocessing algorithms, e.g. by providing additional information on the geometry of the system [57].

Ultimately, this newly implemented imaging scheme matches the goal of counting individual atoms and determining their position with full site resolution [57], while leaving the resonant cavity transition reserved for the quantum channel.

2.4 Summary and conclusions

In this chapter I have introduced the experimental apparatus involved in the operation of our atom-FFPC module. Furthermore, I have presented the basic toolbox of techniques for control and detection of the internal and external degrees of freedom of single atoms.

Concretely, regarding control I discussed the basic atom cooling and trapping techniques that we employ in an experimental sequence, including a small magneto-optical trap (MOT), an intracavity lattice, and atom transport with a conveyor belt to deliver the atoms from the MOT into the cavity. I also showed our scheme for state initialization by optical pumping on the D_1 line, which is also used as illumination light for fluorescence imaging. In this regard, we used a special method to calibrate the intracavity power when the system does not allow direct measurement. As a third control module, I introduced the Raman scheme to couple the qubit states of the atoms. We use a particular Raman beam geometry, with one of the beams being also the intracavity lattice, that allows us to drive the motional sidebands along all the lattice directions. Along this line, I advanced briefly the Raman cooling scheme that we use for cooling in 3D with only one Raman-beam pair, and that will be the basis for the new imaging technique in Chapter 4.

On the detection side, I presented two techniques. First, the non-destructive cavity-based detection permits to retrieve the internal state and the presence of a single atom by monitoring the induced vacuum Rabi-splitting with the cavity-probe reflection. Second, a new imaging scheme on the D_1 line, instead of the previously used D_2 line, enables the position and number detection of cavity-coupled atoms, without restricting the cavity quantum channel. This scheme relies on the Raman imaging method that will be presented in Chapter 4. In this chapter I focused on the general concept and on the characterization of the imaging system.

This chapter will serve as a basis for the subsequent chapters where I present extensions to the atom control toolbox, including novel techniques for cooling (Chapter 3), imaging (Chapter 4) and denser loading of multiple atoms (Chapter 5), specifically developed for compatibility with high-bandwidth cavities.

Ground–state cooling of a single atom inside a high–bandwidth cavity

COOLING has been fundamental for the ultimate control of individual atoms that is achievable nowadays [70, 95]. Multiple and diverse laser-cooling techniques have been developed over the past decades [59, 60], complementing the existing trapping techniques, unlocking an unprecedented level of control of the atomic motion and position. The enormous advantage of isolated and controlled atoms is that they become a clean and simple system close to the idealized case, that can be studied, understood and manipulated with high precision. Furthermore, cooling the atomic motion improves the trapping time of the atoms thus allowing higher repetition rates of the experiment or application, and improving its reproducibility by making different atoms indistinguishable.

In the case of atom-cavity modules as light-matter interfaces for quantum nodes, the atom has to be confined at an antinode of the cavity field within a fraction of the wavelength, to ensure optimal coupling efficiency. Besides a tight trapping potential, this requires cooling the atomic motion in the trap close to the oscillatory ground state. As discussed in chapters 1 and 2, high-bandwidth optical cavities constitute an important cavity-QED regime, that is especially useful for atom-photon quantum interfaces that involve interactions with temporally very short pulses, as emitted by e.g. quantum dot light sources. In chapter 2 we introduced the fiber Fabry-Pérot cavity (FFPC) at the heart of our experiment, which offers a highly interesting regime featuring strong atom-light coupling together with a high-bandwidth interface. However, the miniaturized construction of such fiber-based cavities (i.e. reduced optical access) and their high-bandwidth characteristic, render the usage of standard atom cooling techniques, such as optical molasses or cavity cooling [109, 110], unfeasible (see Appendix A.1). As an alternative we find that degenerate Raman sideband cooling (dRSC) [113, 117] can be successfully applied.

In this chapter* I report successful cooling of a single ^{87}Rb atom to its one-dimensional motional ground state while coupled to the high-bandwidth FFPC in our experiment, based on the publication [1] included in Appendix A. We overcome the challenge of cooling inherent to such high-bandwidth atom-cavity modules, by adapting the dRSC technique to our cavity and lattice system, by which Raman cooling transitions are driven by the trapping lattice itself. This technique was developed before in the field of

* **Statement of published work:** The content of this chapter is a summary of the publication reprinted in Appendix A, and with the same title as the chapter: *Ground-state cooling of a single atom inside a high-bandwidth cavity*, E. Uruñuela, W. Alt, E. Keiler, D. Meschede, D. Pandey, H. Pfeifer, and T. Macha, *Physical Review A* **101**, 023415 (2020) [1].

Statement of author contribution: The concept and measurement plan was developed by T. Macha in [76], while I completed the calibrations of the experimental setup. Together with T. Macha, I prepared and performed the measurements, and analyzed the data that conducted to the published results. Furthermore, I participated in the writing process of the manuscript together with the other co-authors.

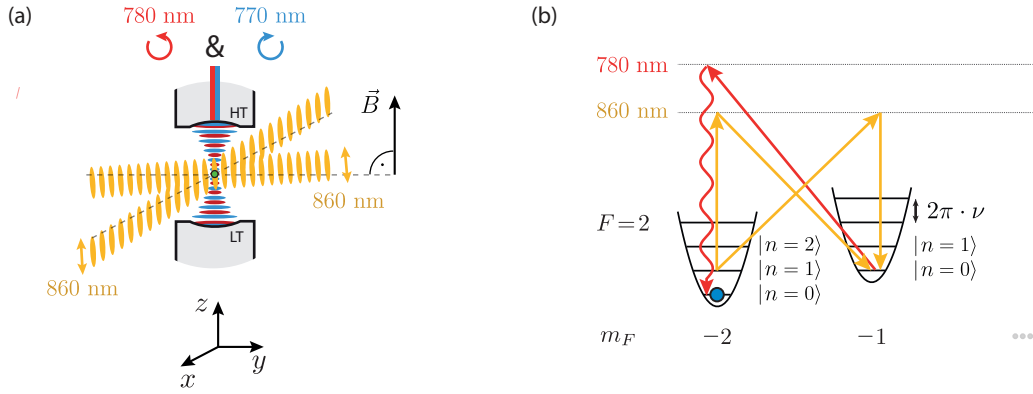


Figure 3.1: Concept for implementation of dRSC inside a cavity. **(a)** Two crossed 860 nm linearly-polarized dipole traps (xy plane) and a 770 nm intra-cavity field with σ^+ polarization (z axis), form a 3D lattice that traps a single atom at the center of the FFPC. The horizontal lattice beams have slightly non-orthogonal angles with respect to the cavity axis. The 780 nm cavity probe with σ^- polarization is used for optical pumping and state preparation. A tunable magnetic bias field is applied along the cavity to define the quantization axis. **(b)** Diagram of one cooling cycle of dRSC in a one-dimensional case. The lattice with non-orthogonal geometry drives two-photon $\sigma^+-\pi$ or $\pi-\sigma^-$ transitions between adjacent m_F levels of the trapped atom, that reduce the motional quantum number $|n\rangle$. The cooling cycle is completed with optical pumping by the cavity probe field. Figure from the publication [1].

dense atomic gases [113, 117]. However, here we show for the first time its implementation inside a cavity and in the single-atom regime. Our implementation offers a versatile and resource-efficient solution for cooling and thus controlling trapped atoms for light-matter interfaces.

A comprehensive description of the experimental setup and techniques needed for the operation of our atom-cavity module was given in chapter 2. In Figure 3.1 (a) we recapitulate the crucial elements that play a role in our implementation of dRSC, (for details also see Appendix A.2). At the heart of the experiment is the high-bandwidth FFPC with parameters $(g, \kappa, \gamma) = 2\pi \times (80, 41, 3)$ MHz (see section 2.1 and table D.1). A single ^{87}Rb atom is trapped in a three-dimensional (3D) optical lattice at the cavity center, coinciding with an antinode of the 780 nm resonant cavity probe field to ensure high coupling. Recalling the lattice configuration: in the horizontal plane two crossed 860 nm red-detuned standing-wave dipole traps ($\text{DT}_{x,y}$) and in the vertical axis a 770 nm blue-detuned intra-cavity lattice (DT_z), with respective estimated axial trap frequencies $\nu_{x,y} \leq 400$ kHz and $\nu_z \leq 280$ kHz, allowing confinement in the Lamb-Dicke regime [103, 104]. A magnetic bias field along the cavity axis defines the lattice polarization scheme as $(P_x, P_y, P_z) = (\pi, \pi, \sigma^+)$. The cavity probe field has σ^- polarization and is resonant with the D_2 line on the $|2\rangle \rightarrow |3'\rangle$ transition. Here and throughout the chapter we use the notation for quantum states $|F, m_f; n\rangle$ introduced in Chapter 2, with the prime symbol marking excited states. We also recall that the beams of DT_x and DT_y are slightly tilted with respect to the xy plane, with angles $\sim 15^\circ$ and $\sim 6^\circ$, respectively (measured more precisely after the publication), an important detail for the cooling method that we will discuss in the following.

3.1 Simple cavity-compatible cooling with degenerate Raman transitions

Our cooling scheme relies on two-photon transitions driven by the lattice beams, that couple the motional states of the atom with its internal states. The cooling concept is depicted in the diagram of Figure 3.1 (b)

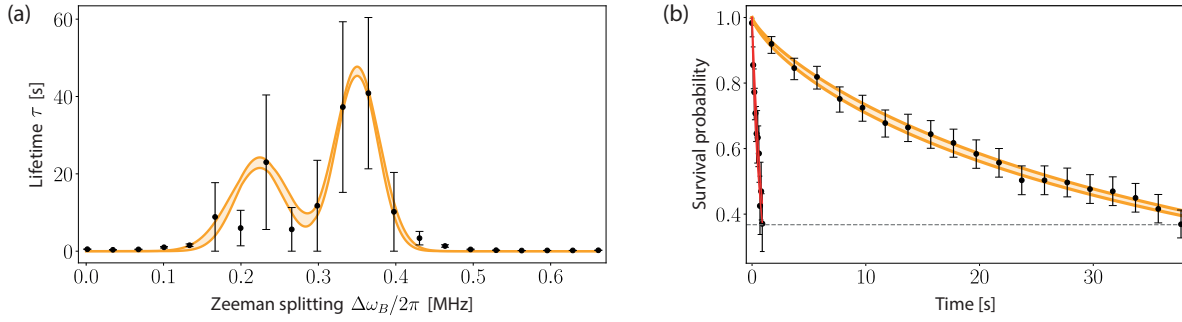


Figure 3.2: Characterization of the dRSC method for atom cooling. **(a)** Measurement of the trapping lifetime τ of a single atom in the 3D lattice while applying dRSC, in dependence to the Zeeman splitting $\Delta\omega_B = 2\pi\nu$. We fit two Gaussians with maxima centered at the Zeeman shift values that fulfill Equation (3.2) for the longitudinal trap frequencies of the different lattice axes $\nu_z = (224 \pm 5)$ kHz and $\nu_{x,y} = (350 \pm 1)$ kHz, indicating the activation of dRSC. Long measurement times per repetition (~ 60 s) limit the number of data samples, thus the error bars are calculated using the bootstrapping method. **(b)** Comparison of survival probability decay curves at the optimum magnetic field, for the cases with dRSC active (yellow line) and with cooling deactivated (red line) by switching off the optical pumping field (cavity probe). With stretched exponential fits we obtain the drastically different lifetimes $\tau_{\text{on}} = (42.9 \pm 1.0)$ s and $\tau_{\text{off}} = (1.0 \pm 0.1)$ s that validate the efficacy of the cooling method. Figure from the publication [1].

for a one-dimensional scenario (further details are given in Appendix A.3). Specifically, we use transitions between adjacent magnetic m_F sublevels of the $|F = 2\rangle$ hyperfine ground state, that simultaneously lower the quantized vibrational level $|n\rangle$ of the atom in the trap:

$$|2, -2; n\rangle \rightarrow |2, -1; n-1\rangle. \quad (3.1)$$

To enable such degenerate Raman transitions, two conditions are necessary. First, the Zeeman shift $\Delta\omega_B$ of adjacent m_F levels has to match the energy spacing of motional states in the trap with oscillation frequency ν [61]:

$$\Delta\omega_B = 2\pi\nu, \quad (3.2)$$

which we achieve by tuning the magnitude B of the magnetic field. Second, the light field of the DT beams needs to provide pairs of photons $\sigma^+-\pi$ or $\pi-\sigma^-$ simultaneously to sustain the required Raman coupling. Contrary to previous implementations that use elliptically polarized beams [113, 117, 118], here the necessary mixture of polarizations is provided by the inclination of the DT beams with respect to the horizontal plane. Additionally, we observe that tilting the direction of the magnetic field, while keeping its magnitude constant, also helps in this regard. To complete the cooling scheme, the weak cavity probe field is used to optically pump the atom without altering the motional state back to $|2, -2; n-1\rangle$, effectively decreasing the motional state by one phonon per loop. The continuous cycle drives the atom down the phonon ladder until reaching the ground state $|2, -2; 0\rangle$, which is dark to the degenerate Raman transitions. An additional repumper beam along DT_x (not shown) in the $\text{D}_2 |1\rangle \rightarrow |2'\rangle$ transition takes care of any off-resonant decay into $|F = 1\rangle$. In this way, the cooling mechanism is always active as soon as the atoms enters the cavity mode, independently of its initial state.

To verify and characterize the cooling mechanism, we measure the average trapping lifetime of the atom for different magnitudes B of the magnetic field up to 1 G, while the cooling is active. We use the non-destructive cavity detection (Section 2.3.1) to continuously monitor the presence of the atom, and from multiple repetitions we extract the trapping lifetime τ with a stretched exponential fit [119,

120] (see also Appendix A.4). The results are shown in Figure 3.2 (a) as a function of the corresponding Zeeman splitting $\Delta\omega_B$. We observe a significant increase in the measured lifetime around the values $\Delta\omega_B = 2\pi \times (350 \pm 1)$ kHz and $\Delta\omega_B = 2\pi \times (224 \pm 5)$ kHz, where the condition of Equation (3.2) is met for the trap frequencies $\nu_{x,y}$ and ν_z , respectively. The broad width of the cooling regions is attributed to inhomogeneous broadening due to the distribution of atom positions in the 3D lattice.

To further validate the cooling effect we analyze the survival probability at the frequency $2\pi \times 350$ kHz of the optimum Zeeman shift, comparing the case with dRSC activated and the case without cooling, which we deactivate by switching off the optical pumping (cavity probe field). In Figure 3.2 (b) we show the decay curves of the two cases, resulting in lifetimes of (42.9 ± 1.0) s under dRSC, as opposed to (1.0 ± 0.1) s without cooling. The main source of atom loss leading to such short lifetimes is parametric heating induced by intensity noise in the intra-cavity lattice DT_z [121, 122], which is efficiently compensated by the dRSC method. The fact that the z direction is also cooled when addressing the frequency for $DT_{x,y}$ indicates the presence of a 3D cooling mechanism. This could be explained by cross-dimensional mixing [115], or by the projection along DT_z of the $DT_{x,y}$ beams driving the Raman transitions, coming from the non-orthogonal geometry.

For a quantitative estimate of the observed cooling effect in DT_z , we perform Raman spectroscopy along the z axis, after a 150 ms dRSC interval. To drive resolved-sideband Raman transitions with tunable frequency for the spectroscopy measurement, we use the Raman setup presented in Section 2.3. From the sideband imbalance in the Raman spectrum [116] (the spectrum is shown in Appendix A), we obtain a mean motional number $\bar{n}_z = (0.13 \pm 0.03)$, corresponding to a one-dimensional ground-state population of $n_{0,z} = (88 \pm 3)\%$ and a residual temperature $T_z \approx 1.2 \mu\text{K}$. A similar measurement with a 100 ms cavity-noise-heating period (without cooling) before the spectroscopy pulse, results in an estimate of $\bar{n}_z = (0.47 \pm 0.06)$ and $T_z \approx 2.3 \mu\text{K}$. These observations confirm an efficient 3D cooling mechanism as previously suggested.

3.2 Summary and conclusions

In this chapter, I have shown the implementation of a simple, cost-efficient and robust atom-cooling technique inside a high-bandwidth optical cavity. Furthermore, I have shown that a slightly non-orthogonal geometry of the optical lattice not only produces the necessary polarizations for Raman coupling, but also induces three-dimensional cooling of the atom. Since, apart from the lattice, only weak optical pumping and a tunable magnetic field are needed, the dRSC method is easily applicable to other cavity experiments due to its simplicity and versatility, even in the case of narrow-linewidth resonators. More generally, this implementation can also be interesting for atoms in lattices without a cavity, e.g. in applications with limited optical access.

Ultimately, overcoming the difficulties of cooling in such high-bandwidth resonators is a valuable contribution to the control toolbox for atom-cavity quantum nodes. The very long trapping lifetimes that it provides for cavity-atom interaction, allow high repetition rates of the experiment, which in turn directly enhances the uptime of the atom-cavity module.

However, since dRSC relies on scattering photons from far off-resonant traps, it entails a slow cooling rate. For some applications faster and more powerful cooling methods are necessary, for instance to compensate strong recoil heating rates during fluorescence imaging of the atoms. Consequently, in our experiment we have also implemented a second cooling technique, namely carrier-free Raman sideband cooling [114] in three dimensions, using the same tools as for Raman spectroscopy. In chapter 4 we will show how we apply this more powerful cooling technique for imaging and locating individual atoms inside of the FFPC.

Raman imaging of atoms inside a high-bandwidth cavity

IMAGING of individual atoms goes hand in hand with cooling and trapping methods for a high level of control [70, 95]. The detection of single atoms has been a vivid subject of research in the past 50 years [54, 55], prompting the development of a broad range of experimental techniques, from which fluorescence imaging has been established as the workhorse for neutral atoms [56, 58]. A successful and non-destructive imaging scheme requires high photon scattering rates in addition to an efficient cooling mechanism to compensate for the energy gain induced by photon recoil. While cooled and pinned in an optical lattice [62, 63], high-resolution imaging [57] provides information on the location of the atoms that can then be used for individual manipulation.

Not surprisingly, imaging is crucial for operating atom-cavity quantum nodes with atomic ensembles. In Chapter 1 we emphasized that coupling multiple atoms to a high-bandwidth cavity [43, 44], instead of a single atom, has the potential to greatly enhance the efficiency of the quantum node [45, 46] and unlock new powerful applications [47, 48, 51, 52]. Most of the multi-atom implementations require critical knowledge on the number of coupled emitters and their relative positions within the cavity mode. In our experiment, we pursue the architecture for quantum nodes presented in Chapter 1 in Figure 1.1 (a) based on a fiber Fabry-Pérot cavity (FFPC): The single-sided high-bandwidth cavity interfaces photonic and atomic qubits and routes the quantum information to the fiber network through the fiber input/output channel, while complementary information is obtained simultaneously through the imaging channel for operation of the quantum node.

However, in high-bandwidth cavities, fluorescence imaging faces a number of experimental difficulties. First, standard cooling techniques are ineffective due to the geometry and the Purcell effect, as already discussed in Chapter 3. Specifically, 3D molasses cooling [60] is unfeasible because of the limited optical access (one axis is blocked by the cavity), and cavity cooling [109, 110] is disabled in the high-bandwidth regime ($\kappa \gg \gamma$). In Chapter 3 we showed our implementation of the dRSC method which allows efficient cooling inside of the FFPC. But it is not powerful enough to compensate the recoil heating of the atoms

* **Statement of published work:** The content of this chapter is a summary of the publication reprinted in Appendix B, and with the same title as the chapter: *Raman imaging of atoms inside a high-bandwidth cavity*, E. Uruñuela, M. Ammenwerth, P. Malik, L. Ahlheit, H. Pfeifer, W. Alt and D. Meschede, *Physical Review A* **105**, 043321 (2022) [2].

Statement of author contribution: I developed the underlying concept, then planned and led the measurement campaign that conducted to the published results. Under my supervision, all upgrades to the experiment, characterizations, measurements and data analysis were performed together with my colleagues M. Ammenwerth, P. Malik and L. Ahlheit (certain measurements and details are part of their M.Sc. theses [65–67]). Subsequently, I conducted the writing process of the manuscript, with the participation of all co-authors.

during fluorescence imaging. Second, the strong Purcell effect desired for an efficient quantum node, also suppresses considerably the free-space photon scattering, by directing most of the photons into the cavity mode, which is highly detrimental for fluorescence imaging orthogonal to the cavity axis [75].

In this chapter*, I present an alternative method for fluorescence imaging of small atomic ensembles coupled to a high-bandwidth FFPC, that overcomes the aforementioned challenges, based on the publication [2] included in Appendix B. Our approach relies on the detection of the repumper fluorescence emitted during three-dimensional (3D) continuous Raman sideband cooling (cRSC). This technique, dubbed Raman imaging, was pioneered by [123, 124] and quickly adopted in the field of quantum gas microscopes [125–127]. We adapt this method to the FFPC setup in our experiment to achieve the node functionality shown previously in Figure 1.1 (a). To circumvent the lack of optical access, we conveniently couple one of the Raman beams and the repumper as intra-cavity fields. Furthermore, to avoid the detrimental Purcell effect we use independent atomic transitions for the imaging channel and for the quantum channel (resonant with the cavity). This implementation allows us to obtain high fidelity pictures of the atoms, while simultaneously using the quantum channel for probing the atom-cavity coupling. In the rest of the chapter (and Appendix B), we explain and characterize the implementation of Raman imaging in our atom-cavity module.

Since the experimental setup was described extensively in Chapter 2, here we only remind of the elements that are essential for our Raman imaging implementation (detailed in Appendix B.2). All involved light fields are shown in the schematic of Figure 4.1 (a). Similarly as in Chapter 3, one or multiple atoms¹ are strongly coupled to our high-bandwidth FFPC² (cavity probe at 780 nm with σ^- polarization), trapped at its center in the 3D optical lattice with configuration known from previous chapters³. Yet, in this case the horizontal lattice beams DT_{xy} are tuned to a wavelength of 868 nm for technical reasons⁴, while the vertical intra-cavity lattice DT_z is kept at 770 nm.

However, for the implementation of resolved-sideband Raman cooling there are also significant differences compared with the dRSC scheme in Figure 3.1 (a). Mainly two new sets of laser fields are added to the setup. To drive Raman transitions, we use the dedicated pair of 770 nm Raman beams (RB1 and RB2), prepared and phase-locked with the setup presented in Section 2.3. We emphasize that the beam RB1 is simultaneously the intra-cavity lattice DT_z , with σ^+ polarization, which enables to drive carrier-free Raman transitions [114]. The beam RB2, impinging along DT_y with π polarization, is generated by a DBR laser which we upgrade for linewidth-reduction to achieve the necessary phase-locking stability (see Appendix B.7). To avoid degenerate Raman transitions used for dRSC, now the magnetic field is increased to ~ 1.8 G along the quantization axis. Additionally, we couple a pair of 795 nm repumper beams with σ^- polarization through the low transmission (LT) cavity mirror, used for optical pumping and state preparation. These repumper beams will also serve to generate fluorescence for imaging the atoms, as will be discussed later in the chapter, rendering the imaging channel on the D_1 line fully independent from the cavity quantum channel on the D_2 line. In the following, we exploit such independence to combine the detection schemes of both channels and acquire complementary information about the atoms: their presence and internal state by nondestructive cavity probing; their number and positions with fluorescence imaging. Since having an efficient cooling mechanism is crucial for imaging, we will first describe the implementation of three-dimensional sideband-resolved Raman cooling in the cavity, and then show its application for fluorescence imaging of the atoms. Still, we should bear in mind that we optimize the method for the purpose of imaging, and not primarily for cooling, as will be shown further in the chapter.

¹ The number and density of loaded atoms can be adjusted with the drive-through loading technique explained in Chapter 5.

² Main CQED parameters $(g, \kappa, \gamma) = 2\pi \times (80, 41, 3)$ MHz, see table D.1 for the complete characterization.

³ Polarization $(P_x, P_y, P_z) = (\pi, \pi, \sigma^+)$; beam waist $(w_x, w_y, w_z) = (11, 13, 5)$ μm ; trap depth ~ 0.5 mK in all directions.

⁴ We obtained a superior stability of the TiSa laser generating the DT_{xy} lattice by mode-lock at a wavelength of 868 nm compared to the previous 860 nm, but this change is irrelevant for the presented results, see Section 2.3.2.

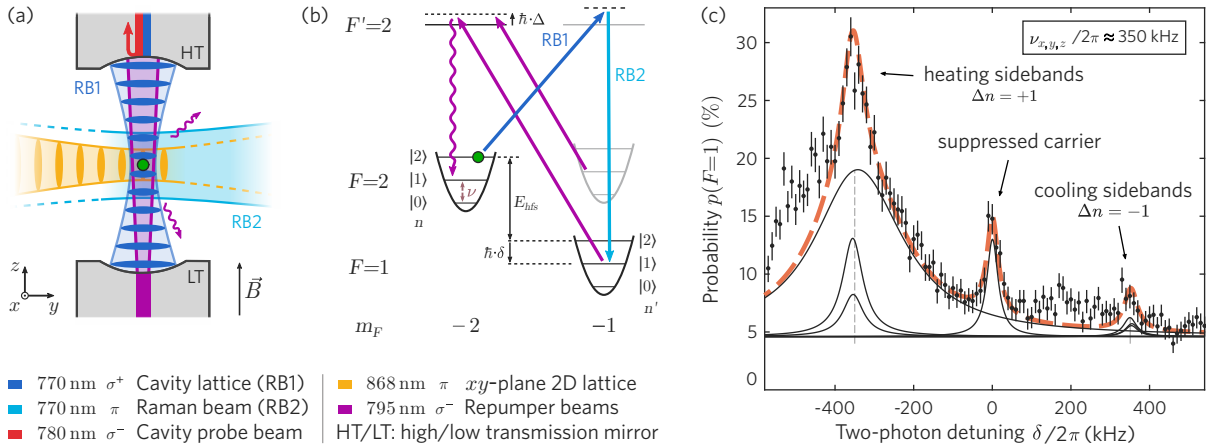


Figure 4.1: Implementation of three-dimensional continuous Raman sideband cooling (cRSC) inside of a high-bandwidth FFPC. **(a)** Schematic of the beam arrangement inside of the cavity for cRSC, depicting all light fields involved. Our implementation of Raman cooling uses a single free-space beam and the remaining beams as cavity fields. **(b)** Representation of the cooling cycle in one dimension. A two-photon transition between atomic hyperfine ground states with the phase-locked Raman beams, followed by optical pumping with the D_1 -line repumper beams, reduces the motional quantum number of the atoms. **(c)** Raman spectrum of a single atom after 5 ms of resonant cRSC. For three-dimensional cooling we overlap the cooling sidebands corresponding to different lattice dimensions at ~ 350 kHz and address them simultaneously with the single Raman beam pair RB1+RB2. Unwanted off-resonant carrier transitions are highly suppressed by using the blue-detuned cavity lattice as RB1. With sideband-ratio thermometry we infer a vibrational ground-state population above 85 % along all lattice dimensions and a residual temperature ~ 1.4 μ K. Figures from the publication [2].

4.1 Three-dimensional resolved Raman sideband cooling in the cavity

For simplicity, the cooling scheme is best explained in a one-dimensional and single-atom scenario following Figure 4.1 (b). Reducing the vibrational quantum number $|n\rangle$ is achieved by Raman transitions between m_F sublevels of the different hyperfine ground states. As a first step, the atom is polarized in $|2, -2\rangle$ with the repumper beams, using here our now familiar notation $|F, m_F; n\rangle$ for the quantum states. The frequency difference of the Raman beams RB1 and RB2 is tuned to the hyperfine splitting between the states $|2, -2\rangle$ and $|1, -1\rangle$ (i.e. the carrier frequency) plus a detuning δ from the carrier. This enables two-photon cooling transitions

$$|2, -2; n\rangle \rightarrow |1, -1; n-1\rangle \quad (4.1)$$

whenever the two-photon detuning δ matches the trap frequency⁵ of the lattice ν_i (along the i axis):

$$\delta = \nu_i, \quad (4.2)$$

namely the resonant addressing condition on the cooling sideband. The cooling mechanism is completed by optical pumping with the 795 nm repumper beams without altering the motional state (in the Lamb-Dicke regime provided by the lattice [103, 104]), bringing the atom back to $|2, -2; n-1\rangle$ and ready for the next Raman transition. The cooling cycle stops when reaching the motional ground state $|2, -2; 0\rangle$, which is a dark state for both the Raman beams and the repumpers.

Most conveniently, with our Raman sideband cooling scheme inside of the cavity, we can not only

⁵ For the sake of clarity, in this chapter and in Appendix B we use the notation ν for angular frequencies, in contrast to Chapter 3 where it denoted linear frequencies.

cool in 1D but in all three dimensions, with the single pair of Raman beams RB1+RB2 (all details in Appendix B.8). To do so, we overlap the cooling sidebands corresponding to each direction of DT_{xyz} at near-degenerate frequencies $\nu_{x,y,z} \approx 2\pi \times 350$ kHz, and we address them simultaneously with a two-photon detuning that satisfies Equation (4.2) for all three lattice dimensions $\delta = \nu_{x,y,z}$. Raman coupling along all the trap directions is allowed by the lattice geometry [115], featuring small angles of DT_{xy} with respect to the plane orthogonal to DT_z ($\theta_x \approx 15^\circ$ and $\theta_y \approx 6^\circ$). However, such configuration of the lattice and Raman beams in Figure 4.1 (a), also implies mismatched Raman Rabi frequencies along the different directions⁶. This motivates the use of a continuous Raman sideband cooling scheme (cRSC), with Raman and repumper beams impinging simultaneously on the atoms at constant intensity, instead of a pulsed sequence (see Appendix B.3).

We evaluate the efficiency of our three-dimensional cRSC technique⁷ by means of Raman spectroscopy of a single atom (see Appendix B.8). After 5 ms of resonant cRSC, with the cavity state detection we measure the probability of Raman transfer from $|F = 2\rangle$ to $|F = 1\rangle$, as a function of the two-photon detuning δ . The resulting spectrum is shown in Figure 4.1 (c), where three observations are relevant. First, the heating sidebands ($\delta < 0$, $\Delta n = +1$) and the cooling sidebands ($\delta > 0$, $\Delta n = -1$) corresponding to the three lattice dimensions are overlapped at the two-photon detunings equal to the chosen trap frequencies ~ 350 kHz. Second, the small amplitude of the carrier peak ($\delta = 0$, $\Delta n = 0$) indicates a strong suppression of carrier transitions by using the cavity lattice as one of the Raman beams (RB1). Note that this disposition not only solves the problem of optical access, but also reduces off-resonant carrier coupling that is detrimental for cooling. Third, the sidebands of all DT_{xyz} have a large cooling-heating amplitude imbalance, a clear signature of the 3D cooling power. By Raman-ratio thermometry, we estimate a vibrational ground-state occupation $n_{0,i} \geq 85\%$ in all lattice dimensions (with $i = x, y, z$), corresponding to a mean motional number $\bar{n}_i \approx 0.17$ and a residual temperature $T_i \approx 1.4$ μ K. Under uninterrupted cRSC, we observe atom trapping lifetimes⁸ of ~ 1 min, thus more powerful than the dRSC method presented in Chapter 3.

4.2 Differential light shifts in a continuous Raman cooling scheme

An underlying challenge of the cRSC scheme comes from the energy shifts induced by the 795 nm repumper light onto the ground-state hyperfine levels. An atom in the dark state $|2, -2\rangle$ is unaffected by the σ^- repumper, while in the state $|1, -1\rangle$ it is subject to the AC-Stark effect, resulting in a differential light shift which modifies the Raman resonance condition. More precisely, the cooling sideband frequency (with respect to the unshifted carrier at $\delta = 0$) gets shifted by an amount δ_{LS} , such that the Raman beams have to be tuned to $\delta = \nu_i + \delta_{LS}$ for addressing the cooling transitions. The strength and direction of the shifts strongly depend on the repumper parameters, namely its detuning Δ and intensity I_{rep} . The effect is amplified with a near-resonant repumper, which is needed for an optimal imaging signal in our case, as we will see later. Hence, for the optimization and operation of cRSC, good knowledge of the induced shifts is essential. To model the differential light shifts, we use the simplified picture of a two-level atom driven by the repumper light field including spontaneous emission. In Appendix B.9 we discuss the justification and limitations of this simple model, and include the detailed derivation. The eigenvalues of the system's non-Hermitian Hamiltonian provide a good approximation for δ_{LS} to first order in the

⁶ The Lamb-Dicke parameters are $(\eta_x, \eta_y, \eta_z) = (0.03, 0.09, 0.11)$ along the respective lattice directions.

⁷ We optimize dRSC for imaging and not specifically for cooling (Figure 4.2), so a higher cooling efficiency is possible with different parameters.

⁸ This lifetime measurement was limited by background gas collisions due to a deteriorated vacuum at that moment, hence with improved vacuum we would expect even longer lifetimes.

saturation parameter $s = I_{\text{rep}}/I_{\text{sat}}$:

$$\delta_{\text{LS}} \approx \frac{\Delta}{2} \frac{\gamma^2}{\Delta^2 + \gamma^2} s + \mathcal{O}(s^2) \quad (4.3)$$

with $2\gamma \approx 2\pi \times 6$ MHz the linewidth of the atomic transition. In the low power limit ($s \ll 1$) or the large detuning limit ($\Delta \gg \gamma$) the induced light shift δ_{LS} scales linearly with intensity and follows a dispersive Lorentzian dependence on Δ . In the experiment, we characterize the differential light shifts δ_{LS} by tracking the displacement of the overlapped cooling sidebands in dependence of the repumper parameters intensity I_{rep} and detuning Δ (with respect to the trap-shifted resonance). The complete characterization and discussion can be found in Appendix B.4. To locate the sidebands, with the cavity presence detection we measure the survival probability after a period of cRSC, over a scan of the two-photon detuning δ . We consider then that the point of highest survival occurs at resonant addressing of the cooling transition, corresponding to the position of the cooling sidebands $\delta = \nu_i + \delta_{\text{LS}}$. Upon comparison of the measurements with the two-level model, we find a good qualitative agreement, but with certain discrepancies that we discuss thoroughly in appendices B.4 and B.9. The most notorious is an asymmetric distortion of δ_{LS} from the expected dispersive shape, affecting prominently the repumper red-detunings ($\Delta < 0$). We partially attribute this effect to oscillations of the atoms in the lattice for a finite temperature, as suggested by an extended model including the atom's kinetic energy (derivation and discussion also in Appendix B.9). The importance of this observation will become clear during the parameter optimization for fluorescence imaging, which is the next stage in our discussion.

4.3 Fluorescence imaging with continuous Raman sideband cooling

With a strong cooling mechanism in place, we now focus on the primary subject of this chapter, namely the fluorescence detection of individual atoms. As stated before, we use the repumper beams as illumination lights, and obtain images of the atoms by detecting the photons scattered during the repumping process of cRSC. We emphasize again that by choosing the illumination (repumper) beams on the D_1 line, we avoid the detrimental Purcell effect for the imaging channel while leaving the quantum channel fully operational on the D_2 line. The 795 nm photons are collected with one of the in-vacuum high-NA lenses surrounding the cavity, and imaged onto an EMCCD camera⁹, by means of the imaging system¹⁰ presented in Section 2.3.5. Although the special design reduced significantly the background scattering of the repumper from the cavity mirrors, full suppression from the field of view was not possible in our miniaturized FFPC setup. Hence for a sufficient fluorescence signal over background, the use of a near-resonant repumper at low intensity is required, which in turn induces strong light shifts on the atoms. Conveniently, our careful characterization of the differential light shifts (Appendix B.4) allows to decouple the complicated parameter dependence, with a feedforward on the two-photon detuning δ that keeps the cooling sideband on resonance.

To optimize continuous Raman sideband cooling as an imaging technique, we aim for the highest signal-to-noise ratio (SNR) of the detected fluorescence. The working principle of cRSC is problematic since it relies on driving the atom to a dark state where it no longer scatters the coveted photons. It is then imperative to find a balance of heating and cooling rates to keep the atoms out of the motional ground state, but close to it for low atom loss. In our system the intra-cavity lattice noise is sufficient for this purpose, instead of using parametric heating as in [123]. But for optimal imaging SNR, we find that the

⁹ Andor iXon 3: CCD chip with 512×512 px², pixel size 16×16 μm^2 , conversion factor (15 ± 1) counts/photon.

¹⁰ Main properties: collection efficiency $\sim 4\%$, magnification $\times 35$, PSF width ~ 0.8 μm equal to 1.72 px on the CCD.

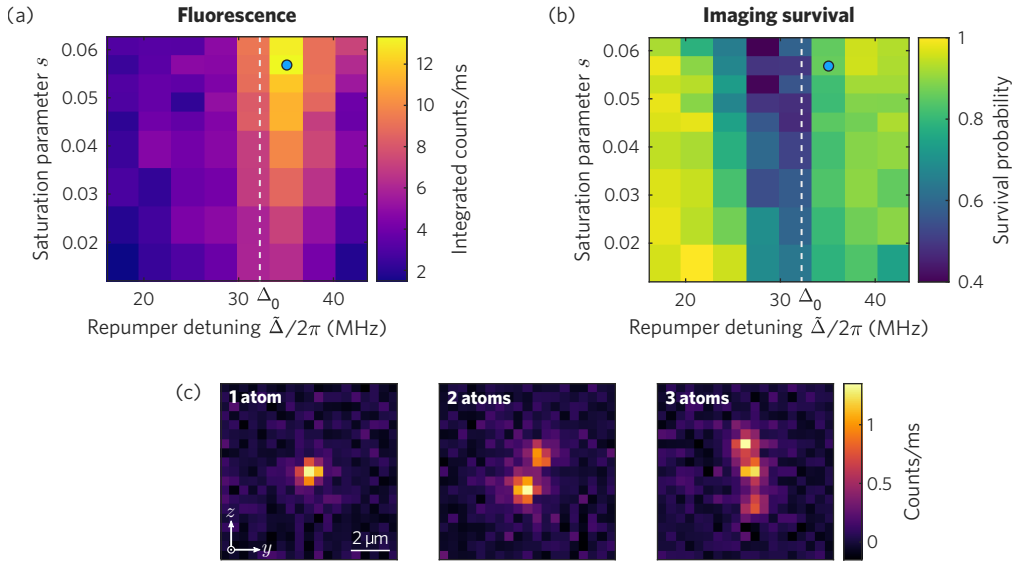


Figure 4.2: Optimization of cRSC inside of our high-bandwidth cavity for fluorescence imaging of atoms. With a 1 s imaging interval, we measure (a) the integrated single-atom fluorescence with the EMCCD camera through the imaging channel, and (b) the imaging survival probability with the non-destructive cavity detection through the quantum channel, as a function of repumper saturation parameter s and free-space detuning $\tilde{\Delta}$. The dashed line at $\tilde{\Delta} = \Delta_0$ indicates the trap-shifted resonance. In (c) we show high fidelity images of small atomic ensembles (1, 2 and 3 atoms) at the center of our FFPC, featuring $\text{SNR} \approx 13$ and survival $> 90\%$, acquired at the optimum repumper parameters $\tilde{\Delta} \approx 2\pi \times 35$ MHz and $s \approx 0.057$ (blue circle in (a) and (b)). Figures from the publication [2].

balance of heating-cooling rates, to enhance photon scattering but keep high survival over the camera exposure time, can be tuned with the repumper parameters. To find the optimum balance, we perform a 2D scan of repumper detuning and intensity. Note that in the experiment, the accessible parameter is the repumper free-space detuning $\tilde{\Delta} = \Delta + \Delta_0$, where Δ is the detuning from the trap-shifted resonance (used in the model), and $\Delta_0 \approx 2\pi \times 32$ MHz the AC-Stark shift by the dipole traps DT_{xy} on the D_1 transition (calibrated with a spectroscopy cell reference, see Section 2.3.2). The resonance condition is then met at $\tilde{\Delta} = \Delta_0$. As a figure for the repumper intensity we use the saturation parameter $s = I_{\text{rep}}/I_{\text{sat}}$ that we calibrate with via optical pumping rates (see Section 2.3). For each set of parameters $\{s, \tilde{\Delta}\}$ and with a 1 s imaging interval under cRSC, we measure simultaneously the integrated fluorescence with the camera, in Figure 4.2 (a), and the atom survival probability with the cavity detection, in Figure 4.2 (b). For these measurements, the power of the Raman beams was fixed to a two-photon Raman Rabi frequency (on the carrier) of $\tilde{\Omega}_0 \approx 2\pi \times 340$ kHz. In Appendix B.5 we include a detailed description of the optimization procedure. Combining the information of the fluorescence and survival maps, we identify a region with favorable conditions for imaging at parameters $\tilde{\Delta} \approx 2\pi \times 35$ MHz and $s \approx 0.057$, marked by the blue circle in Figure 4.2 (a, b). This choice of parameters is characterized by a survival probability above 90% and a scattering rate per atom of $\sim 2 \times 10^4$ photon s^{-1} , thus providing ~ 800 photons at the camera in the 1 s exposure time. The resulting $\text{SNR} \approx 13$ is sufficient to capture clear images of individual atoms inside of the FFPC, as the ones shown in Figure 4.2 (c), allowing to determine the number of atoms and their position with full site resolution [57].

Beyond optimization, the qualitative behavior of fluorescence and survival in the 2D parameter maps of Figure 4.2 (a, b), also gives insight into the underlying heating dynamics of the imaging process. A thorough discussion is included in Appendix B.5; here we only summarize the most prominent observations. While the fluorescence shape follows the expected Lorentzian-like function around the

trap-shifted repumper resonance (except for a small blueshift, coming from the images postselection procedure), the survival map shows an unexpected asymmetry with higher atom losses on the red detuning side than on the blue. When increasing the repumper intensity the survival dip shifts further to the red, resulting in the observed asymmetric V-shaped survival probability map. We attribute this effect to parameter-dependent heating rates, generated by dipole-force fluctuations (DFFs) [58, 105] affecting the trapped atoms during the repumping cycles of cRSC (see Appendix B.10). The origin of DFFs in our case can be understood as following. An atom confined in the lattice potential and illuminated by the repumper light, undergoes rapid scattering cycles between ground and excited states of the ^{87}Rb D_1 line. Since the polarizability ratio between the states $5^2S_{1/2}$ and $5^2P_{1/2}$ at the lattice wavelength of 868 nm is $\chi \approx -0.59$, the atom spends a fraction of time in the antitrapping potential of the excited state, before scattering back into the trapping ground state. Such fluctuation of the dipole force usually cause an increase of the atom's kinetic energy, depending on the shape of the potentials and the detuning of the driving field (cooling was also observed in [128]). Indeed, with our experimental conditions, the parameter-dependent shape of dressed-state potentials plays an important role as we explain in Appendix B.10.1. It gives rise to a strong heating effect for small repumper red detunings, in the region in which the oscillations of atoms in the trap can access non-centered lattice positions where the repumper becomes resonant, as described in [58]. A standard practice to avoid DFFs is to operate with far-detuned illumination, yet at the cost of decreased fluorescence or the need of higher intensity. However, if near-resonant illumination is required as in the case of imaging with cRSC, for a compromise of high fluorescence and high survival, blue detunings are beneficial in preventing DFFs-induced heating and red detunings should be avoided. We validate the role of DFFs with a semiclassical Monte Carlo simulation of scattering under near-resonant illumination, for a trapped atom in a 1D lattice. Details of the Monte Carlo simulation algorithm can be found in Appendix B.10.2. The simulation results shown in Appendix B.5 confirm that DFFs is the main heating mechanism that lead to the asymmetric survival probabilities observed in Figure 4.2 (b).

4.4 Summary and conclusions

In this chapter I have shown that continuous Raman sideband cooling (cRSC) is a powerful method for imaging individual atoms coupled to a high-bandwidth cavity, overcoming the challenges inherent to the strong Purcell effect. An independent and simultaneous operation of the cavity quantum channel and the imaging channel is guaranteed by reserving a different atomic line for each channel. Our implementation of cRSC in three dimensions with only one free-space beam and cavity fields, is ideal for architectures with limited optical access, going in line with the miniaturization trend in quantum technologies.

Through optimization using the repumper parameters, we find a convenient balance between photon-scattering rate and cooling efficiency. Furthermore, we observe the presence of heating induced by dipole-force fluctuations, that is avoided with a small blue detuning of the illumination-repumper light. It should be noted that the heating effect of DFFs is not limited to our particular FFPC setup, on the contrary it is relevant for most experiments involving near-resonant illumination of lattice-trapped atoms. With this, we demonstrate an imaging SNR of ~ 13 and a residual motional ground-state occupation above 85 %, sufficient for high fidelity detection of individual atoms in optical lattices.

The ability to determine the number and positions of cavity-coupled atoms in a non-destructive way, paves the way for creating and controlling predefined atomic arrays inside of the resonator, that could be manipulated by individual addressing with e.g. by movable tweezers. Ultimately, this imaging technique extends the available toolbox for control and manipulation of atom-cavity systems. In that way, it enhances the capabilities of the current prototypes of cavity-based quantum nodes, thus giving one step forward in the unfolding development of quantum networks.

Until now, for loading multiple atoms into the cavity we have relied on a probabilistic and sparse loading technique from the MOT into the conveyor belt. For experiments with atomic arrays, a technique for denser loading is needed. We developed a technique based on dynamical loading with the optical conveyor belt, which we will present in Chapter 5.

Delivery of small atomic ensembles into a fiber microcavity

COUPLING small atomic ensembles to our high-bandwidth fiber-based Fabry-Pérot cavity (FFPC) [21–23], i.e. upscaling the cavity-atom quantum node in our experiment, is one of the main motivations of this thesis. As discussed in Chapter 1, the strong interactions of multiple atoms with the cavity electromagnetic field –instead of a single one– can greatly extend the capabilities of the atom-cavity quantum node and opens the door to promising applications [43–48, 51, 52]. With this goal in mind, in previous chapters we have demonstrated novel techniques for an improved control of atoms inside of FFPCs [1, 2], specifically for cooling in Chapter 3 and for imaging in Chapter 4. Still, a missing piece of the extended atom control toolbox is a method to load small atomic ensembles into the fiber cavity and ensuring strong coupling for all atoms.

In our particular system (see Chapter 2), this implies that the atoms should be confined within the narrow cavity mode of $\sim 10\ \mu\text{m}$ waist diameter. Previously in our experiment [75], the technique to couple multiple atoms was to transport to the cavity center the full chain of atoms loaded from the atom cloud of the MOT into the optical conveyor belt. However, with this so called *feedforward loading*, the atoms get distributed within a $\sim 60\ \mu\text{m}$ region in the one-dimensional (1D) lattice, much larger than the cavity mode. This poses two main problems: (1) only a few atoms from the resulting sparse atom chain will couple to the cavity; (2) the atoms that do couple to the cavity have a broad radial position distribution within the cavity mode causing undesired inhomogeneous effects (e.g. in the individual coupling strength, cooling efficiency, trapping frequency) and a significant reduction of the effective collective coupling [24]. Thus, to increase the density of atoms close to the cavity center it becomes necessary to compress the original position distribution of atoms in the 1D lattice.

A large number of robust techniques have been developed over the past years for increasing the filling factor of optical lattices [129–136] and for transporting atoms over macroscopic distances [87, 137–141], e.g. for atom-delivery into optical cavities [88, 89, 142–144]. The feasibility of the different compression techniques for our system has been reviewed in detail in Ref. [67]. In summary, the compressed MOT loading [132] and the time-dependent lattice compression [135, 136] cannot be used in our experiment, due to the impossibility to create a MOT inside of the cavity and to modify the crossing angle of the lattice beams, respectively. The quarter cycle compression realized in Ref. [133, 134] is a feasible alternative which was initially considered as the best choice for our experiment. Nevertheless, the implementation in

* **Contribution statement:** The work leading to the results presented in this chapter was carried out as a team effort under my coordination, with my colleagues and proud members of the FCQED-lab crew: L. Ahlheit, P. Malik and M. Ammenwerth. Of the results included in this chapter, some details and preliminary measurements are part of the M.Sc. thesis by L. Ahlheit [67].

our system requires complex algorithms to compensate the anharmonicity of the trapping potential [102] as studied systematically in Ref. [74], and the particular geometry of our lattice which will be reviewed in Section 5.1.1. Moreover, the atom densities achievable by this technique get quickly limited by light-induced collisions [99, 100], with the occurrence probability increased by the low availability of trapping sites in a 1D lattice. Recently, in Ref. [144] an optical elevator was implemented to load large atomic arrays at the center of a FFPC. This approach, though, is not applicable for small atomic ensembles with individual addressing that we envisage, and is also subject to the inhomogeneous effects discussed earlier.

In this chapter*, I present the development and implementation of a new and simple method for delivering multiple atoms to a three-dimensional (3D) lattice at the center of our FFPC, which we call *drive-through loading*. Contrary to other loading and compression methods, it does not need additional optical elements or laser beams, nor involves complicated algorithms; it relies only on the intensity and phase control of the optical lattice beams. As the name suggests, it makes use of the well known conveyor belt technique, already implemented in our setup [87, 88, 138], to drive the atom chain in the 1D lattice through the 3D lattice region. During the drive-through transport the atoms roll into the crossing of the lattice beams, and accumulate around the center of the lattice. Certainly, this observed drive-through loading effect only occurs within particular ranges of critical experimental parameters. Throughout the chapter the underlying mechanism will be discussed and the involved parameters investigated.

Even though this technique was developed in the particular context of our experiment, it is worth noting that it can have a broader range of applications in different experimental contexts. It can be particularly interesting for cold-atom-delivery into miniaturized devices requiring the interaction with cold atoms but presenting a restricted optical access, such as optical microcavities (as in our case), and further integrated photonic devices [29, 145–148] and optomechanical platforms [149–153]. More generally, it can be useful in numerous experimental systems where the loading from a distant MOT is required, either by the unfeasibility of its direct overlap with the final trapping lattice, or by a preference to avoid it.

5.1 Intracavity lattice loading by drive-through transport

Before diving into details of the experimental implementation, this section is dedicated to give a simple overview of the drive-through loading method, and to provide an intuitive understanding of the observed effect that we exploit for the multi-atom loading technique.

Even though the particular goal of this loading method in our experiment is to deliver atoms to the FFPC, the presence of the cavity does not have any influence on the drive-through effect. Still, it will play a crucial role as a measurement device that will be used for the characterization and optimization of the effect in Section 5.2. But for now, it is important to note that just the optical lattices together with the ability to manipulate them dynamically, give rise to the drive-through loading effect.

5.1.1 Overview of the drive-through loading method

We start this discussion with a timely review of the optical lattice configuration in our setup, which was presented in the overview of the scientific apparatus in Chapter 2. The 3D lattice is aligned with the center of the fiber cavity, allowing to trap small ensembles of single atoms in ~ 100 individual lattice sites inside of the cavity interaction region. As shown in Figure 5.1 (a), the horizontal xy -plane is formed by two crossed red-detuned standing-wave dipole traps DT_x and DT_y (preserving the previous notation),

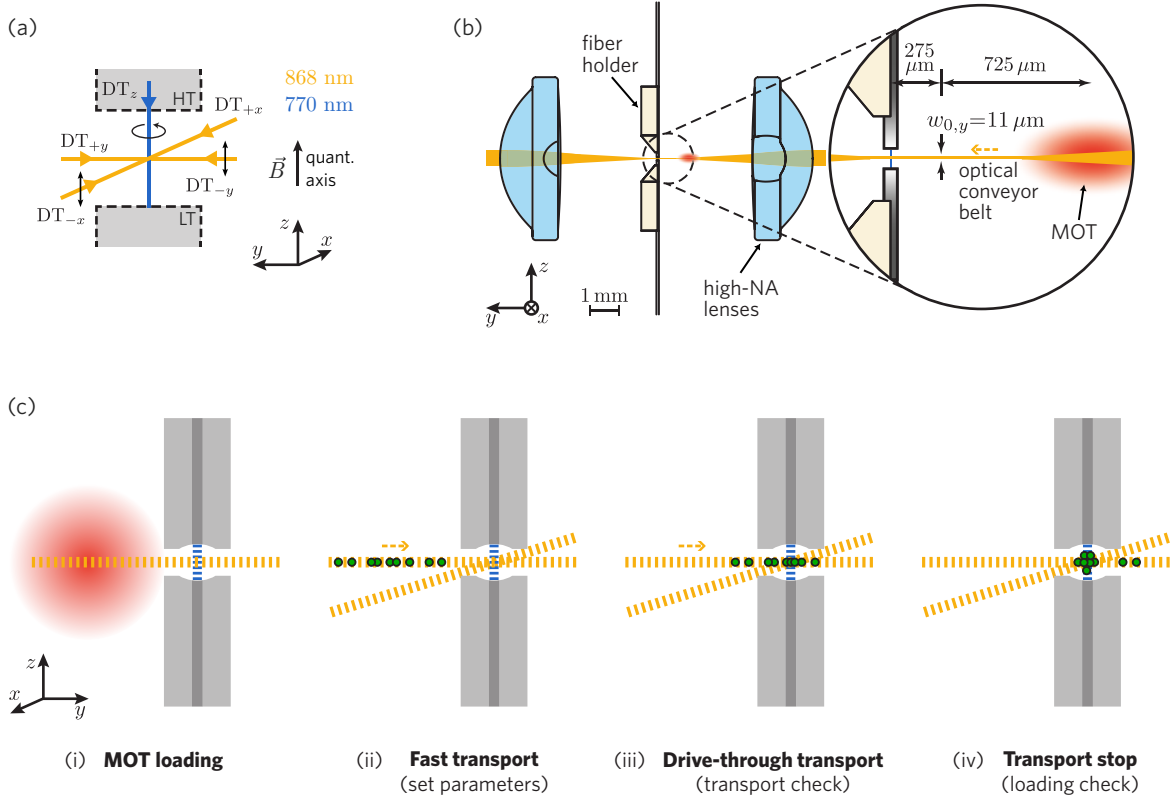


Figure 5.1: Setup and concept for drive-through loading. (a) Configuration of the five beams to generate the intracavity 3D optical lattice: in the xy -plane two pairs of counter-propagating beams ($DT_{\pm x}$ and $DT_{\pm y}$), with wavelength 868 nm and π polarization; along the z -axis the standing-wave intracavity field of the Lock laser (DT_z), with wavelength 770 nm and σ^+ polarization. The black arrows indicate the electric field polarization with respect to the quantization axis defined by the magnetic bias field along the cavity axis. (b) Optical alignment of the conveyor-belt lattice DT_y to facilitate the delivery of atoms into the cavity from the MOT ~ 1 mm away. To allow sufficient trap depth at the MOT region and at the intracavity lattice, the focus of the beams $DT_{\pm y}$ is placed between these two regions at $\sim 275 \mu\text{m}$ from the cavity. (c) Drive-through loading sequence to load small atomic ensembles into the intracavity lattice. From left to right: (i) atoms are captured by the MOT and loaded into the 1D lattice DT_y ; (ii) a first fast transport (800 $\mu\text{m}/200$ ms) brings the atoms close to the cavity ($\sim 200 \mu\text{m}$ from the center), where the experimental parameters for drive-through loading are selected; (iii) the drive-through transport shuttles the atoms through the intracavity lattice region where they can accumulate or just cross depending on the chosen parameters, while their presence in the conveyor belt is monitored by the cavity *transport check*; (iv) the transport stops after all shuttling lattice sites are on the other side of the cavity ($\sim 100 \mu\text{m}$ past the center), and at this point the cavity *loading check* measures the presence of loaded atoms. Figures adapted from Ref. [74, 75].

with a wavelength of 868 nm¹. In the z direction, the intracavity blue-detuned field of the Lock laser creates the trapping lattice DT_z with a wavelength of 770 nm². The specific lattice polarizations are $(P_x, P_y, P_z) = (\pi, \pi, \sigma^+)$, defined along the cavity axis (which is also the quantization axis defined by the B -field), and the corresponding waist radii of the lattice beams are $(w_{0,x}, w_{0,y}, w_{0,z}) = (11, 11, 5) \mu\text{m}$. This configuration provides the trap depth of ~ 0.5 mK in all lattice directions, that we use as standard in the experiment (see chapters 3 and 4, and also Ref. [41]).

We recall from Chapter 2 that, due to lack of optical access, to deliver cold atoms to the cavity a MOT is created ~ 1 mm away, as shown in Figure 5.1 (b). Atoms are loaded from the MOT into the DT_y 1D lattice and shuttled to the intracavity 3D lattice with the conveyor belt technique [87, 88, 138]. To ensure a sufficient trap depth both at the position of the MOT (to collect a sufficient number of atoms) and at the cavity position, the transport lattice DT_y is not focused at the cavity center but between the MOT and the cavity: it features a focus offset $y_0 = -275 \mu\text{m}$ from the 3D lattice intersection³. Thus, in contrast to DT_x and DT_z , the spot size of DT_y at the lattice intersection is not the beam waist $w_{0,y} = 11 \mu\text{m}$, but the larger value $w_y = 13 \mu\text{m}$ reported in previous chapters, see Equation (5.4). This generates an asymmetry in the lattice geometry that will be discussed later.

The basic experimental sequence for drive-through loading is shown in Figure 5.1 (c). After the MOT loading, the 1D chain of atoms in the conveyor lattice DT_y is shifted with a first transport to just before entering the cavity ($y \approx -200 \mu\text{m}$). There, relevant experimental parameters are selected, followed by a second transport⁴ that drives the atoms through the intracavity lattice region. While inside of the cavity, the atoms are cooled with the dRSC method presented in Chapter 3. Although it was initially expected that all atoms are transported through and past the cavity unaffected, for certain parameters we observed a finite probability of finding an atom still inside after the transport. During the drive-through transport, these atoms roll into the trap intersection and accumulate in the 3D lattice: the drive-through loading effect. In the rest of this chapter, we investigate this effect and the experimental parameters to control its behavior, with the aim of utilizing it for loading multiple atoms into the narrow cavity mode. Given the complexity of the conditions involved in the phenomenon, before the experimental implementation we use a simple model to gain a basic understanding of the effect and to identify possible critical parameters.

5.1.2 One-dimensional classical transport model and numerical simulation

To obtain an intuitive understanding of the drive-through loading effect, we employ a one-dimensional classical model of the atoms in the dynamical lattice potential, moving at a constant velocity during the conveyor-belt transport. A quantum mechanical treatment of atomic transport can be found in Ref. [101, 154]. Here, the atoms are modeled as classical point particles, evolving in the moving potential landscape (see Figure 5.2) originating from the dipole-force exerted by the lattice electromagnetic field on the atoms [61] (recall Section 2.3.2).

The one dimensional approach was chosen to simplify the physical interpretation and reduce the required computational resources. The classical perspective is justified by a number of reasons: (i) for cold atoms loaded from the MOT with a mean temperature of 40 μK , the recoil energy E_{rec} transferred by

¹ The choice of the wavelength of 868 nm for the DT_{xy} lattice was to improve the stability of the TiSa laser source, with the mode-lock working best at that wavelength.

² The 770 nm wavelength for the DT_z allows simultaneous coupling of the Lock and Probe fields with the cavity for the resonance stabilization, see Chapter 2 and Ref. [22].

³ We define the axis origin $y = 0$ at the intersection of the 3D-lattice beams at the center of the cavity.

⁴ The transport is performed in two stages, between which the parameters for the drive-through loading are set. The reason is to minimize effects unrelated to the drive-through mechanism but dependent on the chosen parameters, e.g. the atom loading from the MOT into the conveyor belt or atom losses in the transport lattice. This improves the sensitivity of our measurements to the drive-through loading processes.

a scattered lattice photon ($\sim 0.15 \mu\text{K}$) is very small compared to the motional quanta ($\sim 3 \mu\text{K}$); (ii) the scattering rate of lattice photons by the atoms is negligible because of far-off detuning (see Section 2.3.2); (iii) the low temperature of the atoms compared to the typical trap depth U_0 and the low transport speeds, render tunneling insignificant for most of the time, i.e. while in the deep-lattice regime $U_0 \gg E_{\text{rec}}$ [155–157]; (iv) the atom transport in the lattice is highly adiabatic, i.e. the atom oscillating in a lattice well is not affected by the shift of the trapping potential, or in other words the kinetic energy transferred by the lattice displacement is much smaller than a vibrational energy quantum. In the classical harmonic oscillator approximation, with a typical transport velocity $v_T \approx 5 \text{ mm/s}$ the travel time of one-lattice-site width is $t_T \approx 90 \mu\text{s}$, and given an axial trapping frequency $\omega_{y,\text{ax}} \approx 2\pi \times 350 \text{ kHz}$ the adiabaticity criterion is met with $t_T \cdot \omega_{y,\text{ax}} \gg 1$ [139, 158].

As a matter of fact, this simplification with a 1D classical model proved to be a surprisingly good approximation for a qualitative analysis, as will become clear in Section 5.2, and to provide essential understanding of the drive-through loading mechanism.

Introduction to the 1D model

The full 1D time-dependent lattice potential $U_{\text{DT}}(y, t)$ is defined by the superposition of the moving axial potential of DT_y and the fixed radial potential of DT_x , valued only along the y axis⁵:

$$U_{\text{DT}}(y, t) = U_y(y, t) + U_x(y), \quad (5.1)$$

with the individual lattice potentials given by

$$U_y(y, t) = U_{0,y} \cdot \left(\frac{w_{0,y}}{w_y(y - y_0)} \right)^2 \cdot \cos^2 \left(\frac{2\pi \cdot (y - y_0 + t \cdot v_T)}{\lambda_{\text{DT}}} \right), \quad (5.2)$$

$$U_x(y) = U_{0,x} \cdot \exp \left(-2 \left(\frac{y}{w_{0,x}} \right)^2 \right), \quad (5.3)$$

and with the spot size of DT_y scaling as

$$w_y(y) = w_{0,y} \sqrt{1 + \left(\frac{y \cdot \lambda_{\text{DT}}}{\pi \cdot w_{0,y}^2} \right)^2}, \quad (5.4)$$

where $U_{0,i}$ is the maximum trap depth and $w_{0,i}$ the beam waist for each lattice direction i , $\lambda_{\text{DT}} = 868 \text{ nm}$ is the common wavelength, and $y_0 = -275 \mu\text{m}$ is the DT_y focus offset from the lattice intersection. The phase factor $t \cdot v_T$ in Equation (5.2) generates the conveyor belt transport by shifting the periodic lattice structure with a constant velocity v_T .

A snapshot of the resulting 1D lattice potential from Equation (5.1) at $t = 0$ is shown in Figure 5.2(a), for the condition $U_{0,y} = U_{0,x}$ (here the wavelength has been scaled by $\times 10$ for better visualization). One can see the complete travel profile of atoms during drive-through loading, from the MOT loading position to the transport stop. At the lattice intersection, DT_x creates a dimple in the potential profile of DT_y , deforming its periodic lattice structure. This can be seen in Figure 5.2(b), showing the intersection region around $y = 0$ (here to scale), now for $U_{0,y} = 0.2 \cdot U_{0,x}$. It is evident that the deformation of the lattice wells is most pronounced where the radial potential shape of DT_x is steepest. As shown in the closeup of Figure 5.2(c), this has the effect of reducing one of the walls of the local lattice site micro-potential, and

⁵ The potential of the blue-detuned DT_z lattice is not considered because, given its repulsive property, the intensity is zero at the center of a trapping site at $z = 0$ on the y axis.

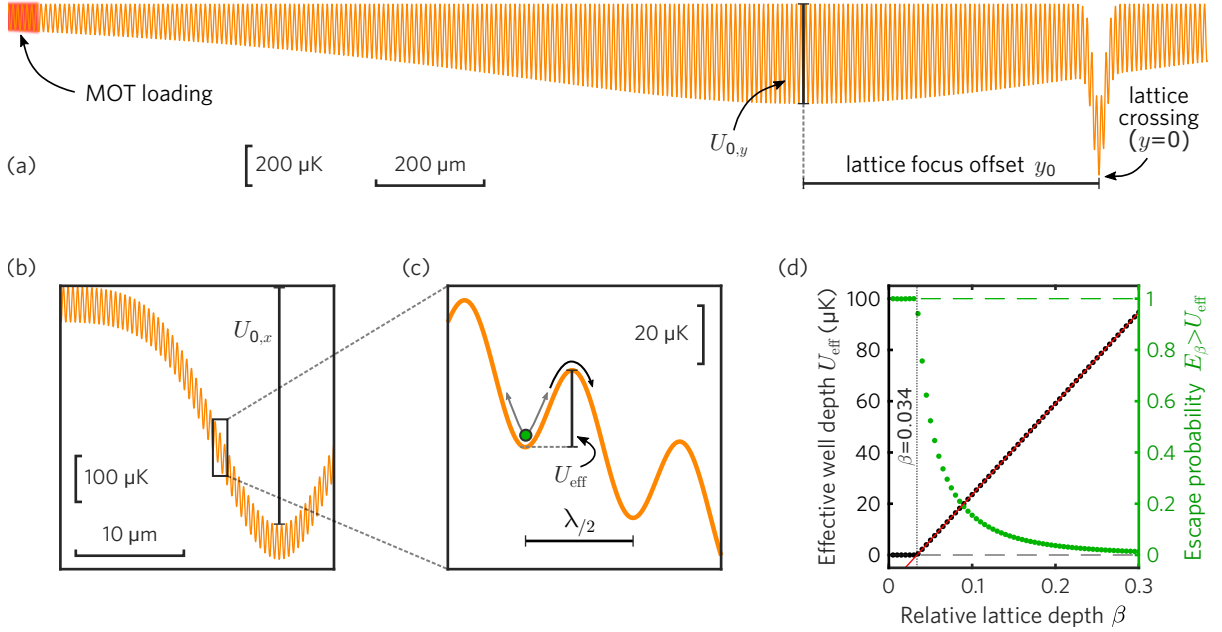


Figure 5.2: One-dimensional classical model of the lattice and atom transport for the drive-through loading effect. **(a)** Snapshot of the 1D lattice moving potential $U_{DT}(y, t)$ from Equation (5.1), resulting from the overlap of orthogonal lattice components DT_y and DT_x , here for equal trap depths $U_{0,y} = U_{0,x}$ and with a $\times 10$ wavelength scaling for better visualization. The transport lattice DT_y connects the MOT loading region at $y \approx -1000 \mu\text{m}$, and the beam crossing with DT_x at $y = 0$ (also the cavity center). The focus of DT_y has an offset $y_0 = -275 \mu\text{m}$ from the lattice intersection point (see main text). **(b)** Detailed view of the intersection region of DT_y with DT_x around $y = 0$, here with $U_{0,y} = 0.2 \cdot U_{0,x}$ and normal wavelength 868 nm . The lattice wells are deformed by the radial Gaussian potential of DT_x , effectively lowering the potential barrier on one side of the trapping sites. **(c)** Close-up of the lattice potential in the region of strongest DT_x slope at $y \approx -6 \mu\text{m}$, where the shallowest trapping potential of a lattice site occurs during transport. The minimum potential barrier, i.e. the effective well depth U_{eff} , sets an energy threshold above which an atom oscillating in the lattice well (shown in green) can escape the lattice-site confinement during transport, triggering the drive-through loading mechanism. The value of U_{eff} is influenced by the relative lattice depth $\beta = U_{0,y}/U_{0,x}$, and by the lattice focus offset y_0 . **(d)** Response of U_{eff} (black dots, left y-axis) to the relative depth β in our model. U_{eff} follows a linear dependence (fit in red) until the value $\beta = 0.034$, below which the lattice-site confinement vanishes. For an ensemble of atoms loaded from the MOT ($T_{\text{mot}} = 40 \mu\text{K}$), the escape probability (green dots, right y-axis) is given by the cumulative modified 1D Boltzmann energy distribution $\varphi(E_{\beta}; \beta, E_{\text{mot}})$ for $E_{\beta} > U_{\text{eff}}$ (see main text). Figures (b) and (c) adapted from Ref. [67].

increasing the other. We define the *effective well depth* U_{eff} as the absolute minimum potential barrier of the deformed lattice sites in the intersection region during transport.

The lattice deformation giving rise to the effective well depth is influenced by two variables: the trap depth $U_{0,y}$ relative to $U_{0,x}$ and the lattice geometry, namely the beam shape, the crossing angle and in our case the focus offset y_0 . Since in the experiment the lattice geometry is fixed, U_{eff} can be solely manipulated by the ratio of intensities of DT_y to DT_x . We define the parameter $\beta = U_{0,y}/U_{0,x}$ as the *relative lattice depth*, that will serve as a tuning knob for the experimental implementation. In Figure 5.2 (d) is plotted the tuning response of U_{eff} with respect to β for the particular geometry of our lattice, and a linear fit to the data (in red). It is interesting to see that the response is nearly linear with a slope of 356 μK , but exhibits a sharp threshold at $\beta \approx 0.034$ below which the effective well depth is zero. We will see in the following that this particular parameter plays a crucial role in triggering the drive-through loading mechanism.

The drive-through loading mechanism

With the 1D model introduced above, we aim to understand the underlying mechanism leading to the drive-through loading effect. As will be discussed below, we identify two necessary conditions of adiabaticity, that have to do with a time-scales imbalance between the atomic motion and the dynamical deformation of the lattice.

The model traces the journey of an atom loaded from the MOT with a mean temperature of $T_{\text{mot}} = 40 \mu\text{K}$ in a lattice site at $y = -1000 \mu\text{m}$, and transported towards the cavity in the conveyor belt. The conveying lattice site is shifted across the 3D lattice intersection region, and stops on the other side at $y = +100 \mu\text{m}$. As a convenient approximation, the energy of the atom E_0 is sampled from a 1D Boltzmann distribution $\varphi(E_0; E_{\text{mot}})$ with the MOT mean energy $E_{\text{mot}} = k_B T_{\text{mot}}$ and considering the density of states of a harmonic oscillator⁶. This approximation comes at the price of underestimating the probability of high atom energies (this choice and further considerations are discussed in Ref. [67]). Already before the drive-through transport, lowering the DT_y lattice $U_{0,y} \mapsto \beta \cdot U_{0,y}$ has the effect of adiabatic cooling the atom [62] by rescaling its energy to $E_\beta = \sqrt{\beta} \cdot E_0$.

During the transport through the lattice intersection, due to the lattice deformation the atom will either continue the transport unaffected or escape from the lattice site, depending on the initial conditions (energy and oscillation phase). As shown in Figure 5.2 (c), if the atom has a higher energy than the effective well depth $E_\beta > U_{\text{eff}}$, then it can escape from the lattice well and roll into the DT_x potential where it oscillates along y in its radial component $U_x(y)$, see Eq. (5.3). For a set of atoms with randomly selected energies and for a given β value, the probability of escaping is then related to the cumulative probability $\varphi(E_\beta > U_{\text{eff}}; \beta, E_{\text{mot}})$ from the modified Boltzmann distribution⁷ with characteristic temperature $\sqrt{\beta} \cdot T_{\text{mot}}$, as depicted in green in Figure 5.2 (d). That is the basic mechanism that triggers the drive-through loading.

But more concretely, the effect does not simply depend on fulfilling the threshold condition $E_\beta > U_{\text{eff}}$ instantaneously. During the dynamical deformation of the lattice-site potential amid the transport, an escape window opens for a time t_{esc} , from the moment the potential barrier drops lower than the atom energy E_β , until it raises again above E_β . The probability of escaping goes in hand with the transport adiabaticity criterion discussed earlier: for success, the escape window time t_{esc} (a function of E_β , β and

⁶ The 1D Boltzmann probability distribution of energies E_0 for an ensemble of atoms loaded from the MOT with mean energy E_{mot} in a harmonic oscillator potential (the lattice sites) is given by $\varphi(E_0; E_{\text{mot}}) = \frac{1}{E_{\text{mot}}} \exp\left(-\frac{E_0}{E_{\text{mot}}}\right)$.

⁷ After adiabatic lowering of the lattice to a relative depth β , the 1D Boltzmann distribution of atom energies E_β is modified to $\varphi(E_\beta; \beta, E_{\text{mot}}) = \frac{1}{\sqrt{\beta} \cdot E_{\text{mot}}} \exp\left(-\frac{E_\beta}{\sqrt{\beta} \cdot E_{\text{mot}}}\right)$. The cumulative probability for $E_\beta > U_{\text{eff}}$, plotted in Figure 5.2 (d), is then given by the integral $\varphi(E_\beta > U_{\text{eff}}; \beta, E_{\text{mot}}) = \int_{U_{\text{eff}}}^{\infty} \varphi(E_\beta; \beta, E_{\text{mot}}) dE_\beta$.

v_T) needs to be compared to the axial oscillation period $\tau_{y,ax,\beta}$ of the atom in the DT_y lattice, i.e. defining the condition

$$c_1 = \frac{t_{\text{esc}}}{\tau_{y,ax,\beta}} \stackrel{!}{\gg} 1, \quad (5.5)$$

with $\tau_{y,ax,\beta} = 2\pi/(\sqrt{\beta} \cdot \omega_{y,ax})$ where we consider the lowering of the lattice by the factor β . This condition means that the atom has a large number of attempts to escape the lattice site (and its oscillation phase plays no role for the escape probability), which is the first necessary condition for the drive-through loading mechanism. Besides, the escape window not only determines the probability, but also the position where the atom escapes and starts to roll into DT_x . If c_1 is large, the escape window opens higher in the potential and the atom gets out as soon as $U_{\text{eff}} < E_\beta$, i.e. on the upper left part of $U_x(y)$.

Once out of the lattice-site potential, the atom oscillates in the transverse potential $U_x(y)$ with the characteristic radial frequency $\omega_{x,\text{rad}}$, and with an amplitude that depends on the escape position within DT_x . Now, the second requirement for drive-through loading is to avoid recapture of the atom in the moving lattice. Otherwise it is dragged out of the crossing region before the transport stops, i.e. the drive-through loading fails. Recapture is most likely at the spatially mirrored position from where it escaped, at the turning point of the oscillation on the right side of the DT_x potential. The recapture condition obeys a different process than the escape one: at the turning point of the oscillation the atom has to coincide with a lattice site, enter while the potential wall is still low enough, and stay within the lattice-site width ($\lambda_{DT}/2$) long enough until the potential wall rises and traps it. Here, the relevant time scales are the recapture time window given by $t_{\text{rec}} = 0.5\lambda_{DT}/v_T$, and the time the atom stays within a lattice-site width at the turning point of the oscillation t_{tp} . In the harmonic approximation this time is given by $t_{\text{tp}} = (\tau_{x,\text{rad}}/\pi) \cdot \arccos(0.5\lambda_{DT}/A_y)$, where $\tau_{x,\text{rad}} = 2\pi/\omega_{x,\text{rad}}$ is the radial oscillation period in DT_x and A_y its y -axis amplitude (given by the y -position of escape). With this, the recapture condition can then be written as $t_{\text{rec}}/t_{\text{tp}} \ll 1$. Hence, to avoid recapture we define

$$c_2 = \frac{t_{\text{rec}}}{t_{\text{tp}}} \stackrel{!}{>} 1, \quad (5.6)$$

as the second condition necessary for the drive-through loading mechanism to succeed, that depends on the parameters E_β , β and v_T .

Given the very different processes governing the two conditions, in our system for certain parameters the recapture condition becomes more strict and less probable than the escape one, thereby generating the drive-through loading effect. This discussion can be illustrated with some quantitative estimations of the conditions (5.5) and (5.6) using our model in Eq. (5.1). For selected values $\beta = 0.045$ and $\beta = 0.02$, the calculated values of relevant parameters and resulting conditions are compiled in Table 5.1. For the calculations we consider an atom with energy $k_B \cdot 5 \mu\text{K}$, a transport velocity $v_T = 5 \text{ mm/s}$, and the oscillation frequencies with our lattice parameters $\omega_{y,ax} \approx 2\pi \times 350 \text{ kHz}$ and $\omega_{x,\text{rad}} \approx 2\pi \times 40 \text{ kHz}$ (for $\beta = 1$ at the cavity center, see sections 5.1.1 and 2.3.2).

One can see how for low values of β it is easier to fulfill the first condition (5.5), while the non-recapturing condition (5.6) remains equally favorable, i.e. there is a high probability that the drive-through loading effect occurs. It follows that when lowering β the unbalance of escape and recapture probabilities increases which is advantageous for drive-through loading. However, we observe that below certain values $\beta \lesssim 0.2$ the recapturing probability increases [67], thereby affecting the probability of drive-through loading. This effect is due to the anharmonicity of the lattice potential [102] in (5.3), that was not considered in the calculation of t_{tp} with the harmonic approximation: if the atom escapes earlier, its oscillation reaches higher positions in the DT_x potential where the slope is smoother, the particle velocity is slower, and the atom spends more time close to the turning point. Then with a longer time $t_{\text{tp}} > t_{\text{rec}}$,

Table 5.1: Quantitative estimations of the variables that determine the escape and recapture conditions responsible for the drive-through loading mechanism. The calculations were made with our 1D model, part analytically and part numerically, for an atom with energy $k_B \cdot 5 \mu\text{K}$ and transport velocity $v_T = 5 \text{ mm/s}$. For two values of the relative depth β we calculate the axial oscillation period $\tau_{y,\text{ax},\beta}$ in the DT_y lattice sites, the radial oscillation period $\tau_{x,\text{rad}}$ in the crossed DT_x lattice, the escape time t_{esc} (numerically), the recapture time t_{rec} , the radial oscillation amplitude A_y after escaping (numerically), the turning-point time t_{tp} , and finally the control values c_1 and c_2 for the conditions (5.5) and Eq. (5.6) respectively. See main text for the parameter definitions.

| β | $\tau_{y,\text{ax},\beta}$ | $\tau_{x,\text{rad}}$ | t_{esc} | t_{rec} | A_y | t_{tp} | c_1 | c_2 |
|---------|----------------------------|-----------------------|-----------------------|--------------------|-------------------------|-------------------------|------------|------------|
| 0.045 | $\sim 13.5 \mu\text{s}$ | $25 \mu\text{s}$ | $\sim 0.5 \text{ ms}$ | $86.8 \mu\text{s}$ | $\sim 6.9 \mu\text{m}$ | $\sim 12 \mu\text{s}$ | ~ 37 | ~ 7.2 |
| 0.020 | $\sim 20.2 \mu\text{s}$ | $25 \mu\text{s}$ | $\sim 2.6 \text{ ms}$ | $86.8 \mu\text{s}$ | $\sim 13.6 \mu\text{m}$ | $\sim 12.2 \mu\text{s}$ | ~ 129 | ~ 7.1 |

the condition (5.6) would be broken, thus entering in the recapture regime.

Active cooling inside of the intracavity lattice (dRSC in the experiment and modeled as a friction force in the simulation, see below) can play a role in increasing the probability that the atom remains in the intersection region, in two ways. On one side it reduces atom loss induced by heating, and on the other it damps the atom oscillations lower into the DT_x potential thus reducing the recapture probability.

In summary, from the above discussion of the 1D model and the drive-through loading mechanism, we identify four critical parameters influencing the effect (for a given mean temperature of the atoms): the relative trap depth β , the transport velocity v_T , the lattice focus offset y_0 , and the cooling strength. We also learn that β is the main parameter to use for optimization of the drive-through loading method. Before the experimental implementation, we use a numerical simulation of the 1D model to understand the rough dependence of the drive-through loading probability on the aforementioned parameters.

Numerical simulation

The numerical simulation was implemented by L. Ahlheit, based on preliminary ideas in Ref. [74]. A comprehensive explanation, including the computational optimization and validation tests, is included in his MSc thesis in Ref. [67]. Here I present a short overview of the implementation with some relevant details.

The simulation solves the classical evolution of a set of atoms (point particles) with the 1D lattice transport model introduced at the beginning of the section. For each particle with a set of parameters $\{\beta, v_T, y_0\}$, the simulation integrates numerically the equation of motion

$$\ddot{y}(t) = \frac{F(y, t)}{m_{\text{Rb}}} - \mathcal{F}(y, \dot{y}), \quad (5.7)$$

with the force $F(y, t) = -\nabla U_{\text{DT}}(y, t)$ given by the lattice potential in Equation (5.1), and m_{Rb} the atomic mass. The function $\mathcal{F}(y, \dot{y})$ represents the interactivity cooling as a friction force⁸ with tunable strength, linear dependence on the particle velocity $\dot{y}(t)$ and Gaussian dependence on the position $y(t)$. Note that the potential $U_{\text{DT}}(y, t)$ is non-conservative due to the movement of the lattice.

For the chosen parameters $\{\beta, v_T, y_0\}$, the simulation computes the single-atom loading probability P_{dt} from the number of successfully loaded atoms, i.e. with final position within the lattice intersection

⁸ In the simulation the atoms are subject to a damping force depending on their velocity, which is a very simplified model of the dRSC method in the experiment, but proves to be useful for a qualitative understanding of the underlying processes.

region, out of an ensemble with initial conditions $\{y(0), \dot{y}(0)\}$ (distributed according to the physical characteristics of our system). Details about the computational implementation of the simulation and the distribution of initial conditions are included in Appendix C.1. The most relevant results for a scan of the relative depth β , are shown in Figure 5.3 along with the experimental measurements, and will be discussed together in Section 5.2. Further simulation results of the other parameter scans are presented in Ref. [67] and included here in Appendix C.2.

From the simulation results we gain the following important conclusions about the drive-through loading effect: (i) we confirm that the relative lattice depth β has a strong influence on the loading probability, hence it is the most critical optimization parameter for the experimental implementation. An optimum is found around the value $\beta \approx 0.025$; for lower depths, considerable losses of atoms occur during transport, while for higher depth the effective well depth U_{eff} is not lowered enough to let the atoms escape from the moving lattice. (ii) The oscillation phase of the atom in the lattice has no relevant effect on the loading probability, as suspected from the adiabaticity conditions. (iii) The transport velocity has little effect on the loading probability in the range $[0.3, 30]$ mm/s, but higher velocities have an adverse effect. (iv) The cooling strength does not modify the amplitude of the loading probability, but it has the effect of shifting it on the β -axis. A stronger cooling favor loading at lower relative depths, whereas a weaker cooling improves loading at higher values of β . For more details on these conclusions and the complete results, see Ref. [67].

Even though these findings highlight the drive-through transport as a promising multi-atom loading technique for the intracavity lattice, featuring above 80 % individual-atom loading probability, the 1D model does not represent the full picture. In the experiment, certain effects that are not considered in the simulation can influence the result, to cite some: the interaction of the atoms can lead to losses at high densities by light-assisted collisions; the 3D structure of the lattice, and the resulting position distribution of the atoms, makes the particle dynamics way more complex than the simple 1D model; the tunneling probability, not considered in the simulation, can indeed play a role at low values of β ; common heating mechanisms are not considered (e.g. by photon scattering and trap laser noise), and the oversimplified cooling model might behave differently than the degenerate Raman cooling active inside of the cavity. Therefore, guided by the findings of the simulation, in the next section I present detailed measurements of the drive-through loading probability as a function of the mentioned relevant experimental parameters.

5.2 Experimental implementation of drive-through atom loading

Based on the empirical observation of the effect during drive-through transport introduced in Section 5.1, and on the learnings from the 1D model in Section 5.1.2, now we aim to implement an efficient multi-atom loading method for our atom-cavity module. This calls for a systematic study, this time experimentally, of the drive-through loading probability for a single atom as a function of critical parameters. Specifically, we identify as such the effective well depth U_{eff} (determined in the experiment by the relative lattice depth $\beta = U_{0,y}/U_{0,x}$), the transport velocity v_T during drive-through and the effect of cooling in the 3D lattice region.

The experimental sequence for the implementation of drive-through loading was briefly described in Section 5.1 (see also Figure 5.1 (c)). It is now convenient to describe the sequence in more detail. Atoms are loaded from the MOT into the transport 1D lattice (DT_y), with an estimated mean temperature of 40 μ K. The average number of loaded atoms can be adjusted by varying the MOT loading time. Then, the chain of atoms in the conveyor is shuttled to approach the cavity at a distance ~ 200 μ m with a first fast transport (800 μ m/200 ms). At this point, the system is updated to the chosen experimental parameters of relative depth β and transport velocity v_T . Subsequently, the drive-through transport takes place for

300 μm , across the 3D lattice region and the cavity mode where Raman cooling can be either activated or disabled. The transport stops at a distance of $\sim 100 \mu\text{m}$ past the cavity center. This guarantees that, in absence of drive-through loading effect, the full string of atoms loaded from the MOT and carried in the conveyor belt has completely crossed the 3D lattice region and abandoned the cavity mode. Consequently, we consider that any atoms remaining in the 3D lattice after transport have been successfully loaded with the drive-through technique.

Throughout the rest of this chapter I will refer to the drive-through sequence as described above when discussing the dependence on the different parameters identified as critical. The effect of the relative lattice depth is studied in Section 5.2.2. Then, the influence of transport velocity and cooling is discussed in Section 5.2.3. We also analyze the role of our particular lattice geometry, precisely the focus offset y_0 between the lattices DT_y and DT_x at the crossing point (although only via simulation since it is not modifiable in the experiment). But first, I will explain the procedure that we employ to assess the loading probability by means of the cavity-based detection.

5.2.1 Indirect measurement of the loading probability with the cavity

Even though the cavity in our experimental setup plays no role for the drive-through loading effect, it provides a useful sensor that we exploit to characterize the loading probability. Specifically, we employ the non-destructive atom detection technique presented in Section 2.3.1 and Figure 2.1, to monitor the presence of atoms inside the 3D lattice region, providing crucial information that we use to determine the loading probability. The Raman imaging technique presented in Chapter 4 is not applicable for this measurement because it does not resolve atoms along the line of sight that overlap in the image. It is, however, suitable for characterizing the spatial distribution of the atoms resulting from the drive-through loading sequence.

Measuring the mean atom number with the cavity detection

As discussed in Section 2.3.1, the cavity probe reflection signal saturates with the coupling of a single atom to the cavity mode. Hence, the cavity presence check provides a binary readout of the absence (low reflection signal) or presence (high reflection signal) of at least one atom inside of the cavity during the interrogation time, but the exact number of coupled atoms can not be directly measured in this manner. However, through statistical analysis from a set of repeated measurements we are able to estimate the mean number of atoms corresponding to the measurement settings. The approach consists in drawing a connection between the probability distribution of the cavity detection (experimentally accessible) and the atom number probability distribution inside the cavity, based on conceptual knowledge of the experimental procedure.

On the one hand, the expected outcome of a particular cavity check for given experimental parameters (denoted with i), follows a binomial distribution that can be reconstructed from multiple measurement repetitions. The resulting positive detection (high-signal) probability $C_i(+)$ corresponds to the probability of at least one atom coupling to the cavity during the probing time, while the negative detection (low-signal) probability $C_i(-) = 1 - C_i(+)$ gives the probability of an empty cavity.

On the other hand, the number of atoms present in the lattice at any given moment (denoted with j), follows Poisson statistics. The probability of having n trapped atoms at time j is expressed as

$$\mathcal{P}_j(n) = \frac{\alpha_j^n}{n!} e^{-\alpha_j}, \quad (5.8)$$

where α_j is the mean number of atoms in the lattice for the given experimental parameters.

As we know that the cavity detection signal saturates with a single atom, then the probability of a positive detection is equivalent to the cumulative Poisson probability of encountering one or more atoms in the cavity during the interrogation interval. But more interesting for us is the negative detection binomial probability resulting from an empty cavity, since it unambiguously corresponds to the Poisson probability of zero atoms. We can then write the connection between the two probability distributions as

$$C_i(+)\equiv\sum_{n=1}^{\infty}\mathcal{P}_i(n), \quad (5.9)$$

$$C_i(-)\equiv\mathcal{P}_i(0), \quad (5.10)$$

and combining equations (5.10) and (5.8) for $n = 0$, we obtain a link between the mean number of trapped atoms α_i and the measured quantity in the experiment, namely the probability of a high-signal cavity detection $C_i(+)$:

$$\alpha_i = -\ln(1 - C_i(+)). \quad (5.11)$$

This expression provides a mechanism to indirectly measure the mean number of atoms coupled to the cavity at any given time, and in the following we will use it to characterize the drive-through loading probability.

Measuring the drive-through loading probability

With a method at hand to obtain the mean number of atoms inside of the cavity, we now focus on measuring the probability of an atom to be loaded into the 3D lattice with the drive-through method, for chosen experimental parameters. The idea is to look for the ratio of atoms remaining in the lattice after transport to the available number of atoms transported by the conveyor belt.

During the drive-through loading sequence, we perform two cavity-based atom-presence checks at particular moments. The first check is done throughout the drive-through transport: we monitor the cavity reflection during the entire transport duration to detect any atom that enters the cavity mode, regardless of only crossing or staying inside the cavity. This check, referred to as *transport check*, is considered positive if there is at least one high-signal detection during drive-through. A positive transport check means that one or more atoms were transported by the conveyor belt into the 3D lattice. The second cavity check, the so called *loading check*, takes place after the drive-through transport has finished. The loading check allows to verify if one or more atoms remain trapped in the 3D lattice inside the cavity mode, i.e. if they were loaded during drive-through by the conveyor belt into the 3D lattice. We remind that, without the drive-through loading effect, we expect all the atoms carried in the conveyor belt to cross the 3D lattice region during transport (positive transport check), but then also to be dragged out of it, such that the cavity would remain empty after the transport (negative loading check).

From a set of measurement repetitions with same parameters, we obtain the binomial probabilities of the transport and loading cavity checks, $C_T(+)$ and $C_L(+)$ respectively. Then, with Equation (5.11) we find the corresponding mean number of atoms present in the 3D lattice during each check. Finally, we define the drive-through loading probability P_{dt} (for each individual atom) for the given experimental parameters as

$$P_{dt} = \frac{\alpha_L}{\alpha_T} \quad (5.12)$$

with α_L the average number of atoms loaded in the 3D lattice by the drive through transport, and α_T the average number of atoms transported by the conveyor belt. We note that atom losses occurring after the MOT loading but before entering the cavity are automatically taken into account by the transport check,

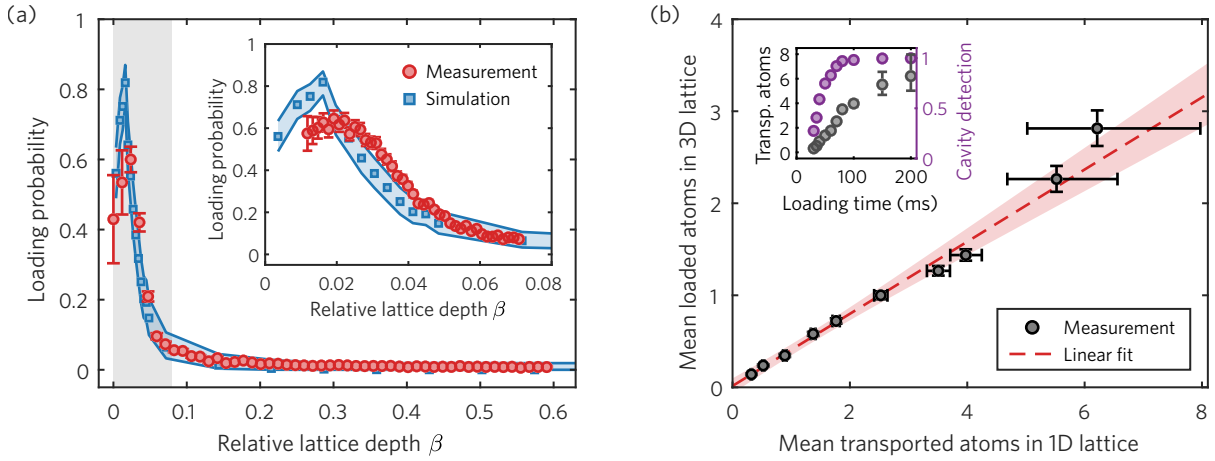


Figure 5.3: Experimental demonstration of the drive-through loading method. **(a)** Single-atom loading probability as a function of the relative trap depth β of the lattice DT_y with respect to the crossed lattice DT_x , for fixed transport velocity $v_T = 3$ mm/s and MOT loading time 80 ms. The measurements via the cavity nondestructive detection (red circles, see main text for the procedure) are shown together with the results of the 1D classical simulation (blue squares). Inset: a finer measurement in the region of maximum loading probability (gray shaded area in main plot), with the same simulation data as in the main graph. **(b)** Mean number of loaded atoms as a function of the mean number of available atoms transported by the conveyor belt into the 3D lattice (black circles). A linear fit (red dashed line and confidence bounds) shows that the drive-through loading probability remains constant (given by the slope) while the number of atoms can be tuned with the MOT loading time. We infer the mean number of atoms from the binomial probability of the cavity detection and the conversion to Poisson statistics, see Equation (5.11). Inset: tuning curve of the number of transported atoms versus the loading time from the MOT into the DT_y transport lattice (gray circles), and the corresponding binomial cavity detection probability (purple circles). This shows the correspondence between cavity detection and atom-number statistics used for the main graph. In (a) and (b), the error bars of the measured data (calculated with the Monte Carlo method) and the shaded band of the simulated data represent the 68% confidence intervals.

such that α_T represent the true number of atoms available for loading.

5.2.2 Demonstration of the drive-through loading method

At this point we have the necessary tools to investigate experimentally the dependence of the drive-through loading on the aforementioned critical parameters, mainly the relative lattice depth $\beta = U_{0,y}/U_{0,x}$. This will allow us to demonstrate the experimental implementation of the drive-through loading technique, to verify its working principle, and to compare the experimental results to the numerical simulation.

Optimizing the loading probability with the relative lattice depth

We start by looking into the influence of the effective well depth U_{eff} , which we learned from the numerical simulation in Section 5.1.2 to be the most critical parameter according to the one-dimensional model. However, in the real case of the experiment with the three-dimensional lattice geometry, the drive-through effect could exhibit a different behavior.

Hence, motivated by the results of the 1D simulation, we study systematically the drive-through loading probability as a function of U_{eff} . We recall the definition of the effective well depth as the minimum trapping potential of a lattice site of DT_y , being deformed during transport by the radial potential of DT_x (see Figure 5.2). In the experiment, U_{eff} can be tuned with the ratio of optical power between the conveyor

belt DT_y and the crossed lattice DT_x , i.e. the relative lattice depth $\beta = U_{0,y}/U_{0,x}$.

Using the procedure described in Section 5.2.1, we measure the drive-through loading probability P_{dt} for a scan of the lattice depth $U_{0,y}$ relative to the depth $U_{0,x}$ which remains constant. In the experimental sequence (see Figure 5.1 (c)), after the fast transport, the conveyor belt lattice DT_y is adiabatically lowered within 2 ms to the selected relative depth β . Then, the drive through transport is performed, after which the lattice is adiabatically raised back to $\beta = 1$ in 2 ms before the loading check. For this measurement we use a MOT loading time of 80 ms into the 1D lattice, and a constant drive-through transport velocity $v_T = 3$ mm/s. As mentioned earlier, cooling in the cavity region is active during drive-through using the dRSC technique (see Chapter 3). For each value of β , the measurement is repeated more than 1000 times for the statistical analysis to obtain the loading probability P_{dt} from equations (5.11) and (5.12).

In Figure 5.3 (a) are shown the measurement results (red circles) of loading probability P_{dt} as a function of the relative depth β , together with the outcome of the 1D simulation explained in Section 5.1.2 (blue squares). One can see that for most of the relative lattice depth values, i.e. towards the deeper side $\beta > 0.3$, the drive-through loading effect is not present and all the atoms are transported across the cavity without accumulating in the 3D region, i.e. the loading probability is zero. Yet, the effect is clearly visible for a significant intensity lowering of the DT_y transport lattice, appearing for values $\beta < 0.03$. Most interestingly, P_{dt} increases prominently for relative depth values $\beta < 0.08$. A finer scan of β measured in this region (gray shaded) is shown in the inset together with the same simulation data as in the main plot. A maximum drive-through loading probability $P_{dt} = (64 \pm 4) \%$ is measured at an optimum depth $\beta \approx 0.02$, whereas the simulation reaches a loading peak of $\sim 82 \%$ at $\beta \approx 0.016$. For lower values of the relative depth, the sharp decrease of loading probability is attributed to strong atom losses during the drive-through transport and to a high recapture probability in the moving lattice before the transport stops (see Section 5.1.2).

It is certainly expected to encounter discrepancies between the results of the simulated model and the measured counterpart, considering the 1D versus 3D geometries and the disregard of quantum effects (tunneling, scattering, light-induced collisions, ...). Nevertheless, we find notable how the qualitative behavior of the measured data and the simulation results in Figure 5.3 (a) match surprisingly well, despite the one-dimensional and classical simplification of the model. The lower maximum loading probability in the experiment compared to the simulation is attributed to heating that causes atom loss during the drive-through transport. The slight mismatch of the β -value of the respective maxima is possibly related to the effect of cooling that was oversimplified in the model, and which will be studied in Section 5.2.3.

Most interesting is to note how the increase of P_{dt} when lowering the DT_y intensity in Figure 5.3 (a), is related to the behavior of the effective well depth U_{eff} shown previously in Figure 5.2 (d). As seen in the figure, it defines an energy threshold that cuts into the energy distribution of the transported atoms. Atoms above this threshold have the possibility to escape out of the transport lattice sites and to accumulate at the lattice intersection. This comparison of figures strengthens the argument that the main trigger of the drive-through loading effect is the reduced effective well depth U_{eff} , with the mechanism explained in Section 5.1.2. More along this line will be discussed in Section 5.2.3.

It is interesting to compare the response of the loading probability P_{dt} when lowering the relative depth β (experiment and simulation) in Figure 5.3 (a), with the behavior of the escape probability when reducing β , related to the effective well depth U_{eff} , as shown previously in Figure 5.2 (d). The similarity between the figures strengthens the argument that the main trigger of the drive-through loading effect is the reduced effective well depth U_{eff} , with the mechanism explained in Section 5.1.2. More along this line will be discussed in Section 5.2.3.

These results show that the drive-through loading mechanism can work efficiently for a proper choice of parameters. With a loading probability exceeding 60 % for each atom, it looks very promising to achieve the accumulation of multiple atoms in the 3D lattice inside of the cavity. However, it is still

unknown if the loading probability would show a dependence on the number of loaded atoms, e.g. due to light-induced collisions or other effects that could affect or enhance it. In the next section we investigate experimentally this matter.

Controlling the cavity-coupled atom number with the drive-through loading

After showing that the drive-through technique works with a high single-atom loading probability for certain relative depths of the lattice (Figure 5.3 (a)), an important question arises: is it a useful technique for loading small atomic ensembles? In other words, we want to know if we can use it to load multiple atoms by increasing the number of available atoms during drive-through, without reducing the probability of loading each atom. To answer this question, we investigate the behavior of the drive-through loading effect as a function of the number of atoms transported by the conveyor belt into the 3D lattice.

We use the same overall experimental sequence than for the investigation of the β -dependence in Figure 5.3 (a), but here we keep the relative lattice depth fixed at $\beta = 0.035$ ⁹. The transport velocity is kept as before at $v_T = 3$ mm/s. The number of atoms carried by the conveyor belt is controlled by the loading time of the MOT into DT_y. For each MOT loading time t_{mot} we follow the measurement procedure as explained in Section 5.2.1, with the statistical analysis based on atom detection by the cavity, taking between 500 and 5000 samples depending on the evaluated uncertainties.

Differently than in the previous measurement (the scan of β), here we are interested in the average number of successfully loaded atoms α_L in the 3D lattice via drive-through loading, as a function of the mean number of transported atoms α_T by the conveyor belt. For each value of t_{mot} , we obtain the mean atom numbers from the binomial probabilities of the transport and loading cavity-checks, $C_T(+)$ and $C_L(+)$ respectively, see (5.11).

The main plot in Figure 5.3 (b) presents the measurement results of α_L for different values of α_T , with each pair of values corresponding to a MOT loading time t_{mot} . The inset shows the tuning curve of α_T as a function of t_{mot} (in gray, left y-axis), together with the corresponding cavity-detection probability $C_T(+)$ (in purple, right y-axis). We observe that the dependence of the number of loaded atoms on the number of transported atoms is nearly linear, with the slope representing the single-atom loading probability P_{dt} . From a linear fit (red dashed line) we obtain the value $P_{\text{dt}} = (39 \pm 4)\%$ that coincides with the result in Figure 5.3 (a) for $\beta = 0.035$.

Still, an evident limitation of this measurement is the restriction to low atom numbers only, i.e. ~ 6 to 8 at most, above which a precise evaluation is not feasible. The extended uncertainties at higher atom numbers are due to the highly nonlinear transformation of Equation (5.11), which is the base for our measurement procedure by the cavity detection (Section 5.2.1). One can see in the inset of Figure 5.3 (b) how the cavity detection probability saturates rapidly for longer MOT loading times, thereby increasing the uncertainty of the corresponding atom number.

Even so, the presented measurement provides a clear picture of the drive-through loading action. The interpretation is simple but important: we are able to tune the number of atoms loaded by drive-through transport and coupled to the cavity, while the single-atom loading probability does not seem to get affected, at least for the few-atoms regime.

Ultimately, the two measurements shown in Figure 5.3 and discussed in this section, demonstrate the working principle of the drive-through loading technique and prove its potential for delivering multiple atoms into the cavity. Nevertheless, it is still relevant to consider the effect of the other critical experimental parameters identified in Section 5.1.2, which we examine in the next section.

⁹ The non-optimal value $\beta = 0.035$ is chosen to lie on the sharp slope of P_{dt} and thus increase the sensitivity to changes.

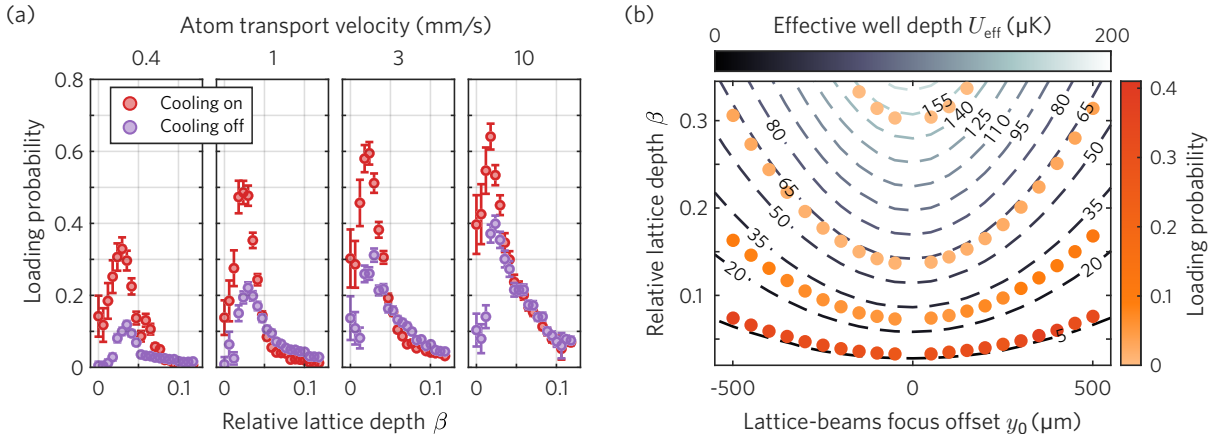


Figure 5.4: Investigation of drive-through loading dependence on other experimental parameters: transport velocity, cooling and lattice geometry. **(a)** Measurement of the loading probability as a function of the relative lattice depth β , for different transport velocities, and for the cases with intracavity cooling (dRSC) activated or deactivated. **(b)** Testing the dependence on the lattice geometry: simulation of loading probability as a function of the lattice-beams focus offset y_0 and the relative lattice depth β (circles in orange color scale). The landscape of effective well depth values U_{eff} in the parameter space $\{y_0, \beta\}$ is depicted as a contour plot (dashed lines in gray scale). The fact that equal values of the loading probability follow isolines of U_{eff} confirms the main role of the effective well depth for the drive-through loading mechanism.

5.2.3 Optimization of other relevant experimental parameters

With the help of the 1D model and the numerical simulation in Section 5.1.2, we identified the experimental parameters relevant for the optimization of the drive-through loading method. Besides the relative lattice depth β (analyzed in Section 5.2.2), we found that transport velocity v_T , the intracavity cooling strength, and the lattice geometry (i.e. the beam focus offset y_0) could play a role. Here we investigate the dependence of the loading probability P_{dt} on such parameters.

Effect of the transport velocity and intracavity cooling

Concretely, we are interested in the way the behavior of P_{dt} versus β observed in Figure 5.3 (a) is affected by the transport velocity and the intracavity cooling. To measure the drive-through loading probability P_{dt} we employ our standard experimental sequence used in Section 5.2.2. In this case the MOT loading time is fixed to 80 ms and the relative depth is scanned in the relevant range $[0, 0.13]$. We then perform a scan of the transport velocity, and for each value of v_T the measurement is repeated with intracavity cooling active and with the cooling disabled. The intracavity degenerate Raman sideband cooling (dRSC, see Chapter 3) is deactivated by switching off the repumper beam and thereby breaking the cooling cycle. For each measurement point we obtain the loading probability P_{dt} from ~ 1000 repetitions, with the statistical analysis explained in Section 5.2.1.

In Figure 5.4 (a) are presented the results of P_{dt} as a function of β , for four transport speeds in the range $[0.4, 10]$ mm/s, with dRSC on and off. The corresponding simulation results indicate an overall good agreement with the measurements, but have been omitted here since they are not relevant for the present discussion. A comparison of simulation and experimental results is displayed in Appendix C.2 of this thesis, and a detailed description is contained in Ref. [67].

Let us examine first the effect of the transport velocity with cooling active, compared to the case of $v_T = 3$ mm/s that we used before. For slower transports the overall loading probability decreases while

for higher velocities it improves. This is because atom losses induced by heating (e.g. from laser noise) are proportional to the time the drive-through transport takes. The change in loading probability is most perceptible at low trap depths, at which the atoms are more likely to escape: we can see the maximum of P_{dt} slightly shifting to the left for faster transport. However, the transport velocity also sets an upper limit. At higher velocities than 15 mm/s we observe that most of the atoms are lost before entering the cavity, heated out of the conveyor belt by the strong acceleration¹⁰. But all in all, we can note that in the range [3, 10] mm/s the loading probability is only marginally affected by the choice of the transport velocity.

On the other hand, the intracavity cooling has a strong effect. While for $\beta > 0.05$ there seems to be no influence, without cooling the atoms at lower relative depths have a sharp drop in loading probability. This is explained by two mechanisms: on one side the cooling action reduces atom losses during transport that are caused by heating; on the other hand it also reduces the recapturing effect that is more probable at lower values of β , see the discussion in Section 5.1.2. Due to the first mechanism, the effect of cooling is stronger for slower transport where atoms are subject to heating for longer. But in general, we observe that the effect of cooling is to increase the final loading probability by counteracting heating, but the overall shape of P_{dt} versus β is not changed. This means that the pure drive-through loading mechanism, as discussed in Section 5.1.2, is not directly influenced by the presence or absence of cooling in most cases. Only in the regime of very low β -values cooling plays a critical role to avoid atom recapturing.

Effect of the lattice geometry

As discussed before in Section 5.1.2, the geometry of the lattice modifies the effective well depth U_{eff} for a given relative lattice depth β . In turn, this is expected to modify the drive-through loading probability P_{dt} at the given settings. Specifically, it is influenced by the Gaussian beam parameters (of all lattice beams), the beam crossing angle and the focus offset y_0 . We aim to test the role of the lattice geometry in the drive-through loading probability, but changing the beam geometry in the experiment is clearly not an option. Nevertheless, for a first evaluation of the effect, we use the numerical simulation from Section 5.1.2 and run it with modified beam focus offset.

In Figure 5.4 (b) we present the simulated results of P_{dt} for a 2D scan of focus offset y_0 and relative depth β (round markers in orange scale). We also plot together a contour map (dashed lines in gray scale) of the effective well depth values U_{eff} corresponding to each value-pair $\{y_0, \beta\}$. The parameters of the simulation runs were chosen in order to sample the parameter-space $\{y_0, \beta\}$ along four isolines of U_{eff} . It is clearly noticeable that along each isoline the loading probability displays a nearly constant value. Such observation confirms that the effective well depth is the main parameter that determines if the drive-through loading mechanism works.

This conclusion highlights the adaptability of the drive-through loading method to other lattice geometries: for a different focus offset or beam-crossing angle, U_{eff} (and thus P_{dt}) will have a different dependence on the relative depth β , but it will most probably be possible to find a suitable range for the drive-through loading to succeed.

Overall, from the measurements presented in this section and shown in Figure 5.4, we can emphasize that the drive-through loading technique is robust against changes in the transport velocity, and in the lattice geometry. An active atom cooling method is necessary to compensate unavoidable heating, but it is not a requirement for the fundamental drive-through loading mechanism.

¹⁰ We employ for simplicity a bathtub-style transport [75, 158] having a velocity profile with sharp corners that imply strong acceleration points. With more complex techniques such as optimal quantum control [101], shorter transport times are achievable without heating, which could further improve the drive-through loading efficiency.

5.3 Summary and conclusions

In this chapter I have presented the development and implementation of a new method for loading atoms from a distant MOT into the intersection of a crossed-beam optical 3D lattice. The technique, known as *drive-through loading*, relies on transporting atoms with a conveyor belt through the intersection of the lattice beams, where the atoms accumulate when the trap depth of the transport lattice is reduced to a small fraction of the intersecting lattice beams. The highlight of this method is its simplicity, avoiding the need of extra laser beams, additional optical elements or complicated algorithms: it only requires control on the intensity and the phase of the transport lattice beam.

After discussing the intuitive understanding of the drive-through loading mechanism with a one-dimensional model, we investigated experimentally the dependence on the relative trap depth β . For this, we employed an indirect statistical measurement of the mean atom-number based on the cavity nondestructive detection. In our system, we demonstrated a promising single-atom loading probability above 60 % for $\beta \approx 2$ %. Results from a numerical simulation using our 1D model showed a surprisingly good match with the measurements, confirming our understanding of the underlying mechanism. Furthermore, we demonstrated experimentally that the number of atoms loaded by drive-through can be controlled by the loading time of the MOT, without affecting the drive-through loading probability per atom. Additionally, we investigated the loading probability on other experimental parameters, namely the transport velocity, the lattice geometry and the presence of atom cooling. Our investigation shows that the drive-through loading effect is quite robust against changes in all the aforementioned parameters, although cooling plays an important role for compensating atom loss due to heating.

Although the proof of principle of this technique is clearly shown in this chapter, combining these measurements with an imaging technique (as the Raman imaging presented in Chapter 4) allows to investigate the resulting position distribution (thus the density) and the behavior for higher atom numbers. Preliminary measurements of the position distribution using Raman imaging were made in Ref. [67] and can be found here in Appendix C.3. Unfortunately our effort to conclude such measurements was interrupted by the irreversible damage or our FFPC (see Appendix D.1).

Yet, these preliminary measurements indeed suggest that the drive-through loading mechanism triggers the accumulation of atoms around the beam-crossing center. For this reason we believe that the method is suited to generate dense atom loading in the 3D lattice. The three-dimensional lattice geometry enhances the loading density because the atoms can accommodate in ~ 100 lattice sites, minimizing multiple occupancy and thus reducing losses, such that placing few tens of atoms inside of the cavity mode should be possible.

In conclusion, the loading technique presented here can be useful in general for experiments and miniaturized quantum technology platforms, with low optical access that rely on the delivery of cold atoms into the system and on optical lattices for trapping. In the particular case of our atom-cavity platform, this loading method is straightforward for coupling small atomic ensembles to our FFPC. This would allow collective effect that enhance light-matter interaction and thus the efficiency of the quantum node, which is one of the main motivations of this thesis.

Summary and Outlook

IN this thesis I have presented three new experimental techniques that enable a better control of individual atoms coupled to high-bandwidth cavities, where standard control techniques face difficulties. The techniques developed here presented here aimed at three specific goals: (i) cooling the atoms inside the resonator, (ii) detecting their number and position with a cavity-independent imaging technique, and (iii) loading small atomic ensembles into the narrow cavity mode.

First, I showed the degenerate Raman sideband cooling (dRSC) to the ground state of single atoms, with a simple and resource efficient implementation adapted to the lattice and cavity geometry. Since, apart of the lattice, only weak optical pumping and a tunable magnetic field are needed, the dRSC method is easily applicable to other cavity experiments due to its simplicity and versatility, even in the case of narrow-linewidth resonators. More generally, this implementation can also be interesting for atoms in lattices without a cavity, e.g. in applications with limited optical access.

Second, I presented the new Raman imaging scheme, relying on Raman cooling transitions to generate fluorescence on the ^{87}Rb D_1 , independent from the D_2 reserved for the quantum channel of the atom-cavity node. With an imaging SNR of ~ 13 and a residual motional ground-state occupation above 85 %, this method allows for high fidelity detection of individual atoms in optical lattices. Furthermore, we investigated the heating effect of dipole-force fluctuations (DFFs), and showed that it can be avoided with a small blue detuning of the illumination light. It should be noted that the heating effect of DFFs is not limited to our particular FFPC setup, on the contrary it is relevant for most experiments involving near-resonant illumination of lattice-trapped atoms.

Third, I developed and demonstrated the drive-through loading technique, based on transporting atoms with a conveyor belt through the intersection of the lattice beams, where the atoms accumulate when the trap depth of the transport lattice is reduced to a small fraction of the intersecting lattice beams. The highlight of this method is its simplicity, avoiding the need of extra laser beams, additional optical elements or complicated algorithms: it only requires control on the intensity and the phase of the transport lattice beam. From the preliminary measurements of the position distribution of atoms in the lattice, we believe that the method is suited to generate dense atom loading in the 3D lattice. The three-dimensional lattice geometry enhances the loading density because the atoms can accommodate in ~ 100 lattice sites, minimizing multiple occupancy and thus reducing losses, such that placing few tens of atoms inside of the cavity mode should be possible. We note that this loading technique presented here is not setup-specific and can be applied in general for experiments and miniaturized quantum technology platforms, with low optical access that rely on the delivery of cold atoms into the system and on optical lattices for trapping.

Ultimately, these three techniques extend the available toolbox for control and manipulation of atom-cavity systems. The ability to load small atomic ensembles in our FFPC, and to determine the

number and positions of cavity-coupled atoms in a non-destructive way, paves the way for creating and controlling predefined atomic arrays inside of the resonator, that could be manipulated by individual addressing with e.g. optical tweezers steered by an acousto-optical deflector [93]. This would allow collective effects that enhance light-matter interaction, with the collective coupling $g_N \propto \sqrt{N_a} \cdot g$, and thus the efficiency of the quantum node. In that way, it enhances the capabilities of the current prototypes of cavity-based quantum nodes, with the possibility to create a network of cavity-quantum registers as envisioned in Ref. [64], thus giving one step forward in the unfolding development of quantum networks.

Bibliography

- [1] E. Uruñuela, W. Alt, E. Keiler, D. Meschede, D. Pandey, H. Pfeifer and T. Macha, “Ground-state cooling of a single atom inside a high-bandwidth cavity”, [Physical Review A 101.2 \(Feb. 2020\) 023415](#), ISSN: 2469-9926 (cit. on pp. vi, 5, 9, 19, 27–29, 39, 73, 78, 95).
- [2] E. Uruñuela, M. Ammenwerth, P. Malik, L. Ahlheit, H. Pfeifer, W. Alt and D. Meschede, “Raman imaging of atoms inside a high-bandwidth cavity”, [Physical Review A 105.4 \(Apr. 2022\) 043321](#), ISSN: 2469-9926 (cit. on pp. vi, 2, 5, 9, 19, 20, 31–33, 36, 39, 79, 95).
- [3] J. P. Dowling and G. J. Milburn, “Quantum technology: the second quantum revolution”, [Philosophical Transactions of the Royal Society of London. Series A: Mathematical, Physical and Engineering Sciences 361.1809 \(Aug. 2003\) 1655](#), ed. by A. G. J. MacFarlane, ISSN: 1364-503X (cit. on p. 1).
- [4] I. H. Deutsch, “Harnessing the Power of the Second Quantum Revolution”, [PRX Quantum 1.2 \(Nov. 2020\) 020101](#), ISSN: 2691-3399 (cit. on p. 1).
- [5] H. J. Kimble, “The quantum internet”, [Nature 453.7198 \(June 2008\) 1023](#), ISSN: 0028-0836 (cit. on pp. 1, 95).
- [6] S. Wehner, D. Elkouss and R. Hanson, “Quantum internet: A vision for the road ahead”, [Science 362.6412 \(Oct. 2018\)](#), ISSN: 0036-8075 (cit. on pp. 1, 95).
- [7] B. Sanguinetti, A. Martin, H. Zbinden and N. Gisin, “Quantum Random Number Generation on a Mobile Phone”, [Physical Review X 4.3 \(Sept. 2014\) 031056](#), ISSN: 2160-3308 (cit. on p. 1).
- [8] G. Gras, A. Martin, J. W. Choi and F. Bussi eres, “Quantum Entropy Model of an Integrated Quantum-Random-Number-Generator Chip”, [Physical Review Applied 15.5 \(May 2021\) 054048](#), ISSN: 2331-7019 (cit. on p. 1).
- [9] N. Gisin and R. Thew, “Quantum communication”, [Nature Photonics 1.3 \(Mar. 2007\) 165](#), ISSN: 1749-4885 (cit. on pp. 1, 95).
- [10] R. Van Meter, *Quantum Networking*, Chichester, UK: John Wiley & Sons, Ltd, Apr. 2014, ISBN: 9781118648919 (cit. on pp. 1, 95).
- [11] L.-M. Duan, M. D. Lukin, J. I. Cirac and P. Zoller, “Long-distance quantum communication with atomic ensembles and linear optics”, [Nature 414.6862 \(Nov. 2001\) 413](#), ISSN: 0028-0836 (cit. on pp. 1, 8, 78, 95).
- [12] L.-M. Duan and C. Monroe, “Colloquium : Quantum networks with trapped ions”, [Reviews of Modern Physics 82.2 \(Apr. 2010\) 1209](#), ISSN: 0034-6861 (cit. on pp. 1, 95).

- [13] N. Sangouard, C. Simon, H. de Riedmatten and N. Gisin,
“Quantum repeaters based on atomic ensembles and linear optics”,
Reviews of Modern Physics 83.1 (Mar. 2011) 33, ISSN: 0034-6861 (cit. on pp. 1, 95).
- [14] S. J. van Enk, H. J. Kimble and H. Mabuchi, “Quantum Information Processing in Cavity-QED”,
Quantum Information Processing 3.1-5 (Oct. 2004) 75, ISSN: 1570-0755 (cit. on pp. 1, 5, 6, 95).
- [15] S. Ritter, C. Nölleke, C. Hahn, A. Reiserer, A. Neuzner, M. Uphoff, M. Mücke, E. Figueroa,
J. Bochmann and G. Rempe,
“An elementary quantum network of single atoms in optical cavities”,
Nature 484.7393 (Apr. 2012) 195, ISSN: 0028-0836 (cit. on pp. 1, 6, 78, 95).
- [16] A. Reiserer and G. Rempe,
“Cavity-based quantum networks with single atoms and optical photons”,
Reviews of Modern Physics 87.4 (Dec. 2015) 1379, ISSN: 0034-6861 (cit. on pp. 1, 6, 95).
- [17] J. I. Cirac, P. Zoller, H. J. Kimble and H. Mabuchi, “Quantum State Transfer and Entanglement
Distribution among Distant Nodes in a Quantum Network”,
Physical Review Letters 78.16 (Apr. 1997) 3221, ISSN: 0031-9007 (cit. on pp. 1, 6, 95).
- [18] H. J. Kimble, “Strong Interactions of Single Atoms and Photons in Cavity QED”,
Physica Scripta T76.1 (1998) 127, ISSN: 0031-8949 (cit. on pp. 1, 6, 95).
- [19] R. Miller, T. E. Northup, K. M. Birnbaum, A. Boca, A. D. Boozer and H. J. Kimble,
“Trapped atoms in cavity QED: coupling quantized light and matter”,
Journal of Physics B: Atomic, Molecular and Optical Physics 38.9 (May 2005) S551,
ISSN: 0953-4075 (cit. on pp. 1, 5, 6, 95).
- [20] S. Haroche and J.-M. Raimond, *Exploring the Quantum*, Oxford University Press, Aug. 2006,
ISBN: 9780198509141 (cit. on pp. 1, 6, 95).
- [21] D. Hunger, T. Steinmetz, Y. Colombe, C. Deutsch, T. W. Hänsch and J. Reichel,
“A fiber Fabry–Perot cavity with high finesse”, *New Journal of Physics* 12.6 (June 2010) 065038,
ISSN: 1367-2630 (cit. on pp. 1, 8, 39, 78, 95).
- [22] J. Gallego, S. Ghosh, S. K. Alavi, W. Alt, M. Martinez-Dorantes, D. Meschede and
L. Ratschbacher,
“High-finesse fiber Fabry–Perot cavities: stabilization and mode matching analysis”,
Applied Physics B 122.3 (Mar. 2016) 47, ISSN: 0946-2171 (cit. on pp. 1, 8, 39, 42, 78, 95, 102).
- [23] H. Pfeifer, L. Ratschbacher, J. Gallego, C. Saavedra, A. Faßbender, A. von Haaren, W. Alt,
S. Hofferberth, M. Köhl, S. Linden and D. Meschede,
“Achievements and perspectives of optical fiber Fabry–Perot cavities”,
Applied Physics B 128.2 (Feb. 2022) 29, ISSN: 0946-2171 (cit. on pp. 1, 2, 5–9, 39, 95).
- [24] J. Gallego, W. Alt, T. Macha, M. Martinez-Dorantes, D. Pandey and D. Meschede,
“Strong Purcell Effect on a Neutral Atom Trapped in an Open Fiber Cavity”,
Physical Review Letters 121.17 (Oct. 2018) 173603, ISSN: 0031-9007
(cit. on pp. 1, 2, 6–10, 14, 18, 39, 78, 95).
- [25] H. Takahashi, E. Kassa, C. Christoforou and M. Keller,
“Strong Coupling of a Single Ion to an Optical Cavity”,
Physical Review Letters 124.1 (Jan. 2020) 013602, ISSN: 0031-9007 (cit. on p. 2).

-
- [26] M. Brekenfeld, D. Niemietz, J. D. Christesen and G. Rempe, “A quantum network node with crossed optical fibre cavities”, *Nature Physics* 16.6 (June 2020) 647, ISSN: 1745-2473 (cit. on pp. 2, 6).
- [27] M. Steiner, H. M. Meyer, C. Deutsch, J. Reichel and M. Köhl, “Single Ion Coupled to an Optical Fiber Cavity”, *Physical Review Letters* 110.4 (Jan. 2013) 043003, ISSN: 0031-9007 (cit. on p. 2).
- [28] A. Pscherer, M. Meierhofer, D. Wang, H. Kelkar, D. Martín-Cano, T. Utikal, S. Götzinger and V. Sandoghdar, “Single-Molecule Vacuum Rabi Splitting: Four-Wave Mixing and Optical Switching at the Single-Photon Level”, *Physical Review Letters* 127.13 (Sept. 2021) 133603, ISSN: 0031-9007 (cit. on p. 2).
- [29] Y. Colombe, T. Steinmetz, G. Dubois, F. Linke, D. Hunger and J. Reichel, “Strong atom–field coupling for Bose–Einstein condensates in an optical cavity on a chip”, *Nature* 450.7167 (Nov. 2007) 272, ISSN: 0028-0836 (cit. on pp. 2, 40, 78, 95).
- [30] A. D. Pfister, M. Salz, M. Hettrich, U. G. Poschinger and F. Schmidt-Kaler, “A quantum repeater node with trapped ions: a realistic case example”, *Applied Physics B* 122.4 (Apr. 2016) 89, ISSN: 0946-2171 (cit. on p. 2).
- [31] T. G. Ballance, H. M. Meyer, P. Kobel, K. Ott, J. Reichel and M. Köhl, “Cavity-induced backaction in Purcell-enhanced photon emission of a single ion in an ultraviolet fiber cavity”, *Physical Review A* 95.3 (Mar. 2017) 033812, ISSN: 2469-9926 (cit. on p. 2).
- [32] Y. H. Lien, G. Barontini, M. Scheucher, M. Mergenthaler, J. Goldwin and E. A. Hinds, “Observing coherence effects in an overdamped quantum system”, *Nature Communications* 7.1 (Dec. 2016) 13933, ISSN: 2041-1723 (cit. on pp. 2, 7).
- [33] M. Khudaverdyan, W. Alt, T. Kampschulte, S. Reick, A. Thobe, A. Widera and D. Meschede, “Quantum Jumps and Spin Dynamics of Interacting Atoms in a Strongly Coupled Atom-Cavity System”, *Physical Review Letters* 103.12 (Sept. 2009) 123006, ISSN: 0031-9007 (cit. on p. 2).
- [34] N. Kalb, A. Reiserer, S. Ritter and G. Rempe, “Heralded Storage of a Photonic Quantum Bit in a Single Atom”, *Physical Review Letters* 114.22 (June 2015) 220501, ISSN: 0031-9007 (cit. on p. 2).
- [35] A. Kuhn, M. Hennrich and G. Rempe, “Deterministic Single-Photon Source for Distributed Quantum Networking”, *Physical Review Letters* 89.6 (July 2002) 067901, ISSN: 0031-9007 (cit. on pp. 2, 7).
- [36] A. Kuhn and D. Ljunggren[†], “Cavity-based single-photon sources”, *Contemporary Physics* 51.4 (July 2010) 289, ISSN: 0010-7514 (cit. on pp. 2, 95).
- [37] P. B. R. Nisbet-Jones, J. Dille, D. Ljunggren and A. Kuhn, “Highly efficient source for indistinguishable single photons of controlled shape”, *New Journal of Physics* 13.10 (Oct. 2011) 103036, ISSN: 1367-2630 (cit. on pp. 2, 78, 95).
- [38] T. Wilk, S. C. Webster, A. Kuhn and G. Rempe, “Single-Atom Single-Photon Quantum Interface”, *Science* 317.5837 (July 2007) 488, ISSN: 0036-8075 (cit. on pp. 2, 6, 95).
- [39] O. Morin, M. Körber, S. Langenfeld and G. Rempe, “Deterministic Shaping and Reshaping of Single-Photon Temporal Wave Functions”, *Physical Review Letters* 123.13 (Sept. 2019) 133602, ISSN: 0031-9007 (cit. on pp. 2, 6, 95).

- [40] S. Langenfeld, P. Thomas, O. Morin and G. Rempe,
“Quantum Repeater Node Demonstrating Unconditionally Secure Key Distribution”,
[Physical Review Letters 126.23 \(June 2021\) 230506](#), ISSN: 0031-9007 (cit. on pp. 2, 6, 95).
- [41] T. Macha, E. Uruñuela, W. Alt, M. Ammenwerth, D. Pandey, H. Pfeifer and D. Meschede,
“Nonadiabatic storage of short light pulses in an atom-cavity system”,
[Physical Review A 101.5 \(May 2020\) 053406](#), ISSN: 2469-9926
(cit. on pp. 2, 6, 14, 18, 21, 42, 95).
- [42] R. H. Dicke, “Coherence in Spontaneous Radiation Processes”,
[Physical Review 93.1 \(Jan. 1954\) 99](#), ISSN: 0031-899X (cit. on pp. 2, 8, 95).
- [43] F. Haas, J. Volz, R. Gehr, J. Reichel and J. Estève,
“Entangled States of More Than 40 Atoms in an Optical Fiber Cavity”,
[Science 344.6180 \(Apr. 2014\) 180](#), ISSN: 0036-8075 (cit. on pp. 2, 31, 39).
- [44] Z. Li, B. Braverman, S. Colombo, C. Shu, A. Kawasaki, A. F. Adiyatullin, E. Pedrozo-Peñafiel,
E. Mendez and V. Vuletić,
“Collective Spin-Light and Light-Mediated Spin-Spin Interactions in an Optical Cavity”,
[PRX Quantum 3.2 \(Apr. 2022\) 020308](#), ISSN: 2691-3399 (cit. on pp. 2, 31, 39).
- [45] M. Fleischhauer, S. Yelin and M. Lukin,
“How to trap photons? Storing single-photon quantum states in collective atomic excitations”,
[Optics Communications 179.1-6 \(May 2000\) 395](#), ISSN: 00304018 (cit. on pp. 2, 31, 39, 95).
- [46] A. V. Gorshkov, A. André, M. D. Lukin and A. S. Sørensen,
“Photon storage in Λ -type optically dense atomic media. I. Cavity model”,
[Physical Review A 76.3 \(Sept. 2007\) 033804](#), ISSN: 1050-2947 (cit. on pp. 2, 31, 39, 95).
- [47] M. J. Kastoryano, F. Reiter and A. S. Sørensen,
“Dissipative Preparation of Entanglement in Optical Cavities”,
[Physical Review Letters 106.9 \(Feb. 2011\) 090502](#), ISSN: 0031-9007 (cit. on pp. 2, 3, 31, 39, 95).
- [48] F. Reiter, D. Reeb and A. S. Sørensen,
“Scalable Dissipative Preparation of Many-Body Entanglement”,
[Physical Review Letters 117.4 \(July 2016\) 040501](#), ISSN: 0031-9007 (cit. on pp. 2, 3, 31, 39).
- [49] Y. Lin, J. P. Gaebler, F. Reiter, T. R. Tan, R. Bowler, A. S. Sørensen, D. Leibfried and
D. J. Wineland,
“Dissipative production of a maximally entangled steady state of two quantum bits”,
[Nature 504.7480 \(Dec. 2013\) 415](#), ISSN: 0028-0836 (cit. on pp. 2, 3).
- [50] D. C. Cole, S. D. Erickson, G. Zarantonello, K. P. Horn, P.-Y. Hou, J. J. Wu, D. H. Slichter,
F. Reiter, C. P. Koch and D. Leibfried,
“Resource-Efficient Dissipative Entanglement of Two Trapped-Ion Qubits”,
[Physical Review Letters 128.8 \(Feb. 2022\) 080502](#), ISSN: 0031-9007 (cit. on pp. 2, 3).
- [51] J. Ramette, J. Sinclair, Z. Vendeiro, A. Rudelis, M. Cetina and V. Vuletić,
“Any-To-Any Connected Cavity-Mediated Architecture for Quantum Computing with Trapped
Ions or Rydberg Arrays”, [PRX Quantum 3.1 \(Mar. 2022\) 010344](#), ISSN: 2691-3399
(cit. on pp. 2, 31, 39).
- [52] J. Argüello-Luengo, A. González-Tudela, T. Shi, P. Zoller and J. I. Cirac,
“Analogue quantum chemistry simulation”, [Nature 574.7777 \(Oct. 2019\) 215](#), ISSN: 0028-0836
(cit. on pp. 2, 31, 39).

-
- [53] F. Reiter, M. J. Kastoryano and A. S. Sørensen, “Driving two atoms in an optical cavity into an entangled steady state using engineered decay”, *New Journal of Physics* 14.5 (May 2012) 053022, ISSN: 1367-2630 (cit. on p. 3).
- [54] D. Meschede and A. Rauschenbeutel, “Manipulating Single Atoms”, *Advances In Atomic, Molecular, and Optical Physics*, Elsevier, 2006 75 (cit. on pp. 3, 31, 95).
- [55] H. Ott, “Single atom detection in ultracold quantum gases: a review of current progress”, *Reports on Progress in Physics* 79.5 (May 2016) 054401, ISSN: 0034-4885 (cit. on pp. 3, 5, 14, 31, 95).
- [56] K. D. Nelson, X. Li and D. S. Weiss, “Imaging single atoms in a three-dimensional array”, *Nature Physics* 3.8 (Aug. 2007) 556, ISSN: 1745-2473 (cit. on pp. 3, 31).
- [57] A. Alberti, C. Robens, W. Alt, S. Brakhane, M. Karski, R. Reimann, A. Widera and D. Meschede, “Super-resolution microscopy of single atoms in optical lattices”, *New Journal of Physics* 18.5 (May 2016) 053010, ISSN: 1367-2630 (cit. on pp. 3, 25, 31, 36, 95).
- [58] M. Martinez-Dorantes, W. Alt, J. Gallego, S. Ghosh, L. Ratschbacher and D. Meschede, “State-dependent fluorescence of neutral atoms in optical potentials”, *Physical Review A* 97.2 (Feb. 2018) 023410, ISSN: 2469-9926 (cit. on pp. 3, 17, 18, 31, 37, 95).
- [59] C. Adams and E. Riis, “Laser cooling and trapping of neutral atoms”, *Progress in Quantum Electronics* 21.1 (Jan. 1997) 1, ISSN: 00796727 (cit. on pp. 3, 27).
- [60] H. J. Metcalf and P. van der Straten, “Laser cooling and trapping of atoms”, *Journal of the Optical Society of America B* 20.5 (May 2003) 887, ISSN: 0740-3224 (cit. on pp. 3, 14, 15, 27, 31).
- [61] R. Grimm, M. Weidemüller and Y. B. Ovchinnikov, “Optical Dipole Traps for Neutral Atoms”, *Advances In Atomic, Molecular, and Optical Physics* 42.C (Jan. 2000) 95, ISSN: 1049-250X (cit. on pp. 3, 10, 14, 16, 17, 29, 42, 78).
- [62] W. Alt, D. Schrader, S. Kuhr, M. Müller, V. Gomer and D. Meschede, “Single atoms in a standing-wave dipole trap”, *Physical Review A* 67.3 (Mar. 2003) 033403, ISSN: 1050-2947 (cit. on pp. 3, 31, 45).
- [63] I. Bloch, “Ultracold quantum gases in optical lattices”, *Nature Physics* 1.1 (Oct. 2005) 23, ISSN: 1745-2473 (cit. on pp. 3, 31, 95).
- [64] D. Hunger, “Quantum logic at a distance”, *Science* 371.6529 (Feb. 2021) 576, ISSN: 0036-8075 (cit. on pp. 3, 58).
- [65] P. Malik, “Linewidth-reduced DBR Laser for Raman Sideband Cooling”, MSc thesis: University of Bonn, 2020 (cit. on pp. 5, 21, 31).
- [66] M. Ammenwerth, “Raman Imaging of Small Atomic Ensembles Inside an Optical Cavity”, MSc thesis: University of Bonn, 2020 (cit. on pp. 5, 18–20, 24, 31).
- [67] L. Ahlheit, “Preparation of Small Atomic Ensembles in a Fiber Cavity”, MSc thesis: University of Bonn, 2020 (cit. on pp. 5, 24, 25, 31, 39, 44–48, 54, 56, 97–100).
- [68] H. Mabuchi, M. Armen, B. Lev, M. Loncar, J. Vuckovic, H. Kimble, J. Preskill, M. Roukes, A. Scherer and S. van Enk, “Quantum networks based on cavity QED”, *Quantum Information and Computation* 1.Special (Dec. 2001) 7, ISSN: 15337146 (cit. on p. 5).
- [69] C. Monroe, “Quantum information processing with atoms and photons”, *Nature* 416.6877 (Mar. 2002) 238, ISSN: 0028-0836 (cit. on p. 5).

- [70] S. Chu, “Cold atoms and quantum control”, *Nature* 416.6877 (Mar. 2002) 206, ISSN: 0028-0836 (cit. on pp. 5, 13, 27, 31).
- [71] J. Bochmann, M. Mücke, C. Guhl, S. Ritter, G. Rempe and D. L. Moehring, “Lossless State Detection of Single Neutral Atoms”, *Physical Review Letters* 104.20 (May 2010) 203601, ISSN: 0031-9007 (cit. on p. 5).
- [72] M. Martinez-Dorantes, W. Alt, J. Gallego, S. Ghosh, L. Ratschbacher, Y. Völzke and D. Meschede, “Fast Nondestructive Parallel Readout of Neutral Atom Registers in Optical Potentials”, *Physical Review Letters* 119.18 (Oct. 2017) 180503, ISSN: 0031-9007 (cit. on pp. 5, 78).
- [73] C. Christoforou, C. Pignot, E. Kassa, H. Takahashi and M. Keller, “Enhanced ion–cavity coupling through cavity cooling in the strong coupling regime”, *Scientific Reports* 10.1 (Dec. 2020) 15693, ISSN: 2045-2322 (cit. on p. 5).
- [74] M. M. Dorantes, “Fast non-destructive internal state detection of neutral atoms in optical potentials”, Ph.D. thesis: University of Bonn, 2016 (cit. on pp. 5, 10–12, 15–17, 24, 25, 40, 41, 47).
- [75] J. C. Gallego, “Strong Coupling between Small Atomic Ensembles and an Open Fiber Cavity”, Ph.D. thesis: University of Bonn, 2017 (cit. on pp. 5, 7–16, 18, 20, 24, 32, 39, 41, 55, 99, 101, 102).
- [76] T. Macha, “Storage of Short Light Pulses in a Fiber–Based Atom–Cavity System”, Ph.D. thesis: University of Bonn, 2018 (cit. on pp. 5, 9–14, 18, 21, 22, 27).
- [77] E. M. Purcell, H. C. Torrey and R. V. Pound, “Resonance Absorption by Nuclear Magnetic Moments in a Solid”, *Physical Review* 69.1-2 (Jan. 1946) 37, ISSN: 0031-899X (cit. on p. 6).
- [78] E. Jaynes and F. Cummings, “Comparison of quantum and semiclassical radiation theories with application to the beam maser”, *Proceedings of the IEEE* 51.1 (1963) 89, ISSN: 0018-9219 (cit. on p. 6).
- [79] B. W. Shore and P. L. Knight, “The Jaynes-Cummings Model”, *Journal of Modern Optics* 40.7 (July 1993) 1195, ISSN: 0950-0340 (cit. on p. 6).
- [80] H. J. Carmichael, *Statistical Methods in Quantum Optics 1*, 1st ed., Berlin, Heidelberg: Springer Berlin Heidelberg, 1999, ISBN: 978-3-642-08133-0 (cit. on p. 7).
- [81] N. Moiseyev, “Quantum theory of resonances: calculating energies, widths and cross-sections by complex scaling”, *Physics Reports* 302.5-6 (Sept. 1998) 212, ISSN: 03701573 (cit. on pp. 7, 96).
- [82] C. W. Gardiner and P. Zoller, *Quantum Noise: A Handbook of Markovian and Non-Markovian Quantum Stochastic Methods with Applications to Quantum Optics*, 3rd ed., Berlin: Springer, 2004 449, ISBN: 978-3-642-06094-6 (cit. on pp. 7, 96).
- [83] L. Giannelli, T. Schmit, T. Calarco, C. P. Koch, S. Ritter and G. Morigi, “Optimal storage of a single photon by a single intra-cavity atom”, *New Journal of Physics* 20.10 (Oct. 2018) 105009, ISSN: 1367-2630 (cit. on p. 7).
- [84] M. Tavis and F. W. Cummings, “Exact Solution for an N -Molecule—Radiation-Field Hamiltonian”, *Physical Review* 170.2 (June 1968) 379, ISSN: 0031-899X (cit. on p. 8).

-
- [85] K. Baumann, C. Guerlin, F. Brennecke and T. Esslinger, “Dicke quantum phase transition with a superfluid gas in an optical cavity”, *Nature* 464.7293 (Apr. 2010) 1301, ISSN: 0028-0836 (cit. on p. 8).
- [86] E. L. Raab, M. Prentiss, A. Cable, S. Chu and D. E. Pritchard, “Trapping of Neutral Sodium Atoms with Radiation Pressure”, *Physical Review Letters* 59.23 (Dec. 1987) 2631, ISSN: 0031-9007 (cit. on pp. 10, 15).
- [87] D. Schrader, S. Kuhr, W. Alt, M. Müller, V. Gomer and D. Meschede, “An optical conveyor belt for single neutral atoms”, *Applied Physics B* 73.8 (Dec. 2001) 819, ISSN: 0946-2171 (cit. on pp. 10, 15, 18, 39, 40, 42, 95).
- [88] S. Kuhr, W. Alt, D. Schrader, M. Müller, V. Gomer and D. Meschede, “Deterministic Delivery of a Single Atom”, *Science* 293.5528 (July 2001) 278, ISSN: 0036-8075 (cit. on pp. 10, 15, 18, 39, 40, 42, 78, 95).
- [89] M. Khudaverdyan, W. Alt, I. Dotsenko, T. Kampschulte, K. Lenhard, A. Rauschenbeutel, S. Reick, K. Schörner, A. Widera and D. Meschede, “Controlled insertion and retrieval of atoms coupled to a high-finesse optical resonator”, *New Journal of Physics* 10.7 (July 2008) 073023, ISSN: 1367-2630 (cit. on pp. 10, 15, 18, 39).
- [90] P. Jessen and I. Deutsch, “Optical Lattices”, *Adv. At. Mol. Opt. Phys.* Vol. 37, C, 1996 95 (cit. on p. 10).
- [91] C. Wieman and T. W. Hänsch, “Doppler-Free Laser Polarization Spectroscopy”, *Physical Review Letters* 36.20 (May 1976) 1170, ISSN: 0031-9007 (cit. on p. 10).
- [92] A. D. Boozer, A. Boca, R. Miller, T. E. Northup and H. J. Kimble, “Cooling to the Ground State of Axial Motion for One Atom Strongly Coupled to an Optical Cavity”, *Physical Review Letters* 97.8 (Aug. 2006) 083602, ISSN: 0031-9007 (cit. on pp. 10, 14, 95).
- [93] E. Uruñuela, “Imaging and addressing of neutral atoms inside a fiber cavity”, MSc thesis: University of Bonn, 2017 (cit. on pp. 10, 20, 25, 58).
- [94] E. D. Black, “An introduction to Pound–Drever–Hall laser frequency stabilization”, *American Journal of Physics* 69.1 (Jan. 2001) 79, ISSN: 0002-9505 (cit. on pp. 13, 78).
- [95] A. Ashkin, “History of optical trapping and manipulation of small-neutral particle, atoms, and molecules”, *IEEE Journal of Selected Topics in Quantum Electronics* 6.6 (Nov. 2000) 841, ISSN: 1077-260X (cit. on pp. 13, 27, 31).
- [96] W. D. Phillips, “Nobel Lecture: Laser cooling and trapping of neutral atoms”, *Reviews of Modern Physics* 70.3 (July 1998) 721, ISSN: 0034-6861 (cit. on p. 14).
- [97] S. Chu, L. Hollberg, J. E. Bjorkholm, A. Cable and A. Ashkin, “Three-dimensional viscous confinement and cooling of atoms by resonance radiation pressure”, *Physical Review Letters* 55.1 (July 1985) 48, ISSN: 0031-9007 (cit. on pp. 15, 18).
- [98] W. D. Phillips and H. Metcalf, “Laser Deceleration of an Atomic Beam”, *Physical Review Letters* 48.9 (Mar. 1982) 596, ISSN: 0031-9007 (cit. on p. 15).
- [99] S. J. M. Kuppens, K. L. Corwin, K. W. Miller, T. E. Chupp and C. E. Wieman, “Loading an optical dipole trap”, *Physical Review A* 62.1 (June 2000) 013406, ISSN: 1050-2947 (cit. on pp. 16, 40).

- [100] J. Wu, R. Newell, M. Hausmann, D. J. Vieira and X. Zhao, “Loading dynamics of optical trap and parametric excitation resonances of trapped atoms”, *Journal of Applied Physics* 100.5 (Sept. 2006) 054903, ISSN: 0021-8979 (cit. on pp. 16, 40).
- [101] M. R. Lam, N. Peter, T. Groh, W. Alt, C. Robens, D. Meschede, A. Negretti, S. Montangero, T. Calarco and A. Alberti, “Demonstration of Quantum Brachistochrones between Distant States of an Atom”, *Physical Review X* 11.1 (Feb. 2021) 011035, ISSN: 2160-3308 (cit. on pp. 16, 42, 55).
- [102] S. Blatt, J. W. Thomsen, G. K. Campbell, A. D. Ludlow, M. D. Swallows, M. J. Martin, M. M. Boyd and J. Ye, “Rabi spectroscopy and excitation inhomogeneity in a one-dimensional optical lattice clock”, *Physical Review A* 80.5 (Nov. 2009) 052703, ISSN: 1050-2947 (cit. on pp. 16, 40, 46).
- [103] D. L. Haycock, S. E. Hamann, G. Klose and P. S. Jessen, “Atom trapping in deeply bound states of a far-off-resonance optical lattice”, *Physical Review A* 55.6 (June 1997) R3991, ISSN: 1050-2947 (cit. on pp. 17, 22, 28, 33).
- [104] D. Leibfried, R. Blatt, C. Monroe and D. Wineland, “Quantum dynamics of single trapped ions”, *Reviews of Modern Physics* 75.1 (Mar. 2003) 281, ISSN: 0034-6861 (cit. on pp. 17, 22, 28, 33, 78, 95).
- [105] J. Dalibard and C. Cohen-Tannoudji, “Dressed-atom approach to atomic motion in laser light: the dipole force revisited”, *Journal of the Optical Society of America B* 2.11 (Nov. 1985) 1707, ISSN: 0740-3224 (cit. on pp. 17, 37, 96).
- [106] B. Arora and B. K. Sahoo, “State-insensitive trapping of Rb atoms: Linearly versus circularly polarized light”, *Physical Review A* 86.3 (Sept. 2012) 033416, ISSN: 1050-2947 (cit. on pp. 18, 95).
- [107] A. Aspect, J. Dalibard, A. Heidmann, C. Salomon and C. Cohen-Tannoudji, “Cooling Atoms with Stimulated Emission”, *Physical Review Letters* 57.14 (Oct. 1986) 1688, ISSN: 0031-9007 (cit. on p. 18).
- [108] J. Dalibard and C. Cohen-Tannoudji, “Laser cooling below the Doppler limit by polarization gradients: simple theoretical models”, *Journal of the Optical Society of America B* 6.11 (Nov. 1989) 2023, ISSN: 0740-3224 (cit. on p. 18).
- [109] P. Maunz, T. Puppe, I. Schuster, N. Syassen, P. W. H. Pinkse and G. Rempe, “Cavity cooling of a single atom”, *Nature* 428.6978 (Mar. 2004) 50, ISSN: 0028-0836 (cit. on pp. 18, 27, 31, 78).
- [110] H. Ritsch, P. Domokos, F. Brennecke and T. Esslinger, “Cold atoms in cavity-generated dynamical optical potentials”, *Reviews of Modern Physics* 85.2 (Apr. 2013) 553, ISSN: 0034-6861 (cit. on pp. 18, 27, 31, 78, 95).
- [111] D. A. Steck, *Rubidium 87 D Line Data*, available online at <http://steck.us/alkalidata> (revision 2.2.2, 9 July 2021). (Cit. on pp. 20, 102).

-
- [112] X. Baillard, A. Gauguet, S. Bize, P. Lemonde, P. Laurent, A. Clairon and P. Rosenbusch, “Interference-filter-stabilized external-cavity diode lasers”, *Optics Communications* 266.2 (Oct. 2006) 609, ISSN: 00304018 (cit. on pp. 21, 95).
- [113] S. E. Hamann, D. L. Haycock, G. Klose, P. H. Pax, I. H. Deutsch and P. S. Jessen, “Resolved-Sideband Raman Cooling to the Ground State of an Optical Lattice”, *Physical Review Letters* 80.19 (May 1998) 4149, ISSN: 0031-9007 (cit. on pp. 21, 27–29, 78).
- [114] R. Reimann, W. Alt, T. Macha, D. Meschede, N. Thau, S. Yoon and L. Ratschbacher, “Carrier-free Raman manipulation of trapped neutral atoms”, *New Journal of Physics* 16.11 (Nov. 2014) 113042, ISSN: 1367-2630 (cit. on pp. 22, 30, 32, 78, 95).
- [115] A. Neuzner, S. Dürr, M. Körber, S. Ritter and G. Rempe, “Increased dimensionality of Raman cooling in a slightly nonorthogonal optical lattice”, *Physical Review A* 98.1 (July 2018) 013401, ISSN: 2469-9926 (cit. on pp. 22, 30, 34, 78, 95).
- [116] C. Monroe, D. M. Meekhof, B. E. King, S. R. Jefferts, W. M. Itano, D. J. Wineland and P. Gould, “Resolved-Sideband Raman Cooling of a Bound Atom to the 3D Zero-Point Energy”, *Physical Review Letters* 75.22 (Nov. 1995) 4011, ISSN: 0031-9007 (cit. on pp. 23, 30).
- [117] V. Vuletić, C. Chin, A. J. Kerman and S. Chu, “Degenerate Raman Sideband Cooling of Trapped Cesium Atoms at Very High Atomic Densities”, *Physical Review Letters* 81.26 (Dec. 1998) 5768, ISSN: 0031-9007 (cit. on pp. 27–29, 78).
- [118] A. J. Kerman, V. Vuletić, C. Chin and S. Chu, “Beyond Optical Molasses: 3D Raman Sideband Cooling of Atomic Cesium to High Phase-Space Density”, *Physical Review Letters* 84.3 (Jan. 2000) 439, ISSN: 0031-9007 (cit. on pp. 29, 78).
- [119] G. Williams and D. C. Watts, “Non-symmetrical dielectric relaxation behaviour arising from a simple empirical decay function”, *Transactions of the Faraday Society* 66 (1970) 80, ISSN: 0014-7672 (cit. on pp. 29, 78).
- [120] K. B. Lee, J. Siegel, S. Webb, S. Lévêque-Fort, M. Cole, R. Jones, K. Dowling, M. Lever and P. French, “Application of the Stretched Exponential Function to Fluorescence Lifetime Imaging”, *Biophysical Journal* 81.3 (Sept. 2001) 1265, ISSN: 00063495 (cit. on pp. 29, 78).
- [121] T. A. Savard, K. M. O’Hara and J. E. Thomas, “Laser-noise-induced heating in far-off resonance optical traps”, *Physical Review A* 56.2 (Aug. 1997) R1095, ISSN: 1050-2947 (cit. on pp. 30, 78).
- [122] M. E. Gehm, K. M. O’Hara, T. A. Savard and J. E. Thomas, “Dynamics of noise-induced heating in atom traps”, *Physical Review A* 58.5 (Nov. 1998) 3914, ISSN: 1050-2947 (cit. on pp. 30, 78).
- [123] B. J. Lester, A. M. Kaufman and C. A. Regal, “Raman cooling imaging: Detecting single atoms near their ground state of motion”, *Physical Review A* 90.1 (July 2014) 011804, ISSN: 1050-2947 (cit. on pp. 32, 35, 95).
- [124] Y. S. Patil, S. Chakram, L. M. Aycock and M. Vengalattore, “Nondestructive imaging of an ultracold lattice gas”, *Physical Review A* 90.3 (Sept. 2014) 033422, ISSN: 1050-2947 (cit. on pp. 32, 95).

- [125] L. W. Cheuk, M. A. Nichols, M. Okan, T. Gersdorf, V. V. Ramasesh, W. S. Bakr, T. Lompe and M. W. Zwierlein, “Quantum-Gas Microscope for Fermionic Atoms”, *Physical Review Letters* 114.19 (May 2015) 193001, ISSN: 0031-9007 (cit. on pp. 32, 95).
- [126] M. F. Parsons, F. Huber, A. Mazurenko, C. S. Chiu, W. Setiawan, K. Wooley-Brown, S. Blatt and M. Greiner, “Site-Resolved Imaging of Fermionic ${}^6\text{Li}$ in an Optical Lattice”, *Physical Review Letters* 114.21 (May 2015) 213002, ISSN: 0031-9007 (cit. on pp. 32, 95).
- [127] A. Omran, M. Boll, T. A. Hilker, K. Kleinlein, G. Salomon, I. Bloch and C. Gross, “Microscopic Observation of Pauli Blocking in Degenerate Fermionic Lattice Gases”, *Physical Review Letters* 115.26 (Dec. 2015) 263001, ISSN: 0031-9007 (cit. on pp. 32, 95).
- [128] R. Taïeb, R. Dum, J. I. Cirac, P. Marte and P. Zoller, “Cooling and localization of atoms in laser-induced potential wells”, *Physical Review A* 49.6 (June 1994) 4876, ISSN: 1050-2947 (cit. on pp. 37, 95).
- [129] A. Kumar, T.-Y. Wu, F. Giraldo and D. S. Weiss, “Sorting ultracold atoms in a three-dimensional optical lattice in a realization of Maxwell’s demon”, *Nature* 561.7721 (Sept. 2018) 83, ISSN: 0028-0836 (cit. on p. 39).
- [130] M. Endres, H. Bernien, A. Keesling, H. Levine, E. R. Anschuetz, A. Krajenbrink, C. Senko, V. Vuletic, M. Greiner and M. D. Lukin, “Atom-by-atom assembly of defect-free one-dimensional cold atom arrays”, *Science* 354.6315 (Nov. 2016) 1024, ISSN: 0036-8075 (cit. on p. 39).
- [131] D. Barredo, S. de Léséleuc, V. Lienhard, T. Lahaye and A. Browaeys, “An atom-by-atom assembler of defect-free arbitrary two-dimensional atomic arrays”, *Science* 354.6315 (Nov. 2016) 1021, ISSN: 0036-8075 (cit. on p. 39).
- [132] W. Petrich, M. H. Anderson, J. R. Ensher and E. A. Cornell, “Behavior of atoms in a compressed magneto-optical trap”, *Journal of the Optical Society of America B* 11.8 (Aug. 1994) 1332, ISSN: 0740-3224 (cit. on p. 39).
- [133] M. T. DePue, C. McCormick, S. L. Winoto, S. Oliver and D. S. Weiss, “Unity Occupation of Sites in a 3D Optical Lattice”, *Physical Review Letters* 82.11 (Mar. 1999) 2262, ISSN: 0031-9007 (cit. on p. 39).
- [134] D. J. Han, M. T. DePue and D. S. Weiss, “Loading and compressing Cs atoms in a very far-off-resonant light trap”, *Physical Review A* 63.2 (Jan. 2001) 023405, ISSN: 1050-2947 (cit. on p. 39).
- [135] W. Williams and M. Saffman, “Compression and localization of an atomic cloud in a time dependent optical lattice”, *Journal of Modern Optics* 55.14 (Aug. 2008) 2187, ISSN: 0950-0340 (cit. on p. 39).
- [136] J. L. Ville, T. Bienaimé, R. Saint-Jalm, L. Corman, M. Aidelsburger, L. Chomaz, K. Kleinlein, D. Perconte, S. Nascimbène, J. Dalibard and J. Beugnon, “Loading and compression of a single two-dimensional Bose gas in an optical accordion”, *Physical Review A* 95.1 (Jan. 2017) 013632, ISSN: 2469-9926 (cit. on p. 39).
- [137] L. Qi, J. Chiaverini, H. Espinós, M. Palmero and J. G. Muga, “Fast and robust particle shuttling for quantum science and technology”, *Europhysics Letters* 134.2 (Apr. 2021) 23001, ISSN: 0295-5075 (cit. on p. 39).

-
- [138] G. T. Hickman and M. Saffman,
“Speed, retention loss, and motional heating of atoms in an optical conveyor belt”,
[Physical Review A 101.6 \(June 2020\) 063411](#), ISSN: 2469-9926 (cit. on pp. 39, 40, 42).
- [139] A. Couvert, T. Kawalec, G. Reinaudi and D. Guéry-Odelin,
“Optimal transport of ultracold atoms in the non-adiabatic regime”,
[EPL \(Europhysics Letters\) 83.1 \(July 2008\) 13001](#), ISSN: 0295-5075 (cit. on pp. 39, 43).
- [140] M. Langbecker, R. Wirtz, F. Knoch, M. Noaman, T. Speck and P. Windpassinger,
“Highly controlled optical transport of cold atoms into a hollow-core fiber”,
[New Journal of Physics 20.8 \(Aug. 2018\) 083038](#), ISSN: 1367-2630 (cit. on p. 39).
- [141] A. Hilton, C. Perrella, F. Benabid, B. Sparkes, A. Luiten and P. Light,
“High-efficiency cold-atom transport into a waveguide trap”,
[Physical Review Applied 10.4 \(Oct. 2018\) 044034](#), ISSN: 2331-7019 (cit. on p. 39).
- [142] S. Nußmann, M. Hijlkema, B. Weber, F. Rohde, G. Rempe and A. Kuhn,
“Submicron Positioning of Single Atoms in a Microcavity”,
[Physical Review Letters 95.17 \(Oct. 2005\) 173602](#), ISSN: 0031-9007 (cit. on p. 39).
- [143] K. M. Fortier, S. Y. Kim, M. J. Gibbons, P. Ahmadi and M. S. Chapman,
“Deterministic Loading of Individual Atoms to a High-Finesse Optical Cavity”,
[Physical Review Letters 98.23 \(June 2007\) 233601](#), ISSN: 0031-9007 (cit. on p. 39).
- [144] F. Ferri, A. La Rooij, C. Leboutellier, P.-A. Bourdel, M. Baghdad, S. Schwartz, S. Garcia,
J. Reichel and R. Long,
“An optical elevator for precise delivery of cold atoms using an acousto-optical deflector”,
[New Journal of Physics 24.4 \(Apr. 2022\) 043013](#), ISSN: 1367-2630 (cit. on pp. 39, 40).
- [145] A. Goban, C.-L. Hung, S.-P. Yu, J. Hood, J. Muniz, J. Lee, M. Martin, A. McClung, K. Choi,
D. Chang, O. Painter and H. Kimble, “Atom–light interactions in photonic crystals”,
[Nature Communications 5.1 \(Sept. 2014\) 3808](#), ISSN: 2041-1723 (cit. on p. 40).
- [146] T. G. Tiecke, J. D. Thompson, N. P. de Leon, L. R. Liu, V. Vuletić and M. D. Lukin,
“Nanophotonic quantum phase switch with a single atom”, [Nature 508.7495 \(Apr. 2014\) 241](#),
ISSN: 0028-0836 (cit. on p. 40).
- [147] N. V. Corzo, J. Raskop, A. Chandra, A. S. Sheremet, B. Gouraud and J. Laurat,
“Waveguide-coupled single collective excitation of atomic arrays”,
[Nature 566.7744 \(Feb. 2019\) 359](#), ISSN: 0028-0836 (cit. on p. 40).
- [148] S. G. Menon, K. Singh, J. Borregaard and H. Bernien,
“Nanophotonic quantum network node with neutral atoms and an integrated telecom interface”,
[New Journal of Physics 22.7 \(July 2020\) 073033](#), ISSN: 1367-2630 (cit. on p. 40).
- [149] M. Aspelmeyer, T. J. Kippenberg and F. Marquardt, “Cavity optomechanics”,
[Reviews of Modern Physics 86.4 \(Dec. 2014\) 1391](#), ISSN: 0034-6861 (cit. on p. 40).
- [150] T. P. Purdy, D. W. C. Brooks, T. Botter, N. Brahms, Z.-Y. Ma and D. M. Stamper-Kurn,
“Tunable Cavity Optomechanics with Ultracold Atoms”,
[Physical Review Letters 105.13 \(Sept. 2010\) 133602](#), ISSN: 0031-9007 (cit. on p. 40).
- [151] E. Shahmoon, D. S. Wild, M. D. Lukin and S. F. Yelin,
“Cavity quantum optomechanics with an atom-array membrane”, (June 2020),
arXiv: [2006.01973](#) (cit. on p. 40).

- [152] A. Jöckel, A. Faber, T. Kampschulte, M. Korppi, M. T. Rakher and P. Treutlein, “Sympathetic cooling of a membrane oscillator in a hybrid mechanical–atomic system”, *Nature Nanotechnology* 10.1 (Jan. 2015) 55, ISSN: 1748-3387 (cit. on p. 40).
- [153] S. Camerer, M. Korppi, A. Jöckel, D. Hunger, T. W. Hänsch and P. Treutlein, “Realization of an Optomechanical Interface Between Ultracold Atoms and a Membrane”, *Physical Review Letters* 107.22 (Nov. 2011) 223001, ISSN: 0031-9007 (cit. on p. 40).
- [154] Q. Zhang, J. G. Muga, D. Guéry-Odelin and X. Chen, “Optimal shortcuts for atomic transport in anharmonic traps”, *Journal of Physics B: Atomic, Molecular and Optical Physics* 49.12 (June 2016) 125503, ISSN: 0953-4075 (cit. on p. 42).
- [155] C. F. Bharucha, K. W. Madison, P. R. Morrow, S. R. Wilkinson, B. Sundaram and M. G. Raizen, “Observation of atomic tunneling from an accelerating optical potential”, *Physical Review A* 55.2 (Feb. 1997) R857, ISSN: 1050-2947 (cit. on p. 43).
- [156] K. Madison, C. Bharucha, P. Morrow, S. Wilkinson, Q. Niu, B. Sundaram and M. Raizen, “Quantum transport of ultracold atoms in an accelerating optical potential”, *Applied Physics B: Lasers and Optics* 65.6 (Dec. 1997) 693, ISSN: 0946-2171 (cit. on p. 43).
- [157] G. Ness, M. R. Lam, W. Alt, D. Meschede, Y. Sagi and A. Alberti, “Observing crossover between quantum speed limits”, *Science Advances* 7.52 (Dec. 2021), ISSN: 2375-2548 (cit. on p. 43).
- [158] X. Chen, E. Torrontegui, D. Stefanatos, J.-S. Li and J. G. Muga, “Optimal trajectories for efficient atomic transport without final excitation”, *Physical Review A* 84.4 (Oct. 2011) 043415, ISSN: 1050-2947 (cit. on pp. 43, 55).
- [159] M. Mücke, J. Bochmann, C. Hahn, A. Neuzner, C. Nölleke, A. Reiserer, G. Rempe and S. Ritter, “Generation of single photons from an atom-cavity system”, *Physical Review A* 87.6 (June 2013) 063805, ISSN: 1050-2947 (cit. on p. 78).
- [160] W. Chen, K. M. Beck, R. Bücker, M. Gullans, M. D. Lukin, H. Tanji-Suzuki and V. Vuletić, “All-Optical Switch and Transistor Gated by One Stored Photon”, *Science* 341.6147 (Aug. 2013) 768, ISSN: 0036-8075 (cit. on p. 78).
- [161] A. Reiserer, N. Kalb, G. Rempe and S. Ritter, “A quantum gate between a flying optical photon and a single trapped atom”, *Nature* 508.7495 (Apr. 2014) 237, ISSN: 0028-0836 (cit. on p. 78).
- [162] H.-J. Briegel, W. Dür, J. I. Cirac and P. Zoller, “Quantum Repeaters: The Role of Imperfect Local Operations in Quantum Communication”, *Physical Review Letters* 81.26 (Dec. 1998) 5932, ISSN: 0031-9007 (cit. on p. 78).
- [163] M. Körber, O. Morin, S. Langenfeld, A. Neuzner, S. Ritter and G. Rempe, “Decoherence-protected memory for a single-photon qubit”, *Nature Photonics* 12.1 (Jan. 2018) 18, ISSN: 1749-4885 (cit. on p. 78).
- [164] R. Keil, M. Zopf, Y. Chen, B. Höfer, J. Zhang, F. Ding and O. G. Schmidt, “Solid-state ensemble of highly entangled photon sources at rubidium atomic transitions”, *Nature Communications* 8.1 (Aug. 2017) 15501, ISSN: 2041-1723 (cit. on p. 78).
- [165] M. Zopf, R. Keil, Y. Chen, J. Yang, D. Chen, F. Ding and O. G. Schmidt, “Entanglement Swapping with Semiconductor-Generated Photons Violates Bell’s Inequality”, *Physical Review Letters* 123.16 (Oct. 2019) 160502, ISSN: 0031-9007 (cit. on p. 78).

-
- [166] T. E. Northup and R. Blatt, “Quantum information transfer using photons”, *Nature Photonics* 8.5 (May 2014) 356, ISSN: 1749-4885 (cit. on p. 78).
- [167] D. Awschalom, K. K. Berggren, H. Bernien, S. Bhave, L. D. Carr, P. Davids, S. E. Economou, D. Englund, A. Faraon, M. Fejer, S. Guha, M. V. Gustafsson, E. Hu, L. Jiang, J. Kim, B. Korzh, P. Kumar, P. G. Kwiat, M. Lončar, M. D. Lukin, D. A. Miller, C. Monroe, S. W. Nam, P. Narang, J. S. Orcutt, M. G. Raymer, A. H. Safavi-Naeini, M. Spiropulu, K. Srinivasan, S. Sun, J. Vučković, E. Waks, R. Walsworth, A. M. Weiner and Z. Zhang, “Development of Quantum Interconnects (QuICs) for Next-Generation Information Technologies”, *PRX Quantum* 2.1 (Feb. 2021) 017002, ISSN: 2691-3399 (cit. on p. 95).
- [168] P. Looock, W. Alt, C. Becher, O. Benson, H. Boche, C. Deppe, J. Eschner, S. Höfling, D. Meschede, P. Michler, F. Schmidt and H. Weinfurter, “Extending Quantum Links: Modules for Fiber- and Memory-Based Quantum Repeaters”, *Advanced Quantum Technologies* 3.11 (Nov. 2020) 1900141, ISSN: 2511-9044 (cit. on p. 95).
- [169] M. Reitz, C. Sommer and C. Genes, “Cooperative Quantum Phenomena in Light-Matter Platforms”, *PRX Quantum* 3.1 (Jan. 2022) 010201, ISSN: 2691-3399 (cit. on p. 95).
- [170] E. Altman, K. R. Brown, G. Carleo, L. D. Carr, E. Demler, C. Chin, B. DeMarco, S. E. Economou, M. A. Eriksson, K.-M. C. Fu, M. Greiner, K. R. Hazzard, R. G. Hulet, A. J. Kollár, B. L. Lev, M. D. Lukin, R. Ma, X. Mi, S. Misra, C. Monroe, K. Murch, Z. Nazario, K.-K. Ni, A. C. Potter, P. Roushan, M. Saffman, M. Schleier-Smith, I. Siddiqi, R. Simmonds, M. Singh, I. Spielman, K. Temme, D. S. Weiss, J. Vučković, V. Vuletić, J. Ye and M. Zwerlein, “Quantum Simulators: Architectures and Opportunities”, *PRX Quantum* 2.1 (Feb. 2021) 017003, ISSN: 2691-3399 (cit. on p. 95).
- [171] D.-J. Han, S. Wolf, S. Oliver, C. McCormick, M. T. DePue and D. S. Weiss, “3D Raman Sideband Cooling of Cesium Atoms at High Density”, *Physical Review Letters* 85.4 (July 2000) 724, ISSN: 0031-9007 (cit. on p. 95).
- [172] C. Henry, “Theory of the linewidth of semiconductor lasers”, *IEEE Journal of Quantum Electronics* 18.2 (Feb. 1982) 259, ISSN: 0018-9197 (cit. on p. 95).
- [173] G. Agrawal, “Line narrowing in a single-mode injection laser due to external optical feedback”, *IEEE Journal of Quantum Electronics* 20.5 (May 1984) 468, ISSN: 0018-9197 (cit. on p. 95).
- [174] Q. Lin, M. A. Van Camp, H. Zhang, B. Jelenković and V. Vuletić, “Long-external-cavity distributed Bragg reflector laser with subkilohertz intrinsic linewidth”, *Optics Letters* 37.11 (June 2012) 1989, ISSN: 0146-9592 (cit. on p. 95).
- [175] W. Ma, B. Xiong, C. Sun, X. Ke, Z. Hao, L. Wang, J. Wang, Y. Han, H. Li and Y. Luo, “Laser frequency noise characterization by self-heterodyne with both long and short delay”, *Applied Optics* 58.13 (May 2019) 3555, ISSN: 1559-128X (cit. on p. 95).
- [176] T. Okoshi, K. Kikuchi and A. Nakayama, “Novel method for high resolution measurement of laser output spectrum”, *Electronics Letters* 16.16 (July 1980) 630, ISSN: 00135194 (cit. on p. 95).
- [177] *Simulation-based fitting routine for laser linewidth estimation from DSH measurement*, <https://de.mathworks.com/matlabcentral/fileexchange/106535> (cit. on p. 95).
- [178] T. A. Hilker, “Spin-Resolved Microscopy of Strongly Correlated Fermionic Many-Body States”, Ph.D. thesis: LMU München, 2017 (cit. on p. 95).

- [179] L. F. Shampine, I. Gladwell and S. Thompson, *Solving ODEs with MATLAB*, Cambridge, England: Cambridge University Press, May 2003, ISBN: 9780521824040 (cit. on p. 97).
- [180] T. Hansch and B. Couillaud, “Laser frequency stabilization by polarization spectroscopy of a reflecting reference cavity”, *Optics Communications* 35.3 (Dec. 1980) 441, ISSN: 00304018 (cit. on p. 102).

Publication: Ground–state cooling of a single atom inside a high–bandwidth cavity

This section contains a reprint of the publication in Ref. [1] and discussed in Chapter 3. It is included here with the agreement of all co-authors and with the permission granted by the American Physical Society (APS). The complete citation reads: E. Uruñuela, W. Alt, E. Keiler, D. Meschede, D. Pandey, H. Pfeifer, and T. Macha, *Ground-state cooling of a single atom inside a high-bandwidth cavity*, (2020), Physical Review A **101**, 023415.

Contents of the publication:

| | | |
|-----|----------------------------------|----|
| A.1 | I. Introduction | 74 |
| A.2 | II. Experimental setup | 74 |
| A.3 | III. Cooling method | 75 |
| A.4 | IV. Results | 75 |
| A.5 | V. Conclusion | 76 |

Ground-state cooling of a single atom inside a high-bandwidth cavity

Eduardo Uruñuela¹,* Wolfgang Alt, Elvira Keiler, Dieter Meschede¹, Deepak Pandey, Hannes Pfeifer, and Tobias Macha¹
Institut für Angewandte Physik, Universität Bonn, Wegelerstraße 8, 53115 Bonn, Germany



(Received 19 September 2019; accepted 10 February 2020; published 28 February 2020)

We report on vibrational ground-state cooling of a single neutral atom coupled to a high-bandwidth Fabry-Pérot cavity. The cooling process relies on degenerate Raman sideband transitions driven by dipole trap beams, which confine the atoms in three dimensions. We infer a one-dimensional motional ground-state population close to 90% by means of Raman spectroscopy. Moreover, lifetime measurements of a cavity-coupled atom exceeding 40 s imply three-dimensional cooling of the atomic motion, which makes this resource-efficient technique particularly interesting for cavity experiments with limited optical access.

DOI: [10.1103/PhysRevA.101.023415](https://doi.org/10.1103/PhysRevA.101.023415)

I. INTRODUCTION

Single atoms coupled to optical resonators are one of the most fundamental platforms in quantum optics and find applications in many tasks of quantum information science [1–5]. As a light-matter interface, they are a promising building block for long-distance quantum communication [6,7] because of their ability to provide single photons of controlled shape [2] and to store quantum information [8] encoded in single photons. Ultimately, the number of possible applications is rising with the resonator bandwidth: High-bandwidth cavities are, for example, needed to interact with the temporally short single-photon pulses emitted by quantum dots [9], which are also excellent sources of highly entangled photon pairs and thus potential building blocks in quantum repeater applications [10]. At the same time, a strong light-matter interaction—as required for the reversible transfer of quantum information—has to be maintained by employing ensembles of atoms and / or decreasing the cavity mode volume [11]. For the latter, fiber Fabry-Pérot cavities (FFPCs) are an attractive choice, since they also feature an intrinsic fiber coupling of the mode field [12,13]. For optimal light-matter coupling, the atom has to be confined within a fraction of the wavelength by cooling the atomic motion close to the oscillatory ground state. A standard technique in narrow-band cavities is *cavity cooling* [14,15]. Its steady-state temperature limit is $T_{\text{cav}} \approx \hbar\kappa/k_B$, where 2κ is the resonator bandwidth and k_B is the Boltzmann constant. Effective cavity cooling is therefore ineffective in the regime of high-bandwidth (i.e., open) resonators with 2κ much larger than the natural atomic linewidth 2γ . In such open-cavity experiments, the optical trap depth required for trapping atoms with high equilibrium temperatures of T_{cav} will be difficult to achieve.

Here, we report on an alternative cooling method based on *degenerate Raman sideband cooling* (dRSC), which was originally developed for the loss-free cooling of neutral atom gases at high densities [16,17]. We apply this method to three-dimensionally (3D) cool a single atom within the cavity

mode using only dipole trap beams, a weak repumping beam, and a tunable magnetic guiding field, which is a simple, resource-efficient configuration and especially beneficial for cavity experiments with limited optical access. By means of Raman spectroscopy and cavity-assisted state detection, we determine a one-dimensional (1D) ground-state population close to 90%.

II. EXPERIMENTAL SETUP

Our setup consists of a single ^{87}Rb atom trapped at the center of a high-bandwidth FFPC [18] with CQED parameters $(g, \kappa, \gamma) = 2\pi \times (80, 41, 3)$ MHz, where g is the single atom-cavity coupling strength. One of the fiber mirrors has a higher transmission, providing a single-sided cavity with a highly directional input-output channel [19]. The cavity is placed at the focus of four in-vacuum, aspheric lenses (NA = 0.5), which strongly focus two pairs of counter-propagating, red-detuned dipole trap (DT) beams at 860 nm [20] in the xy plane, as depicted in Fig. 1(a). They create a two-dimensional (2D) optical lattice, which enables atom trapping in the Lamb-Dicke regime [21]. One of the lattices acts as a conveyor belt [22] to transport single atoms from a magneto-optical trap (MOT) into the cavity. Confinement in the z direction is provided by the intracavity, blue-detuned lock laser field at 770 nm, which is additionally used for stabilizing the resonator length via the Pound-Drever-Hall method [23]. Hence, the atom is located with subwavelength precision at the nodes of the lock laser standing wave. These points coincide with the antinodes of a probe laser field, which is an odd number of free spectral ranges away [18]. The σ^- -polarized probe field and the cavity are resonant with the $|F = 2, m_F = -2\rangle \rightarrow |F' = 3, m_F = -3\rangle$ hyperfine transition of rubidium at 780 nm. As a consequence, the presence of an atom modifies the cavity-resonance frequency, which is detected as an increased reflection of probe light. A magnetic guiding field B of up to 1 G is applied along the cavity axis.

III. COOLING METHOD

In order to drive trap-induced, degenerate Raman transitions, the DT beams need to be able to address σ^\pm and π

*e.urunuela@iap.uni-bonn.de

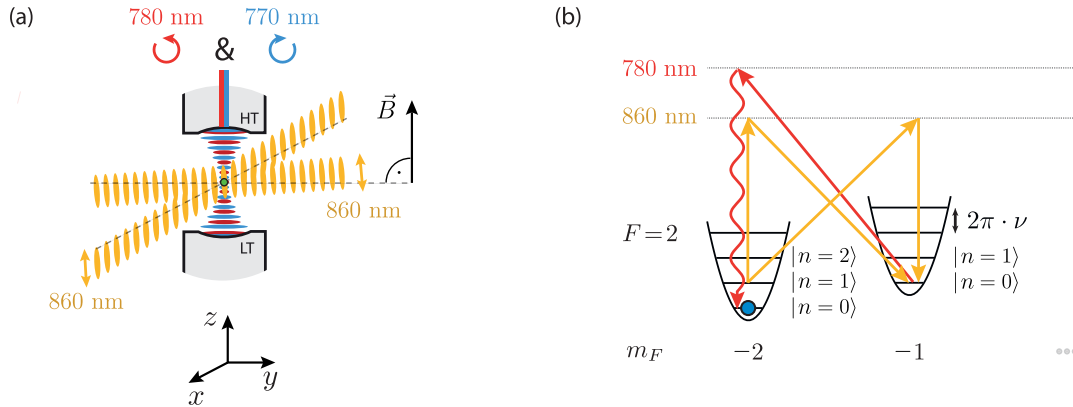


FIG. 1. (a) Optical fields involved in the degenerate Raman sideband cooling (dRSC) process. The 860-nm dipole trap beams have a slightly nonorthogonal angle with respect to the cavity axis, along which the magnetic guiding field \vec{B} is aligned. Two optical pumping beams enter along the dipole trap (not shown) and along the cavity axis, for the latter in the form of 780-nm probe light entering through the high-transmission (HT) mirror. The low-transmission (LT) mirror makes for a directional, single-sided cavity. A 770-nm lock laser is used to stabilize the resonator length via the Pound-Drever-Hall method. Its field creates an intracavity standing wave which traps the atoms along the z direction. (b) The schematic drawing shows the method of decreasing the quantized motional state $|n\rangle$ in an approximately harmonic trap potential with trap frequency ν . The red-detuned dipole traps can drive $\pi\text{-}\sigma^-$ and $\sigma^+\text{-}\pi$ Raman transitions. Additionally, since the 860-nm trap beams are not orthogonal to the cavity axis, they can couple to motional eigenstates in all directions. By optical pumping, the population in $F = 1$ (not shown) and $m_F \neq -2$ states is transferred back toward $|F, m_F\rangle = |2, -2\rangle$, such that Raman cooling will be constantly active if Eq. (1) is fulfilled.

transitions simultaneously, while the Zeeman splitting $\Delta\omega_B$ caused by the magnetic field B has to match an integer multiple n of the axial trap frequency ν [24]:

$$\Delta\omega_B = n2\pi\nu. \quad (1)$$

In previous implementations [16,17,25], the lattice consisted of three coplanar laser beams, two of which were linearly polarized in the lattice plane perpendicular to the quantization axis. The third one was elliptically polarized to enable Raman coupling. In our experiment, the different polarization components are generated by the geometric configuration of the dipole trap beams; see Fig. 1(a). The beams of $DT_{x,y}$ are slightly inclined with respect to the plane normal to the quantization axis (for $DT_x \leq 15^\circ$ and for $DT_y \sim 8^\circ$). Hence, the beams of the individual DTs (with linear polarization) are not purely π polarized and m_F -state-changing two-photon transitions are allowed.

In order to describe the Raman process, we express the internal hyperfine state $|F\rangle$ of the atom with its magnetic sublevel $|m_F\rangle$ and its excited vibrational state $|n\rangle$ as a set of discrete energy states $|F, m_F; n\rangle$. By the combined action of the probe light and a repumper resonant with the $|F = 1\rangle \rightarrow |F' = 2\rangle$ transition, the atom is optically pumped to the state $|2, -2; n\rangle$; see Fig. 1(b). The Raman processes are driven by $DT_{x,y}$ as $\pi\text{-}\sigma^-$ or $\sigma^+\text{-}\pi$ transitions $|2, -2; n\rangle \rightarrow |2, -1; n-1\rangle$, reducing the oscillatory quantum number n by one. As a result, the atomic population is cooled into the state $|2, -2; 0\rangle$, which is a dark state with respect to Raman transitions. Simultaneously, the presence of the atom is continuously interrogated by probe light. This allows to record the atom trapping lifetime τ in dependence of the Zeeman splitting $\Delta\omega_B$.

IV. RESULTS

In Fig. 2(a), long trapping times are observed whenever the absolute value of the magnetic field leads to a Zeeman level shift on the order of the trap frequency ν_x, ν_y or ν_z , which identifies degenerate Raman transitions. From a fit of two Gaussians, the values $\nu_x = \nu_y = (350 \pm 1)$ kHz and $\nu_z = (224 \pm 5)$ kHz are extracted. The width of the Gaussians indicate inhomogeneous broadening caused by different atom positions in the 3D trapping region. Considering the optical power in the beams and the beam diameters, we estimate upper limits for the trap frequencies of $\nu_x = \nu_y = 400$ kHz and $\nu_z = 280$ kHz, in agreement with the measurement.

In a next step, $\Delta\omega_B$ is fixed to $2\pi \times 350$ kHz, which constitutes the optimum value for cooling. Here, we investigate in more detail the survival probability for different cooling times. We find a $1/e$ lifetime of (42.9 ± 1.0) s by fitting the data with a stretched exponential [26,27] of the type:

$$e^{-(t/\tau)^k}, \quad (2)$$

with a lifetime τ and a stretching parameter $k = (0.8 \pm 0.1)$. While this function is a phenomenological approach, it represents the average decay for an ensemble of decay processes with a distribution of lifetimes τ_i , which depend on the inhomogeneous atom confinement in the dipole traps. In the absence of optical pumping (probe light) and thus dRSC, the average lifetime is only (1.0 ± 0.1) s due to heating processes induced by the cavity-resonant dipole trap. Here, a common problem is the transfer of relative frequency noise between cavity resonance and laser frequency into intracavity intensity fluctuations, causing additional parametric excitation of the atoms along the cavity axis [28,29].

To gain insight into the temperature of the atom in the critical z direction, we perform Raman spectroscopy using a

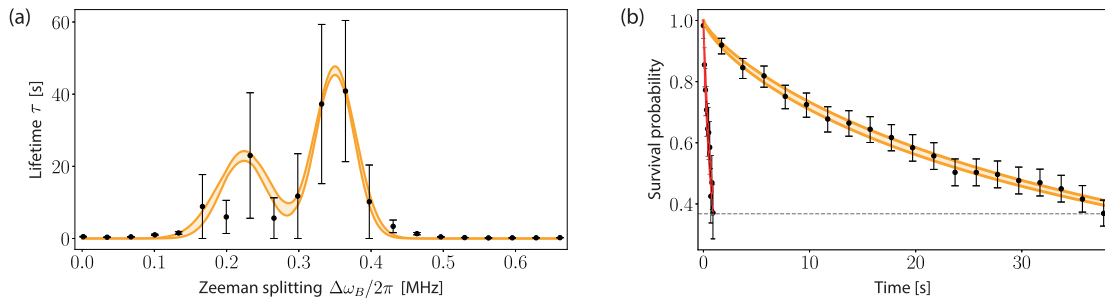


FIG. 2. (a) A measurement of the atom trapping time τ as a function of the Zeeman splitting $\Delta\omega_B$. A fit of two Gaussians (yellow line) indicates dRSC whenever the absolute value of the magnetic field leads to a Zeeman level shift close to the trap frequencies. Since each measurement takes 60 s, only a few trials per point are available. To accurately estimate the mean lifetime, we employ the bootstrapping method, resulting in a larger margin of error. (b) Measurements of the survival probability at a fixed magnetic field lead to drastically different lifetimes depending on whether optical pumping by probe light, and thus dRSC, is present (yellow line) or absent (red line). From stretched-exponential fits [see Eq. (2)], $1/e$ lifetimes (dashed, black line) of (42.9 ± 1.0) s and (1.0 ± 0.1) s are obtained, respectively.

second 770-nm laser which is phase locked to the previously introduced lock laser and enters the cavity as a running wave from the side. The Raman light has a tunable frequency offset δ around the hyperfine splitting of $+2\pi \times 6.834$ GHz. To record a spectrum, the atom is prepared in the state $|2, -2\rangle$ by dRSC and motional state-changing transitions are driven between the states $|2, -2\rangle$ and $|1, -1\rangle$ by a 200- μ s-long Raman pulse, which exceeds the coherence time. During the pulse, degenerate Raman transitions are prevented by an increased magnetic field. By a cavity-assisted, nondestructive readout of the hyperfine state, we measure the atomic population remaining in $|F = 2\rangle$ as a function of the two-photon detuning; see Fig. 3. The running-wave Raman beam is sent along y , with DT_y off, such that only odd-order sidebands along z are observed. They change the motional state by $\Delta n_z = \pm 1, \pm 3, \dots$, while the carrier transition is suppressed [30,31]. The noise peaks (“servo bumps”) of our Raman laser phase-locked loop appear as additional features at ± 1.3 MHz of any Raman transition, but they are mainly visible for the strong heating sideband. The depths of the dips depend on the technical details of the Rabi spectroscopy pulse and do not play a role in calculating the mean motional excitation number \bar{n}_i along the direction i . Assuming a thermal equilibrium, \bar{n}_i is given by the relation

$$\bar{n}_i = \frac{R_i}{1 - R_i},$$

where R_i is the ratio of the areas under the cooling and the heating sideband. Since in the presented spectra the sidebands overlap, we extract this ratio from a fit considering all expected sidebands. The resulting mean motional excitation along z is $\bar{n}_z = (0.13 \pm 0.03)$. This corresponds to a one-dimensional ground-state population $n_{0,z} = 1/(1 + \bar{n}_z)$ of $(88 \pm 3)\%$. To validate our interpretation of the Raman spectrum, we record a second spectrum with atoms at higher temperatures by introducing a 100-ms-long waiting time before each spectroscopy pulse during which the atoms heat up. As a consequence, the cooling sideband becomes clearly visible. In this case, the mean motional quantum number is $\bar{n}_z = (0.47 \pm 0.06)$.

V. CONCLUSION

We have applied a simple and robust method to cool a single atom inside a high-bandwidth resonator to its one-dimensional motional ground state. The long trapping lifetime of 40 s under continuous, nondestructive probing of the atom’s presence allows interesting applications such as determining the atomic position within the cavity by imaging the probe

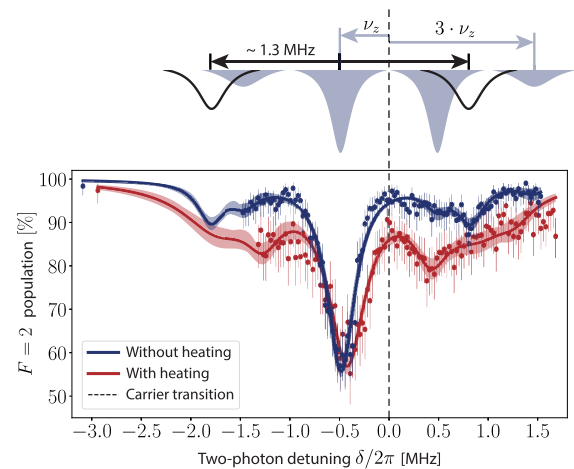


FIG. 3. Carrier-free Raman spectroscopy. The atomic population not transferred by the Raman pulse, i.e., remaining in $|F = 2\rangle$, is plotted vs the two-photon detuning from the hyperfine ground-state splitting. A schematic drawing of the expected sidebands ($\pm\nu_z, \pm 3\nu_z, \dots$) is shown above the measured Raman spectra. The “servo bumps” of the phase-locked loop between lock and Raman laser give rise to additional sidebands (black line in the schematic drawing above). For a Raman spectrum after dRSC (blue data points), a fit (blue line) yields a mean motional excitation along z of $\bar{n}_z = (0.13 \pm 0.03)$, which indicates that dRSC is capable of cooling the atoms to the motional ground state. In order to elucidate the cooling sideband, we measure a second Raman spectrum (red points) after the atoms were heated by a controlled, 100-ms-long interruption of dRSC. Now, with hotter atoms, a cooling sideband becomes visible on the right side of the suppressed carrier transition (black, dashed line).

light scattered into free space. Without cooling, the atom trapping lifetime in each 1D red dipole trap, i.e., *outside* the cavity region, is limited by optical phase-noise to only ≈ 15 s. Thus, the observation of a significantly longer lifetime *inside* the cavity region suggests that the atoms are cooled in three dimensions. A possible explanation could be cross-dimensional mixing [31] or the ability to address motional transitions along all dimensions by small tilting angles of the dipole traps driving Raman transitions. For the latter, these inhomogeneously broadened transitions (see Fig. 2) might then simultaneously address oscillations in different directions at slightly different trapping frequencies.

Since only weak optical pumping and a tunable magnetic bias field are required, the dRSC method has the potential to complement established techniques such as cavity cooling—even for narrow-band cavities, where cavity cooling works

well. Neutral atoms trapped in free space equally profit from this method.

It is worthwhile to point out that the tools used for Raman spectroscopy can directly be applied for carrier-free ground-state Raman cooling in three dimensions, if the Raman beam is sent diagonally in the xy plane. In our setup, this method will supersede dRSC as soon as the cooling conditions need to be (de)activated faster than the timescale on which the magnetic field can be changed.

ACKNOWLEDGMENTS

This work has been funded by the Deutsche Forschungsgemeinschaft (DFG, German Research Foundation) Project No. 277625399-TRR 185 and the Bundesministerium für Bildung und Forschung (BMBF), Verbundprojekt Q.Link.X.

-
- [1] M. Mücke, J. Bochmann, C. Hahn, A. Neuzner, C. Nölleke, A. Reiserer, G. Rempe, and S. Ritter, *Phys. Rev. A* **87**, 063805 (2013).
 - [2] P. B. R. Nisbet-Jones, J. Dilley, D. Ljunggren, and A. Kuhn, *New J. Phys.* **13**, 103036 (2011).
 - [3] W. Chen, K. M. Beck, R. Bucker, M. Gullans, M. D. Lukin, H. Tanji-Suzuki, and V. Vuletić, *Science* **341**, 768 (2013).
 - [4] A. Reiserer, N. Kalb, G. Rempe, and S. Ritter, *Nature (London)* **508**, 237 (2014).
 - [5] S. Ritter, C. Nölleke, C. Hahn, A. Reiserer, A. Neuzner, M. Uphoff, M. Mücke, E. Figueroa, J. Bochmann, and G. Rempe, *Nature (London)* **484**, 195 (2012).
 - [6] H.-J. Briegel, W. Dür, J. I. Cirac, and P. Zoller, *Phys. Rev. Lett.* **81**, 5932 (1998).
 - [7] L.-M. Duan, M. D. Lukin, J. I. Cirac, and P. Zoller, *Nature (London)* **414**, 413 (2001).
 - [8] M. Körber, O. Morin, S. Langenfeld, A. Neuzner, S. Ritter, and G. Rempe, *Nat. Photon.* **12**, 18 (2018).
 - [9] R. Keil, M. Zopf, Y. Chen, B. Höfer, J. Zhang, F. Ding, and O. G. Schmidt, *Nat. Commun.* **8**, 15501 (2017).
 - [10] M. Zopf, R. Keil, Y. Chen, J. Yang, D. Chen, F. Ding, and O. G. Schmidt, *Phys. Rev. Lett.* **123**, 160502 (2019).
 - [11] Y. Colombe, T. Steinmetz, G. Dubois, F. Linke, D. Hunger, and J. Reichel, *Nature (London)* **450**, 272 (2007).
 - [12] D. Hunger, T. Steinmetz, Y. Colombe, C. Deutsch, T. W. Hänsch, and J. Reichel, *New J. Phys.* **12**, 065038 (2010).
 - [13] T. E. Northup and R. Blatt, *Nat. Photon.* **8**, 356 (2014).
 - [14] P. Maunz, T. Puppe, I. Schuster, N. Syassen, P. Pinkse, and G. Rempe, *Nature (London)* **428**, 50 (2004).
 - [15] H. Ritsch, P. Domokos, F. Brennecke, and T. Esslinger, *Rev. Mod. Phys.* **85**, 553 (2013).
 - [16] S. E. Hamann, D. L. Haycock, G. Klose, P. H. Pax, I. H. Deutsch, and P. S. Jessen, *Phys. Rev. Lett.* **80**, 4149 (1998).
 - [17] V. Vuletić, C. Chin, A. J. Kerman, and S. Chu, *Phys. Rev. Lett.* **81**, 5768 (1998).
 - [18] J. Gallego, W. Alt, T. Macha, M. Martinez-Dorantes, D. Pandey, and D. Meschede, *Phys. Rev. Lett.* **121**, 173603 (2018).
 - [19] J. Gallego, S. Ghosh, S. K. Alavi, W. Alt, M. Martinez-Dorantes, D. Meschede, and L. Ratschbacher, *Appl. Phys. B* **122**, 47 (2016).
 - [20] M. Martinez-Dorantes, W. Alt, J. Gallego, S. Ghosh, L. Ratschbacher, Y. Völzke, and D. Meschede, *Phys. Rev. Lett.* **119**, 180503 (2017).
 - [21] D. Leibfried, R. Blatt, C. Monroe, and D. Wineland, *Rev. Mod. Phys.* **75**, 281 (2003).
 - [22] S. Kuhr, W. Alt, D. Schrader, M. Müller, V. Gomer, and D. Meschede, *Science* **293**, 278 (2001).
 - [23] E. D. Black, *Am. J. Phys.* **69**, 79 (2001).
 - [24] R. Grimm, M. Weidemüller, and Y. B. Ovchinnikov, *Adv. At. Mol. Opt. Phys.* **42**, 95 (2000).
 - [25] A. J. Kerman, V. Vuletić, C. Chin, and S. Chu, *Phys. Rev. Lett.* **84**, 439 (2000).
 - [26] G. Williams and D. C. Watts, *Trans. Faraday Soc.* **66**, 80 (1970).
 - [27] K. B. Lee, J. Siegel, S. Webb, S. Lévêque-Fort, M. Cole, R. Jones, K. Dowling, M. Lever, and P. French, *Biophys. J.* **81**, 1265 (2001).
 - [28] M. E. Gehm, K. M. O'Hara, T. A. Savard, and J. E. Thomas, *Phys. Rev. A* **58**, 3914 (1998).
 - [29] T. A. Savard, K. M. O'Hara, and J. E. Thomas, *Phys. Rev. A* **56**, R1095 (1997).
 - [30] R. Reimann, W. Alt, T. Macha, D. Meschede, N. Thau, S. Yoon, and L. Ratschbacher, *New J. Phys.* **16**, 113042 (2014).
 - [31] A. Neuzner, S. Dürr, M. Körber, S. Ritter, and G. Rempe, *Phys. Rev. A* **98**, 013401 (2018).

List of References

In the publication presented above (Ref. [1]), the bibliography follows an internal numbering. To include the corresponding entries in the global bibliography of this thesis, the following table gives the explicit link between the internal citation index of the paper, and the global citation index of the thesis.





- | | |
|--|--|
| [1] corresponds to Ref. [159] (p. 74). | [17] corresponds to Ref. [117] (pp. 74, 75). |
| [2] corresponds to Ref. [37] (p. 74). | [18] corresponds to Ref. [24] (p. 74). |
| [3] corresponds to Ref. [160] (p. 74). | [19] corresponds to Ref. [22] (p. 74). |
| [4] corresponds to Ref. [161] (p. 74). | [20] corresponds to Ref. [72] (p. 74). |
| [5] corresponds to Ref. [15] (p. 74). | [21] corresponds to Ref. [104] (p. 74). |
| [6] corresponds to Ref. [162] (p. 74). | [22] corresponds to Ref. [88] (p. 74). |
| [7] corresponds to Ref. [11] (p. 74). | [23] corresponds to Ref. [94] (p. 74). |
| [8] corresponds to Ref. [163] (p. 74). | [24] corresponds to Ref. [61] (p. 75). |
| [9] corresponds to Ref. [164] (p. 74). | [25] corresponds to Ref. [118] (p. 75). |
| [10] corresponds to Ref. [165] (p. 74). | [26] corresponds to Ref. [119] (p. 75). |
| [11] corresponds to Ref. [29] (p. 74). | [27] corresponds to Ref. [120] (p. 75). |
| [12] corresponds to Ref. [21] (p. 74). | [28] corresponds to Ref. [122] (p. 75). |
| [13] corresponds to Ref. [166] (p. 74). | [29] corresponds to Ref. [121] (p. 75). |
| [14] corresponds to Ref. [109] (p. 74). | [30] corresponds to Ref. [114] (p. 75). |
| [15] corresponds to Ref. [110] (p. 74). | [31] corresponds to Ref. [115] (p. 75). |
| [16] corresponds to Ref. [113] (pp. 74, 75). | |

Publication: Raman imaging of atoms inside a high–bandwidth cavity

This section contains a reprint of the publication in Ref. [2] and discussed in Chapter 4. It is included here with the agreement of all co-authors, and with the permission granted by the American Physical Society under Open Access terms (CC BY 4.0 license). The complete citation reads: E. Uruñuela, M. Ammenwerth, P. Malik, L. Ahlheit, H. Pfeifer, W. Alt and D. Meschede, *Raman imaging of atoms inside a high-bandwidth cavity*, (2022), Physical Review A **105**, 043321.

Contents of the publication:

| | | |
|------|--|----|
| B.1 | I. Introduction | 80 |
| B.2 | II. Experimental setup and methods | 81 |
| B.3 | III. Imaging with Raman cooling | 82 |
| B.4 | IV. Differential light shifts during continuous Raman sideband cooling | 83 |
| B.5 | V. Balancing cooling and heating dynamics with imaging parameters | 85 |
| B.6 | VI. Conclusion | 86 |
| B.7 | Appendix A: Linewidth-reduction prepares DBR laser for phase locking | 87 |
| B.8 | Appendix B: Three-dimensional continuous Raman sideband cooling with one free-space beam only and intracavity fields | 88 |
| B.9 | Appendix C: Justification and limitations of the two-level light-shifts model | 89 |
| B.10 | Appendix D: Dipole-force fluctuations and Monte Carlo simulation | 91 |
| | B.10.1 Scattering in dressed-state potentials | 92 |
| | B.10.2 Details of the Monte Carlo loop algorithm | 92 |

Raman imaging of atoms inside a high-bandwidth cavityE. Uruñuela ^{*}, M. Ammenwerth, P. Malik, L. Ahlheit , H. Pfeifer , W. Alt , and D. Meschede
Institute for Applied Physics, University of Bonn, Wegelerstr. 8, 53115 Bonn, Germany

(Received 17 February 2022; accepted 30 March 2022; published 29 April 2022)

High-bandwidth, fiber-based optical cavities are a promising building block for future quantum networks. They are used to resonantly couple stationary qubits such as single or multiple atoms with photons routing quantum information into a fiber network at high rates. In high-bandwidth cavities, standard fluorescence imaging on the atom-cavity resonance line for controlling atom positions is impaired since the Purcell effect strongly suppresses all-directional fluorescence. Here, we restore imaging of ^{87}Rb atoms strongly coupled to such a fiber Fabry-Pérot cavity by detecting the repumper fluorescence which is generated by continuous and three-dimensional Raman sideband cooling. We have carried out a detailed spectroscopic investigation of the repumper-induced differential light shifts affecting the Raman resonance, dependent on intensity and detuning. Our analysis identifies a compromise regime between imaging signal-to-noise ratio and survival rate, where physical insight into the role of dipole-force fluctuations in the heating dynamics of trapped atoms is gained.

DOI: [10.1103/PhysRevA.105.043321](https://doi.org/10.1103/PhysRevA.105.043321)**I. INTRODUCTION**

A major goal pursued in quantum communication science during the last decades has been to create quantum networks [1,2] that would allow us to distribute quantum information in an analogous way to classical information with the present internet [3,4]. In such proposed networks, flying qubits (i.e., photons) are excellent carriers of quantum information in fiber-based networks connecting quantum nodes capable of generating, processing, and storing quantum information in the form of stationary matter qubits [5]. It has been demonstrated [6–8] that optical cavities can enhance light-matter interaction to the level required for efficient interfacing of incoming and outgoing photonic information at the nodes of future quantum networks.

Much research effort is still invested in finding the best-suited physical platform for the nodes [9–11], having to fulfill challenging technical requirements to enable efficient and coherent exchange of quantum information between the photons and the matter counterpart. Several different physical platforms are considered for the realization of such nodes [12], of which atoms stored in and strongly coupled to optical cavities offer a good compromise of efficient light-matter interaction and long storage times of quantum information [13–16]. Hence, fiber-based optical cavities [17–19] coupling to atomic matter qubits make an attractive solution for directly routing quantum information via fiber links.

A promising regime of fiber-based Fabry-Pérot cavities (FFPCs) is to realize strong atom-field coupling g along with

a cavity of high-bandwidth κ [20], characterized by $g, \kappa \geq \gamma$ and $g \approx \kappa$, with γ the free space decay rate of the atom. The main breakthrough of such miniaturized cavities is that they allow for information flow at high rates of order κ , while still providing the necessary conditions for the strong-coupling regime with cooperativity $C = \frac{g^2}{2\kappa\gamma} \gg 1$. This unique feature of FFPCs is possible due to their small mode volume V that boosts the coupling strength $g \propto \frac{1}{\sqrt{V}}$. The single-sided configuration of Fig. 1(a) further positions FFPCs as an ideal platform for quantum nodes: the intrinsic fiber coupling to a single input-output channel enables convenient and efficient routing of photons carrying quantum information from and to the optical fiber, i.e., the quantum channel, mediated by the cavity-coupled atoms.

In recent years, important basic functionalities of quantum nodes have been demonstrated in proof-of-principle experiments, with a single atom (or few atoms) in FFPCs and in bulk cavities. These advances include highly efficient and deterministic single-photon sources [21,22], the storage and retrieval of a single photon into a single atom [23] even beyond the adiabatic regime [24], the bandwidth conversion of a single photon mediated by a single cavity-coupled atom [25], and recently prototypes for quantum memories and quantum repeaters [26].

The functionality of the atom-cavity system can be extended by increasing the number of atoms [27] to overcome the limit for the single-atom coupling strength (g is bounded by the smallest mode volume V technically achievable), by means of the Dicke enhancement with N identically coupled atoms, yielding $g_N \propto \sqrt{N}g$. The Dicke enhanced rate g_N [28–31] can boost the coherent photon-atom ensemble interaction to the level that Purcell effect can be tuned to match the bandwidths of very diverse quantum emitters, e.g., semiconductor quantum dots ($\gamma \approx 1$ GHz) and neutral atoms ($\gamma \approx 6$ MHz). Ensembles of atoms in cavities have also been envisaged as promising platforms for quantum simulators [32].

^{*}e.urunuela@iap.uni-bonn.de

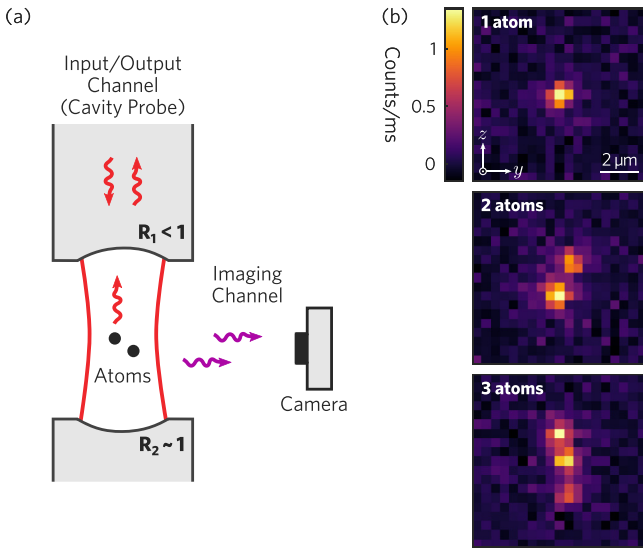


FIG. 1. (a) A fiber based, single-sided high-bandwidth optical cavity (reflectivities $R_1 < R_2 \simeq 1$) serves to efficiently interface atomic qubits with photonic quantum information routed on a fiber network. (b) Images of small atomic ensembles (1, 2, and 3 atoms) at the center of our high-bandwidth cavity registered with repumper fluorescence during continuous Raman sideband cooling in 3D (exposure time 1 s).

The necessary level of control for both single and multi-atom implementations requires optical tweezers or lattices for trapping, and motional control of the atoms [33–35]. The atom-cavity coupling strength is governed by the local field strengths and hence knowledge of the atoms positions within the cavity is essential for operating efficient protocols, e.g., for photon storage [30] or dissipative entanglement [36]. In the case of the FFPC setup shown in Fig. 1(a) this knowledge is extracted through a secondary imaging channel, independently of the primary fiber quantum channel. Fluorescence imaging, complemented by cooling measures to compensate scattering-induced heating and atom loss, has been established for long as the workhorse for positional detection of individual neutral atoms [37,38].

High-bandwidth cavities, however, are impairing the standard methods of both cooling and imaging since the strong Purcell effect causes almost all light emitted by the atoms at the cavity resonance line to be routed into the fiber channel, which amounts to suppressing fluorescence in the direction transverse to the cavity axis [20]. Also, the convenient cavity cooling technique [39] does not exist for $\kappa \gg \gamma$, it is switched off by the large cavity decay.

Alternative cooling schemes compatible with high-bandwidth cavities and restricted FFPC geometries have been established previously using Raman sideband cooling techniques [40,41]. Here we show that the detection of the repumper fluorescence (which is not subject to the Purcell effect) emitted during the Raman cooling cycles, provides enough intensity to allow imaging of the atoms trapped in a three-dimensional (3D) lattice superimposed on the cavity field.

The technique dubbed Raman imaging was pioneered by [42,43] and quickly adopted in the field of quantum gas

microscopes [44–46] as a powerful method for single-site resolved and loss-free imaging of dense atomic ensembles in optical lattices [35]. In our experiment, we customize this method to the FFPC setup in Fig. 1(a), where the restricted optical access renders coupling of one of the Raman beams and the repumper copropagating with the fiber quantum channel advantageous. The detrimental Purcell effect is avoided by choosing atomic transitions for the imaging channel with large detuning from the quantum channel (resonant with the cavity). This implementation allows us to obtain clear pictures of the trapped atoms with 1 s exposure time, as shown in Fig. 1(b), while simultaneously probing the atom-cavity coupling through the reserved quantum channel.

Combining the information obtained from both the imaging and the fiber quantum channel not only allows us to optimize the imaging scheme, but also to perform an in-depth analysis of the underlying physical effects. We study the repumper-induced differential light shifts that occur during Raman sideband cooling and analyze the complex parameter space governing both the scattering rate and the balance between cooling efficiency and heating rates. Our analysis provides useful parameter regions for a compromise between high survival rate and an acceptable imaging signal-to-noise ratio. Additionally, we gain physical insight into the underlying heating dynamics for atoms in optical lattices under near-resonant illumination, originating from dipole-force fluctuations [38,47]. For certain parameters we observe high heating rates which we discuss and validate with a semi-classical Monte Carlo simulation of scattering dynamics in dressed-state potentials.

II. EXPERIMENTAL SETUP AND METHODS

In our experiment, few ^{87}Rb atoms are trapped in a 3D lattice and strongly coupled to a high-bandwidth fiber Fabry-Pérot cavity (FFPC) with parameters $(g, \kappa, \gamma) = 2\pi \times (80, 41, 3)$ MHz [18,20]. A simplified diagram of the experimental setup is shown in Fig. 2(a).

To obtain a directional single-sided resonator, a mirror with high transmission (HT) is used at the input-output-channel side. A 780 nm cavity probe beam is coupled through this port to resonantly interrogate the atoms. The cavity is stabilized to a length that features a simultaneous resonance with the probe light at the D2 line of ^{87}Rb , and with 770 nm light forming a blue-detuned intracavity optical lattice (DT_z). In this configuration, trapping sites at intensity minima of DT_z coincide with intensity maxima of the probe standing wave at the cavity center, providing an atom-cavity interaction in the strong-coupling regime [20].

The atoms are trapped in a 3D lattice at the center of the cavity. In the xy plane, the lattice is formed by two near-orthogonal red-detuned 868 nm standing-wave dipole traps (DT_x and DT_y), and in the z axis by the blue-detuned 770 nm intracavity lattice (DT_z). With a depth of ≈ 0.5 mK in each direction this allows for trapping in the Lamb-Dicke regime [48], in a region defined by the waist of the beams $(w_x, w_y, w_z) = (13, 11, 5)$ μm . The lattice polarizations are defined as $(P_x, P_y, P_z) = (\pi, \pi, \sigma^+)$, with the quantization axis of our system set parallel to the cavity axis by applying a magnetic guiding field of ≈ 1.8 G. The dipole trap along the

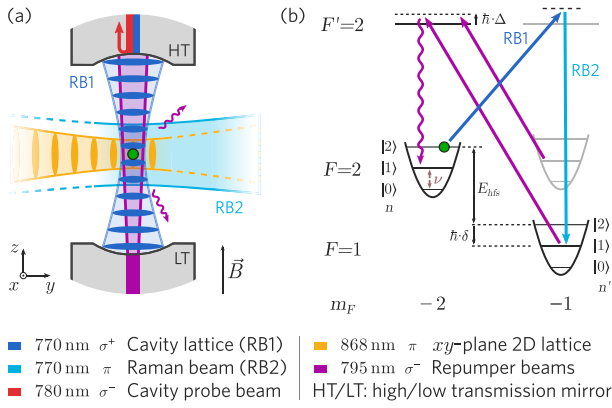


FIG. 2. Experimental setup and employed transitions for imaging of ^{87}Rb atoms inside a high-bandwidth cavity. (a) Atoms are confined in the xy plane by a red-detuned 2D lattice (x direction not shown), and along the cavity by a blue-detuned lattice. The 770 nm intracavity field also acts as a first Raman beam (RB1), and the second one (RB2) is overlapped with the y -axis lattice. The repumper beams induce scattering of photons on the D1 line that are collected to image the atoms onto an EMCCD camera. We probe the cavity on the D2 line to detect the presence and internal state of the atom. (b) Representation of the 1D cooling scheme. The frequency difference of RB1 and RB2 equals the Zeeman-shifted energy splitting between the involved hyperfine levels E_{hfs} , plus a two-photon detuning δ . To drive Raman transitions on the cooling sideband, δ is tuned to the near-harmonic trap frequency ν . To close the cooling cycle and obtain images with high SNR, the repumper beams are kept detuned from the D1 line by Δ .

y axis serves as an optical conveyor belt [49,50] to transport single atoms to the cavity center. The conveyor belt is loaded from a magneto-optical trap (MOT) 1 mm away.

For Raman cooling we use two-photon transitions that couple the internal and external degrees of freedom of the atom. The intracavity optical lattice DT_z also plays the role of the first Raman beam (RB1). The second 770 nm Raman beam (RB2) is phase locked to DT_z and copropagates along DT_y enabling momentum transfer on each cooling cycle. For long term frequency stability, the source for RB2 is a distributed Bragg reflector (DBR) laser. It is upgraded with an external optical feedback to reduce its linewidth and enable phase locking (see Appendix A). To achieve Raman coupling for all three lattice directions, the lattice beams $\text{DT}_{x,y}$ are not fully orthogonal to DT_z , but feature small angles with respect to the normal plane of the vertical lattice ($\theta_x \approx 15^\circ$ and $\theta_y \approx 6^\circ$). This geometry ensures that the difference of the Raman beam wave vectors has a projection along all lattice dimensions. With uninterrupted cooling we observe vacuum-limited trapping $1/e$ lifetimes of ≈ 1 min for single atoms in the lattice.

To close the cooling cycles we couple two σ^- -polarized 795 nm optical pumping beams through the lower transmission cavity mirror (LT). One of them is used to pump the atomic population from the lower to the higher hyperfine ground state, while the other is used to polarize the atoms in $m_F = -2$. For the rest of the paper we refer to them together as repumper beams (in plural), and in singular to the hyperfine-changing repumper alone. These beams also pro-

vide illumination light for fluorescence imaging of the atoms. They are tuned to the atomic D1 line, hence they provide an imaging channel that is fully independent from the cavity interaction on the D2 line, and thus insensitive to the Purcell effect.

To obtain information about the atoms inside the FFPC we use two schemes. First, a nondestructive cavity probe measurement determines the presence of an atom inside the cavity and its internal state. If an atom couples to the cavity mode, the induced vacuum-Rabi splitting increases the reflection signal of the cavity-resonant probe light, featuring a binary readout of the atom-cavity coupling state [20,51]. Second, fluorescence imaging provides knowledge on the number of atoms and their position within the cavity mode. For this, photons scattered by the atoms are collected with an in-vacuum high-NA lens along the x axis and recorded with an EMCCD camera. The combination of these two detection techniques allows us to extract complementary and independent information on the atom trapping lifetime and on the photon-scattering rate, respectively, which we use for the subsequent analysis.

III. IMAGING WITH RAMAN COOLING

Our imaging technique of atoms inside fast cavities is based on inducing scattering of photons with near-resonant illumination while keeping the atoms close to their motional ground state. This is achieved by applying resolved Raman sideband cooling in all three lattice dimensions, and simultaneous imaging of the photons scattered during the repumping transition onto the EMCCD camera.

To describe this cooling method, we consider the case of a single atom in a one-dimensional lattice in the Lamb-Dicke regime, as shown in Fig. 2(b). In the harmonic approximation for a cold atom at the bottom of the trap, the quantized motional energy levels are given as $E_n = \hbar\nu(n + 1/2)$, with $n = 0, 1, 2, \dots$, and $\nu/2\pi$ being the trap oscillation frequency. In the following, we use the notation $|F, m_F; n\rangle$ to represent the full atomic quantum state, with its ground-state $5^2S_{1/2}$ hyperfine level denoted by $|F\rangle$, its magnetic sublevel by $|m_F\rangle$ and its vibrational state by $|n\rangle$.

A cooling cycle starts with the atom optically pumped to the ground state $|2, -2; n\rangle$, by means of the repumper beams tuned to the D1 transitions between hyperfine F and F' levels $1 \rightarrow 2'$ and $2 \rightarrow 2'$ respectively. The Raman beams RB1 and RB2 are phase locked with a frequency difference corresponding to the energy splitting E_{hfs} between the outermost hyperfine levels $|2, -2\rangle$ and $|1, -1\rangle$ (Zeeman-shifted by -1.27 MHz), plus a two-photon detuning δ . We note that throughout the paper this detuning is referenced to the carrier transition without light shifts at $\delta = 0$. We tune the two-photon Raman resonance on the cooling sideband with $\delta = \nu$, thus driving the transition $|2, -2; n\rangle \rightarrow |1, -1; n-1\rangle$. A 5 THz single-photon detuning suppresses off-resonant scattering by the Raman beams. The repumper beams, detuned by Δ from the excited state $5^2P_{1/2} |2', -2\rangle$, pump the atom from the lower hyperfine state back to $|2, -2; n-1\rangle$ effectively reducing its oscillation energy by one quantum. This cycle continues until the ground state of the atomic motion, or until an equilibrium is reached of cooling vs heating processes, due to e.g., photon recoil during repumping.

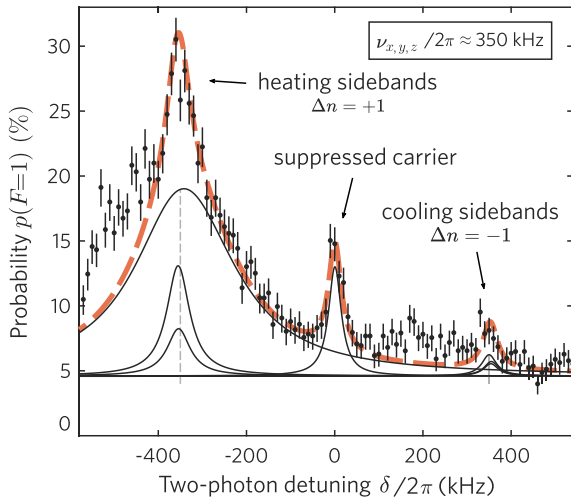


FIG. 3. Raman spectrum of a single atom in the 3D lattice after 5 ms of continuous Raman sideband cooling (cRSC), addressing the overlapped cooling sidebands with a single Raman-beam pair (see main text and Appendix B). The usage of the intracavity field as a Raman beam highly suppresses unwanted off-resonant carrier transitions [40,41]. We observe the cooling efficacy by a motional ground-state population $>85\%$ in each direction estimated from sideband imbalance, and by single-atom $1/e$ trapping lifetimes of ≈ 1 min.

To implement Raman sideband cooling in 3D, in contrast to addressing each lattice dimension with independent beams or with multitone pulses at the different sideband frequencies [42,44,52], we address the cooling transitions along all directions simultaneously with the single Raman-beam pair RB1 + RB2. For this, we tune the three trap frequencies to near-degeneracy at $\nu_{x,y,z}/2\pi \approx 350$ kHz (for more details see Appendix B), and we drive the overlapped cooling sidebands with the Raman two-photon detuning $\delta = \nu_{x,y,z}$.

A pulsed scheme to drive the cooling transitions, with alternating Raman and repumping pulses [45], is not applicable with the geometry of our beams, since the different directions feature distinct Lamb-Dicke parameters $(\eta_x, \eta_y, \eta_z) = (0.03, 0.09, 0.11)$. This entails mismatched Rabi frequencies on the different (but overlapped) cooling sidebands, and thus different π -pulse times for each direction, making the optimization difficult. For this reason we have opted for continuous Raman sideband cooling (cRSC), activating the Raman and repumper beams simultaneously with constant intensity during the entire cooling interval.

A Raman spectrum measured after optimization using a cRSC interval of 5 ms is displayed in Fig. 3. It shows a large imbalance of all cooling and heating sidebands which gives a clear signature of the high 3D cooling power, with an estimated residual temperature $T \approx 1.4 \mu\text{K}$ corresponding to $>85\%$ motional ground-state population in each direction (see Appendix B). Note that usage of the intracavity field as one of the Raman beams not only solves the problem of optical access, but also suppresses off-resonant coupling on the carrier transition [40,41].

We obtain fluorescence images of the atoms by collecting the 795 nm photons scattered during the repumping cycle of

cRSC, with an in-vacuum 0.5-NA lens, and recording them with the EMCCD camera (Andor iXon 3). The main properties of the imaging system are collection efficiency $\approx 4\%$, magnification $\times 35$, point spread function width $\approx 0.8 \mu\text{m}$ corresponding to 1.72 px on the CCD. The imaging fidelity is limited by background scattering from the cavity mirrors that cannot be fully suppressed from the field of view in our miniaturized FFPC setup. This sets a strong condition on employing low repumper intensity. To maintain a sufficiently high scattering rate, this requires the repumper to be near resonant. An optimal imaging signal-to-noise ratio (SNR) [37] is found for a two-photon Raman Rabi frequency (on the carrier) $\tilde{\Omega}_0/2\pi \approx 340$ kHz, a repumper blue detuning ≈ 3 MHz and a repumper intensity $\approx 0.057 I_{\text{sat}}$ (see Fig. 5). For such parameters we measure a scattering rate per atom of $\approx 2 \times 10^4$ photons/s which allows us to collect about 800 photons during a 1 s exposure time (atom survival probability $>90\%$). The fluorescence images shown in Fig. 1(b) have a SNR ≈ 13 , which is sufficient to count individual atoms and determine their position with full site resolution [37].

IV. DIFFERENTIAL LIGHT SHIFTS DURING CONTINUOUS RAMAN SIDEBAND COOLING

Successful imaging requires high photon-scattering rates in addition to efficient cooling. Both processes are affected by the detunings of involved lasers from atomic resonances, more precisely the Raman two-photon detuning δ and the repumper detuning Δ . Hence, good knowledge and control of the light shifts of the atomic levels during the imaging and cooling processes is essential.

For continuous Raman sideband cooling (cRSC), the sideband transition frequency needs to resonantly connect motional states with different quantum numbers (see Fig. 2). Therefore, we have to consider the light shifts induced by the repumper onto the ground-state hyperfine levels. In the following, we use the notation $|F, m_F\rangle$ for a ground state ($|F, m_F'\rangle$ for an excited state) introduced in Sec. III. The upper hyperfine state $|2, -2\rangle$ is an uncoupled dark state to the σ^- repumper, but the coupling to the lower hyperfine state $|1, -1\rangle$ results in a differential light shift δ_{LS} which modifies the resonance of the Raman transition. This shift grows when tuning the repumper close to resonance in order to increase the number of scattered photons for high imaging signal-to-noise ratios.

The frequency of the cooling sideband δ_c (Fig. 2) is therefore shifted by an amount δ_{LS} with respect to the position of the carrier in the absence of light shifts. Since the optimal detuning $\delta = \delta_c$ (resonant addressing) depends on the parameters of the repumper, the optimization of imaging and cooling has to be carried out in a coupled 3D parameter space of Raman detuning δ , repumper intensity I_{rep} , and repumper detuning Δ . To tackle this problem, we characterize the repumper-induced differential light shifts prior to the imaging optimization.

As a model for the differential light shifts δ_{LS} we use a simple driven two-level system. The ground-state $|1, -1\rangle$ is coupled to the excited state $|2, -2'\rangle$ by the repumper light field, at Rabi frequency Ω and with a detuning Δ . The system is described by a non-Hermitian Hamiltonian, with energy

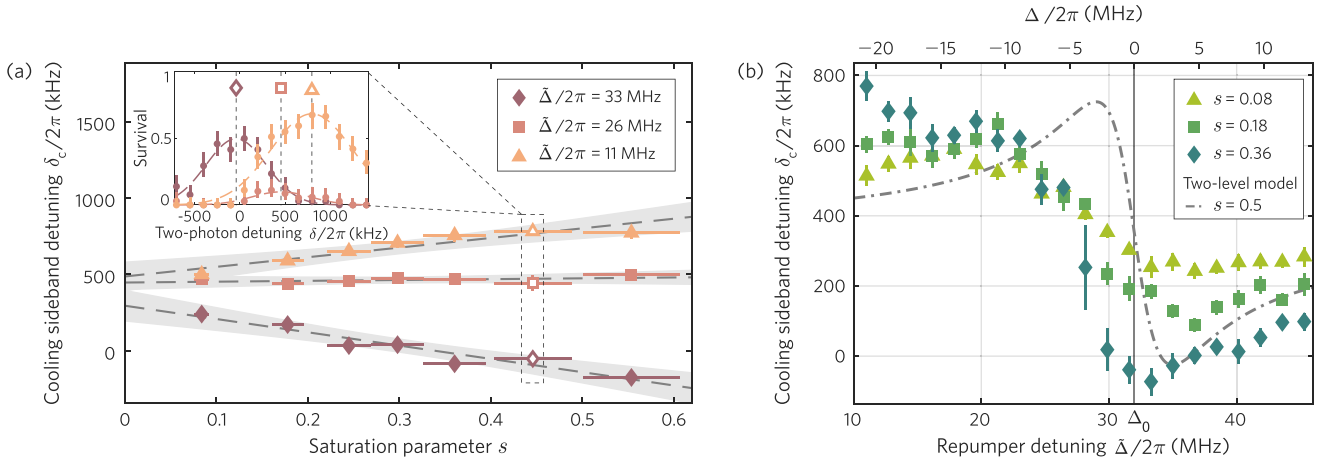


FIG. 4. Differential light shifts (i.e., cooling sideband detuning $\delta_c = \delta_{LS} + \nu$) induced by the near-resonant repumper beams on the hyperfine ground states of ^{87}Rb . (a) Dependence on repumper saturation parameter $s = I_{\text{rep}}/I_{\text{sat}}$ for selected detunings $\tilde{\Delta}$ shows linear scaling. Inset shows, for each set of parameters $\{s, \tilde{\Delta}\}$, the value of δ_c is the Gaussian fit center of the survival probability vs two-photon detuning δ . (b) Dispersive-shaped light shifts dependence on the repumper detuning for selected s values. The dash-dotted curve shows the model Eq. (1) for $s = 0.5$, inflecting at the trap-shifted resonance $\tilde{\Delta} = \Delta_0$. All error bars represent 68% confidence intervals.

eigenvalues \mathcal{E} and light shifts $\delta_{LS} = \mathcal{E}/\hbar$ given to first order in the saturation parameter $s = 2(\Omega/2\gamma)^2 = I_{\text{rep}}/I_{\text{sat}}$ by

$$\delta_{LS} \approx \frac{\Delta}{2} \frac{\gamma^2}{\Delta^2 + \gamma^2} s + O(s^2). \quad (1)$$

In the low-power limit ($s \ll 1$) or the large-detuning limit ($\Delta \gg \gamma$) the induced light shift δ_{LS} scales linearly with intensity and follows a dispersive Lorentzian dependence on the detuning. Details on this calculation are given in Appendix C.

We calibrate the saturation parameter $s = I_{\text{rep}}/I_{\text{sat}}$ by monitoring saturation of the optical pumping rates between hyperfine ground states for a single atom as a function of the intensity I_{rep} . The repumper detuning with respect to free space also includes the AC-Stark shift induced by the dipole traps on the D1 transition. We define the total detuning with respect to the free-space resonance as $\tilde{\Delta} = \Delta + \Delta_0$, with Δ the detuning from the trap-shifted resonance (used in the model) and Δ_0 the dipole-trap induced light shift. For a trapped atom at the bottom of the lattice potential, the resonance condition is met for $\tilde{\Delta} = \Delta_0$, with the shift $\Delta_0/2\pi = 32(3)\text{MHz}$ calibrated independently with respect to a spectroscopy cell reference.

We measure the differential light shift by detecting the displacement of the cooling sideband as a function of the saturation parameter in Fig. 4(a) and of the repumper detuning in (b). We load a single atom into the resonator, precool it with degenerate Raman sideband cooling (dRSC) [53] to reach the Lamb-Dicke regime, pump it to the state $|2, -2\rangle$, and then cool it with cRSC for a fixed time. We use the fiber quantum channel to probe the presence or absence of the atom inside the resonator, before and after the cooling slot. This measurement is repeated multiple times with different sets of parameters $\{\delta, s, \tilde{\Delta}\}$ to map the survival probability to the parameter space for cRSC. For each set of repumper parameters $\{s, \tilde{\Delta}\}$, the light-shifted sideband frequency $\delta_c = \delta_{LS} + \nu$ is found as the value of δ maximizing the survival

probability [inset of Fig. 4(a)], thus matching the Raman resonance condition $\delta = \delta_c$ which provides the most efficient cooling. In Fig. 4(a) we show selected scans of the measured parameter map $\delta_c(s, \tilde{\Delta})$, featuring the detuning δ_c for three illustrative values of $\tilde{\Delta}$, as a function of the repumper saturation parameter s , documenting the expected linear dependence on the repumper intensity, with the slope determined by the detuning. We observe that the repumper detuning at which the differential light shift becomes zero for all intensities occurs at $\tilde{\Delta}/2\pi \approx 28$ MHz, showing a small offset to the red with respect to the trap-shifted resonance calibrated independently.

In Fig. 4(b) we have plotted the measurements of δ_c as function of the repumper detuning $\tilde{\Delta} = \Delta + \Delta_0$, for three selected values of s showing dispersive curves with inflection points near resonance, at $\Delta/2\pi \approx -4$ MHz and $\tilde{\Delta}/2\pi \approx 28$ MHz [in agreement with the zero-shift line in Fig. 4(a)]. For comparison we show the two-level model Eq. (1) for $s = 0.5$. According to the model, the strongest differential light shifts ($\delta_{LS} = \delta_c - \nu$) are expected for repumper detunings of $\Delta = \pm\gamma$, and the inflection point at resonance $\Delta = 0$ (or $\tilde{\Delta} = \Delta_0$).

The dispersive shape of the measured differential shift δ_c is expected but deviates from the simple model of Eq. (1). The deviation may be traced to several influences: (1) The spatial distribution of atoms results in interactions with a range of laser beam intensities both in the optical traps, the Raman beams and the very narrow intracavity repumper beam which lead to a smoothing of the observed dispersive curve compared with the sharp model curve. (2) The technically challenging calibration of repumper intensity can underestimate the s parameter, leading to higher amplitudes than expected from Eq. (1). (3) The data show stronger shifts for blue repumper detunings ($\tilde{\Delta} > \Delta_0$) than for red ($\tilde{\Delta} < \Delta_0$), and the zero-shift condition at a smaller detuning than expected. We attribute these observations to detuning-dependent heating rates causing extended oscillations of the atoms in the trapping potential [38], analyzed further in Sec. V.

V. BALANCING COOLING AND HEATING DYNAMICS WITH IMAGING PARAMETERS

The optimization of fluorescence imaging of atoms inside the resonator necessarily requires a trade-off of two competing processes in this imaging technique: (1) photon scattering that causes heating of the atom, and (2) Raman sideband cooling that counteracts the heating effect. As discussed in Sec. III [see also Fig. 2(b)], the working principle of Raman sideband cooling relies on pumping the atom to the motional ground state (in full notation $|2, -2; 0\rangle$), which is a dark state decoupled both from the Raman and the repumping light. On the other hand, continuous scattering of photons is required for imaging during the camera exposure time. Therefore, the atoms have to be heated out of the dark state but still kept close to the motional ground state for small atom loss. In Ref. [42] parametric heating was used for this purpose, however in our case the intracavity lattice noise is sufficient to drive the atoms out of the ground state.

For optimal imaging with continuous Raman sideband cooling, we find that the balance of heating-cooling rates and scattering can be tuned with the parameters of the repumper light. We have explored its effect on the heating-cooling trade-off and photon-scattering rate, and optimize for a high SNR. The complexity of the parameter space is reduced by keeping the Raman two-photon cooling sideband on resonance using the differential light shifts measurements during cRSC, analyzed in Sec. IV. Then, we simultaneously measure the imaging fluorescence intensity and the atom survival probability as a function of the repumper detuning and intensity.

For the corresponding measurements we use an experimental sequence similar to the light shifts measurements in Sec. IV: we begin with loading a single atom into the 3D lattice at the FFPC center, dRSC precooling, and initializing in the state $|2, -2\rangle$. Then, a first cavity-based atom detection is applied to probe the presence of an atom, followed by an EMCCD image acquisition under cRSC with 1 s exposure, at the end a second cavity detection is performed to verify the survival of the atom in the trap.

The fluorescence signal is obtained by integrating the EMCCD counts over a 33×33 pixels large image region corresponding to a $15 \times 15\text{-}\mu\text{m}^2$ -large area at the center of the cavity. Reduced fluorescence due to atom loss is excluded by selecting the images based on successful presence and survival detections. Also, images with more than one atom are discarded by postprocessing with an atom detection algorithm. To quantify the balance of heating-cooling rates we take as a figure of merit the probability of a successful survival cavity-based detection conditioned on a prior successful presence detection before the imaging interval.

The results for fluorescence intensity and imaging survival probability are shown as two-dimensional (2D) color maps in Fig. 5(a), where cross sections for selected s values are given in Fig. 5(b). The combined information of fluorescence and survival maps (upper and lower panel, respectively) permits to identify a region favorable for imaging with $\text{SNR} \approx 13$, of high fluorescence ($\approx 2 \times 10^4$ photons/s) and high survival ($>90\%$), at parameters $\tilde{\Delta}/2\pi \approx 35$ MHz and $s \approx 0.057$. These parameters were used to capture the images in Fig. 1(b) with one, two, and three atoms.

Qualitatively the behavior of the fluorescence intensity [purple slices in Fig. 5(b)] exhibits a symmetric Lorentzian-like function as expected for a resonant spectrum with amplitude increasing with repumper intensity. We attribute a small ≈ 3 MHz blueshift of the Lorentzian center from the trap-shifted resonance to residual effects of atom loss for the cases of undetected more-than-one atom images.

The imaging survival map [Fig. 5(a) lower panel and green slices in Fig. 5(b)] shows an unexpected behavior. If considering only scattering-induced heating, we would expect the lowest survival rate on resonance, with the dip becoming deeper and broader for higher intensities. This is indeed the case at low intensities, i.e., for $s < 0.02$. However, for higher intensities the survival dip experiences a clear shift towards red detunings with a linear dependence on the intensity. This results in an asymmetric V shape of the imaging survival map with higher survival probabilities on the blue detuning side than on the red. The model of the atom motion inside the trap for finite temperature introduced in Sec. IV predicts a constant redshift, but not a power-dependent shift. The observed asymmetric behavior indicates heating rates induced by the repumper beams that depend both on their detuning and intensity.

During the scattering cycles induced by the repumper field, the atoms undergo rapid transitions between ground state and excited state, which are associated with trapping and antitrapping potentials, respectively. For our 868 nm lattice the estimated polarizability ratio of the ^{87}Rb excited state $5^2P_{1/2}$ over the ground state $5^2S_{1/2}$ is $\chi \approx -0.59$ [54]. We therefore attribute this asymmetry to dipole-force fluctuations (DFFs) [38,47].

To gain insight into the effect of DFFs in our measurements, we set up a one-dimensional semiclassical Monte Carlo simulation of the scattering process of an atom trapped in a lattice potential under near-resonant illumination, based on Ref. [38]. The simulation combines the classical motion of an atom in the dressed-state potentials, with the position-dependent transition rates between dressed states and the corresponding probabilities of scattering events. For an ensemble of atoms with a set of repumper parameters, it calculates the time-dependent photon emission rate and the increase of mean kinetic energy. From the time evolution of these values we extract the mean scattering rate and the exponential loss rate of atoms escaping from the trap. More details on the theory of DFFs and on the Monte Carlo simulation are presented in Appendix D.

In Fig. 5(c) we show the simulated 2D maps of atom loss rates and photon-scattering rates as a function of repumper detuning and intensity. A qualitative comparison with the results of the measurement in Fig. 5(a) shows the striking similarities between the simulated loss rates and the measured survival probabilities. Moreover, the map of photon scattering is in good agreement with the detected fluorescence. Our model supports DFFs as the main effect governing the heating dynamics that lead to the observed asymmetric survival rates. For a compromise of high fluorescence and at the same time high survival probability with the repumper close to resonance, a red detuning should be avoided, while a blue detuning can prevent DFFs-induced heating. This holds for the cases where the AC-Stark shift induced by dipole traps increases

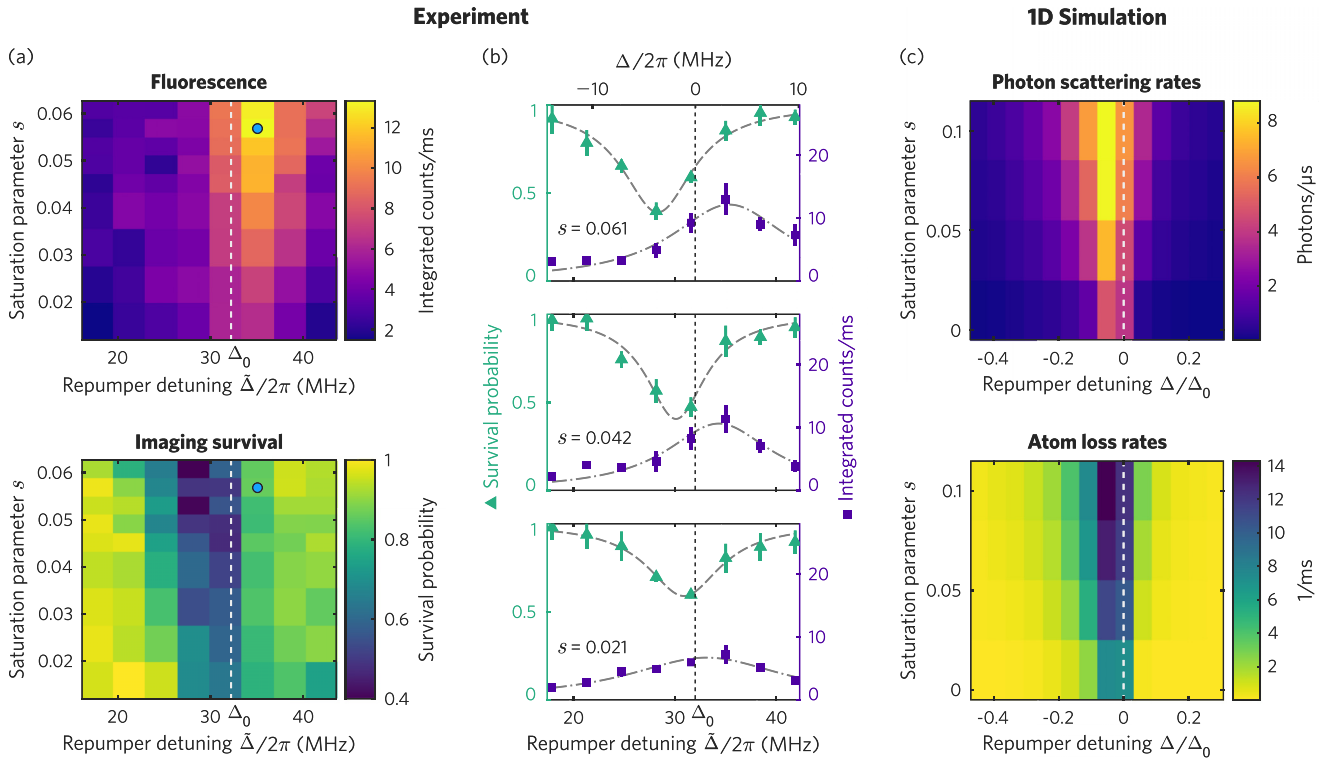


FIG. 5. Balancing cooling-heating rates and fluorescence for imaging with cRSC. (a) Measured mean fluorescence per atom and survival probability for 1 s of cRSC as function of repumper detuning $\tilde{\Delta}$ and repumper saturation parameter $s = I_{\text{rep}}/I_{\text{sat}}$. The Raman addressing is kept resonant on the cooling sideband by compensating the differential light shifts induced by the repumper beam. The blue marker shows the optimum parameters at which the atom pictures in Fig. 1 were taken with $\text{SNR} \approx 13$. (b) Cross sections of the fluorescence and survival maps versus detuning for selected intensities, shown with fitted Lorentz functions as a guide to the eye. The minimum in survival shifts towards red repumper detunings for an increase in intensity, contrary to the fluorescence peak that remains fixed close to resonance. We attribute the asymmetry of the survival behavior to DFFs-induced heating. (c) Photon-scattering rates and atom loss rates computed with a one-dimensional (1D) semiclassical Monte Carlo simulation of scattering in dressed-state potentials. The asymmetric shape of the atom loss rates validates DFFs as the source of heating in the measurement.

the energy of the atomic transition. Such parameter-dependent heating rates also offer an explanation for the asymmetric deformation of the light-shifts measurements previously shown in Fig. 4(b).

VI. CONCLUSION

In summary, we have shown that imaging of single atoms trapped inside a high-bandwidth FFPC can be successfully implemented, despite the strong Purcell effect. Note that the fluorescence suppression by the Purcell effect is closely related to the observation of a glowing laser medium being visually dimmed when the laser mode ignites. Our experimental realization takes advantage of our continuous Raman cooling scheme by using the scattered repumper photons, which are not resonant with the cavity. Our imaging technique requires only a single free-space beam together with intracavity fields, making it ideal for situations with limited optical access, e.g., in miniaturization trends in quantum technologies.

The signal-to-noise ratio in our experiment is limited by background scattering from the cavity mirrors. In contrast to other experiments relying on large detunings [38,44], this enforces low power intensities and small detunings to obtain a high SNR. Here, we have demonstrated an imaging SNR

of 13 based on a compromise between photon-scattering rate and three-dimensional sideband cooling efficiency. During the imaging process more than 85% of the population remains in the motional ground state per direction, sufficient for high fidelity detection of single atoms in the optical lattice. The optimization of the relevant parameters was enabled by a detailed spectroscopic investigation during cRSC. This also shed light onto deviations from the expected light shifts, revealing a parameter-dependent heating mechanism that we attributed to dipole-force fluctuations impairing the atom survival at red detunings, but avoided at blue detunings. This was further validated by a Monte Carlo simulation of the atom's scattering dynamics in the position-dependent dressed-state potentials. The observed DFFs heating effect is not limited to our particular FFPC setup with cRSC. On the contrary, it is expected to be a relevant effect in most experiments involving near-resonant illumination of atoms trapped in a lattice, depending on the polarizabilities of the states involved.

While global positioning of the atomic ensemble is controlled with our optical conveyor belt, the imaging technique shown in this work represents an important step towards ultimate position control and manipulation of single atoms in miniature optical cavities. It enables to determine the number and position of the atoms within the resonator in a

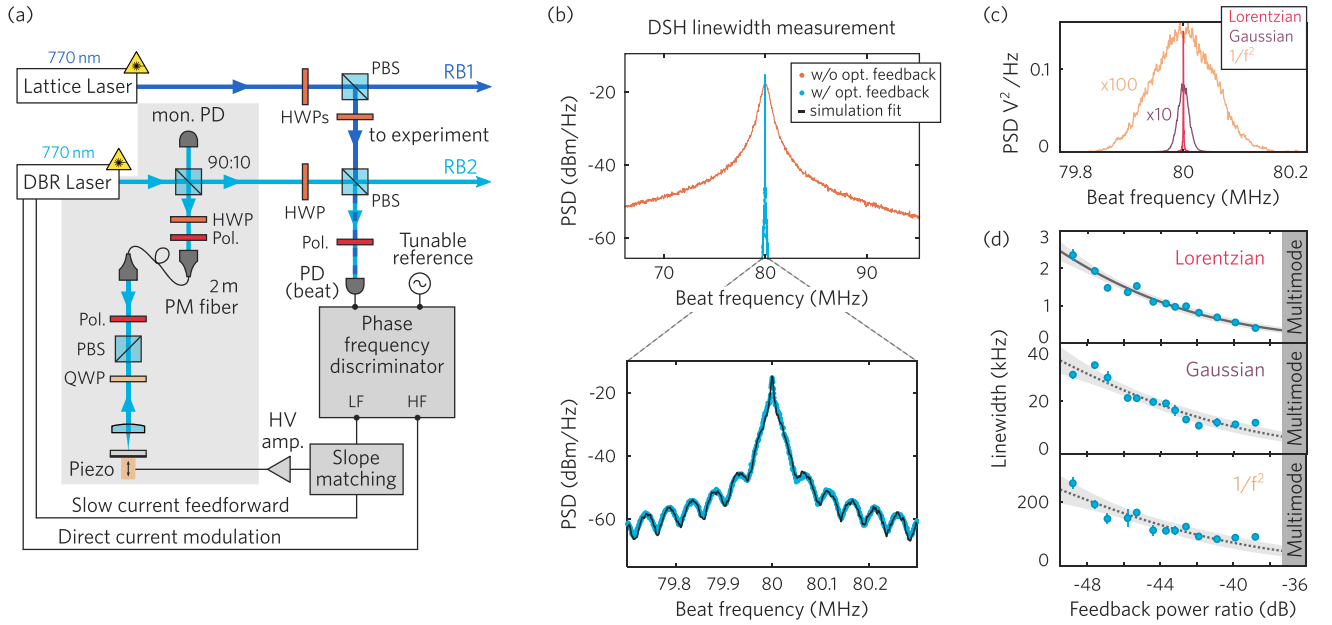


FIG. 6. (a) Experimental setup for linewidth reduction of the DBR laser RB2 and phase locking to the lattice laser RB1. (b) Delayed self heterodyne (DSH) spectrum of the DBR laser with and without optical feedback (feedback power ratio of -40 dB). A linewidth reduction in two orders of magnitude can be observed when the laser is subject to optical feedback (blue curve). Lower panel: close-up of the DSH spectrum and simulation based fitting to extract linewidth components. (c) Pure lineshapes corresponding to the three laser frequency-noise components, namely white (Lorentzian), flicker (Gaussian) and random-walk frequency noise ($1/f^2$) extracted with the simulation-based fitting routine. (d) Estimated linewidth corresponding to each frequency-noise component as a function of the feedback power ratio.

nondestructive manner, and paves the way for creating atomic arrays with predefined number and positions in the cavity. This can be implemented in the experiment by integrating single-atom addressing optical tweezers controlled by a spatial light modulator.

ACKNOWLEDGMENTS

This work has been funded by the Deutsche Forschungsgemeinschaft (DFG, German Research Foundation) with Project No. 277625399-TRR 185 *OSCAR*, under Germany's Excellence Strategy - Cluster of Excellence Matter and Light for Quantum Computing (ML4Q) EXC 2004/1 - 390534769, as well as by the Bundesministerium für Bildung und Forschung (BMBF), project FaResQ. We thank T. Macha, D. Pandey, and M. Martinez-Dorantes for insightful discussions and technical support in the early stage of the presented work.

APPENDIX A: LINEWIDTH-REDUCTION PREPARES DBR LASER FOR PHASE LOCKING

The two-photon Raman cooling transitions are driven in our setup by the 770 nm lasers RB1 and RB2 in Fig. 2(b) with frequency difference ≈ 6.8 GHz. The primary RB1 laser field is drawn from an interference filter stabilized diode laser [55] with rms-linewidth of order few kHz. It is injected into the FFPC and serves not only as a blue-detuned optical lattice for atom trapping but also to simultaneously stabilize the cavity length at the atomic resonance line at 780 nm. For this purpose its wavelength is referenced to an optical frequency comb.

To obtain sufficiently high resolution for driving coherent Raman transitions between hyperfine levels, the secondary 770 nm Raman beam (RB2) is phase locked to RB1. We have chosen a distributed Bragg reflector (DBR) laser which offers convenient and mode hop free tuning over several GHz, and good long term frequency stability. The drawback of DBR components, however, is a generally large Schawlow-Townes-Henry linewidth [56] of order a few hundred kHz, too broad for realizing sufficient feedback bandwidth for phase locking. It is known that external optical feedback can help to reduce the DBR linewidth [57], a road we have followed here.

We outline the application of optical feedback from a 2-m-long external feedback path to reduce the linewidth of a DBR laser diode based on the work in Ref. [58]. We use a delayed self-heterodyne (DSH) linewidth measurement and a simulation-based fitting routine [59] to analyze and estimate all the linewidth components under the influence of varying optical feedback strengths. A current feed-forward was implemented to achieve mode-hop-free tuning of the laser frequency over the free spectral ranges of the external cavity. With that, continuous tuning of up to 2 GHz was achieved. Furthermore, we present the phase locking setup for Raman sideband cooling in our experiment in Fig. 6(a).

To reduce the Lorentzian linewidth of the 770 nm DBR laser, an external optical feedback path is implemented [highlighted in gray in Fig. 6(a)]. Approximately 4% of the emitted laser light reflected at the 90:10 beam splitter (BS) is coupled into a 2-m-long polarization maintaining (PM) fiber. From the fiber output, the laser light passes a quarter-wave plate (QWP), a polarizing beam splitter (PBS), and a polarizer (Pol.) and is focused on a mirror mounted on a piezo using a lens in a

cat's eye configuration. The light reflected at the mirror is then coupled back into the fiber and fed into the laser diode. The polarization optical elements are used to adjust the feedback power. The monitor photodiode (mon. PD) placed at the free arm of the 90:10 BS is used to monitor the feedback power. At a fixed external feedback path length of 2 m, the feedback power ratio (ratio of the power entering back into the DBR laser to emitted power) can be varied from -50 dB to -30 dB.

To measure the linewidth of the laser subject to varying optical feedback levels, we use a DSH method first described in Ref. [60]. It consists of a Mach-Zehnder-type interferometer, where the light passing one of the arms is frequency shifted by $\delta_f = 80$ MHz and the other passing a 4.9 km optical fiber delay. The spectrum of the beat signal of the recombined arms is analyzed. Figure 6(b) shows a DSH spectrum with and without the optical feedback. When the laser is not subject to optical feedback [orange curve in top panel of Fig. 6(b)], the DSH spectrum is a broad Gaussian curve with an estimated linewidth of ≈ 700 kHz. With optical feedback, the width of the DSH spectrum reduces by at least two orders of magnitude [blue curve, top panel of Fig. 6(b) and close-up view in lower panel]. The spectrum shows a Lorentzian at the modulation frequency with periodic ripples on the wings indicating the residual coherence between the interferometer arms.

To extract the different linewidth components from the spectrum, we use a simulation-based fitting routine based on Ref. [59]. It emulates the experimentally recorded spectra by simulating the photodiode signal with numerically generated phase noise contributions. The phase noise signal $\phi(t)$ is generated by the superposition of a white $\phi_w(t)$, flicker $\phi_f(t)$ and random-walk frequency noise $\phi_r(t)$ source with \mathcal{A}_w , \mathcal{A}_f , and \mathcal{A}_r as the amplitudes of the corresponding noise sources:

$$\phi(t) = \mathcal{A}_w \phi_w(t) + \mathcal{A}_f \phi_f(t) + \mathcal{A}_r \phi_r(t). \quad (\text{A1})$$

The power spectral density (PSD) of the heterodyne signal is calculated and the noise amplitudes are adjusted to fit the numerically simulated spectrum to the experimental data using a Nelder-Mead simplex optimization. Figure 6(c) shows exemplary simulated spectra of the different noise components. Our code for the simulation-based linewidth measurement is openly available in the repository [61].

Once the noise parameters are found, the Lorentzian linewidth $\delta\nu$ of the laser is estimated by fitting the PSD of white phase noise by $\mathcal{S}_w(f) = \frac{\delta\nu}{\pi f^2}$. The fitted Lorentzian linewidth of the laser as a function of the feedback power ratio is shown in the top panel of Fig. 6(d). Lorentzian linewidths as low as 500 Hz are reached with optical feedback ratio close to -36 dB. With larger feedback powers the laser becomes multimode as also observed in Ref. [58]. The simulation based fitting also allows us to extract weak components of higher-order frequency noise. Here, we include flicker noise ($1/f$), which results in a Gaussian lineshape, and frequency random-walk noise ($1/f^2$). The retrieved linewidth for both with respect to feedback power is presented in the lower two panels of Fig. 6(d).

For the experiment we fixed the feedback ratio at -43 dB, where the Lorentzian linewidth is sufficiently low for our purposes. The flicker and the random-walk noise are suppressed using a fast phase lock, with the setup shown in Fig. 6(a).

The two lasers are combined on a polarizing beam splitter (PBS) and the corresponding beat signal is detected on a photodiode (PD beat). A phase frequency discriminator (PFD) is used to compare the beat signal of the linewidth-reduced DBR laser and RB1 to a tunable stable reference to quantify frequency and phase deviations. The low-frequency (LF) and the high-frequency (HF) error signals are further processed to phase lock the two lasers. The HF error signal is used to compensate for the fast phase fluctuations. Its corresponding feedback is directly applied to the laser diode current via a loop filter. The LF error signal is used to correct for slow frequency drifts (order of kHz). Its corresponding feedback signal is applied to the piezo of the mirror at the end of the external feedback path after being amplified by a high-voltage amplifier. As the external feedback path has a corresponding free spectral range of 56 MHz, the frequency tunability is regained by a current feed-forward. Currently, the mode-hop free tuning range of up to 2 GHz is limited by the maximum stroke of the piezo of the external feedback mirror.

APPENDIX B: THREE-DIMENSIONAL CONTINUOUS RAMAN SIDEBAND COOLING WITH ONE FREE-SPACE BEAM ONLY AND INTRACAVITY FIELDS

In Sec. III we summarized our continuous Raman sideband cooling (cRSC) scheme focusing on the 1D case. Here we explain in detail how we extend this scheme to cool with respect to all directions of our 3D lattice, with only a single free-space beam (RB2) and the remaining beams as intracavity fields (RB1 and repumpers). For details on the setup see Fig. 2. To drive the cooling transitions corresponding to all lattice dimensions simultaneously, the key point is to bring the relevant motional oscillator frequencies close to degeneracy in all three directions.

We evaluate Raman spectra of single atoms trapped in our cavity in order to identify the different heating and cooling sidebands. A single atom is loaded into the cavity, precooled with degenerate Raman sideband cooling (dRSC) [53], and prepared into $|2, -2\rangle$. Next, a $500 \mu\text{s}$ Raman pulse with variable two-photon detuning δ drives Rabi oscillations between the states $|2, -2\rangle$ and $|1, -1\rangle$, after which the state of the atom is probed by means of nondestructive cavity probing [20]. Within the trapping lifetime of about one minute, the same atom can be re-initialized, cooled, and recycled by applying 5 ms of cRSC at $\delta/2\pi = 350$ kHz before the spectroscopy pulse, for up to 600 measurement cycles with different δ values. Additionally, we use the cavity detection to postselect the measurements upon the presence of an atom before and after each spectroscopy sequence.

We record the Raman spectra by monitoring the probability of an atom to be transferred to $|F = 1\rangle$ as a function of the Raman two-photon detuning. In Fig. 7(a) we show the spectrum recorded before overlapping the sidebands. The error bars of the data points represent the 68% confidence interval of the binomial distribution of each measurement. A fit to the spectrum using seven Lorentzian curves allows us to extract the oscillation frequencies corresponding to each lattice dimension. After intensity adjustment of the lattice beams the spectrum in Fig. 7(b) shows almost degenerate sideband frequencies.

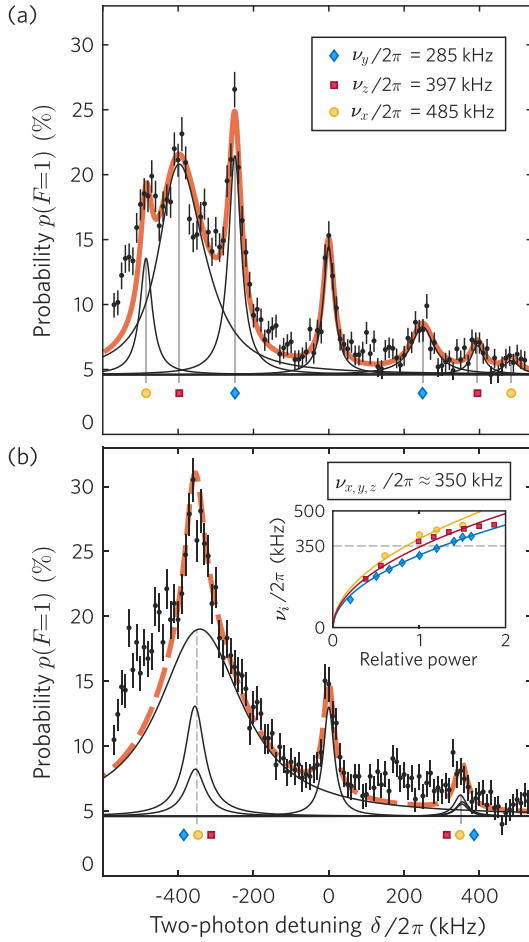


FIG. 7. Raman spectra of an atom trapped in the 3D lattice inside the FFPC. (a) For unequal trapping frequencies the first-order heating ($\delta < 0$) and cooling ($\delta > 0$) sidebands corresponding to each lattice dimension can be identified. The trap frequencies ν_i are extracted by fitting the data with the sum of seven Lorentzians (orange line, individual peaks in black). The carrier transition is highly suppressed as a consequence of using the blue-detuned intracavity lattice as a Raman beam [40,41]. (b) Raman spectrum after independently tuning the lattice beam intensities (inset) superposes all three trap frequencies (sidebands) into near-degeneracy around 350 kHz (the dashed orange curve serves as a guide to the eye). The asymmetry of the sidebands proves the efficiency of the 3D-cRSC scheme ($> 85\%$ ground-state fraction).

On the left side of the spectra ($\delta < 0$) we identify the heating sidebands ($\Delta n = +1$) for each lattice dimension and the corresponding cooling sidebands ($\Delta n = -1$) on the right side ($\delta > 0$). Note that, for Fig. 7(a), cooling the atoms with dRSC and off-resonant cRSC was sufficient to allow the measurement. As a consequence of using a blue-detuned intracavity lattice as Raman beam RB1, the atoms are trapped near the antinodes which causes the carrier transition ($\Delta n = 0$) at $\delta = 0$ to be highly suppressed [40,41]. The broad shape of the z heating sideband originates from inhomogeneous broadening due to the radial position distribution of the atoms in the narrow-waist intracavity lattice. The z distribution is negligible since the trapping occurs within the Rayleigh length of the cavity mode. The nonzero

spectrum baseline reflects a $|2, -2\rangle$ state preparation efficiency of $\approx 95\%$.

Based on these measurements we calibrate the displacement of each sideband for different intensities of the lattice beams [inset of Fig. 7(b)]. We typically tune all three trap frequencies to $\nu_{x,y,z}/2\pi \approx 350$ kHz shown in the spectrum of Fig. 7(b). Setting the Raman beams detuning to $\delta/2\pi = 350$ kHz and switching the repumper beams (Fig. 2) on simultaneously, cRSC is active along all lattice dimensions, as discussed in Sec. III. From the ratio of heating-cooling sideband amplitudes we estimate a ground-state occupation of more than 85% in all lattice dimensions, corresponding to mean motional excitations $\bar{n} \approx 0.17$ and a residual temperature of 1.4 μ K.

APPENDIX C: JUSTIFICATION AND LIMITATIONS OF THE TWO-LEVEL LIGHT-SHIFT MODEL

In Sec. IV of the main text we discuss the measurement of the differential light shifts (Fig. 4) as a function of repumper intensity and detuning during cRSC. We analyze our data with respect to a simple two-level model in the low-power limit.

While the linear dependence on the power in Eq. (1) agrees with the experiment [Fig. 4(a)], the dispersive relation of repumper detuning Δ vs δ_c shows clear deviations from the measurement [Fig. 4(b)]. Although a rough dispersive shape is observed, the measured relation is broadened and shows an asymmetric distortion towards red detunings of the repumper. The deviations from the two-level model can be caused by a multitude of both experimental factors and physical effects. Here we detail the validity of the used model and some possible effects affecting the observed light shifts.

The two-level model focuses on the repumper coupling only and ignores the Raman interaction. We also assume that all atoms are subject to the same laser intensities. The ground-state $|1, -1\rangle = |1\rangle$ (to be short) is coupled to the excited state $|2', -2\rangle = |2'\rangle$ with repumper Rabi frequency Ω and detuning Δ , while the second ground state $|2, -2\rangle = |2\rangle$ is considered a dark state for σ^- polarization [gray levels in Fig. 8(a)]. The system is described by a non-Hermitian Hamiltonian [63,64], which in matrix representation reads

$$H = \hbar \begin{pmatrix} -\Delta - i\gamma & \Omega/2 \\ \Omega/2 & 0 \end{pmatrix}, \quad (C1)$$

where the complex detuning $i\gamma$ introduces the finite linewidth of the optical transition. The light shift δ_{LS} for this two-level system is obtained by computing the energy eigenvalues $\mathcal{E} = \hbar\delta_{\text{LS}}$,

$$\mathcal{E} = \frac{\hbar}{2} \text{Re}(-\Delta - i\gamma + \sqrt{(2s-1)\gamma^2 + \Delta^2 + 2i\gamma\Delta}), \quad (C2)$$

where Re denotes the real part, $2\gamma \approx 2\pi \times 6$ MHz is the linewidth of the transition, and $s = 2(\frac{\Omega}{2\gamma})^2 = \frac{I_{\text{rep}}}{I_{\text{sat}}}$ is the saturation parameter. To first order in s ($\Omega \ll 2\gamma$) or large detuning ($\Delta \gg 2\gamma$), the light shift becomes

$$\delta_{\text{LS}} = \frac{\mathcal{E}}{\hbar} \approx \frac{1}{2}\gamma^2 \frac{\Delta}{\Delta^2 + \gamma^2} s + O(s^2), \quad (C3)$$

which is Eq. (1) in the main text in Sec. IV.

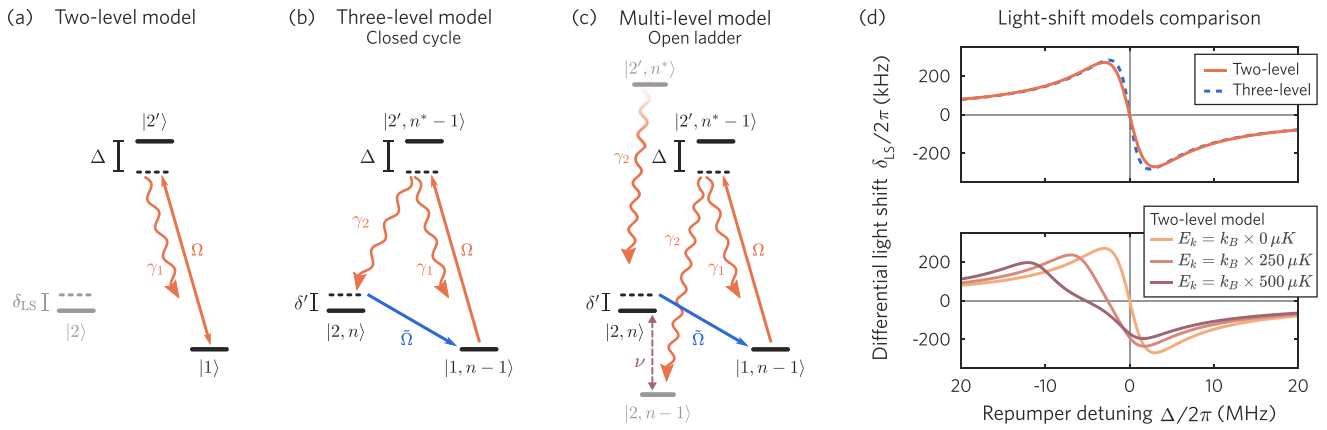


FIG. 8. Differential light shifts models. (a) Two-level model used in the main text to fit the experimental data. (b) Three-level model including the Raman Rabi coupling [62] for closed cycle treatment (c) Adjacent motional and relevant atomic levels. (d) Comparison of the two light-shifts models (upper panel) for ^{87}Rb , and of the two-level model when considering atomic oscillations in the lattice for different kinetic energies of the trapped atoms (lower panel). All of the plots consider a repumper saturation parameter $s = 0.36$ and a trap depth $U_0 = k_B \times 0.5 \text{ mK}$.

To investigate the validity and limitations of the two-level approximation we explore the role of the Raman-coupled second hyperfine level for our model [Raman Rabi frequency $\tilde{\Omega}$, Fig. 8(b)]. This scheme was first presented in Ref. [62], and we will show that it modifies the calculated light shifts only marginally. In Fig. 8(c) we include, for the sake of completeness, adjacent relevant motional levels for our discussion of the Raman cooling process, yielding the characteristic open ladder of lowering motional states.

The motional atomic energy levels relevant for the Raman cooling process have quantum numbers n and energy spacing $\hbar\nu$, see Figs. 8(b) and 8(c). A cooling cycle starts in the state $|2, n\rangle$, i.e., with an atom with motional excitation n . Raman coupling transfers the atom with Rabi frequency $\tilde{\Omega}$ and two-photon detuning δ' into the state $|1, n-1\rangle$ and thereby reduces the number of motional excitations by one. The Raman two-photon detuning is denoted with $\delta' = \delta - \nu$ here, since we consider only the Raman cooling sideband and neglect carrier and heating transitions. Optical repumping occurs at a Rabi frequency Ω and with detuning Δ , via the excited state $|2', n^* - 1\rangle$. Note that the excited state (excitation number n^*) experiences a different trapping potential than the ground states. In the Lamb-Dicke regime, where scattering events changing the motional state n are unlikely, the excited state decays either back into the state $|1, n-1\rangle$ at a rate γ_1 , or into the state $|2, n-1\rangle$ at a rate γ_2 . In the latter case the cooling cycle is completed and the atom was cooled from the n manifold into the $(n-1)$ manifold. Following Ref. [62], we note that the cooling occurs through the scattering mediated via the excited state $|2', n^* - 1\rangle$, and thus the cooling rate is proportional to the population of the excited state ρ_{ee}^{st} , as long as the system has not yet reached the dark motional ground state.

To quantify the continuous Raman cooling rate as a function of the repumper parameters, the approach in Ref. [62] is to find a steady-state solution ρ_{ee}^{st} for the excited-state population. Under the assumptions of negligible population of the motional ground state and of balanced decay rates into and out of each n manifold, the additional adjacent levels of the

open ladder system in Fig. 8(c) can be neglected, rendering the closed-cycle three-level model in Fig. 8(b) the next approximation beyond the two-level model in Fig. 8(a).

Using a Lindblad master-equation approach and for $\Gamma \gg \Omega \gg \tilde{\Omega}$, with the atomic linewidth $\Gamma = 2(\gamma_1 + \gamma_2)$, the steady-state excited-state population is approximated as

$$\rho_{ee}^{\text{st}} \approx \frac{\Omega^2 \tilde{\Omega}^2}{2\tilde{\Omega}^2(\Gamma^2 + 4\Delta^2) + 4\alpha\delta'^2\Gamma^2 + \alpha(\Omega^2 + 4\delta'\tilde{\delta})^2}, \quad (\text{C4})$$

where $\tilde{\delta} = \Delta - \delta'$ is the relative detuning and $\alpha = \frac{\gamma_2}{\gamma_1 + \gamma_2}$ is the effective repumping efficiency. Details of the derivation can be found in Ref. [62]. Since the survival probability of atoms in the experiment is proportional to the cooling rate and in turn proportional to ρ_{ee}^{st} , we look for the two-photon detuning δ'_m that maximizes the excited-state population, therefore matching the differential light shift $\delta_{\text{LS}} = \delta'_m$. By imposing the condition $\frac{\partial \rho_{ee}^{\text{st}}}{\partial \delta'} = 0$, we find that δ'_m obeys

$$0 = (\delta'_m)^3 - \frac{3}{2}\Delta(\delta'_m)^2 + \left[\frac{\Delta^2}{2} - \frac{\Omega^2}{4} + \frac{\Gamma^2}{8} \right] \delta'_m + \frac{\Delta\Omega^2}{8}. \quad (\text{C5})$$

The solution depends on the repumper Rabi frequency Ω and the repumper detuning Δ , and using the relation $\delta'_m = \delta_{\text{LS}} = \delta_c - \nu$ it can be compared with the two-level model [Eq. (C3)] used in the main text, and to the measured quantity δ_c (see Sec. IV).

The comparison of the differential light shifts δ_{LS} calculated with both models is shown in the upper panel of Fig. 8(d) for equal parameters. The results deviate slightly in the central region between the extrema, with the three-level model showing only a slightly sharper dispersive shape in the limit of low repumper intensities. Therefore, explicit accounting for the Raman cooling cycle does not explain the discrepancy to the experimentally determined light shifts. Even though the more elaborate model from [62] gives insight into the Raman cooling rates in the full parameter region (detuning and intensity from the repumper and the Raman beams), we find that the two-level model suffices to describe the light shifts

in the low intensity regime of our experiment with respect to light-matter interactions.

As a consequence, the observed broadening and asymmetric distortions of light shifts towards red detuning have to be attributed to effects that are not included in the theoretical description of the Raman cooling process, including: frequency fluctuations of the laser sources, spatial inhomogeneities of laser intensities, and both statistical and thermal distribution of atoms among and within their lattice sites.

Laser frequency fluctuations of the repumper beam lead to a broadening, or flattening of the observed dispersive curve. The magnitude of this noise in our experiment is on the order of few MHz with a Gaussian distribution. The broadening would be symmetric since it corresponds to a convolution of the idealized measurement with the Gaussian but does not explain the asymmetric distortion towards red detunings.

The repumper is conveniently coupled through one of the fiber cavity mirrors which, however, has the drawback to create a narrow beam profile, leading to a highly inhomogeneous repumper intensity distribution sensed by the atoms. The result is an effective reduction of the average intensity in the measurements which leads to a flattening of the measured curve compared with the model for a given repumper intensity, but again would not introduce any asymmetric distortion.

The above described two and three-level models assume that an atom is fixed at the bottom of the trapping potential and therefore experiences a fixed light shift of the optical repumping transition. Atoms with finite kinetic energy will, however, perform oscillations in the lattice site and therefore be exposed to varying light shifts within an oscillation period [38,47,65]. In the harmonic approximation, the time-dependent position of an atom inside a lattice well is given as

$$x(t) = \left(\frac{2E_k}{mv^2}\right)^{1/2} \sin(vt), \quad (C6)$$

with m being the atomic mass, E_k the kinetic energy, and v the angular trapping frequency. The corresponding light shift of the optical repumping transition leads to a position-dependent detuning

$$\Delta(x) = \Delta + \frac{1}{2\hbar}mv^2x^2(1 - \chi), \quad (C7)$$

where Δ is the AC-Stark-shifted detuning, meeting the resonance condition $\Delta = 0$ at the bottom of the trapping potential, and χ is the ratio of polarizabilities of ground and excited state ($\chi = \alpha_e/\alpha_g$). In particular, for small red detunings there are positions in the atom oscillation trajectory where the resonance condition is reached [$\Delta(x) = 0$], which is not possible for blue detunings. We note that this holds for all cases where the AC-Stark shift increases the energy of the atomic transition. This process can be taken into account by averaging the differential light shift over one oscillation period:

$$\begin{aligned} \bar{\delta} &= \frac{v}{2\pi} \int_0^{2\pi/v} \delta_{LS}(x(t)) dt \\ &= -\frac{1}{2}\gamma^2 \text{Re}[(\Delta^2 - \gamma^2 - \Delta\xi) + i\gamma(2\Delta - \xi)]^{-1/2} \text{ s}. \end{aligned} \quad (C8)$$

Here, $\delta_{LS}(x(t))$ is the light shift derived from Eq. (C2) evaluated with the position-dependent detuning $\Delta(x)$, Re denotes

the real part of the expression, and $\xi = E_k/\hbar$ is the oscillation amplitude in units of the detuning. The resulting dispersive curve for a ^{87}Rb atom with different kinetic energies in a 868 nm lattice ($\chi \approx -0.59$ [54]) with a trap depth $U_0 = k_B \times 0.5$ mK is shown in the lower panel of Fig. 8(d).

The most prominent effects on the dispersive curve with increasing temperature are the shift of the inflection point ($\delta_{LS} = 0$) towards red detuning, the reduction of its amplitude and the increased separation of the extrema. While we observe a clear distortion of the shape for high temperatures it still does not account alone for the observed asymmetric distortion in the experiment.

The analysis with respect to motional excitations of the atoms, however, gives a hint towards the underlying origin of the asymmetry. The curves in Fig. 8(d) are computed for a fixed position of the atom and identical intensities for all radiation fields. This assumption is no longer valid since in the experiment heating processes occur due to dipole-force fluctuations caused by the repumper and depending on detuning and intensity [38,47,65] (see Sec. V and Appendix D). They are especially strong for a red-detuned repumper which for $\Delta < 0$ increases the mean kinetic energy of the atoms and shifts the observed δ_{LS} accordingly. As this process is dependent on the repumper detuning, it can explain the observed asymmetric distortion of the dispersive curve. A distinct footprint of this process can be found in the measurement of the survival probability presented in Fig. 5(a). There, the survival drops stronger for $\Delta < 0$ indicating a higher mean temperature for this set of experimental parameters.

APPENDIX D: DIPOLE-FORCE FLUCTUATIONS AND MONTE CARLO SIMULATION

In the experiment, we observe an asymmetry in the survival probability measurement of Fig. 5(a), which we relate to heating rates that are dependent on the repumper parameters. We attribute those parameter-dependent heating rates to dipole-force fluctuations (DFFs) affecting an atom during the scattering cycles of the repumping process. The origin of DFFs in our case is the following: an atom confined in the lattice and illuminated by the repumper field cycles between the ground state $|g\rangle = |5^2S_{1/2}\rangle$ and the excited state $|e\rangle = |5^2P_{1/2}\rangle$. For ^{87}Rb at the lattice wavelength of 868 nm the polarizability ratio of the states $|e\rangle$ and $|g\rangle$ is $\chi = \alpha_e/\alpha_g \approx -0.59$, such that the atom experiences a repulsive force for the fraction of time that it spends in the antitrapping potential of $|e\rangle$, before scattering back into the trapping potential of $|g\rangle$. These fluctuations of the dipole force usually lead to an increase of the kinetic energy of the atom [38,65], although situations leading to cooling have also been observed [47].

To gain insight into the effect of DFFs, we implement a semiclassical Monte Carlo simulation of scattering under near-resonant illumination in a 1D optical lattice, following the work in Ref. [38]. Since the repumper field is close to resonance, we use the dressed-states formalism to simulate the motional dynamics of the atom, while taking into account the coherent atom-light coupling. From the simulation we obtain the maps shown in Fig. 5(c) of photon-scattering rates and atom loss rates as functions of the repumper detuning and

intensity, which validate the hypothesis of DFFs as the main source of heating.

1. Scattering in dressed-state potentials

Here, we summarize how we treat the simultaneous interaction of the atom with the two relevant light fields: the 868 nm trapping field and the 795 nm repumper field. The interaction of the atom with the lattice field is considered as a pure position dependent AC-Stark shift of the bare states $|g\rangle$ and $|e\rangle$, giving rise to the associated trapping and anti-trapping potentials $U_g(\mathbf{r})$ and $U_e(\mathbf{r}) = \chi U_g(\mathbf{r})$ respectively, with $|U_g(0)| = U_0$. The additional illumination with the near-resonant repumper field drives scattering transitions between the two atomic states and their respective potentials, generating dynamics with coherent atom-field coupling.

To include the interaction with both light fields in the motional dynamics of the atom, as in Ref. [38], we use the dressed-states formalism to describe the evolution of the atom-field system, with scattering events occurring between the repumper-dressed states $|-\rangle$ and $|+\rangle$. The associated dressed-state potentials are given by

$$U_{\pm}(\mathbf{r}) = U_g(\mathbf{r}) + \frac{\hbar}{2}[-\Delta(\mathbf{r}) \pm \sqrt{\Delta^2(\mathbf{r}) + \Omega^2}], \quad (\text{D1})$$

with Ω being the repumper Rabi frequency on resonance and $\Delta(\mathbf{r})$ the position-dependent detuning taking into account the light shifts induced by the lattice,

$$\Delta(\mathbf{r}) = \tilde{\Delta} + \frac{U_g(\mathbf{r}) - U_e(\mathbf{r})}{\hbar}, \quad (\text{D2})$$

where $\tilde{\Delta}$ is the free-space detuning of the light field from the atomic transition. We note that, for large values of the detuning $\Delta(\mathbf{r})$, the potentials $U_{\pm}(\mathbf{r})$ almost preserve the shape of the bare-state potentials $U_g(\mathbf{r})$ and $U_e(\mathbf{r})$. When approaching resonance, in the regime where the condition $\Delta(\mathbf{r}) = 0$ can be met, the shape of the dressed-state potentials and thus the corresponding dipole forces, strongly depend on the parameters of the illumination light, showing the importance of using the dressed-states formalism for the simulation.

We follow the approach in Ref. [38] using the secular approximation of the optical Bloch equations, to obtain the steady-state transition rates between dressed states and their associated potentials [65]

$$\begin{aligned} \Gamma_{++} &= \Gamma_{--} = \Gamma \sin^2 \theta(\mathbf{r}) \cos^2 \theta(\mathbf{r}), \\ \Gamma_{-+} &= \Gamma \sin^4 \theta(\mathbf{r}), \quad \Gamma_{+-} = \Gamma \cos^4 \theta(\mathbf{r}), \end{aligned} \quad (\text{D3})$$

with $\theta(\mathbf{r})$ being the mixing angle defined as

$$\theta(\mathbf{r}) = \frac{1}{2} \arctan \left(-\frac{\Omega}{\Delta(\mathbf{r})} \right) + \frac{\pi}{2} H(\Delta(\mathbf{r})), \quad (\text{D4})$$

where $H(\cdot)$ is the Heaviside step function.

The Monte Carlo simulation combines the classical motion of a two-level atom in the lattice dressed-state potentials with the semiclassical treatment of scattering induced by the illumination with repumper light. We use the position-dependent transition rates of Eq. (D3) to calculate and weight the probabilities at a given position that the atom undergoes a scattering event and if it results in a change of potential $U_{\pm}(\mathbf{r}) \rightarrow U_{\mp}(\mathbf{r})$. Between scattering events (with random sampling), the classical equations of motion in the current potential are solved to

determine the position and probabilities of the next scattering event. Events with change of potential will result in heating by DFFs additional to the photon recoil, while in the case of scattering without state change only the recoil will contribute to the heating dynamics.

2. Details of the Monte Carlo loop algorithm

The simulation describes the coupled motion and scattering dynamics of a two-level atom (with ^{87}Rb parameters) trapped in a one-dimensional optical lattice with depth $U_0 = k_B \times 0.5$ mK, illuminated with near-resonant repumper light, and considering the dressed-states approach. The polarizability ratio between the two bare atomic states $|g\rangle$ and $|e\rangle$ in the lattice is $\chi = -0.59$. We extract the photon-scattering rates (independent of atom losses) and the atom loss rates shown in Fig. 5(c) as functions of the repumper saturation parameter $s = 2(\Omega/2\gamma)^2$ and the free-space detuning $\tilde{\Delta}$, from the simulated evolution of an ensemble of 500 independent atoms for each set of parameters. We use a linear model to fit the number of total scattered photons per elapsed time, and an exponential model for the increase of kinetic energy from which we determine the atom loss rates. For each atom with a given set $\{s, \tilde{\Delta}\}$ we run the following algorithm, starting with the initial conditions:

(i) Initial total energy E_0 drawn randomly from a 1D Boltzmann distribution with a mean temperature $T = 100 \mu\text{K}$.

(ii) Initial position and momentum randomized by performing one evolution step of the atom in the potential $U_g(r)$, for a random time taken as a fraction of the harmonic-oscillator period with trapping frequency $\nu = 350$ kHz: $\{r = 0, p = \sqrt{2mE_0}\} \rightarrow \{r_0, p_0\}$.

(iii) Initial state $|-\rangle$ or $|+\rangle$ selected by a weighted coin flip with probabilities $P_- = |\langle g|-\rangle|^2 = \cos^2 \theta(r)$ and $P_+ = |\langle g|+\rangle|^2 = \sin^2 \theta(r)$, with $\theta(r)$ being the mixing angle from Eq. (D4).

The Monte Carlo loop follows the next steps:

(1) Start loop iteration i with the atom's position r_i , momentum p_i , total energy E_i and occupied dressed state determined by the previous iteration (for $i = 0$ take the initial conditions).

(2) If in the state $|-\rangle$ ($|+\rangle$), calculate the maximum value of the transition rates Γ_{--} , Γ_{-+} (Γ_{++} , Γ_{+-}) within the range of accessible positions at the current energy E_i , using Eq. (D3).

(3) Draw random times from the exponential distributions $\rho_{\alpha} = R_{\alpha, \max} \exp(-R_{\alpha, \max} t)$, with $R_{\alpha, \max}$ the maximum values of the two rates from step 2 (for the current dressed state). The minimum value between the two resulting times is taken as the time τ_i elapsed until the next possible scattering event. The transition rate associated with time τ_i is defined as $R_i(r)$ and its maximum value $R_{i, \max}$.

(4) Evolve the system for a time τ_i by solving the equations of motion in the dressed-state potential $U_{-}(r)$ [$U_{+}(r)$] in Eq. (D1), to find $\{r_{i+1}, p_{i+1}\}$.

(5) Determine if the scattering event takes place by a weighted coin flip with the success probability $g = R_i(r_{i+1})/R_{i, \max}$. If the event fails to occur, return to step 3.

(6) If the scattering event occurred, update the occupied dressed state accordingly, sum one count to the number of scattered photons, update the new atom's momentum p_{i+1} by adding the photon recoil, and calculate the total energy E_{i+1} .

(7) The simulation terminates, if the new position r_{i+1} exceeds the bounds of the trapping potential or if the limit of total time is reached. Otherwise start the next iteration in step 1 with updated values.

-
- [1] N. Gisin and R. Thew, Quantum communication, *Nat. Photonics* **1**, 165 (2007).
- [2] R. V. Meter, *Quantum Networking* (John Wiley & Sons, Ltd, Hoboken, 2014).
- [3] H. J. Kimble, The quantum internet, *Nature (London)* **453**, 1023 (2008).
- [4] S. Wehner, D. Elkouss, and R. Hanson, Quantum internet: A vision for the road ahead, *Science* **362**, eaam9288 (2018).
- [5] L.-M. Duan, M. D. Lukin, J. I. Cirac, and P. Zoller, Long-distance quantum communication with atomic ensembles and linear optics, *Nature (London)* **414**, 413 (2001).
- [6] S. J. van Enk, H. J. Kimble, and H. Mabuchi, Quantum information processing in cavity-QED, *Quantum Inf. Process.* **3**, 75 (2004).
- [7] S. Ritter, C. Nölleke, C. Hahn, A. Reiserer, A. Neuzner, M. Uphoff, M. Mücke, E. Figueroa, J. Bochmann, and G. Rempe, An elementary quantum network of single atoms in optical cavities, *Nature (London)* **484**, 195 (2012).
- [8] A. Reiserer and G. Rempe, Cavity-based quantum networks with single atoms and optical photons, *Rev. Mod. Phys.* **87**, 1379 (2015).
- [9] L.-M. Duan and C. Monroe, Colloquium: Quantum networks with trapped ions, *Rev. Mod. Phys.* **82**, 1209 (2010).
- [10] N. Sangouard, C. Simon, H. de Riedmatten, and N. Gisin, Quantum repeaters based on atomic ensembles and linear optics, *Rev. Mod. Phys.* **83**, 33 (2011).
- [11] D. Awschalom, K. K. Berggren, H. Bernien, S. Bhave, L. D. Carr, P. Davids, S. E. Economou, D. Englund, A. Faraon, M. Fejer, S. Guha, M. V. Gustafsson, E. Hu, L. Jiang, J. Kim, B. Korzh, P. Kumar, P. G. Kwiat, M. Lončar, M. D. Lukin *et al.*, Development of quantum interconnects (QuICs) for next-generation information technologies, *PRX Quantum* **2**, 017002 (2021).
- [12] P. van Loock, W. Alt, C. Becher, O. Benson, H. Boche, C. Deppe, J. Eschner, S. Höfling, D. Meschede, P. Michler, F. Schmidt, and H. Weinfurter, Extending quantum links: Modules for fiber- and memory-based quantum repeaters, *Adv. Quantum Technol.* **3**, 1900141 (2020).
- [13] J. I. Cirac, P. Zoller, H. J. Kimble, and H. Mabuchi, Quantum State Transfer and Entanglement Distribution among Distant Nodes in a Quantum Network, *Phys. Rev. Lett.* **78**, 3221 (1997).
- [14] H. J. Kimble, Strong interactions of single atoms and photons in cavity QED, *Phys. Scr.* **1998**, 127 (1998).
- [15] R. Miller, T. E. Northup, K. M. Birnbaum, A. Boca, A. D. Boozer, and H. J. Kimble, Trapped atoms in cavity qed: Coupling quantized light and matter, *J. Phys. B: At., Mol. Opt. Phys.* **38**, S551 (2005).
- [16] S. Haroche and J.-M. Raimond, *Exploring the Quantum* (Oxford University Press, Oxford, UK, 2006).
- [17] D. Hunger, T. Steinmetz, Y. Colombe, C. Deutsch, T. W. Hänsch, and J. Reichel, A fiber Fabry-Perot cavity with high finesse, *New J. Phys.* **12**, 065038 (2010).
- [18] J. Gallego, S. Ghosh, S. K. Alavi, W. Alt, M. Martinez-Dorantes, D. Meschede, and L. Ratschbacher, High finesse fiber Fabry-Perot cavities: Stabilization and mode matching analysis, *Appl. Phys. B: Lasers Opt.* **122**, 47 (2016).
- [19] H. Pfeifer, L. Ratschbacher, J. Gallego, C. Saavedra, A. Faßbender, A. von Haaren, W. Alt, S. Hofferberth, M. Köhl, S. Linden, and D. Meschede, Achievements and perspectives of optical fiber Fabry-Perot cavities, *Appl. Phys. B: Lasers Opt.* **128**, 29 (2022).
- [20] J. Gallego, W. Alt, T. Macha, M. Martinez-Dorantes, D. Pandey, and D. Meschede, Strong Purcell Effect on a Neutral Atom Trapped in an Open Fiber Cavity, *Phys. Rev. Lett.* **121**, 173603 (2018).
- [21] A. Kuhn and D. Ljunggren†, Cavity-based single-photon sources, *Contemp. Phys.* **51**, 289 (2010).
- [22] P. B. R. Nisbet-Jones, J. Dille, D. Ljunggren, and A. Kuhn, Highly efficient source for indistinguishable single photons of controlled shape, *New J. Phys.* **13**, 103036 (2011).
- [23] T. Wilk, S. C. Webster, A. Kuhn, and G. Rempe, Single-atom single-photon quantum interface, *Science* **317**, 488 (2007).
- [24] T. Macha, E. Uruñuela, W. Alt, M. Ammenwerth, D. Pandey, H. Pfeifer, and D. Meschede, Nonadiabatic storage of short light pulses in an atom-cavity system, *Phys. Rev. A* **101**, 053406 (2020).
- [25] O. Morin, M. Körber, S. Langenfeld, and G. Rempe, Deterministic Shaping and Reshaping of Single-Photon Temporal Wave Functions, *Phys. Rev. Lett.* **123**, 133602 (2019).
- [26] S. Langenfeld, P. Thomas, O. Morin, and G. Rempe, Quantum Repeater Node Demonstrating Unconditionally Secure Key Distribution, *Phys. Rev. Lett.* **126**, 230506 (2021).
- [27] M. Reitz, C. Sommer, and C. Genes, Cooperative quantum phenomena in light-matter platforms, *PRX Quantum* **3**, 010201 (2022).
- [28] R. H. Dicke, Coherence in spontaneous radiation processes, *Phys. Rev.* **93**, 99 (1954).
- [29] M. Fleischhauer, S. Yelin, and M. Lukin, How to trap photons? Storing single-photon quantum states in collective atomic excitations, *Opt. Commun.* **179**, 395 (2000).
- [30] A. V. Gorshkov, A. André, M. D. Lukin, and A. S. Sørensen, Photon storage in Λ -type optically dense atomic media. I. cavity model, *Phys. Rev. A* **76**, 033804 (2007).
- [31] Y. Colombe, T. Steinmetz, G. Dubois, F. Linke, D. Hunger, and J. Reichel, Strong atom-field coupling for Bose-Einstein condensates in an optical cavity on a chip, *Nature (London)* **450**, 272 (2007).
- [32] E. Altman, K. R. Brown, G. Carleo, L. D. Carr, E. Demler, C. Chin, B. DeMarco, S. E. Economou, M. A. Eriksson, K.-M. C. Fu, M. Greiner, K. R. Hazzard, R. G. Hulet, A. J. Kollár, B. L. Lev, M. D. Lukin, R. Ma, X. Mi, S. Misra, C. Monroe *et al.*, Quantum simulators: Architectures and opportunities, *PRX Quantum* **2**, 017003 (2021).

- [33] I. Bloch, Ultracold quantum gases in optical lattices, *Nat. Phys.* **1**, 23 (2005).
- [34] D. Meschede and A. Rauschenbeutel, Manipulating Single Atoms, in *Advances In Atomic, Molecular, and Optical Physics* (Elsevier, London, 2006), pp. 75–104.
- [35] H. Ott, Single atom detection in ultracold quantum gases: A review of current progress, *Rep. Prog. Phys.* **79**, 054401 (2016).
- [36] M. J. Kastoryano, F. Reiter, and A. S. Sørensen, Dissipative Preparation of Entanglement in Optical Cavities, *Phys. Rev. Lett.* **106**, 090502 (2011).
- [37] A. Alberti, C. Robens, W. Alt, S. Brakhane, M. Karski, R. Reimann, A. Widera, and D. Meschede, Super-resolution microscopy of single atoms in optical lattices, *New J. Phys.* **18**, 053010 (2016).
- [38] M. Martinez-Dorantes, W. Alt, J. Gallego, S. Ghosh, L. Ratschbacher, and D. Meschede, State-dependent fluorescence of neutral atoms in optical potentials, *Phys. Rev. A* **97**, 023410 (2018).
- [39] H. Ritsch, P. Domokos, F. Brennecke, and T. Esslinger, Cold atoms in cavity-generated dynamical optical potentials, *Rev. Mod. Phys.* **85**, 553 (2013).
- [40] R. Reimann, W. Alt, T. Macha, D. Meschede, N. Thau, S. Yoon, and L. Ratschbacher, Carrier-free Raman manipulation of trapped neutral atoms, *New J. Phys.* **16**, 113042 (2014).
- [41] A. Neuzner, S. Dürr, M. Körber, S. Ritter, and G. Rempe, Increased dimensionality of Raman cooling in a slightly nonorthogonal optical lattice, *Phys. Rev. A* **98**, 013401 (2018).
- [42] B. J. Lester, A. M. Kaufman, and C. A. Regal, Raman cooling imaging: Detecting single atoms near their ground state of motion, *Phys. Rev. A* **90**, 011804(R) (2014).
- [43] Y. S. Patil, S. Chakram, L. M. Aycocck, and M. Vengalattore, Nondestructive imaging of an ultracold lattice gas, *Phys. Rev. A* **90**, 033422 (2014).
- [44] L. W. Cheuk, M. A. Nichols, M. Okan, T. Gersdorf, V. V. Ramasesh, W. S. Bakr, T. Lompe, and M. W. Zwierlein, Quantum-Gas Microscope for Fermionic Atoms, *Phys. Rev. Lett.* **114**, 193001 (2015).
- [45] M. F. Parsons, F. Huber, A. Mazurenko, C. S. Chiu, W. Setiawan, K. Wooley-Brown, S. Blatt, and M. Greiner, Site-Resolved Imaging of Fermionic ${}^6\text{Li}$ in an Optical Lattice, *Phys. Rev. Lett.* **114**, 213002 (2015).
- [46] A. Omran, M. Boll, T. A. Hilker, K. Kleinlein, G. Salomon, I. Bloch, and C. Gross, Microscopic Observation of Pauli Blocking in Degenerate Fermionic Lattice Gases, *Phys. Rev. Lett.* **115**, 263001 (2015).
- [47] R. Taïeb, R. Dum, J. I. Cirac, P. Marte, and P. Zoller, Cooling and localization of atoms in laser-induced potential wells, *Phys. Rev. A* **49**, 4876 (1994).
- [48] D. Leibfried, R. Blatt, C. Monroe, and D. Wineland, Quantum dynamics of single trapped ions, *Rev. Mod. Phys.* **75**, 281 (2003).
- [49] D. Schrader, S. Kuhr, W. Alt, M. Müller, V. Gomer, and D. Meschede, An optical conveyor belt for single neutral atoms, *Appl. Phys. B: Lasers Opt.* **73**, 819 (2001).
- [50] S. Kuhr, Deterministic delivery of a single atom, *Science* **293**, 278 (2001).
- [51] A. D. Boozer, A. Boca, R. Miller, T. E. Northup, and H. J. Kimble, Cooling to the Ground State of Axial Motion for One Atom Strongly Coupled to an Optical Cavity, *Phys. Rev. Lett.* **97**, 083602 (2006).
- [52] D.-J. Han, S. Wolf, S. Oliver, C. McCormick, M. T. DePue, and D. S. Weiss, 3D Raman Sideband Cooling of Cesium Atoms at High Density, *Phys. Rev. Lett.* **85**, 724 (2000).
- [53] E. Uruñuela, W. Alt, E. Keiler, D. Meschede, D. Pandey, H. Pfeifer, and T. Macha, Ground-state cooling of a single atom inside a high-bandwidth cavity, *Phys. Rev. A* **101**, 023415 (2020).
- [54] B. Arora and B. K. Sahoo, State-insensitive trapping of Rb atoms: Linearly versus circularly polarized light, *Phys. Rev. A* **86**, 033416 (2012).
- [55] X. Baillard, A. Gauguet, S. Bize, P. Lemonde, P. Laurent, A. Clairon, and P. Rosenbusch, Interference-filter-stabilized external-cavity diode lasers, *Opt. Commun.* **266**, 609 (2006).
- [56] C. Henry, Theory of the linewidth of semiconductor lasers, *IEEE J. Quantum Electron.* **18**, 259 (1982).
- [57] G. Agrawal, Line narrowing in a single-mode injection laser due to external optical feedback, *IEEE J. Quantum Electron.* **20**, 468 (1984).
- [58] Q. Lin, M. A. V. Camp, H. Zhang, B. Jelenković, and V. Vuletić, Long-external-cavity distributed Bragg reflector laser with sub-kilohertz intrinsic linewidth, *Opt. Lett.* **37**, 1989 (2012).
- [59] W. Ma, B. Xiong, C. Sun, X. Ke, Z. Hao, L. Wang, J. Wang, Y. Han, H. Li, and Y. Luo, Laser frequency noise characterization by self-heterodyne with both long and short delay, *Appl. Opt.* **58**, 3555 (2019).
- [60] T. Okoshi, K. Kikuchi, and A. Nakayama, Novel method for high resolution measurement of laser output spectrum, *Electron. Lett.* **16**, 630 (1980).
- [61] Simulation-based fitting routine for laser linewidth estimation from DSH measurement, <https://de.mathworks.com/matlabcentral/fileexchange/106535>.
- [62] T. A. Hilker, Ph.D. thesis, LMU München, Faculty of Physics, 2017.
- [63] N. Moiseyev, Quantum theory of resonances: Calculating energies, widths and cross-sections by complex scaling, *Phys. Rep.* **302**, 212 (1998).
- [64] C. W. Gardiner and P. Zoller, *Quantum Noise*, 3rd ed. (Springer-Verlag, Heidelberg, 2004).
- [65] J. Dalibard and C. Cohen-Tannoudji, Dressed-atom approach to atomic motion in laser light: The dipole force revisited, *J. Opt. Soc. Am. B* **2**, 1707 (1985).

List of References

In the publication presented above (Ref. [2]), the bibliography follows an internal numbering. To include the corresponding entries in the global bibliography of this thesis, the following table gives the explicit link between the internal citation index of the paper, and the global citation index of the thesis.

- | | |
|---|---|
| [1] corresponds to Ref. [9] (p. 80). | [32] corresponds to Ref. [170] (p. 80). |
| [2] corresponds to Ref. [10] (p. 80). | [33] corresponds to Ref. [63] (p. 80). |
| [3] corresponds to Ref. [5] (p. 80). | [34] corresponds to Ref. [54] (p. 80). |
| [4] corresponds to Ref. [6] (p. 80). | [35] corresponds to Ref. [55] (p. 80). |
| [5] corresponds to Ref. [11] (p. 80). | [36] corresponds to Ref. [47] (p. 80). |
| [6] corresponds to Ref. [14] (p. 80). | [37] corresponds to Ref. [57] (pp. 80, 82). |
| [7] corresponds to Ref. [15] (p. 80). | [38] corresponds to Ref. [58] (pp. 80, 83, 85, 86, 89, 91). |
| [8] corresponds to Ref. [16] (p. 80). | [39] corresponds to Ref. [110] (p. 80). |
| [9] corresponds to Ref. [12] (p. 80). | [40] corresponds to Ref. [114] (pp. 80, 82, 88). |
| [10] corresponds to Ref. [13] (p. 80). | [41] corresponds to Ref. [115] (pp. 80, 82, 88). |
| [11] corresponds to Ref. [167] (p. 80). | [42] corresponds to Ref. [123] (pp. 80, 82, 85). |
| [12] corresponds to Ref. [168] (p. 80). | [43] corresponds to Ref. [124] (p. 80). |
| [13] corresponds to Ref. [17] (p. 80). | [44] corresponds to Ref. [125] (pp. 80, 82, 86). |
| [14] corresponds to Ref. [18] (p. 80). | [45] corresponds to Ref. [126] (pp. 80, 82). |
| [15] corresponds to Ref. [19] (p. 80). | [46] corresponds to Ref. [127] (p. 80). |
| [16] corresponds to Ref. [20] (p. 80). | [47] corresponds to Ref. [128] (pp. 80, 85, 89, 91). |
| [17] corresponds to Ref. [21] (p. 80). | [48] corresponds to Ref. [104] (p. 81). |
| [18] corresponds to Ref. [22] (pp. 80, 81). | [49] corresponds to Ref. [87] (p. 81). |
| [19] corresponds to Ref. [23] (p. 80). | [50] corresponds to Ref. [88] (p. 81). |
| [20] corresponds to Ref. [24] (pp. 80, 81, 88). | [51] corresponds to Ref. [92] (p. 81). |
| [21] corresponds to Ref. [36] (p. 80). | [52] corresponds to Ref. [171] (p. 82). |
| [22] corresponds to Ref. [37] (p. 80). | [53] corresponds to Ref. [1] (pp. 83, 88). |
| [23] corresponds to Ref. [38] (p. 80). | [54] corresponds to Ref. [106] (pp. 85, 89). |
| [24] corresponds to Ref. [41] (p. 80). | [55] corresponds to Ref. [112] (p. 87). |
| [25] corresponds to Ref. [39] (p. 80). | [56] corresponds to Ref. [172] (p. 87). |
| [26] corresponds to Ref. [40] (p. 80). | [57] corresponds to Ref. [173] (p. 87). |
| [27] corresponds to Ref. [169] (p. 80). | [58] corresponds to Ref. [174] (p. 87). |
| [28] corresponds to Ref. [42] (p. 80). | [59] corresponds to Ref. [175] (p. 87). |
| [29] corresponds to Ref. [45] (p. 80). | [60] corresponds to Ref. [176] (p. 87). |
| [30] corresponds to Ref. [46] (p. 80). | [61] corresponds to Ref. [177] (p. 87). |
| [31] corresponds to Ref. [29] (p. 80). | [62] corresponds to Ref. [178] (p. 89). |

[63] corresponds to Ref. [81] (p. 89).

[65] corresponds to Ref. [105] (pp. 89, 91).

[64] corresponds to Ref. [82] (p. 89).

The drive-through loading method: supplementary details

This appendix provides supplementary information and results about the drive-through loading method presented in Chapter 5, that are either preliminary or not critical for the discussion in the main text.

In Section C.1 are included important details about the implementation of the numerical simulation. Section C.2 contains a comparison of simulation results with the corresponding experimental results shown in Section 5.2.3 (effect of transport velocity and cooling on the loading probability). Finally Section C.3 presents preliminary measurements of the position distribution of atoms in the lattice resulting from drive-through loading, obtained with the Raman imaging method presented in Chapter 4.

C.1 Numerical simulation of 1D transport: implementation details

Here I present a short summary of the most relevant technical details regarding the implementation of the 1D numerical simulation of atomic transport that was discussed in Section 5.1.2. For further information and a comprehensive description see Ref. [67].

Our computational implementation uses a fifth-order Runge-Kutta method [179] considering discrete time steps Δt . The recursive algorithm calculates the position and velocity of the particle, for all time frames of the drive-through transport, based on the values of the previous time step $\{y(t), \dot{y}(t)\} \rightarrow \{y(t + \Delta t), \dot{y}(t + \Delta t)\}$, for given initial condition $\{y(0), \dot{y}(0)\}$. These initial values are defined by the energy of the atom E_β and an initial random phase ϕ_0 of the oscillations in the lattice. The energy E_β is picked from the 1D Boltzmann distribution of the MOT (truncated by the maximum trapping depth during MOT loading), and modified by β as discussed previously. The phase ϕ_0 has the effect of distributing the initial energy E_β onto kinetic and potential components. The former determines the velocity of the particle, while the latter gives the initial position inside of the starting lattice well, i.e. $\{E_\beta, \phi_0\} \mapsto \{y(0), \dot{y}(0)\}$. At the end of the simulation, the atom is considered as loaded into the lattice intersection region if its final position is within the range $[-20, +20] \mu\text{m}$.

To obtain the drive-through loading probability for chosen values $\{\beta, v_T, y_0\}$, we run the simulation with 192 independent particles. The parameter space of initial conditions $\{E_\beta, \phi_0\}$ is sampled with 16 equally spaced energies (with probabilities weighted with the Boltzmann distribution), and for each energy 12 initial phases with uniform distribution (the phases are random and with no special weights during the MOT loading). The single-atom loading probability P_{dt} is calculated from the number of successfully loaded atoms out of the total 192 simulation runs. The results for a scan of the relative depth β are shown and discussed in Section 5.2 along with the experimental measurements, see Figure 5.3 (a).

The analysis of the lattice geometry effect on the loading probability is presented in Section 5.2.3, see Figure 5.4(b). Further simulation results of the other parameter scans are presented in Ref. [67] and included below in Section C.2.

C.2 Effect of transport velocity and cooling: comparison of experiment and simulation

In Section 5.2.3 we showed and interpreted the measurement results of drive-through loading probability as a function of the transport velocity v_T , and the absence or presence of cooling during the process. There, in Figure 5.4, selected measurements were presented that contributed to the discussion. Also, the corresponding simulation results were omitted since they were not crucial for the results.

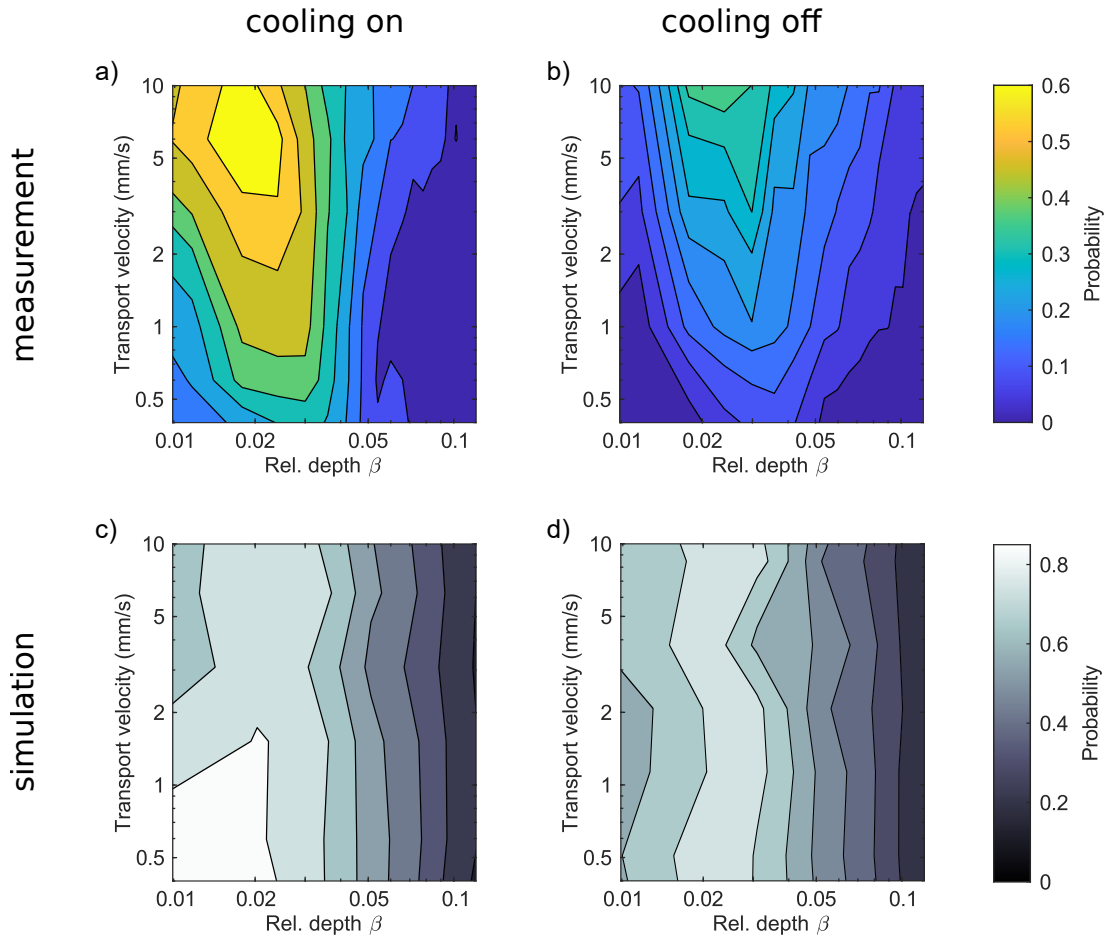


Figure C.1: Comparison of drive-through loading measurements and simulation to analyze the effect of transport velocity and cooling. The single-atom loading probability as a function of relative depth β is shown for the case with cooling (a-c) and without cooling (b-d), resulting from experimental measurements (blue-yellow scale) and from the simulation (grey scale). Figure from Ref. [67].

For completeness, here I include the full set of measurements and the comparison to the simulation results, see Figure C.1, as first presented in Ref. [67]. Differently than in Figure 5.4(a) where we plotted the data as individual scans, here we represent it all together as contour plots with the loading probability

encoded in color scales. This representation allows to appreciate and compare the overall behavior landscape of the drive-through loading probability with respect to the studied parameters. There are two main conclusions from the comparison: (i) In the simulation the transport velocity plays no role, whereas in the measurements lower velocities are detrimental. The reason is that atom losses caused by external heating effects are reduced for shorter transports, as discussed in Section 5.2.3. (ii) for the measurements, cooling increases the loading probability overall and is more prominent for low relative depths, whereas for the simulation it only plays a role for the low β region ($\beta < 0.02$). The explanation is that in the experiments the cooling compensates heating effects and also reduces recapturing of the atoms that undermines the drive-through loading effect (see Section 5.1.2), while in the simulation only the avoided recapturing plays a role since external heating effect are not considered. For a more detailed explanation refer to [67].

C.3 Preliminary characterization of the atom position distribution

To characterize the loading density inside the cavity achievable with the drive-through loading method, we have performed preliminary measurements of the position distribution of atoms via Raman imaging (see Chapter 4). The images are postprocessed with a position-detection algorithm to obtain the position distribution. The details of the measurement can be found in Ref. [67]. To benchmark the resulting distribution by drive-through loading, we compare position distributions obtained with two other techniques used alternatively in the experiment: the *feedforward transport* shuttles the full chain of atoms loaded from the MOT into the center of the cavity, while the *feedback transport* uses the cavity-based detection to stop the conveyor-belt shuttling when a first well-coupled atom is detected [75].

In Figure C.2 (a-c) we see the 2D histograms of the position distributions in the yz -plane following each loading technique. Since we are mostly interested in the position distribution along the transport y -axis, we average vertically the regions of interest (between white dashed lines). The normalized atom position probabilities along the y -axis are shown in Figure C.2 (d) for all three loading methods. We observe that the feedforward and feedback transports result in a very similar distribution, with a maximum at pixel ~ 24 , whereas the drive-through loading creates a distribution that peaks 10 pixels to the left at pixel ~ 14 . To interpret this observation it is necessary to know the crossing position of the different lattice beams. Identifying the position of the lattices DT_x and DT_z is done by inducing atom loss via parametric modulation of one lattice at a time, then spotting the center of the beam as the position of higher losses. With this procedure, we discovered a misalignment of the 3D lattice by $\sim 4.57 \mu\text{m}$, with the position at pixel ~ 24 corresponding to the intersection of the cavity mode with the conveyor belt (DT_z and DT_y), and the position at pixel ~ 14 to the intersection of DT_x and DT_y . Here we use that 1 pixel in the camera image corresponds to $\sim 457 \text{ nm}$ in the lattice plane at the cavity position, see Section 2.3.5.

Such diagnosis of the lattice misalignment allows important discussions about the loading techniques following Figure C.2 (d). On one hand, the feedforward and feedback methods have a higher loading probability at the cavity center (at the crossing DT_{yz}), as it is expected by design (i.e. they are programmed to bring the atoms there) and because cooling is highest at that position (see Chapter 3) so the survival probability is higher (also the imaging quality is higher there which could bias the atom detection). Still, we note that some atoms are also loaded in the crossing with DT_x where the trapping potential is deeper. On the other hand, the drive-through method has the highest loading probability at the intersection of DT_{xy} , exactly as expected from the development of the technique (Chapter 5), even when that position is not at the cavity center. We emphasize this because at such position the lattice misalignment creates harder conditions for the atoms to survive the loading and imaging sequence (less efficient cooling) and to be detected (lower image quality). Thus, the observation that the atom distribution peaks at the DT_x despite

the harder conditions points towards a highly effective loading by drive-through. In order to confirm this idea we carried out the sensitive realignment of the lattice, with the aim of repeating the position distribution measurements at the now common intersection of DT_{xyz} . Unfortunately final measurements could not be concluded due to the permanent damage suffered by the cavity (see Appendix D.1).

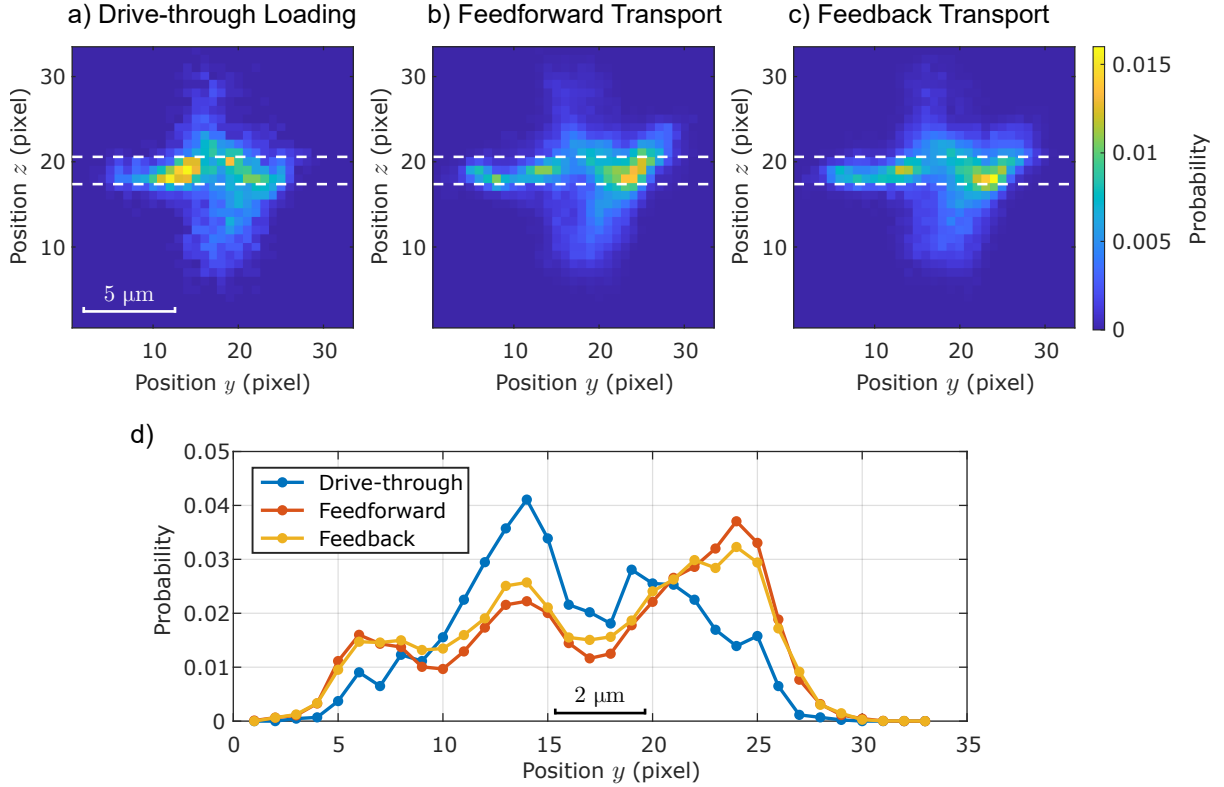


Figure C.2: Preliminary characterization of the atom position distribution resulting from drive-through loading, compared to alternative loading methods, measured with Raman imaging (Chapter 4) and postprocessed with a position-detection algorithm [67]. The histogram of detected atoms positions in the cavity region is shown after (a) drive-through-loading, (b) feedforward transport, and (c) feedback transport. (d) To compare the distributions along the transport axis, the vertical average of the region of interest (in a-c, between white dashed lines) is plotted together for all three cases. Note that in all the figures 1 pixel in the camera image corresponds to ~ 457 nm inside of the cavity (see Section 2.3.5). Figure from Ref. [67].

Our high-bandwidth FFPC: supplementary material

D.1 Cavity finesse degradation and permanent damage

Since the start of operation of the fiber-cavity experiment, an unexpected gradual degradation of the cavity finesse was observed [75]. On the 14/10/2020 a pump runaway self-bakeout incident occurred that resulted in the loss of the cavity finesse. It was not possible to recover it with an oxygen treatment as usual. Attempts to clean the cavity mirror with powerfull laser from the cided resulted in the permanent damage.

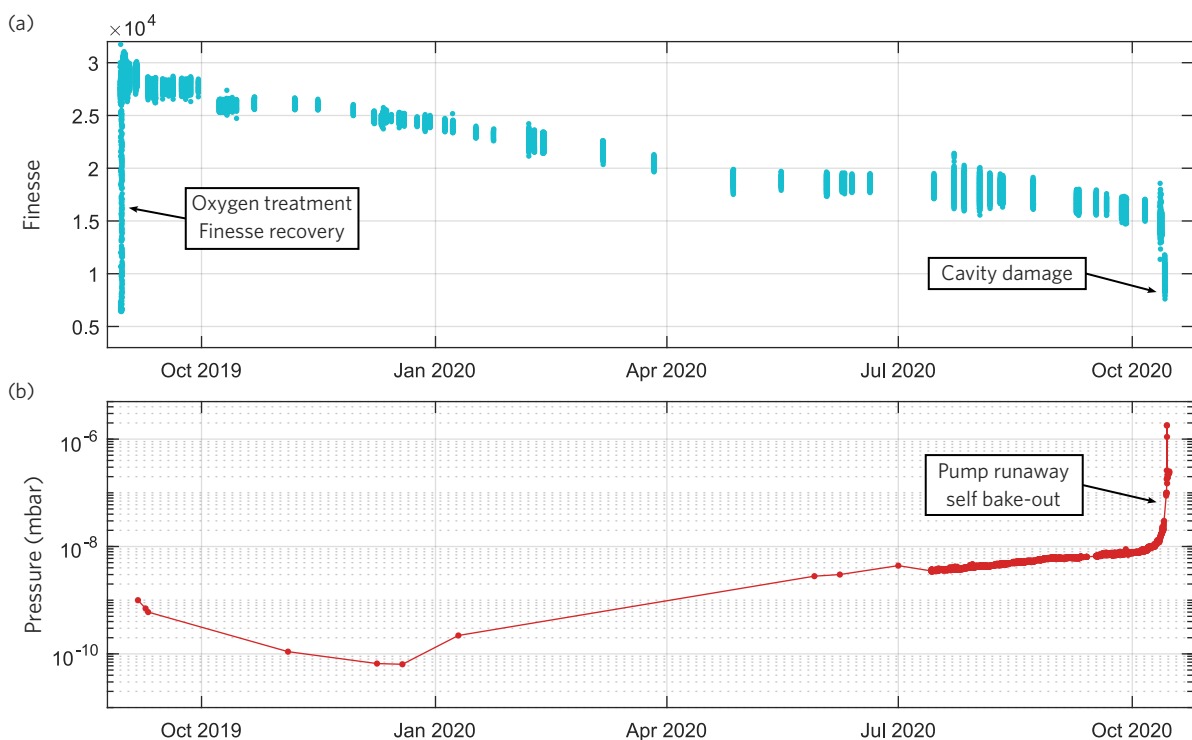


Figure D.1: Finesse decay and cavity damage. (a) Finesse degradation and (b) pressure rise in the vacuum system, recorded over the course of the last year of the cavity life, that ended on the 14/10/2020 the pump runaway self-bakeout and the resulting cavity damage.

D.2 Relevant parameters of our FFPC system

Most relevant parameters of the FFPC system in our experiment — and used for the results of this thesis — are compiled in Table D.1. The characterizations and measurements were made in Ref. [75]. Certain discrepancies from the values in Table D.1 to the parameters $(g, \kappa, \gamma) \approx 2\pi \times (80, 41, 3)$ MHz presented in this thesis are due to the finesse degradation of the cavity, presented in Appendix D.1.

Table D.1: Relevant parameters of our FFPC system, as characterized in [75]. The reported parameter uncertainties were either directly measured or propagated from other measurements. The maximum atom-light coupling rate g_{\max} is calculated for the ideal case of a single atom at the center of the cavity at an antinode of the cavity mode. The finesse and the cavity linewidth measurements were performed under normal atmosphere before installing the cavity in the vacuum system [22].

| Parameter | | Value | Extracted from |
|----------------------------|------------------------------|----------------------------------|--|
| Mirrors (HT/LT) | | | |
| Transmission | \mathcal{T} | $(126 \pm 13) / (13 \pm 3)$ ppm | direct measurement |
| Losses (scat. and abs.) | \mathcal{L} | $(26 \pm 5) / (25 \pm 5)$ ppm | finesse and transmission |
| Cavity geometry | | | |
| Length | L_{cav} | (93.36 ± 0.03) μm | lock-probe beat length |
| Mode waist | w_0 | (4.40 ± 0.04) μm | cavity geometry |
| Input mode matching | ϵ_{HT} | $0.60 + -0.02$ | reflection dip asymmetry |
| Cavity spectroscopy | | | |
| Free spectral range | $\Delta\nu_{\text{FSR}}$ | $(1\,606.7 \pm 0.5)$ GHz | cavity length |
| Cavity full width | $\Delta\nu_{\text{FWHM}}$ | (50.8 ± 1.0) MHz | sideband-modulated dip |
| Finesse (780 nm) | \mathcal{F} | $(32\,800 \pm 1\,100)$ | FSR-FWHM ratio |
| Finesse (770 nm) | $\mathcal{F}_{\text{lock}}$ | $(27\,200 \pm 1\,000)$ | FSR-FWHM ratio |
| Pol.-mode splitting | $\Delta\nu_{\text{spl}}$ | (9.0 ± 0.3) MHz | Hänsch-Couillaud setup [180] |
| Lock-probe beat length | d_{beat} | (31.12 ± 0.01) μm | |
| CQED parameters | | | |
| Atom-light coupling | $g_{\max}/2\pi$ | (121.6 ± 1.1) MHz | ^{87}Rb D ₂ -line cycling transition |
| Cavity field decay | $\kappa_{\text{total}}/2\pi$ | (24.5 ± 0.8) MHz | measured cavity linewidth |
| Atomic dipole decay | $\gamma/2\pi$ | 3.03 MHz | rubidium natural decay [111] |
| Single-atom cooperativity | C | (100 ± 4) | |

Acknowledgements

Today marks the start of the last step of an important stage in my life. It has been a long road full of exciting experiences and challenges, ... and coffee, that is now condensed in the ~ 100 pages of this dissertation. Getting here would not have been possible without the help and support of many persons, to whom I am highly grateful.

First, I would like to thank Prof. Dieter Meschede for the opportunity to work in his group. It has been a very motivating experience, and I much appreciate the freedom I was given to follow my curiosity.

A sincere thank you goes to Dr. Wolfgang Alt for all his support and for being always available, and having the best answers and explanations to my many questions and doubts.

This thesis would not be here without three very talented (former) master students, the FCQED Phoenix crew: Pooja Malik, Lukas Ahlheit and Maximilian Ammenwerth. We had a lot of fun in the lab, between linewidth reduction, atom sticking and Raman imaging. You were really hard to convince that we were indeed seeing atoms in the psychedelic camera background!

I am very grateful to my predecessors in the FCQED lab, Miguel Martínez, Jose Gallego and Tobias Macha, who were great teachers, colleagues and friends. A special thanks to Tobi with whom I spent most of the time in the laboratory, and who taught me well how to tame the moody lab. I am also thankful to Hannes Pfeifer and Deepak Pandey, for their support and fruitful discussions.

Big thanks should also go to Manolo Rivera, Gautam Ramola and Richard Winkelmann, my colleagues from the neighboring lab realm of quantum walks, great friends with whom I had very fun times and interesting discussions.

The administrative team made my life at the IAP always easier and always with a smile: huge thanks to Dietmar Haubrich, Annelise Miglo, Fien Latumahina, as well as to the teams of the electronic and mechanical workshops.

Also, I want to thank all the amazing proofreader of my thesis: Nina Stiesdal, Hannes Busche, Lukas, Manolo and Richard. You made a great contribution to this dissertation!

Lastly, a special gratitude to those that supported me during the final writing phase: to Richard, Tangi Legrand and Frank Vewinger for the company and all the interesting and rewarding discussions, and also to the whole NQO team for fully adopting me in their group life.

Un lugar muy especial en estos agradecientos es para Natalia, quien compartió todo este proceso conmigo, en las buenas y en las malas, y siempre me dio su apoyo incondicional. Natalia, no tengo palabras para agradecerte.

Quiero agradecer también a mis padres y hermanos por todo su apoyo durante estos años. Ustedes sentaron las bases para este logro. Finalmente quiero expresar mi gratitud al resto de mi familia que, desde lejos, siempre me hizo sentir su gran apoyo.